ANALYSIS OF THE HYDRODYNAMICS OF RECTANGULAR PLUNGING JETS AND THE SUBSEQUENT SCOURING IN BROKEN-UP ROCK BEDS

by

Jacques Calitz

Thesis presented in partial fulfilment of the requirements for the degree of

Master of Engineering Sciences in the Faculty of Civil Engineering at Stellenbosch University

Supervisor: Adele Bosman

March 2016

Declaration

By submitting this dissertation electronically, I declare that the entirety of the work contained therein is my own, original work, that I am the owner of the copyright thereof (unless to the extent explicitly otherwise stated) and that I have not previously in its entirety or in part submitted it for obtaining any qualification.

Signature: . . . . . .

Date: . . . . . .

Abstract

The scour mechanisms of rock are highly variable, equally so the geotechnical and hydrodynamic conditions of each study area, which complicate the prediction of scouring. Cases such as Kariba Dam and Ricobayo Dam are examples where, due to inadequate scour prediction methods, scouring caused major damage to the downstream riverbed. Rock scouring due to plunging jets is thus an important area of study.

Various studies have been done to predict the scour hole depth and its extent using physical laboratory models and their subsequent empirical formulas. A classification method, the Erodibility Index method (EIM) by Annandale (1995), was also developed to give an indication of the depth of scouring. Physically based methods, such as the Comprehensive Scour Method (CSM) including the Quasi-steady impulsion method (QSI) by Bollaert (2002 and 2014), tried to incorporate several of the rock scour mechanisms, to determine both the depth and extent of the scour hole.

The current study focused on using a 1:40 physical laboratory model to ascertain the applicability of using PVC blocks to replicate rock blocks and the subsequent scouring thereof. The drop height, as well as the tailwater, varied between the different tests. The PVC blocks were able to replicate the scour hole to a relatively good extent and could sustain steep slopes replicating the repose angle of rock. The subsequent scour holes from the physical laboratory models were compared to the depths calculated using empirical formulas and the classification method by Annandale (1995) (EIM). The methods overestimated the depths, and the EIM was found to be very sensitive to both the hydrodynamic and geotechnical boundary conditions. The physically based method proposed by Bollaert (2002) (CSM) overestimated the scour hole extent, as compared to the physical laboratory model scour hole, but the scour hole profile (shape and depth), was in agreement.

The use of Computation Fluid Dynamics (CFD) to simulate hydraulic problems has become more viable, due to advancements in computational power. The hydrodynamic characteristics of the jet in the air and in the plunge pool was modelled in 2D using FLUENT, as the scour mechanisms of rock cannot presently be modelled using commercial CFD codes. The hydrodynamic conditions in the air were modelled with good comparison to both that of the physical laboratory model, as well as the calculated conditions of

the jet in the air, while the hydrodynamic conditions (velocity and pressure) in the plunge pool were overestimated in comparison to current methods available, as used in the EIM as well as the CSM and QSI methods, due to possible flow confinement and deflection effects.

In conclusion, the study firstly confirmed the applicability of using PVC blocks to model scouring due to plunging jets in rock beds, and secondly it established the use of current scour prediction methods in validating small scale scour hole profiles (shape and depth). The use of 2D CFD modelling, in predicting the hydrodynamic conditions of the plunging jet in the air and plunge pool, was also introduced with relative success.

Opsomming

Die voorspelling van erosie is gekompliseerd as gevolg van erosie meganismes van rots wat baie wisselend is, asook die unieke geotegniese en hidrodinamiese kondisies van elke area wat bestudeer word. Gevalle soos Kariba Dam en Ricobayo Dam is goeie voorbeelde waar, as gevolg van onvoldoende erosie voorspellings metodes, die rots erosie grootskaalse skade aan die stroom-af rivierbedding veroorsaak het. Rots erosie wat deur vallende water strale teweeggebring is, is dus 'n baie belangrike area en vereis deeglike navorsing.

Verskeie studies is al gedoen om die diepte en omvang van die resulterende erosiegat te bepaal deur gebruik te maak van fisiese modelle en die daaropvolgende emperiese formules. 'n Klassifiserende metode, die Erodibility Index method (EIM) deur Annandale (1995), is ontwikkel om 'n indikasie van die erosie diepte te gee. Fisies gebaseerde metodes, soos die Comprehensive Scour Method (CSM) insluitend die Quasi-steady impulsion method (QSI) deur Bollaert (2002 en 2014), het soveel moontlik gepoog om van die rots erosie meganismes te inkorporeer, om beide die diepte asook die omvang van erosie van die erosie gat te bepaal.

Die huidige studie is toegespits op die gebruik van 'n 1:40 fisiese model om die toepaslikheid van die gebruik van PVC blokke om rots blokke na te boots en die daaropvolgende erosie vas te stel. Die valhoogte, asook die plons dompel waterhoogte, is verander tussen toetse. Die PVC blokke was instaat om die erosie gat redelik goed na te boots en kon 'n steil gradiënt volhou aan die sykante van die erosie gat. Die daaropvolgende erosie gate van die fisiese model is vergelyk met die dieptes soos bepaal deur die emperiese fomules, asook die dieptes van die klassifiserende metode deur Annandale (1995) (EIM). Die metodes het die dieptes oorskat en die EIM metode was baie sensitief in terme van die hidrodinamika en geotegniese grens kondisies. Die fisiese gebaseerde metodes, soos ontwikkel deur Bollaert (2002) (CSM), het die erosie gat se omvang oorskat in vergelyking met die fisiese model. Die erosie gat profiel het wel ooreengestem met die profiel van die fisiese model.

Die gebruik van Computation Fluid Dynamics (CFD) om hydroliese probleme te simuleer is deesdae meer uitvoerbaar, as gevolg van die vooruitgang in rekenaartegnologie en kapasiteit. Die hidrodinamiese

eienskappe van die water straal in die lug, asook in die dompel poel, is gemodelleer in 2D, deur gebruik te maak van FLUENT. Die erosie meganismes kan huidiglik nie deur kommersiele CFD sagteware gemodelleer word nie. Die gemodelleerde hidrodinamiese toestand van die water straal in die lug het goed ooreengestem met beide die fisiese model asook die berekende eienskappe. Die hidrodinamiese aspekte in die dompel poel (druk en snelheid), is oorskat in vergelyking met die huidig beskikbare metodes om die hidrodinamika van die water straal te bepaal soos gebruik in die CSM en EIM metodes. Die geskatte waarde van die hidrodinamiese toestande was groter – dit kan toegeskryf word aan die moontlike effek van defleksie en beperking van watervloei.

Ter opsomming, die studie het eerstens vasgestel wat die toepaslikheid van PVC blokke is om rots erosie as gevolg van water strale te modelleer en tweedens het die studie vasgestel dat huidige erosie vooruitskattings metodes gebruik kan word vir klein skaalse modelle. Die gebruik van 2D CFD modelle, om die hidrodinamiese kondisies van water strale in die lug en dompel poel te beraam, is met redelike sukses toegepas.

Table of Contents

List of figures

List of tables

List of symbols

A	Plunging jet footprint at plunge pool free surface (impact area of jet) (m^2)
A	Surface area of the block impacted by the impulse force (m^2)
a	Acceleration of the block caused by the unbalanced force (m/s^2)
a	Size of rock blocks (m)
a	Width of channel (m)
A_i	Jet footprint (impact area of jet) at different elevations below water surface (m^2)
b	Jet or channel with at issuance
b	Height of channel (m)
B, D_j	Jet thickness at impact with free surface (m)
B_g	Core thickness of rectangular jet (m)
B_i	Approach flow depth over the spillway or the initial jet thickness (h_0 in some literature)
B_j	Impingement thickness of the jet (m)
B_u	Half of the thickness or diameter of the jet at impact with the plunge pool free surface (m)
C'_p	Fluctuating pressure coefficient
C_{air}	Pressure wave celerity in air.
C_j	Mean air-wave speed or wave celerity (m/s)
C_{liq}	Pressure wave celerity in water.
C_p	Average dynamic pressure coefficient
C_{sp}	Average stream power decay coefficient
D	Mean block diameter (m)
d	Diameter of a sphere with the same volume as a water drop (m)
D_h	Hydraulic diameter (m)
D_i	Thickness (B_i) or diameter (D_i) of jet at issuance (m)
D_{in}	Minimum diameter of the core (m)
D_j	Diameter of core at impact with free surface of plunge pool (impact diameter) (m)
d_r	Characteristic size of a mean/average rock block (m)
d_s	Mean particle diameter (m)
d_s	Particle diameter representing a cumulative percentile (m)
F	Froude number
F	Unbalanced force due to maximum pressure fluctuation (N)
g	Gravitational acceleration (m/s^2)
H	Vertical fall distance or Drop height (Z in some literature).(m)
h_0	Energy head at the crest of the weir (flow depth over weir) (m)
H_m	Mean head at plunge pool (m)
h_v	Velocity head (m)
J	Jet length
J_a	Joint alteration number

J_n	Joint set number
J_p	Length of jet core
J_r	Joint roughness number
K	Bulk modulus of elasticity of mixed fluid (N/m^2)
k	Turbulent kinetic energy
K	Proportional coefficient for break-up length of rectangular jet or nappe flow
K_2	Coefficient allowing for air resistance
K_b	Particle/block size factor
K_d	Interparticle bond (discontinuity shear) strength factor
K_h	Erodibility index (EI)
K_h	Erodibility index/ resistance of bed
K_m	Mass strength factor
K_s	Relative shape and orientation (ground shape) factor
L	Characteristic length
L_b	Break-up length (m)
L_f	Joint or fracture length (m)
L_j	Trajectory length (L in some literature) (m)
L_{sc}	Scour length (m)
m	Mass of the block (kg)
P	Magnitude of agitating agent (stream power)/ rate of energy dissipation
P_{mean}	Relative pressure or average dynamic pressure at the bottom of the pool (N/m^2)
q	Unit discharge or proportional discharge (at issuance) ($m^3/s/m$)
Q	Discharge at issuance (m^3/s)
q	Unit discharge at issuance ($q = Q/b$) where b = issuance channel width ($m^3/s/m$)
Q	Volumetric discharge of jet (m^3/s)
r	Radial distance from the centreline of the jet (m)
r_{max}	Maximum radial distance from centreline (m)
RQD	Rock quality designation
S	Source term
t	Time
T_u	Initial turbulence
U	Mean velocity at issuance (m/s)
u’	Instantaneous RMS (root-mean-square) value of axial velocity fluctuations at issuance (m/s)
V	Mean flow velocity (m/s)
V	Velocity at the point (m/s)
V(Z)	Velocity at depth Z (m/s)
V_{air}	Minimum jet velocity required to entrain air (m/s)
V_b	Volume of the rock block (m^3)
V_i	Issuance velocity (U_0 or V_0 in some literature) (m/s)
V_j	Velocity at impact with plunge pool free surface (m/s)
V_z	Jet velocity at depth z from the plunge pool free surface
X	Distance along trajectory from issuance (m)

x	Horizontal distance along trajectory (m)
x	Horizontal distance travelled by the jet
x_1	Horizontal distance to point of maximum scour (m)
y	Vertical distance along trajectory (m)
Y	Plunge pool depth (m)
y_0	Tailwater level (m)
y_b	Brink depth (m)
y_c	Critical depth (m)
y_s	Scour depth (m)
Z	Depth below plunge pool free surface (m)
Z_{core}	Distance for jet to become developed or diffused generally taken as 4-5 times D_j (diameter of the core at impact) (m)
α	Adjustment factor (for air entrainment)
Γ	Diffusion coefficient
ΔE	Energy loss in terms of head per unit length of flow (m)
Θ'	Angle of impact with plunge pool (β other literature)
ρ_0, ρ_{liq}	Density of fluid (kg/m^3)
ρ_a, ρ_{air}	Density of air (kg/m^3)
σ	Surface tension of water
Φ	Kinetic energy velocity coefficient
IC	Initial condition at issuance
P	Mean pressure (dynamic)
V	Total volume (m^3)
We	Weber number
u	Characteristic velocity in domain (m/s)
β	Volumetric air water ratio or free air content.
β	Percentage of free air content (%)
ε	Lateral spreading of the jet (m)
ε	Viscous dissipation
θ	Issuance angle (°)
μ	Dynamic molecular viscosity
μ	Dynamic molecular viscosity of cell (subscript 1 and 2 refers to the phases)
ν	Kinematic viscosity (m^2/s)
ξ	Jet lateral spread distance. (m)
ρ	Fluid mixture density
ρ	Density of the cell (subscript 1 and 2 refers to the phases)
ρg_i	Gravitational body force
ω	Specific dissipation rate
ω	Specific dissipation rate
ϕ	Dependent variable (scalar quantity)
$-\overline{u_i' u_j'}$	Specific Reynolds stress tensor (turbulence stresses)
$\widetilde{G_k}$	Generation of turbulent kinetic energy due to mean velocity gradients
T_u^*	Initial turbulence intensity of a nappe spillway

u_i'	Axial velocity fluctuations
h_{up}	Height through which particle is lifted (m)
$h_{up}\ and\ h_{down}$	Upstream and downstream wall jet thickness (m)
$\Gamma_k\ and\ \Gamma_\omega$	Effective diffusivities
A_{exp}	Exposure area of rock block (m2)
C_I	Net upward pressure coefficient
C_d	Discharge coefficient
C_d	Drag coefficient of sphere
C_{joint}	Joint pressure coefficient
C_{surf}	Surface pressure coefficient
C_{uplift}	Net uplift pressure coefficient
D_h	Hydraulic radius (m)
D_{out}	Outer diameter of jet at impact with plunge pool free surface (m)
D_ω	Cross-diffusion term
$F_{\Delta t}$	Net impulse on the block (BS3D) (N.s)
F_0	Total downward impulse due to fluctuating pressure on the block (N)
F_{QSL}	Quasi-steady uplift force
F_i	External body forces and other source terms
Fr_i	Initial Froude number
F_{sh}	Total shear and interlocking forces - instantaneous (N)
F_u	Total upward impulse due to transient pressure in joint (N)
G_ω	Generation of ω
$I_{\Delta t,pulse}$	Impulse on rock block (Ns)
J_x, J_y, J_z	Average spacing of joint sets (in meters)
P_{pool}	Stream power in the pool at a certain depth (W/m2)
$S_k\ and\ S_\omega$	Defined source terms
U_i	Mean velocity (i^{th} direction fluid velocity component)
$V_{\Delta t,pulse}$	Average velocity experienced by rock block during time period
$V_{\Delta t}$	Initial velocity (m/s)
V_{air}	Volume of air (m^3)
V_i	Velocity at issuance (m/s)
V_{liq}	Volume of liquid (m^3)
W_g	Submerged weight of rock block
$Y_k\ and\ Y_\omega$	Dissipation of k and ω
q_{total}	Initial discharge (before impact with bottom) ($m^3/s/m$)
$q_{up}\ and\ q_{down}$	Up and downstream deflected discharges
x_b	Length of the block (m)
x_i	Coordinate component
y_0	Flow depth over the structure i.e. overflow weir (critical depth) (m)
z_b	Height of the block (m)
γ_b	Unit weight of rock blocks (N/m^3)
γ_m	Unit weight of the mixture (N/m^2)
$\gamma_m QH$	The power stays the same of that at impact with plunge pool free surface (W)
δ_{ij}	Kronecker delta

δ_{out}	Outer or lateral spread of jet (^{0})
λ_b	Material unit weight (N/m^3)
λ_s	Unit weight of good quality material (rock) (N/m^3)
μ_T	Turbulent or eddy viscosity
ρ_i	Average density of the air entrained jet at impact with plunge pool free surface (kg/m^3)
ρ_{liq}	Density of the air water mixture (kg/m^3)
ρ_s	Mass density of rock (kg/m^3)
ρ_w	Density of water (kg/m^3)
α_2	Volume fraction of secondary phase
Δt	Maximum duration (s)
$\Delta t, pulse$	Time interval of certain pressure pulse (s)
Δx	Smallest cell size in domain (m)

List of acronyms

2D	Two dimensional
3D	Three dimensional
CFD	Computational fluid dynamics
CFM	Comprehensive fracture mechanics
CSM	Comprehensive scour model
DI	Dynamic impulsion
DNS	Direct numerical simulation
EI	Erodibility index
EIM	Erodibility index
FDM	Finite difference method
FVM	Finite volume method
LES	Large eddy simulation
PISO	Pressure implicit with splitting of operators
QSI	Quasi-steady impulsion
RANS	Reynolds averaged Navier-Stokes equations
RMS	Root-mean-square
RNG	Renormalised group
RQD	Rock Quality Designate
SIMPLE	Semi-implicit method for pressure-linked equations
SIMPLEC	Semi-implicit method for pressure-linked equations corrected/consistent
SST	Shear stress transport
UCS	Uniaxial compressive strength
UDF	User defined functions
VOF	Volume of fluid

1 Introduction

1.1 Background

Plunging jets is a measure used to relieve dams of excess water to the downstream river below, especially in an event such as flooding. If the erosive capacity of the jet is large enough, which it normally is for high-head dams, a scour hole forms in the downstream plunge pool. If the extent of the scour hole becomes excessive, it can endanger the dam and surrounding structures. Estimation of the ultimate scour hole geometry is thus paramount during the design stages of the dam to ensure the structure is not endangered by the scour hole during its lifetime. Scour mechanisms responsible for scour holes are unfortunately difficult to assess, especially in the case of rock beds. Several studies have been undertaken to try to incorporate the hydraulic properties of the plunging jet, as well as the rock mass properties, to try and estimate the scour hole depth and extent. Due to the complexity of the different scouring mechanisms of rock, no perfect formulation has been developed encompassing all the rock scouring mechanisms, which in turn has led to multiple cases of scouring occurring where inadequate estimation methods were applied. Well known cases, such as Kariba Dam and Ricobayo Dam, where scouring has occurred and endangered the structure, are good examples where accurate prediction methods could have limited or eliminated the adverse effects on the downstream riverbed as well as the grade control structure.

1.2 Objectives and motivation

An extensive literature study, regarding scouring of rock beds due to rectangular plunging jets, brought to light that:

- Previous physical laboratory model studies, which tried to simulate the scour hole profile (shape and depth), were not able to correctly model the rock scour mechanisms, including the extent of the scour hole. Physical laboratory models have been able to model one or the other, but not both simultaneously. Cohesive or non-cohesive sediment with a binder was used rather than non-cohesive sediment as the latter could not sustain steep slopes, which are present in prototype rock scour

holes, and the density of the non-cohesive sediment misrepresented the prototype rock. There was thus a need for further study in trying to model the scour hole profile (shape and depth) using a physical laboratory model material to simulate the broken up rock bed and the scour mechanisms of rock correctly.

- The current preferred physically based methods, used to determine the scour hole depth and extent, are the Erodibility Index Method (EIM), developed by Annandale (1995), which is a classification method, as well as the Comprehensive Scour Model (CSM), which includes the Quasi-Steady Impulsion Method (QSI), which was developed by Bollaert (2002 and 2014). These methods were developed for prototype conditions. The latter method was also developed for circular jets rather than rectangular jets. There was thus a need for further study into the applicability of using the methods for smaller scale studies, as well as their validity when examining rectangular jets. Very little literature was also available on the application of the Quasi-Steady Impulsion Method; consequently, further validation of the method was required.
- Computational fluid dynamics (CFD) methods have been used more frequently as there have been advancements in the computational power available. The use of CFD methods on plunging jets has been mainly focused on sediment beds or determining the hydrodynamic characteristics of the plunging jet. CFD, however, has not been compared to the current methods in determining the hydrodynamics of the jet, as used by the scouring prediction methods (EIM and CSM including QSI), or used in conjunction with the rock scour prediction methods.

The main objective of this study was, therefore, to provide clarification and possible solutions to some of the above limitations in current literature and to give a clearer understanding on the available scour prediction techniques.

1.3 Methodology

PVC blocks have been used in physical laboratory model studies to simulate scouring of the broken up rock mass for an unlined spillway, at the University of Stellenbosch, South Africa [134]. The PVC blocks produced relatively good results and could sustain steeper slopes in comparison to non-cohesive sediment (without the use of a binder). Steeper slopes are characteristic of prototype rock scour holes. The use of

PVC blocks in the physical laboratory model, to replicate the broken up rock mass, was subsequently proposed in order to examine the extent of the scour hole and to determine the possible regression towards the issuance structure. The use of PVC blocks has not been considered previously in physically modelling rock scouring due to plunging jets.

The current methods used for predicting rock scouring, are mainly physically based and attempt to incorporate all the mechanisms of rock scouring. The main methods include the Erodibility Index Method, as well as the Comprehensive Scour Model including Quasi-Steady Impulsion Method. Other methods are also available, but their applicability to rock blocks and their confidence level and complexity make them less desirable. The author proposed using the current prediction methods to compliment the physical laboratory model, as the physical laboratory model was based on a hypothetical prototype case. The methods available were, however, developed for prototype conditions and no literature was found demonstrating their applicability in applying them to small-scale models. As the physical laboratory model was to use rectangular jets, the applicability in using the methods for rectangular, rather than circular jets, was also to be established. The CSM and QSI prediction methods were also used to determine if the PVC blocks could replicate the scour hole formed in rock beds, as the prediction methods have been used with relative success in assessing prototype rock scour hole geometries.

The study looked at the validity of using CFD models for the representation of a free falling jet and whether the produced results were applicable for use in place of, or in conjunction with, the physically based scour prediction methods. Due to the fact that CFD models are currently unable to model the scouring mechanisms of rock, CFD was proposed to simulate the hydrodynamic characteristics of the jet in the air and plunge pool, as well as at the rock bed. The pre-excavated and fixed bed positions, as determined from the physical laboratory model, were used in conjunction with the DI and QSI scour profile calculations. The results from the CFD modelling were subsequently evaluated by comparing the simulation results with the actual results from the physical laboratory model and the results from the calculated values of the methods used in the CSM and EIM method (velocity decay, pressures and jet characteristics).

Physically based methods are used in this thesis to describe the methods (CSM including QSI and EIM) which take into account the physical processes involved in rock scouring.

1.4 Report contents

The report consists of two main parts, namely the literature study (Section 2 and 3) and the results of the scour analysis (Section 4, 5 and 6). Each of the parts was subsequently split into several sections as described below. The report layout is shown graphically in Figure 1-1.

Literature review

- Section 2 gives a brief background on scouring of plunging jets in rock beds as found in literature.
- Section 3 includes a discussion on all the current scour prediction techniques, which includes the physical laboratory model, empirical formulas and physical based prediction techniques.

Scour hole analysis

- Section 4 describes the set-up conditions and results from the 1:40 scale physical laboratory model.
- Section 5 includes the results of the empirical formulas and physically based (EIM and CSM including the QSI method) scour prediction methods. A comparison with the physical laboratory model results (Section 4) is also included.
- Section 6 contains a discussion on CFD and the subsequent results of the CFD modelling. A comparison of the results of the physical laboratory model (Section 4) with the physically based prediction methods (Section 5) is also included.

Section 7 and 8 includes the conclusions and recommendations.

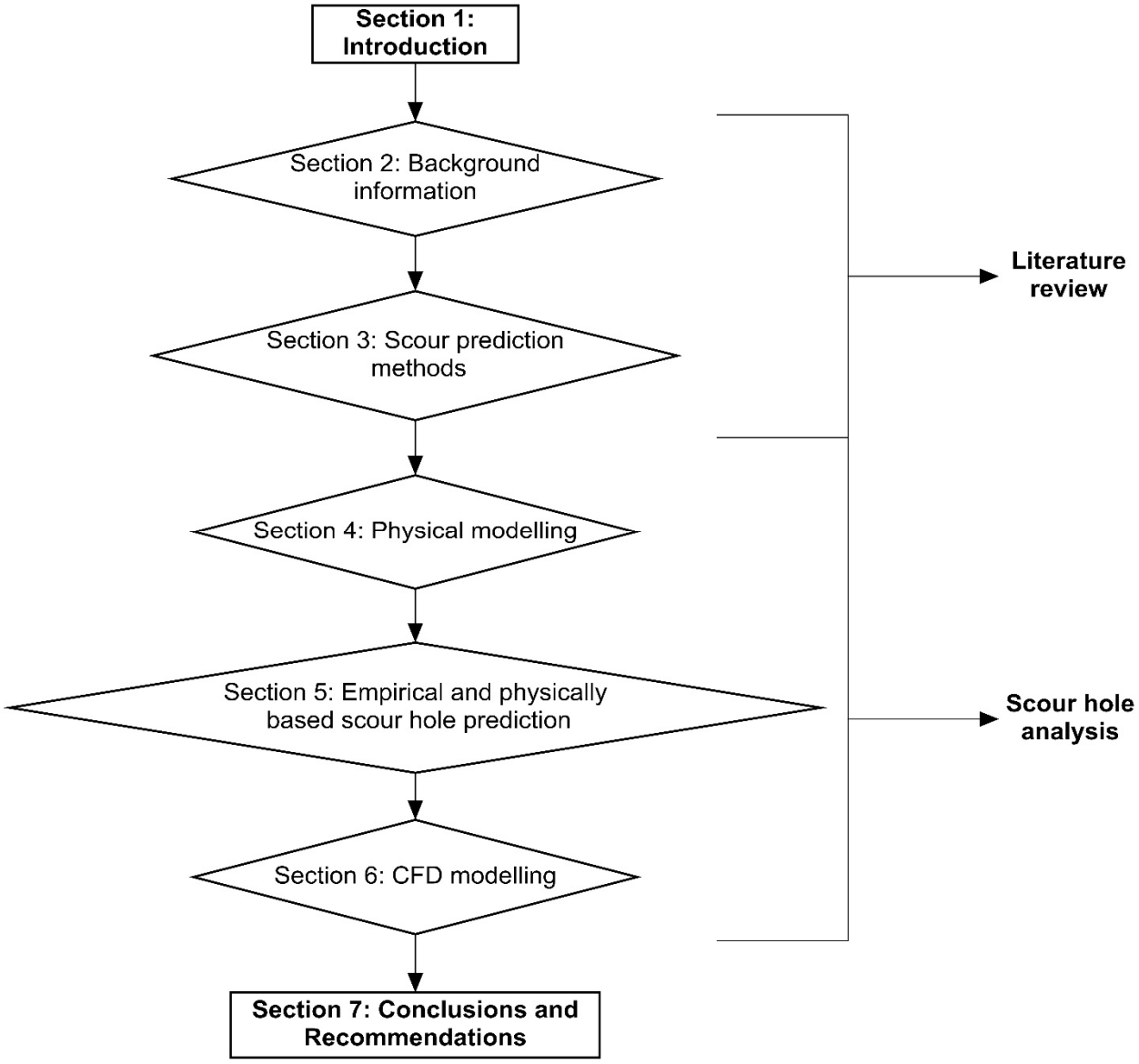

Figure 1-1 - Report structure

The terms scouring and erosion as well as free falling and plunging have been used interchangeably in this thesis.

2 Literature study, Part A: Background information

Free falling, or plunging jets, are often used to pass excess flood water from dams to the watercourse below (downstream river), which inevitably leads to the formation of a scour hole in the plunge pool below the dam. A plunge pool is an economic energy dissipater as it acts as a deceleration zone, which decreases the flow velocities and causes high turbulence. It, however, needs to be ensured that the scour hole occurs at a sufficient distance from the structure; simultaneously, the scour depth should not become excessive as this would endanger the structure [6].

The discussion that follows explains briefly the basics of rock scouring and primarily focuses on the scouring due to plunging jets.

2.1 Scouring types

The common types of scouring that can occur can be split into two main processes or types: general and local scouring [1,2,3]. General and local scour are both discussed below.

2.1.1 General scour

General scour occurs due to changes in the natural flow, or sediment load, or supply, for example due to flooding [4]. General scour is generally caused by long-term unidirectional velocity gradients. General scour is characteristic by typically having a time scale that is longer than local scour, primarily affects longitudinal riverbed changes over large distances and is predominantly a result of natural processes. It can, however, also occur over a short time period in cases such as flooding. There are several general scouring types, namely overall degradation, constriction scour, bend scour and confluence scour.

2.1.2 Local scour

Localised scouring occurs due to the impact or influence of human-imposed hydraulic structures on the natural flow structure such as in cases pertaining to dams and piers. Vortex formation and dissipation, which occur due to the influence of structures, can cause local scour. Local scour is usually superimposed

on general scour and is reliant on the type of structure that affects the flow structure. Local scour also generally occurs within a short distance of the influencing structure [4]. Plunging jets discharged from dams can be classified as a form of local scour.

2.2 Scouring in different transport regimes

The process of local scouring, principally on sediment beds, can in turn be split up into two main regimes of sediment transport, namely clear water and live bed scour. These regimes become applicable in cases such as where smaller fractured rock particles are transported or are going to be transported out of the rock matrix [1,2,15]. The two transport regimes are discussed below.

2.2.1 Clear water scour

Clear water scour occurs in the absence of general scour, as well as when no sediment transport occurs from the upstream flow to the downstream flow. The sediment concentration equals zero in the upsteam flow in clear water scour conditions [148]. Clear water scour is characteristic of a static equilibrium scour hole state, which is reached when the rock particles or fragments are no longer removed by the local flow. Clear water scouring is usually associated with deeper scour holes compared to live bed scour, as there is more transport capacity. It is generally easier to analyse than live bed scour as the effect of the suspended particles complicates the analysis of the scour hole. Clear water scour can occur when the upstream flow is at rest, for example in the case of a dam.

2.2.2 Live bed scour

Live bed scour is general scour superimposed on local scour. Live bed scour occurs when the upstream flow transports sediment downstream and can be described as the continuous transport of particles. The sediment concentration of the upstream flow is equal to one [148]. A dynamic equilibrium state of the scour hole is reached when the rate of upstream sediment transport equals the rate of material eroded from the scour hole by the local flow. Sediment transport decreases the erosive capacity of the water because a part of the transport capacity has already been expended. Live bed scour is also more variable with time, compared to clear water scour, as illustrated in Figure 2-1.

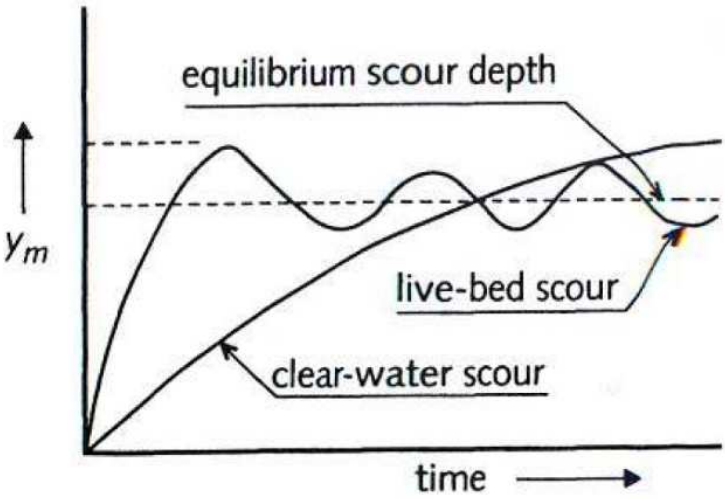

Figure 2-1 - Scour depth (live and clear water) as a function of time [1]

Bed load and suspended load can occur in general as well as live bed scouring. Suspended load occurs when particles, mostly fine particles, are entrained in the flow. Bed load occurs when the particles, primarily coarser or larger particles, are dragged or rolled along the bed. Dissolved load can also occur for some rock types and occurs when chemicals in solution are transported by the flow [5,16]. A graphic representation of the three particle transport processes is shown in Figure 2-16.

The condition of the scour hole depth can be in two states, either dynamic or static, similar to the conditions as discussed above for clear water and live bed scouring. A dynamic scour depth generally takes place when a flood occurs and the particles are in suspension in the scour hole, and are consequently not transported downstream or eroded out of the scour hole. A static scour depth conversely occurs after the flood has passed and when the particles, which were suspended during flood conditions, are no longer suspended, and have now settled into the scour hole. These scour hole conditions are especially noticeable in sediment beds [6]. The static scour depth is generally lower than the dynamic scour depth and when considering the maximum equilibrium depth, the dynamic case should be considered [6].

2.2.3 Phases of scour hole

The scour hole evolution is characterised by four general phases, namely initiation, development, stabilisation and equilibrium phase. The maximum scour hole depth is generally reached at the equilibrium phase as this phase represents the stage where the local flow is unable to transport or erode the particles [3].

2.3 Free falling jet

2.3.1 Spillways

Free falling or plunging jets can be described as jets (water jets in this case) that pass through an unbounded medium, such as air, below grade control structures such as dams. Free falling jets can occur downstream of several spillway types [7,8]. Three of the main spillway types that produce free falling jets, primarily for arch dams, are shown in Figure 2-2 to Figure 2-4 in Table 2-1.

Table 2-1 - Spillway types

Overflow spillway	**Ski jump spillway**	**Spillway outflow under pressure**
Overflow or overtopping spillway also referred to as surface spillways [9] or nappe e.g. Baserca Dam, Spain. 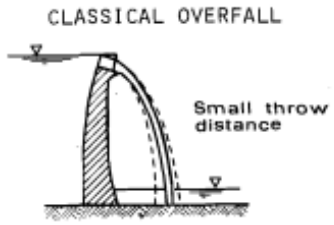 ***Figure 2-2 - Overflow nappe [24]***	Chute spillways with flip bucket or ski jump e.g. Tarbela Dam, Pakistan (ski jump) - Flow deflected at toe. 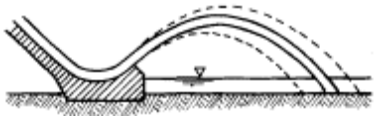 ***Figure 2-3 - Ski jump spillway [82]***	Gates underneath dam (outflow under pressure) e.g. Cahora-Bassa Dam, Mozambique. 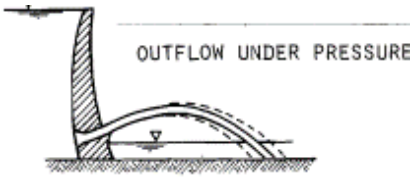 ***Figure 2-4 - Spillway outflow under pressure [82]***

Free falling jets can be rectangular (plane) or circular (axial symmetry) in shape and are dependent on the issuance conditions, for example the spillway characteristics such as the sluice gate geometry [1,148]. Pressure fluctuations at the plunge pool bottom, for plane rectangular jets, have been found to be higher than circular jets, which were presumed to be due to the non-symmetrical diffusion and spreading of the rectangular jet. Circular jets conversely diffuse more symmetrically or radially, while rectangular jets diffuse laterally or uni-directionally [10,11]. It should, however, be noted that when the cross sectional average velocity for different jet geometries was considered, the different cross sectional effects were found to be relatively small [6].

2.3.2 Multiple jets

Multiple jets can be discharged from high-head dams to pass the excess floodwater from the upstream watercourse [12]. The different jet spacing configurations can have different effects on the downstream impact area. The spacing of the jets can be adjacent or non-adjacent to each other.

2.3.2.1 *Non-adjacent jets*

Non-adjacent jets occur when two or more jets are discharged from sluice gates spaced one or more sluice gate apart (non-adjacent). It has been found that only partial mixing of the non-adjacent jets occurs in the air due to the distance between the jets. At the impact with plunge pool free surface the mixed part is generally the most critical part to consider for scouring (see Figure 2-5) [12].

2.3.2.2 *Adjacent jets*

Adjacent jets occur when two or more jets are discharged from sluice gates next to each other (adjacent). The adjacent jets have been found to form one large jet core in the air. No diffusion of the jets occur due to them being adjacent to each other as shown in Figure 2-5 [12].

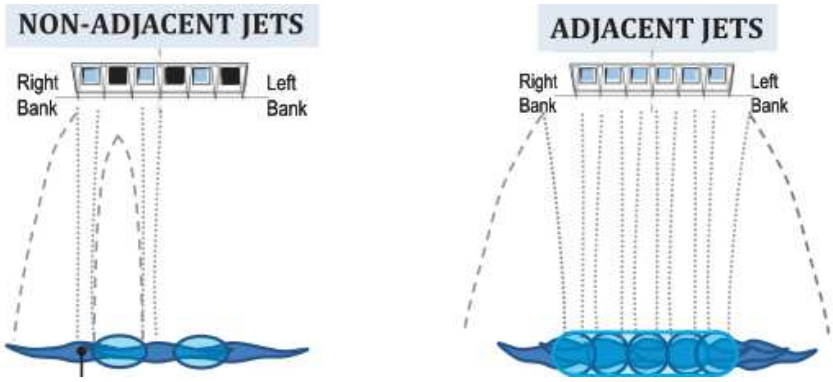

Figure 2-5 - Non-adjacent and adjacent jets [12]

Studies have been done using jets that are spaced or offset vertically, as opposed to horizontally as described above, and combinations of a wall (underflow) and plunging jets have also been tested [13,14].

2.3.3 *Jet regions*

As the plunging water jet moves through the air and water (plunge pool), two distinct jet regions with different characteristics have been identified, namely the undeveloped and developed jet region (refer to Figure 2-6) [1,15,16].

2.3.3.1 *Undeveloped jet region*

The undeveloped jet region is characterised by the solid or potential core region, which is non-aerated and has been found to have a high erosion potential. The potential core acts as a momentum sink and preserves the erosive power of the jet. An aerated shell of water generally surrounds the potential core. As the jet falls from a height through the air, or as it travels through water, the core region contracts in respect to its width and the velocity is assumed equal to the efflux in this region (potential core).

2.3.3.2 *Developed jet region*

The developed jet region occurs when the jet falls from a high enough height or in the case where it enters and moves through a deep enough plunge pool, the jet core contracts completely. When the undeveloped jet region breaks up and loses its coherence it can be described as a developed jet region. In the case of the free falling jet the outer disturbances increase to where the pressure fluctuations penetrate the undeveloped jet's core and the jet core loses its coherence and becomes developed [8].

A jet can further be classified as either submerged or unsubmerged (free falling). A submerged jet is said to occur if the jet is of the same fluid as the surrounding stationary medium [1].

2.4 Boundary conditions

To model and analyse a problem correctly by means of physical laboratory models, computer models or mathematical formulas, the boundary conditions need to be defined correctly to ensure accurate representation of the prototype or reality conditions.

2.4.1 Boundary conditions

To assess scouring, the loading and strength parameters of the domain needs to be specified. The loading parameters are defined by the hydraulic boundary conditions, while the strength parameters are defined by the geotechnical and morphological boundary conditions. The flow pattern is characterised from the loading and strength parameters and is a measure of the erosion and it is thus paramount for accurate boundary conditions to be defined [1]. Some of the most important boundary condition factors for hydraulic, geotechnical and morphological aspects are summarised in Table 2-2 as found in literature [43,117].

Table 2-2 - Boundary conditions

Rock boundary conditions	
Hydraulic boundary conditions	Flow velocities, water levels (tailwater level, depth of flow over the spillway), discharge and turbulence intensity at issuance, jet geometry at issuance and impact, fall or drop height, velocity at impact at the plunge pool [16]. Fluid density and kinematic viscosity [1].
Morphological and geotechnical boundary conditions	Rock mass type (sedimentary, igneous and metamorphic) Material density Rock mass structure Depth of rock layers Rock quality designate (RQD) Uniaxial compressive strength of the rock (UCS) Uniaxial tensile strength (tensile properties of rock) Young's modulus of elasticity Rock mass discontinuities (joints and fracturing condition, degree and orientation) Number of joint sets Joint set: dip angle and dip direction, persistency, typical length, spacing, width, friction angle Faulting and bedding plane spacing Size of the rock blocks Fatigue failure properties and the rocks fracture toughness Weathering of rock mass and joint fill material [7] Cohesive strength of rock - resistance to shear forces of secondary currents and periphery of scour hole and between blocks. Ideally, a scour hole should confine the water jet [8].

The basic form of any bed material can be characterised into two main gels, namely physical and chemical gels. Physical gels are characterised as discrete elements touching each other, such as non-cohesive sediment and highly fractured or weathered rock. With chemical gels on the other hand, the sediment and rock particles or blocks are connected by fixed bonds, such as cohesive sediment, cemented soil and intact rock [96].

The geographic and geotechnical conditions of the study area should always be taken into consideration and explored to ensure an accurate representation of the prototype conditions. For example, an existing bay of stronger material on the one side of a downstream river channel can cause the lateral hydraulic forces to be reflected and subsequently increase the in scour in other areas and can displace the position of the maximum scour depth [17]. Another case is where the ground conditions, such as the rock and sediment type or structure, varies with depth and thus increases the difficulty in predicting the scour depth as the resistance to scouring differs with depth [18]. The width of the downstream channel is also an important factor to take into account [16]. Kariba Dam is an example where the UCS and type of jointing of the rock differed at the downstream North and South banks which shifted the position of the maximum scour depth [12].

It is thus paramount to ensure the boundary conditions (hydrological, geotechnical and morphological) are defined correctly as they influence the scouring potential and extent. Some of the above-mentioned boundary conditions are explained in more detail in later sections.

2.4.2 Type of rock

The type of rock, which the rock bed consists of, is one of the most important boundary conditions to consider. There are three main rock types or groups, which are summarised in Table 2-3 [3].

Table 2-3 - Rock types

Rock type	Definition and mode of formation	Rock families
Igneous	Formed from the solidification and crystallisation of molten silicate magma. Care should be taken if weathered and vesicular.	Granite, diorite, gabbro, rhyolite, andesite, basalt, serpentine
Metamorphic	Formed by heat and pressure effects on igneous and metamorphic rocks. Care should be taken if weathered.	Slate, phylite, schist, gneiss, marble
Sedimentary	Formed by the sedimentation and lithification of mineral grains. Care should be taken if poor tabular shape and abrasion resistance.	Quartzite, sandstone, siltstone, shale, limestone, chalks

2.5 Mechanisms of scour

The mechanisms of scouring can be split into two main sections of focus. The first section is the hydraulics of the jet that includes the jet impingement in the air and into the plunge pool (liquid phase) and aeration of jet in the air and plunge pool (gaseous phase) (Section 2.5.1). The second section is the resistance of the rock or bed material (solid phase) (Section 2.5.2).

The discussion below outlines the main factors relating to the mechanisms of scour found in literature by the author, for both the mechanisms of scour of the jet and the bed material that is of interest for this particular study.

2.5.1 Erosive capacity of the jet

The break-up of the jet in the air and plunge pool, as well as the behaviour of the jet in the plunge pool including effects such as confinement, determines the erosive capacity of the jet. The scour potential of the jet is related to the energy left at impingement with the bed after the fall in the air and the diffusion in the plunge pool. If the jet's energy is fully dissipated at impingement, no more scouring would occur [7].

The jet can be split in two parts, namely the free falling jet in the air (Section 2.5.1.1) and the jet behaviour in the plunge pool (Section 2.5.1.2).

2.5.1.1 *Free falling jet*

The condition of the flow of a free falling jet is transient and turbulent. Turbulent flow occurs when the Reynolds number is generally higher than 2300 [171,184]. The inertial forces, which dictate the changes in flow motion, are also much higher in turbulent flow than that of the viscous forces, which dominates laminar flow [49]. Turbulence is, however, very complex and variable making it difficult to analyse.

The behaviour of the jet through the air has been found to be dependent on several factors, namely fall height, issuance velocity, initial turbulence, entrained air and initial jet shape (initial geometry). The trajectory and impact energy is dependent on the jet velocity, air drag and initial jet geometry, while the break-up and diffusion of the jet is reliant on the initial turbulence intensity. Several researchers, such as Häusler (1983) [22] among others, have suggested that the jet is never fully broken up or developed for the full height of fall, in the majority of high-head dams [7,19,43]. As the jet falls through the air, it generally consists of two regions: an expanding outer aerated shell and a decaying core (see Figure 2-6).

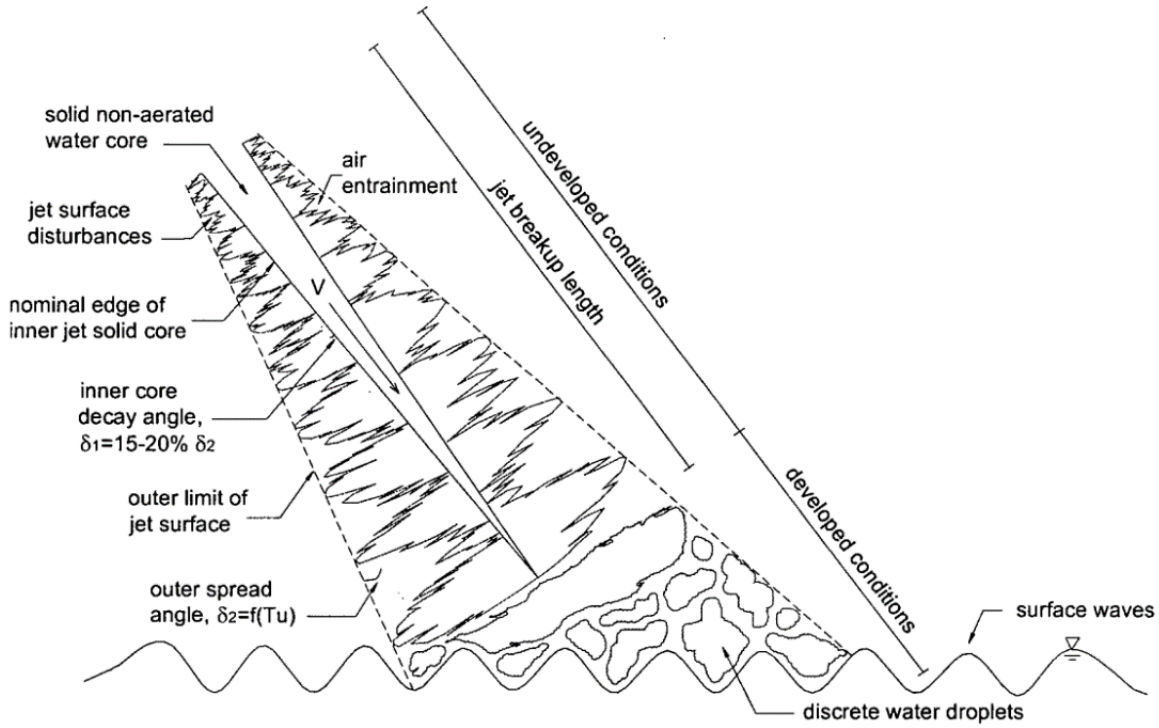

Figure 2-6 - Free falling jet behaviour in the air (developed and undeveloped regions) [8]

The break-up and air entrainment of the free falling jet are influenced by the surface tension and turbulence. The surface tension resists the growth of surface disturbances and keeps the jet together (undeveloped jet) and is influenced by the Weber number (see Table 2-5) [60]. Turbulence, on the other hand, can be defined as irregular velocity fluctuations. A free falling jet usually has strong turbulence at its free surface [20].The break-up and air entrainment of the jet determines the magnitude and areal extent of the erosive capacity of the jet such as the pressures at the bottom of the plunge pool [24].

Due to the jet core still remaining intact at impact with the plunge pool free surface (undeveloped jet) for most cases, some researchers, including Häusler (1983) [22] and Ervine and Falvey (1987) [21], suggested that air drag has a negligible effect and that aeration during the free fall should either be ignored, or the width of the jet at impact should be decreased to account for it [22]. Aeration (air to water ratio), however, has been found by several other researchers, such as Pagliara *et al. (2005) [62]*, to reduce the solid core of the jet and increase the dissipation of potential energy as the jet moves through the tailwater. Aeration should be considered when assessing scouring because it can reduce the scouring potential as the air to water ratio increases [7,62]. It is also an important factor in rock fracturing, subsequently discussed later in Section 2.5.2.

Aeration of the jet usually occurs when the turbulence intensity is high enough and due to gravitational acceleration. Aeration can occur if the surface eddies (kinetic energy) are larger than the surface tension and the flow is fully turbulent [23]. Air entrainment has a negligible influence on the deceleration of the jet (velocity) [8].

Researchers, such as Ervine *et al.* (1997) [24], found that the increase in fall height increases the jet's velocity (high kinetic energy) and increases the scour potential vertically (scour depth and downstream material mound) but decreases it laterally (hole width and length) as the core region contracts [24]. Scouring potential has also been found to be dependent on prolonged large discharge, due to floods and not necessarily on the velocity and head difference [25]. Physical tests have also shown that increase in discharge decreases the free falling jet's outer width at impact at the plunge pool, while a decrease in discharge causes an increase in outer jet width or thickness (jet is broken more rapidly due to air drag in lower discharges) [17].

2.5.1.1.1 Initial turbulence

Initial turbulence defines the rate of increase in the outward (jets outer limits) and inward (core contraction) development of surface disturbances of the water jet and is described by the Reynolds number. [19,60] The initial turbulence intensity can be defined using Eqn. 2-1.

$$T_u = \frac{u'}{U} \qquad \text{Eqn. 2-1}$$

Where:

u'	=	Instantaneous RMS (root-mean-square) value of axial velocity fluctuations at issuance (m/s)
U	=	Mean velocity at issuance (m/s)
T_u	=	Initial turbulence

Initial turbulence values for different types of spillways have been proposed through research by Bollaert (2002) and are shown in Table 2-4 [26,36,103].

Table 2-4 – Initial turbulence (T_u) values for different spillway types

Spillway type	T_u
Free overfall or nappe	<3%
Flip bucket or ski jump jets	3-5%
Orifice jets, intermediate outlet or bottom outlet	3-8%

Smooth jets have been found to occur at initial turbulence values of 1-3%, while turbulent jets occur at values between 3-8% [21,27]. The different spillways' hydraulic characteristics, such as their turbulence intensities and kinetic energy correction factors, was summarised in a table using the results of various studies, which can be found in Appendix A [19]. Castillo (2014) suggested using an initial turbulence value of 1.2% for prototype nappe spillway flow cases discharging rectangular jets [110].

2.5.1.1.2 Lateral or outer spread of the jet and contraction of the core

As air is entrained, the jet expands due to conservation of mass. Ervine & Falvey (1987) and Ervine *et al. (1997)* looked at the outer spread angles of free falling jets and found a relationship between the outer spread angle, distance from issuance and the initial turbulence intensity (Eqn. 2-2) [8,21,24,27].

$$\frac{\delta_{out}}{X} = 0.38Tu \qquad \text{Eqn. 2-2}$$

Where:

X = Distance along trajectory from issuance (m)

δ_{out} = Outer or lateral spread of jet (°)

Outer spread angles of the jet have been found to be between 3 - 4% (Eqn. 2-3) [21,27].

$$\frac{\delta_{out}}{X} = 3 - 4\% \ (angle\ roughly\ between\ 1.7 - 2.3\ degrees) \qquad \text{Eqn. 2-3}$$

The angle of core decay is generally smaller than angle of lateral spread (see Figure 2-6). The inner angles of jet spread or core contraction can be calculated using Eqn. 2-4 [21,24,27]. The inner spread angles of the core are generally between 0.5 - 1%.

$$\frac{\delta_{in}}{X} = 0.5 - 1\% \ (angle\ roughly\ between\ 0.3 - 0.6\ degrees) \qquad \text{Eqn. 2-4}$$

By increasing the jet spreading and the air entrainment of the free falling jet, the pressure fluctuations and mean pressure at the plunge pool bottom have been found to decrease [24].

2.5.1.1.3 Angle of the jet at issuance and impact

The angle of the discharging jet at issuance as well as at impact is an important factor when examining scouring of a plunging jet. The change in the scour hole depth has been found to be marginal for impact angles between 60° and 90° [1]. The angle of impact is especially important when determining the diffusion of the jet in the plunge pool. The distance the jet travels through the plunge pool is taken as the tailwater level, at angles of impact between 60 and 90°, while for smaller angles it is taken as the exact distance the jet has travelled through the plunge pool [36]. Researchers, such as Nejad *et al.* (2011) [28], have also found that the higher the angle of impact, the higher the mean and fluctuating pressures are and that the maximum pressures occur when the angle of impact is 90° [28]. For sediment beds, the effect of the impact angle is more pronounced as it effects both the scour hole geometry and the speed at which the downstream mound of eroded material is removed [7,62].

2.5.1.1.4 Break-up length

The break-up length of the jet is defined as the length where an undeveloped jet changes to a developed jet. It represents the length of an undeveloped jet to lose coherence (no core anymore) and to break-up into blobs or drops of water that disintegrates into smaller drops or blobs as the drop height increases. Velocities decreases in the developed jet region, but maximum velocity still occurs at the centreline of the jet [31]. The break-up length is dependent on the air entrainment, initial velocity and initial geometry of the jet. When a developed jet falls through the air, the air dag is more significant and amplifies the outer disturbances of the falling jet due to the non-coherent structure, as it is a mass (conglomeration) of individual water particles and it has no solid core region, which reduces the erosive power of the jet. The water particles experiences not only aerodynamic drag force as it passes through the air, but also gravitational forces. The individual water particles can reach terminal velocity, which occurs when the air drag equals the weight of the water particle [8,96].

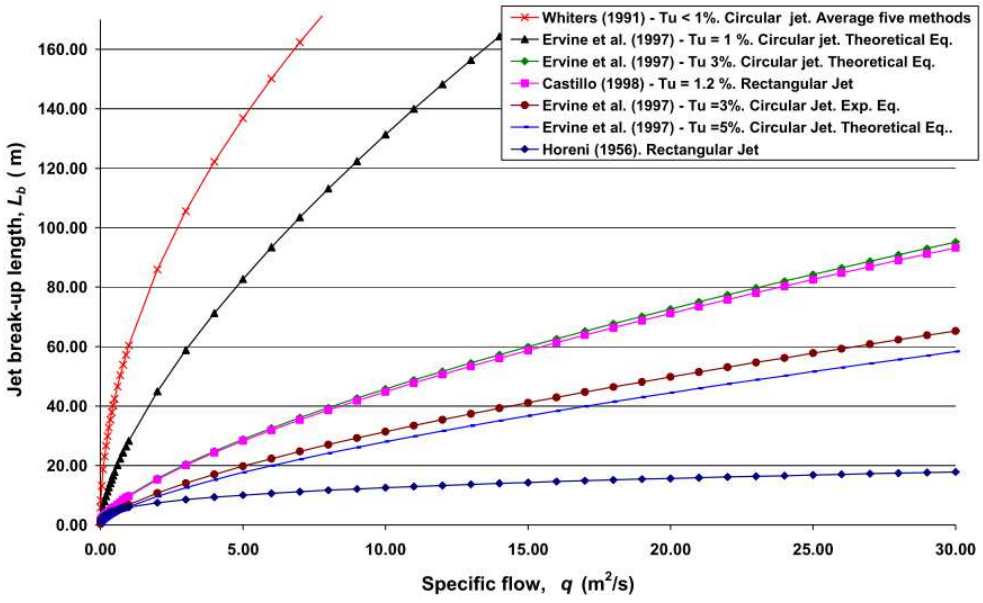

Figure 2-7 - Break-up length method comparison [31]

Figure 2-7 presents the different break-up lengths for different unit discharges, as determined by several researchers, including Castillo (2007) and Horeni (1956), to illustrate the variance in break-up lengths calculated from the formulas, proposed in Table 2-5, for circular and rectangular jets [31]. This also illustrates that circular jets are more compact than rectangular at the same specific flow [115].

The break-up length for circular and rectangular jets at different turbulence intensities have been studied by several researchers and the subsequent formulas to calculate the break-up length are summarised in Table 2-5 and Table 2-6 [29,82,171].

Table 2-5 - Break-up length formulas for rectangular jets

Rectangular or nappe jets			
Author	**Break-up length (L_b) formula**	**Turbulence intensity**	**Equation number**
Horeni (1956) [30,31]	$\boldsymbol{L_b = 6q^{0.32}}$ **(Q < 0.25m³/s only)**		Eqn. 2-5
Castillo (2007) [31]	$\boldsymbol{L_b = \frac{0.85 B_i {F_{ri}}^2}{(1.07 {T_u}^* {F_{ri}}^2)^{0.82}}}$		Eqn. 2-6
	$\boldsymbol{{T_u}^* = \frac{q^{0.43}}{IC}}$		Eqn. 2-7
	$\boldsymbol{IC = \frac{14.95 g^{0.5}}{K^{1.22} {C_d}^{0.19}}}$ **Where:** $\boldsymbol{C_d = 2.1}$ **and** $\boldsymbol{K = 0.85}$		Eqn. 2-8

The initial Froude number describes the nature of the flow at issuance. It can be calculated using Eqn. 2-9 [138].

$$\boldsymbol{Fr_i = \frac{V_i}{\sqrt{g h_0}}} \qquad \text{Eqn. 2-9}$$

Where:

Fr_i = Initial Froude number where subcritical flow ($Fr_i < 1$), Critical flow ($Fr_i = 1$) and Supercritical flow ($Fr_i > 1$)

g = Gravitational acceleration (m/s²)

Table 2-6 - Break-up length formulas for circular jets

Circular jets			
Author	**Break-up length (L_b) formula**	**Turbulence intensity**	**Equation number**
Baron (1949) [32]	$L_b = 60Q^{0.39}$	0.3%	Eqn. 2-10
	$L_b = 1.7\frac{We}{(10^{-4}Re)^{\frac{5}{8}}}$	3%	Eqn. 2-11
	$We = \frac{\rho V_i^2 D_i}{\sigma}$		Eqn. 2-12
Ervine *et al.* (1997) [24]	$L_b = \frac{1.05 D_i Fr_i^2}{C^{0.85}}$		Eqn. 2-13
	$C = \frac{1}{\left(\sqrt{\frac{2L_b}{D_i Fr_i^2}+1}\right)\left(\sqrt{\frac{2L_b}{D_i Fr_i^2}+1}-1\right)}$		Eqn. 2-14
	Or $C = 1.14 . T_u . Fr_i^2$		Eqn. 2-15
Ervine *et al.* (1980) [27]	$L_b = 17.4Q^{0.31}$	3%	Eqn. 2-16
	$L_b = 4.1Q^{0.2}$	8%	Eqn. 2-17
Ervine and Falvey (1987) [29, 21]	$L_b = 50D_j \; to \; 100D_j$	3-8%	Eqn. 2-18

Where:

D_i	=	Jet diameter at issuance (m)
Q	=	Discharge at issuance (m^3/s)
q	=	Unit discharge at issuance (q = Q/b) where b = issuance channel width ($m^3/s/m$)
V_i	=	Uniform initial jet velocity (m/s)
σ	=	Surface tension of water (0.0728 N/m) [33]
Fr_i	=	Initial Froude number (see Eqn. 2-9)
L_b	=	Break-up length (m)
T_u^*	=	Initial turbulence intensity of a nappe spillway
IC	=	Initial condition at issuance
We	=	Weber number
D_j	=	Core diameter of jet at impact (m)
K	=	Proportional coefficient for break-up length of rectangular jet or nappe flow (approximately 0.85) [115]
C_d	=	Discharge coefficient (approximately 2.1) for hydrodynamic spillway case [115] or 1.85 for sharp weir crest [110]
B_i	=	Approach flow depth over the spillway or the initial jet thickness (h_0 in some literature) (m)

2.5.1.2 *Jet in the plunge pool*

The condition of the jet in the plunge pool can be either developed or undeveloped - similarly to that of the jet in the air and is dependant on the coherence of the jet (core). The jet's structure in the plunge pool has been classsified into two flow zones (see Figure 2-8), namely the flow establishment zone and the flow established zone, which are discussed in detail as follows:

- The flow establishment zone (undeveloped jet region) is where the core is still present and core width is relatively small to that of the tailwater level [34]. Shearing at outer boundaries of the undeveloped jet decreases the velocities, but the velocity at the core is the same as efflux (same as the velocity at impact with the plunge pool free surface). The core takes a wedge-like shape due to turbulance penetration (see Figure 2-8).

- The flow established zone (developed jet region) is where the jet is fully diffused. The velocity profile in this region is close to Gausian distribution (maximum velocity at the centre and minimum at the boundaries) and a linear increase in width for both circular and plane submerged jets has been observed [8,34,35]. For the jet to become developed, the turbulent surface fluctuations need to be large enough to penetrate the core [24].

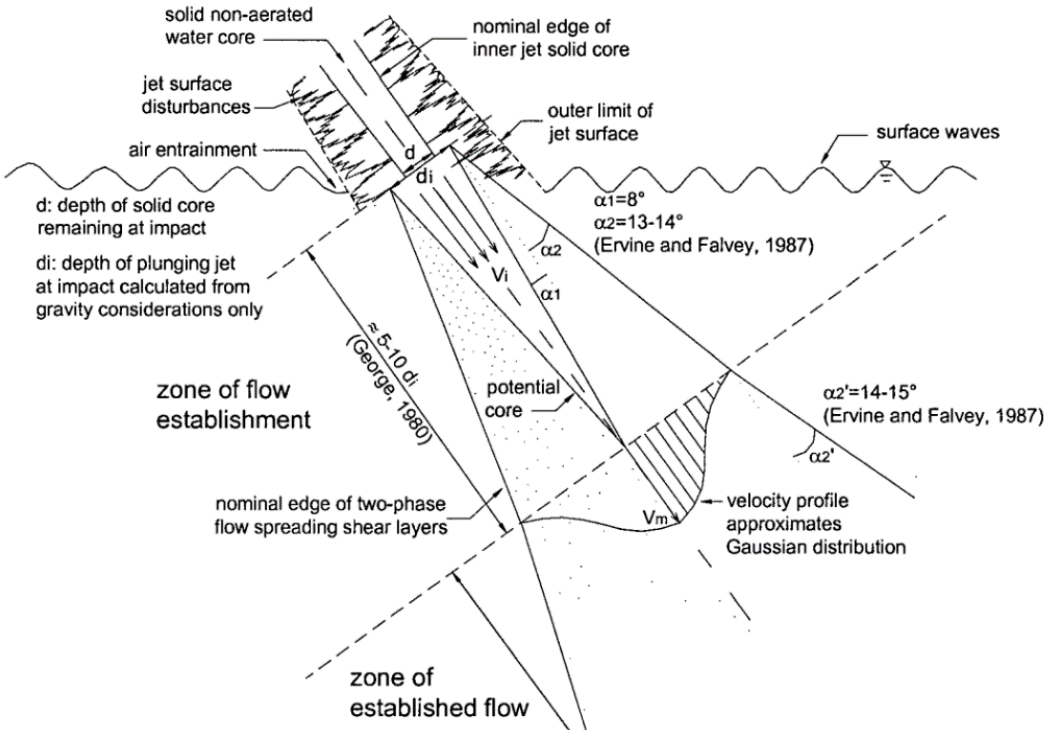

Figure 2-8 - Behaviour of the jet in the plunge pool [8]

The amount of jet diffusion and how much of the core will remain at impact with the bed, is dependent on the jet velocity and turbulence at impact with the plunge pool free surface and the depth of the water cushion or tailwater level. If high turbulence occurs at impact with the plunge pool, the jet would break-up and diffuse quicker than with lower turbulence [7,19]. Diffusion of the jet continues untill all the initial energy is dissipated, or when it encounters a boundary (impingement region i.e. riverbed) [17]. The impingement region is where the most severe hydrodynamic action takes place. In this region the hydrostatic pressures are progressively transformed into fluctuating pressures and shear stress [8]. A K-value, which is dependent on jet outlet conditions at issuance, has been used to describe the jet's core condition at impact. Various values of K have been calculated experimentally and theoretically by several researchers which were subsequently tabulated by Bollaert (2002) [11,36]. K-values vary between 4.8 and 9 and are multiplied by the diameter (d) for circular jets and the thickness (b) for rectangular jets to determine the core length [36].

The core condition of a circular jet at impact with the plunge pool bottom (undeveloped or developed jet) has also been studied by Bollaert (2002) [36]. The core is said to remain at impact for a circular jet when $Y/D_j < 4$; transition occurs when $4 < Y/D_j < 6$ and no core is said to be visible or to occur when $Y/D_j > 6$ as shown in Figure 2-9 [93,94]. Where Y is the depth of the water cushion generally taken as the vertical plunge pool depth and D_j is the core diameter at impact with the free surface of the plunge pool (see Figure 2-10).

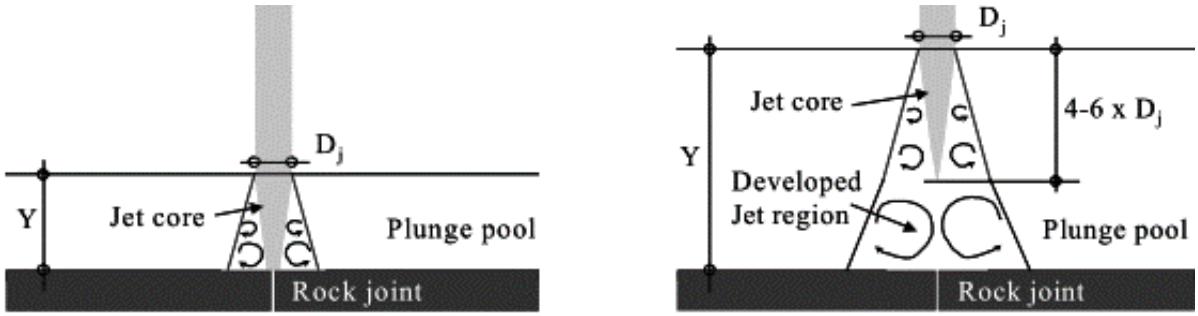

Figure 2-9 - Undeveloped circular jet at impact (Y/D_j <4-6) (left) and developed circular jet impact (Y/D_j > 4-6) (right) [103]

Castillo (2006) proposed that for rectangular jets the value D_j should be replaced with the outer impingement width (B_j) (refer to Figure 2-10 and Figure 2-11). Castillo (2006) also proposed using a ratio of Y/B_j smaller than 4 or 5.5 for an undeveloped jet to occur [37,115]. The value of B_j for rectangular jets takes into account the lateral spread of the jet while for circular jets it is not taken into account in the value of D_j (see Figure 2-10).

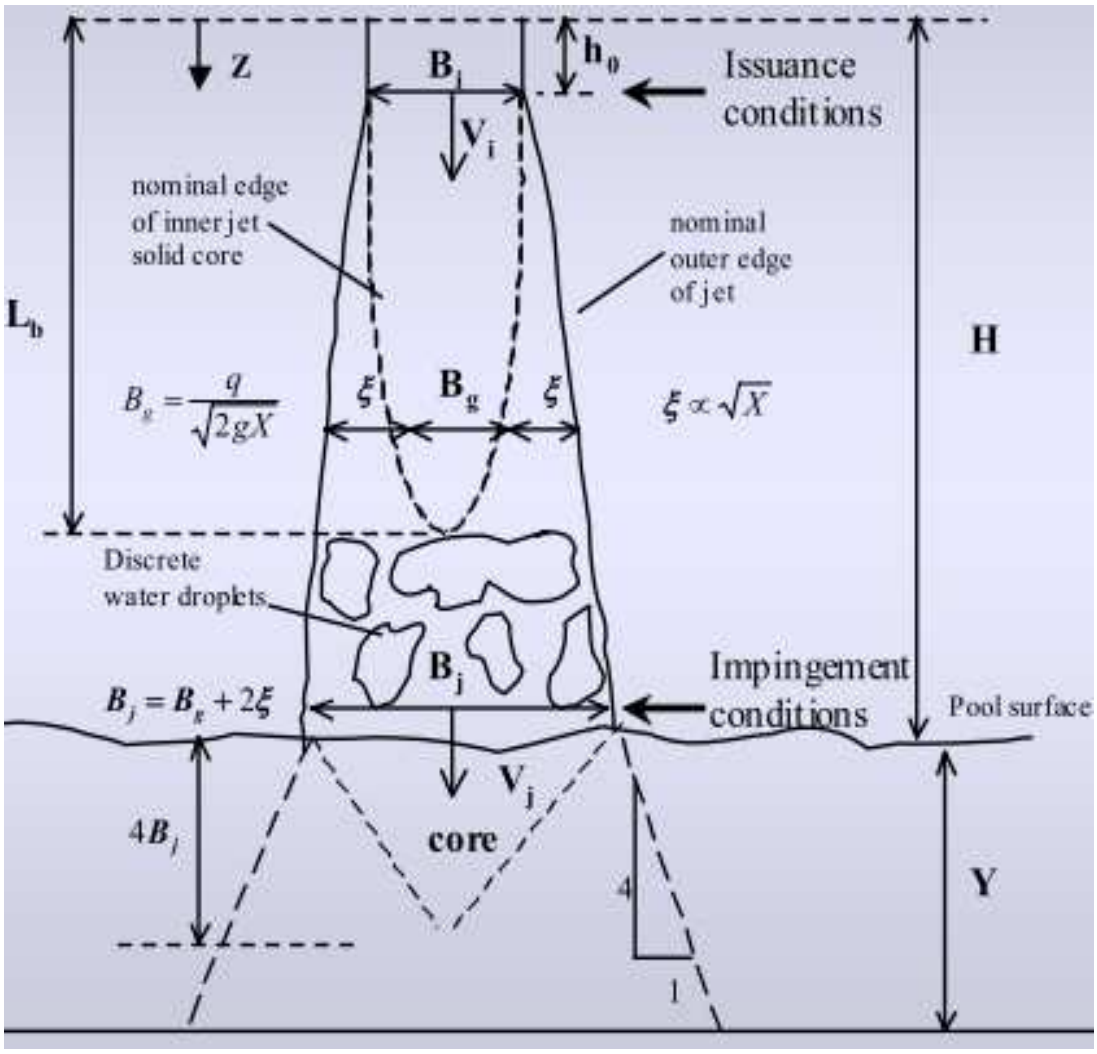

Figure 2-10 - Rectangular jet impingement [115]

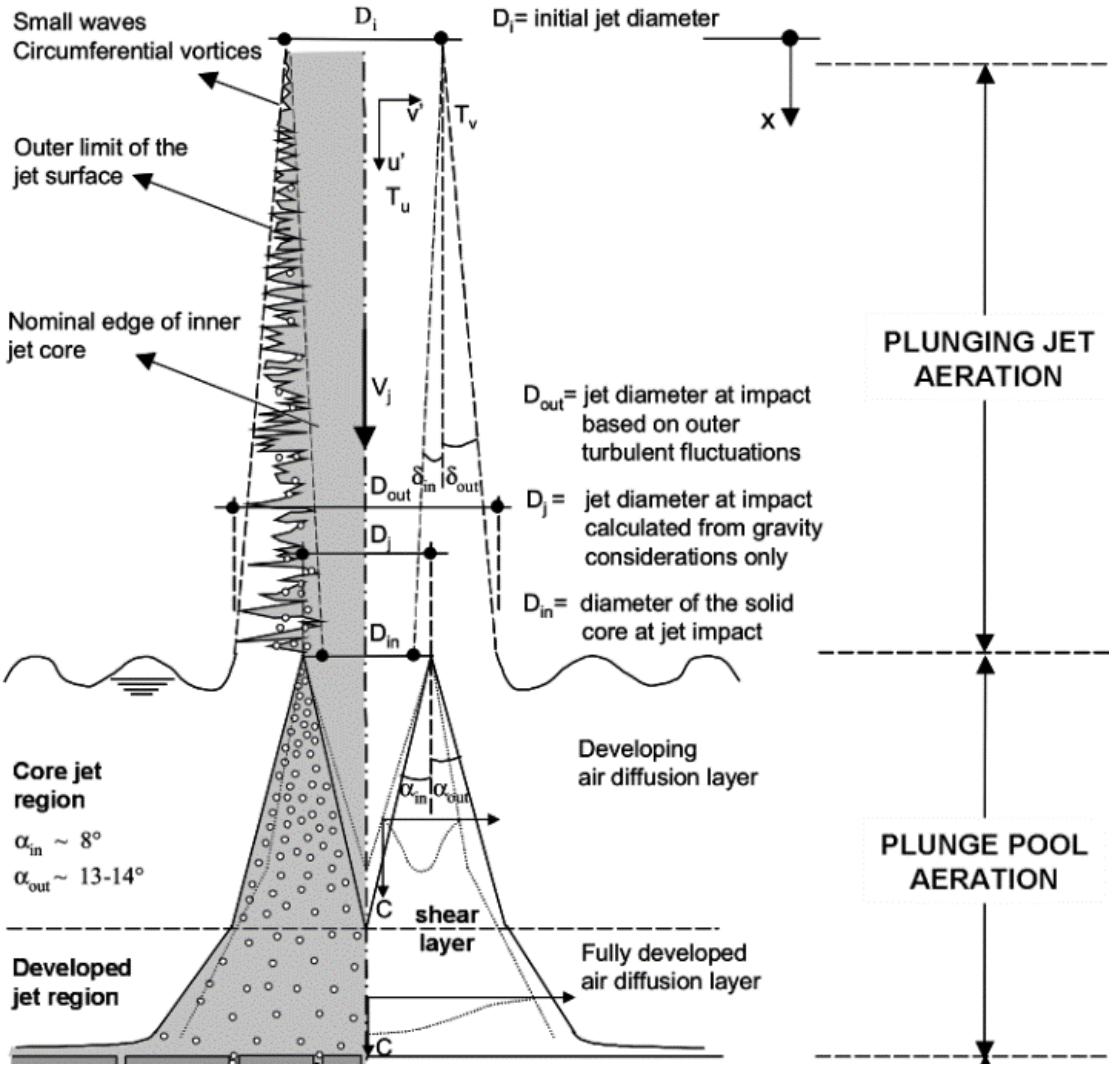

Figure 2-11 - Circular jet impingement [36]

The core length is dependent on the inner angle of diffusion or core contraction. Typical angles of core contraction and jet expansion in the plunge pool for different flow conditions are shown in Table 2-7 and are visually represented in Figure 2-8 for a rough turbulent jet [21,24,27,36].

Table 2-7 - Angle of core contraction and jet expansion in the plunge pool

Flow condition	Angle of jet spread or core contraction
Almost laminar round jets	• Core contraction angle (4-5°) • Outer boundary expansion angle (6-7°) - at plunge pool surface Outer boundary expansion angle (10-12°) - deeper in plunge pool (when jet is broken up)
Smooth turbulent jet (small amounts of air entrained)	• Core contraction angle (7-8°) • Outer boundary expansion angle (10-11°) Outer boundary expansion angle (14°) - deeper in plunge pool (when jet is broken up)
High or rough turbulent jet	• Core contraction angle (8°) • Outer boundary expansion angle (13-14°) Outer boundary expansion angle (14-15°) - deeper in plunge pool (when jet is broken up)

The plunge pool's bottom hydrodynamic condition depends on what type of jet impacts the bottom and the plunge pool geometry and are discussed below for undeveloped and developed jets respectively [7,19].

- For an undeveloped jet, with the core still intact, quasi-steady pressures are generated by a turbulent shear layer radially outward at impact (this layer causes pressure fluctuations) [19]. A core jet at impact is characteristic of a high mean pressure with low pressure fluctuations.

- For a developed jet, with no core, a fully turbulent air-water shear layer interacts with the surrounding water and the plunge pool bottom. Turbulent eddies constitute the shear layer and the shear layer's growth in the plunge pool is caused by the momentum exchange with the plunge pool (core convergence and increase in jet cross section) [63]. The impact at the pool bottom produces large dynamic pressure fluctuations but lower mean pressures [38,39].

At the impingement region, both suction and pressures are present, but the pressures are generally considerably higher by comparison. Maximum pressures generally occur along the centre-line of jet (jet axis) and decreases outward. In a wide scour hole pressure fluctuations have been found to become negligible a short distance from jet impact (no confinement of the jet) and the pressure fluctuations are thus influenced by the scour hole geometry [10].

The scour hole's depth has been found to decrease with, namely an increase in the tailwater level and a decrease in velocity and discharge of the jet [1,62]. A non-zero critical tailwater level has, however, been found to give the maximum scour depth and depends on the ratio of fall height and tailwater level [7,40]. Furthermore the tailwater or the depth of the water cushion is increased with an increase in discharge and scour depth, thus aiding in energy dissipation [41]. Figure 2-12 shows a visual representation of the jet, impacting a shallow and a deep tailwater level and its behaviour in the plunge pool [42].

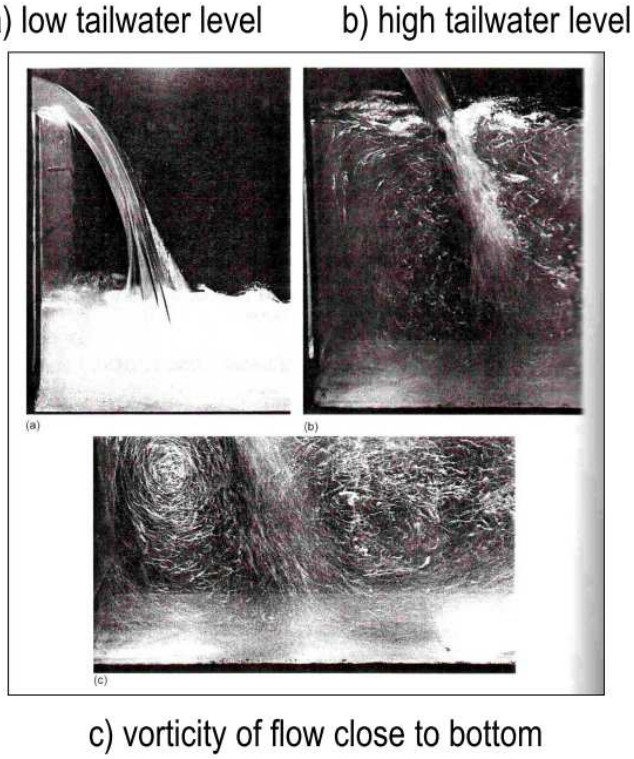

Figure 2-12 - Visual representation of a jet impacting a deep and shallow plunge pool [42]

The total water load or pressure on the pool floor consists of three components and they vary with scour hole development and area as follows [8]:

- Mean dynamic water pressures (jet impact);
- Pressure fluctuations (time dependant dynamic pressures);
- Reynolds shear stresses.

There is usually a high air concentration at impact with the plunge pool for high velocity jets, but it is lower at the point of impact with the plunge pool bottom and within the fissures. Values of between 1 to 10 percent have been found in the fissures [8,43]. The air content can be either free or dissolved [96].

The wall jet that forms from the radiating flow from the point of impact of the plunging jet at the plunge pool bottom causes shearing and fluctuating pressures along the stationary bed [44].

2.5.2 Bed material (Rock scour mechanisms)

The mechanisms of scour of the bed material are dependent on the bed material's response under the dynamic action of the water jet [7]. The bed material usually consists of sediment (cohesive or non-cohesive) or rock. Due to the focus of this study having been on rock scour, for literature on scour in sediment beds (cohesive and non-cohesive) due to plunging jets, see [45,46,47,48,49,50,51,52].

The penetrating water, from the impacting jet, causes hydrostatic pressures between rock pieces (in between the cracks and joints) and water that flows over the rock produce eddies and turbulence, resulting in differential pressure differences (dynamic and fluctuating pressures) on individual rock blocks or particles [96]. Progressive dislodgement (uplift) is caused by the tugging and pulling action of the water [100]. The early stages of scour, where the most notable scour generally occurs, happen over a relatively short amount of time. The later stages i.e. fatigue also cause some scour but not to the extent of that of the early stages [44].

Large scale eddies produce pressure fluctuations with low frequencies and high amplitudes, while smaller scale eddies produce high frequency and low amplitude pressure fluctuations. Larger scale eddies have been found to play a large role in the scouring process of rock [53]. With small size rock material, shear flow is more predominant than with non-cohesive sediment, while for larger and more irregular blocks the shape, dimensions and protrusions impact the scour mechanism [54,55].

Rock does offer some resistance to the erosive capacity of the water and often consists of layers of competent rock and can differ in depth, but in the case of high velocity jets such as in the case where water is discharged from high-head dams, erosion of some extent would probably occur.

If erosion is to occur, the rock can be eroded in various ways. The main types of rock scour mechanisms, as found in literature, are summarised below [7,56,57,58,64].

2.5.2.1 *Fracturing (brittle fracture and fatigue failure)*

Both mean and fluctuating pressures and the propagation of discontinuities, such as cracks, joints, as well as fissures of the bedrock, cause the formation of complicated fissure networks and subsequent hydrofracturing to occur. Hydrofracture is defined as the mechanical destruction, which entails the splitting or breaking up of the bedrock by the dynamic action of the water jet into rock blocks [53,59]. The condition and orientation of the discontinuities, open or tight ended joints, and the bedding plane orientation affect the build-up of pressures and rate of penetration of the water jet [8]. Hydrofracture can be divided into brittle fracture and fatigue failure.

(i) Brittle fracture

Brittle fracture occurs if the stress intensity, caused by water pressures at the edges of closed end fractures, exceeds the fracture toughness of the rock (in situ), and instantaneous rupture of the rock occurs (growth of fissures that leads to failure). This causes the rock mass to break into individual rock blocks or causes the existing blocks to break into smaller pieces. The stresses that are induced are governed by the fracture geometry and support by surrounding rock mass such as the adjacent rock blocks [55]. Brittle fracturing generally occurs during flooding, due to peak pressures being caused by the increase in flow and occurs primarily in the pre-existing fractures [60]. The fracture toughness is an important parameter to quantify when determining brittle fracturing.

Fracture toughness (k_{Ic}) is dependent on the UCS (unconfined compressive strength), mineralogical content/composition (rock type) and in situ stress field (σ_c). Figure 2-13 shows the fracture toughness range for different rock types and it can be calculated using Eqn. 2-19 [54,55].

$$\boldsymbol{K_{Ic} = (0.008\ to\ 0.01) \times UCS + (0.054 \times \sigma_c) + 0.4} \qquad \text{Eqn. 2-19}$$

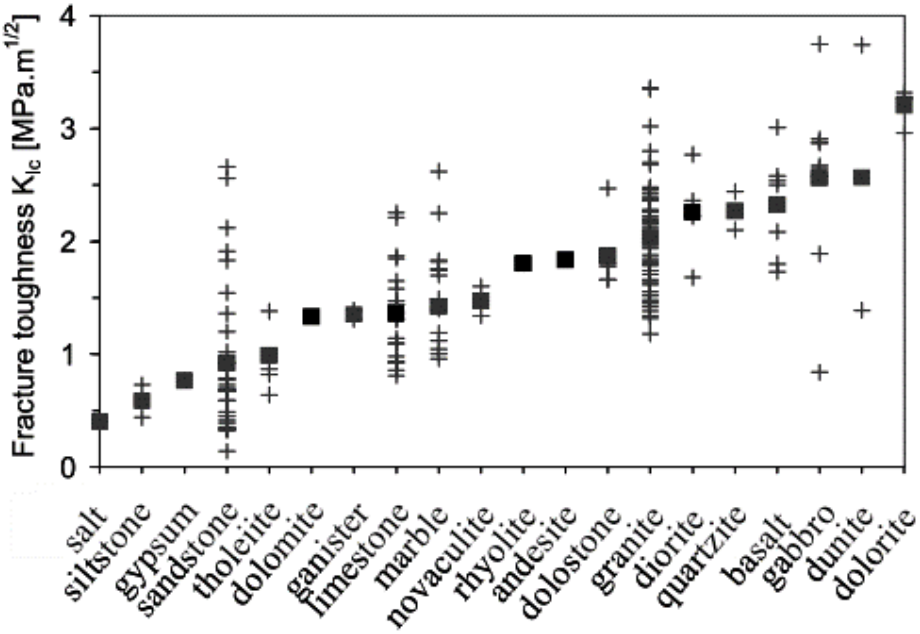

Figure 2-13 - Fracture toughness for different rock types [36]

(ii) Fatigue failure

Fatigue failure occurs if the stress intensity caused by the water pressures does not exceed the fracture toughness of the rock, but time dependant failure may still occur. The air-water transient pressure pulses or waves inside rock can cause the existing fractures to propagate in the medium to long term. Failure depends on the intensity and the number of pressure pulses.

If an air-water mixture impacts the pool floor, the compressibility of the air-water mixture that enters the joint causes non-linear transient pressure behaviour. Air entrainment is important to take into account, as at resonance frequencies, when the jet and rock resonance frequencies are close to each other or the same, pressure amplifications can be severe and can become the triggering mechanism of scour [43]. At low pressures, small wave celerities and high air content is present, while at high pressures, high wave speed and low air content occur [38]. Open joints and joints with soft infill are more easily penetrated by the air-water mixture than intact rock with tight joints [7].

2.5.2.2 *Rock uplift (displacement) or block removal*

Individual rock block removal through uplift (displacement) is a principal mechanism of rock scour. The process is influenced by the 3D orientation of rock discontinuities. These blocks are often formed by the discontinuity system caused by brittle fracture or fatigue failure.

Rock block removal can occur through gravity or flowing water. In the case of flowing water, removal can occur due to several processes. These processes can be summarised as follows:

- Uplift (quasi vertical ejection - dependent on the rock's mass density);
- Quasi-steady uplift (dependent on block protrusions and local flow velocities);
- Horizontal displacement (dependent on size, dimensions and protrusions of the blocks in comparison to the surrounding rock mass);
- A combination of the uplift and horizontal displacement; or
- Turbulent uplift force (turbulent pressure fluctuations).

The type of removal is dependent on the protrusion, size and dimensions of the rock blocks [60]. Rock block removal can occur due to shear flow (predominantly smaller blocks), flow turbulence (breaking up of blocks into smaller pieces) and pressures in joints (uplift, brittle fracturing and fatigue failure) [54,55,60].

The weight of the rock blocks and the forces (uplift and resistance forces) acting on, and within the rock mass, are very important factors when examining rock block removal and are explained below.

(i) Uplift force

Lift forces during turbulent flow are dependent on circulation around the rock block [133]. Water pressures from the impacting water jet (stochastic in nature) are transmitted through the vertical joints in the rock mass. Instantaneous pressure difference above and below the blocks causes transient uplift forces (fluctuating). When transient uplift forces are higher than the resistance forces of the rock block it can cause lifting, sliding or a rotational failure stress and the block can be dislodged and swept away (see Figure 2-14) [59]. Uplift generally occurs with a minimum overpressure and maximum under pressure [117].

Rock block removal can be split into kinetic failure modes (rigid blocks) such as lifting and sliding (pre translation rotation), slumping and torsional sliding (translation and rotation) and flutter (dynamic load). At a fraction of the design flow potential, kinetic sliding or rotation failure is known to have occurred such as at Ricobayo Dam, Spain.

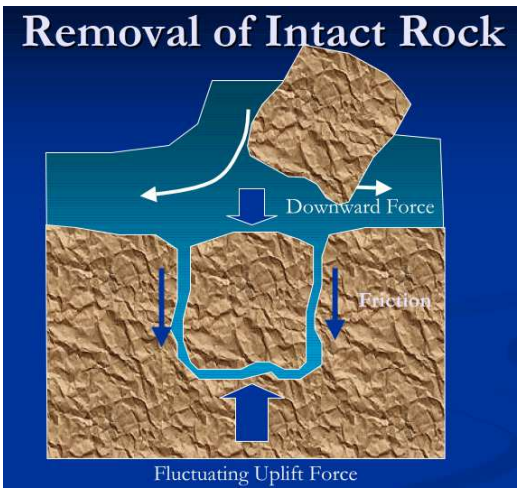

Figure 2-14 - Rock block removal [64]

(ii) Resistance forces

The forces resisting the uplifting action are primarily the mass of block (downward forces), cohesive force between the blocks and the eventual shear and interlocking forces between the block and the rock mass [53,54].

2.5.2.3 *Abrasion*

Abrasion is usually ignored when determining rock scour, as the process itself occurs over a very lengthy period. When the velocities and mean dynamic pressures decrease enough, abrasion can become the primary form of erosion, in comparison to the other mechanisms of rock scouring [8]. Abrasion can be described as layer-by-layer erosion

As the scour hole deepens, more energy is needed to remove the trapped eroded rock material in the scour hole, especially the larger rock blocks. The trapped, eroded rock material is then generally eroded over time by a process of ball milling which involves the abrasion and dislodging of the rock particles in the scour hole. Abrasion is described as the gradual grinding of recirculated particles against scour hole sides and also occurs due to collisions with the other rock material in the scour hole. The recirculating particles can also dislodge the particles in the rock matrix. Abrasion only occurs if the fluid flow is more abrasive in comparison to rock resistance, and is enhanced if surface weathering is present in the exposed rock [54,55]. If the abraded rock material is small enough, it is transported out of the scour hole [8,116]. The entrained particles can aid in dissipating energy [34].

2.5.2.4 *Peeling*

Peeling is a combination of both brittle fracturing or fatigue failure, and quasi-steady pressure forces. Peeling occurs mostly in thin, nearly horizontal, layered rock such as sedimentary rock and is caused by flow turbulence and local flow deviations which are caused by rock protrusions [60]. Flow deviations cause lift and drag forces on exposed blocks and corresponding fluctuating pressures may cause brittle fracturing and fatigue failure [54,55].

The different rock scour mechanisms are illustrated graphically in Figure 2-15.

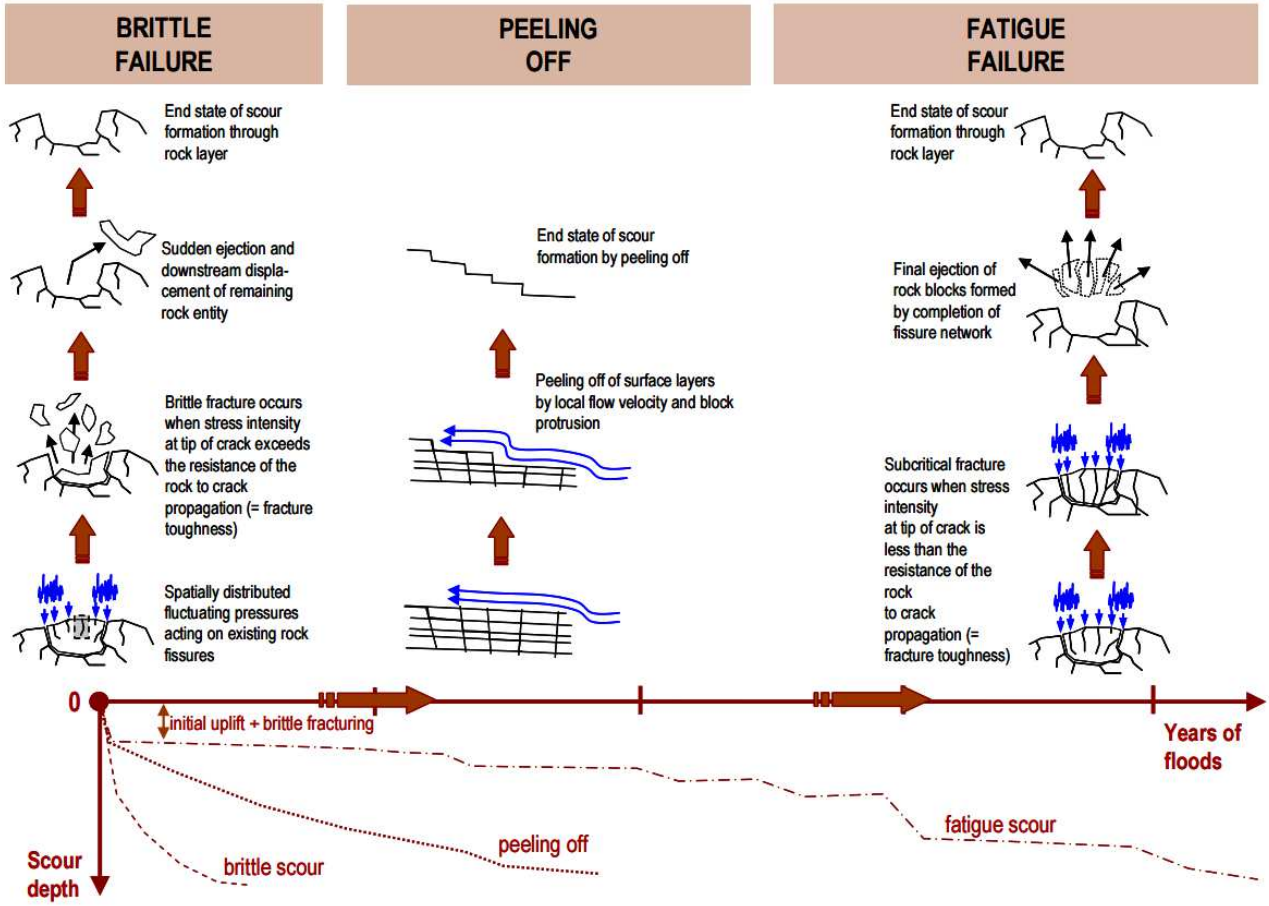

Figure 2-15 - Main scour mechanisms and their time scale [55,60]

Rock scour is, however, limited to the likelihood of dislodgement of material as well as the transport beyond the scour hole [8]. The type of particle transport of the eroded rock downstream can differ for different flow conditions. This is evident in flows that are more vigorous where larger particles, which were initially bed load, can become suspended load due to a higher turbulence intensity of the flow. The transport mode is thus not only dependant on the size of the transported particles, but also on the type

of flow [61]. Figure 2-16 is a visual representation of the different particle load conditions that can occur during transport by the water. The eroded rock particles, transported as suspended and bed load, can form a ridge downstream of the scour hole [16]. Physical laboratory model tests have shown that a low tailwater level with continuous ridge removal, formed from the eroded material deposited downstream, produces the maximum scour depth [62].

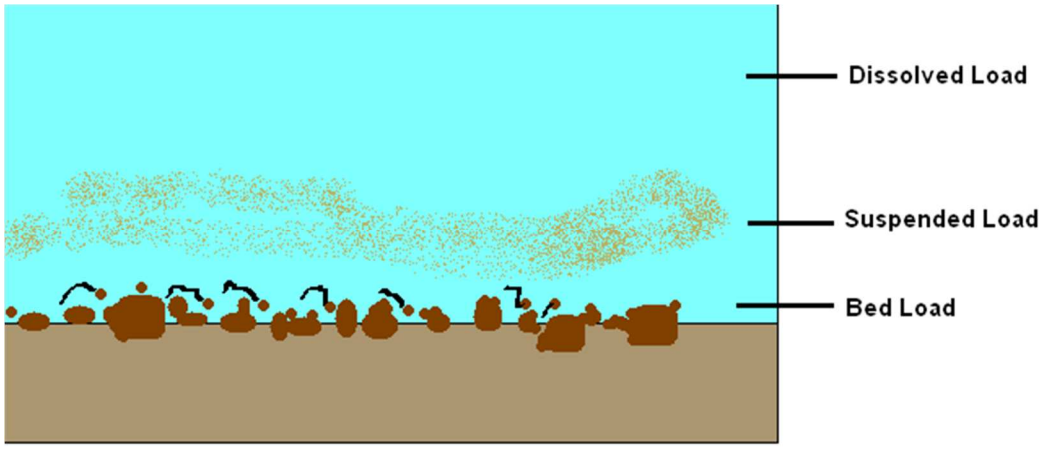

Figure 2-16 - Sediment load (bed, suspended and dissolved load) [5]

Bollaert proposed some possible shapes of rock scour holes as illustrated in Figure 2-17 [63]. The first is representative of highly fractured/low erosion resistant rock or granular material, the second is of rock with fracturing in the horizontal direction with high erosive resistance and the third is of a rock bed highly jointed in a particular direction.

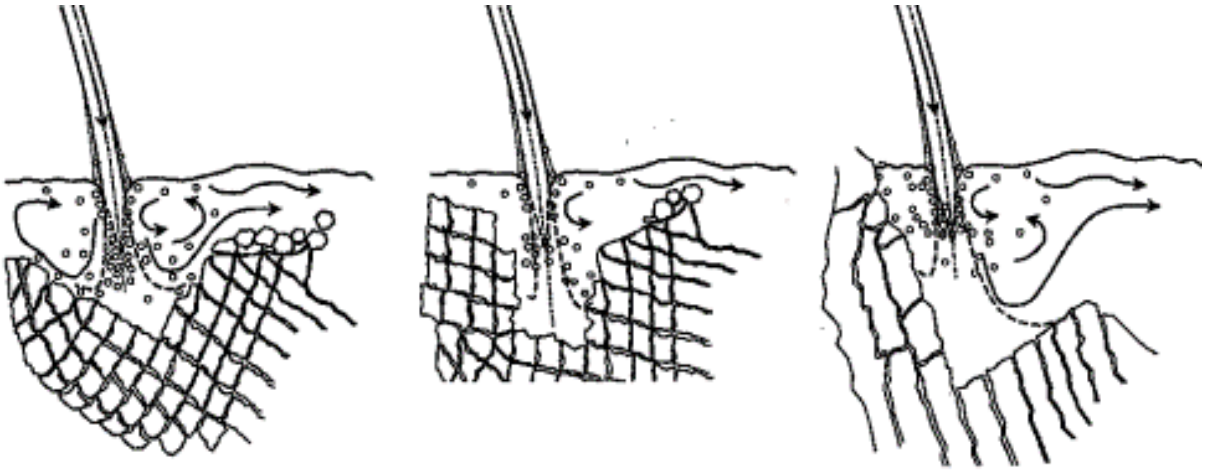

Figure 2-17 - Example scour hole geometries for fractured rock beds [63]

In summary, the main hydraulic aspects are the fluctuating pressures, resonance in rock fractures, entrained air and the deviations in flow along the rock bed, while the main rock scour mechanisms are brittle fracture, fatigue failure and removal of rock blocks [64].

2.5.3 Conceptual models

Annandale (1995) proposed a conceptual model to explain rock scouring [8,95]. Rock scour is viewed as a process of progressive dislodgement and is illustrated in Figure 2-18. The model consists of three stages, namely:

- Jacking - material units are jacked out of rest position by the instantanuous differential (mean and fluctuating) pressures on rock blocks (upper and lower surfaces) and of existing joints.
- Dislodgement - units are dislodged due to the flowing water if material/blocks are destabilised. This occurs if normal (plucking) and tangential(dragging) forces are large enough.
- Displacement - units are displaced. The displaced material is deposited when the transport capacity is diminished.

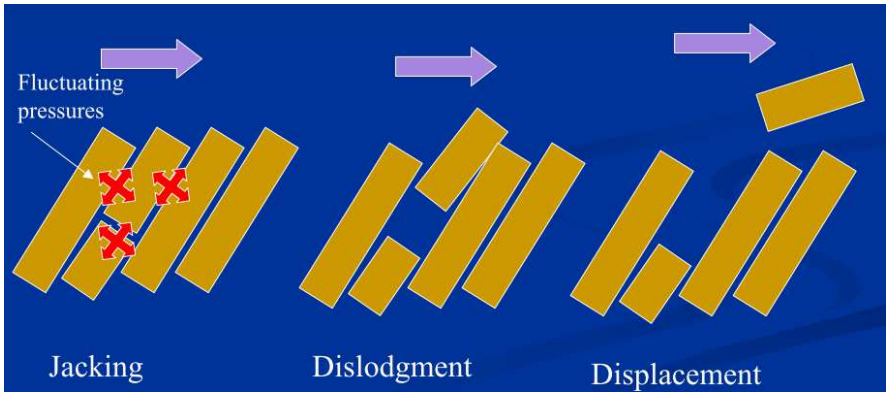

Figure 2-18 - Annandale's conceptual model of rock scour [64]

2.6 Scouring effects (Prototype Cases)

Scouring of riverbeds due to plunging jets downstream of structures (high-head dams) is an important area of study. If scouring is left unchecked, it can have severe consequences and several cases are available where scour have had great destructive impact. Cases like Kariba Dam and Ricobayo Dam are clear illustrators of the severe consequences of scouring and they illustrate the need to study scouring and develop adequate prediction methods and are summarised below.

2.6.1 Kariba Dam

Kariba Dam is one of the best-known and well-documented examples of uncontrolled scouring found in literature, with the largest artificially created plunge pool in the world. Kariba Dam is located on the border between Zambia and Zimbabwe on the Zambezi River. The dam is a double curvature arch dam which was constructed in the 1950's. Some of the most important information regarding the dam's boundary conditions is shown in Table 2-8 as found in literature [12, 65, 66, 174].

Table 2-8 - Kariba Dam boundary conditions

Kariba Dam properties	
Dam height	128m
Spillway sluice gate sill	33m below dam crest
Number of sluice gates	6
Sluice gate size	9.1m (high) by 8.8m (wide)
Discharge of each sluice	1500 m^3/s (q of 159.1$m^3/s/m$)
Total discharge	9000 m^3/s
Depth of scour hole	± 80m below tailwater level
Tailwater level	20m Castillo [115] and 40.5m Whittaker [82]
Rock type	Gneiss rock (relatively hard)
Size of downstream	220m lateral and 190m longitudinal
Velocity at issuance	20 m/s
Drop height (H)	75m up to bed (thus 57m) [115]

Kariba Dam's most observable scouring occurred during 1962 to 1982 (see Figure 2-19). This was due to the fact that multiple sluice gates were opened, frequently and for long periods. Since 1982 the sluice

gates were opened occasionally and when opened, only one, and occasionally more sluice gates were opened, for only short periods, together with long periods of no gate functioning [66].

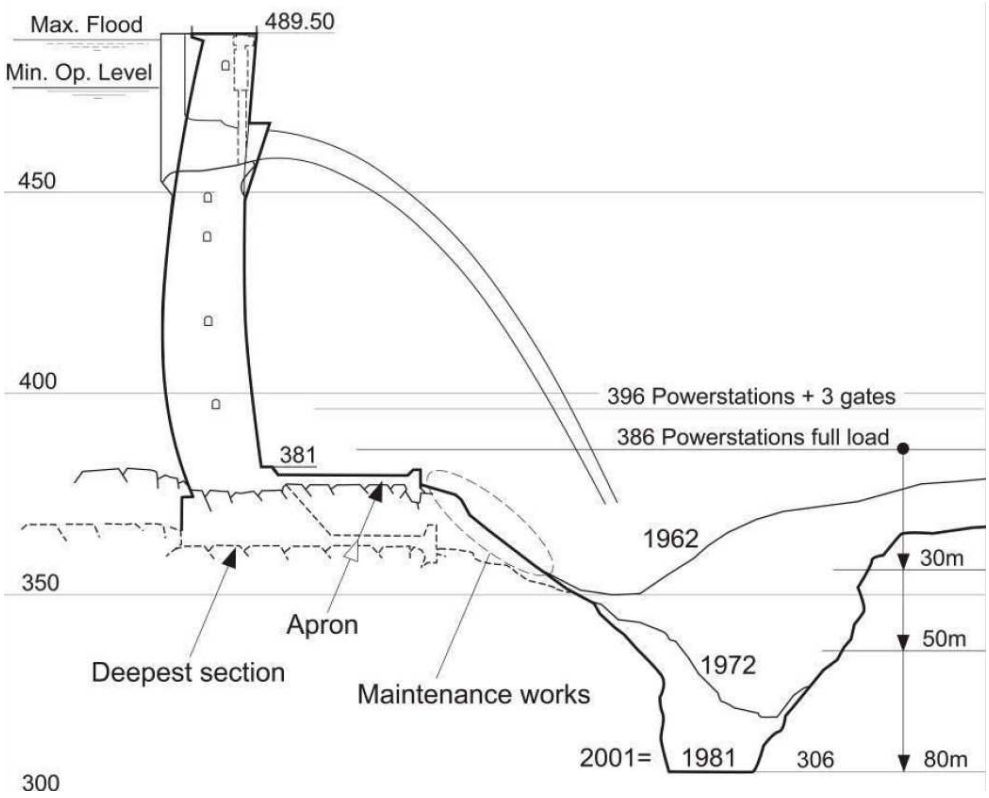

Figure 2-19 - Kariba Dam scouring 1962 - 1982 [65]

The sluice gates are operated at relatively low velocities and they are located in the upper parts of the dam wall, resulting in the jets impacting closer to the dam wall and thus threatening the dam's foundations [66]. Of the dam's available six sluice gates, the four central sluice gates have been used most frequently, while the two side sluice gates had been operated the least of the six. The rock mass along the southern banks also differ from that of the northern banks. The northern bank consists of very good quality gneiss rock (UCS 150-200MPa) with both vertical and horizontal joint sets, while the southern bank consists of medium strength (UCS 50-100MPa) gneiss rock with only vertical joints. The lower quality rock of the southern bank thus erodes much easier than the northern bank, but less or equal to that of the rock of the central pool area [12].

Some maintenance work has been carried out on Kariba Dam, but the main concern is the possibility of extensive spillage due to extreme flooding in future, that could continue the growth of the plunge pool and endanger the dam's integrity [66]. A rehabilitation program for Kariba Dam has recently been set in

motion. This is due to the fact that the dam's foundations are in danger, due to the scour hole regression towards the dam, and due to a chemical reaction with the concrete gates, causing inefficient and ineffective spillway gate operation [67].

2.6.2 Ricobayo Dam

The Ricobayo Dam is located in Spain. The dam had an unlined rock spillway, with an original capacity of 4 650m^3/s, that discharged over a granite cliff. The dam, in contrast to Kariba Dam's high discharge scouring, is known for the sliding failure of rock blocks at relatively small discharges. Multiple rock blocks failed by kinematic sliding at discharges of 100 to 400 m^3/s during the first few years of operation, which was well below the design capacity of the spillway [56]. Later scouring also occurred at discharges well below that of the maximum capacity.

The granite rock mass at Ricobayo Dam has two main joint sets dipping vertically and horizontally. A fault line, which occurs in the spillway foundation, runs perpendicular to the spillway channel. Both the joint orientations and the fault played a role in the scouring that occurred [68].

Figure 2-20 - Scour progression of Ricobayo Dam for the different discharges [56]

Several scour remediation techniques have been applied to Ricobayo Dam after the 1936 flood event. Lining of the plunge pool (failed in 1940 but pool was not deepened), concrete protection was added to the spillway channel and at the end of the spillway (at the drop) and concrete splitters were added to the end of the spillway (see Figure 2-21) [68].

Figure 2-21 - Scour remediation of Ricobayo Dam [56]

2.6.3 Main rock scouring effects

A summary of the main rock scouring effects as found in literature, is listed below [1,3,6].

- The stability of part, or the whole of the structure, can be threatened by scouring, if the scour hole regression comes too close to the structure, resulting in the destabilisation of its foundations [1,82].
- An increased seepage gradient below the structure can endanger structural stability [82].
- The scour hole can endanger the downstream stability of the channel and side slopes.
- If the energy dissipater collapses or fails, it can have severe consequences on the downstream area [82].
- The eroded material may mound downstream and raise the tailwater level. This may, in turn, increase the hydraulic loading on the structure or interfere with the outlet structure, if bottom outlets are used [82].
- The jet spraying action should be controlled and an assessment of its effect on the surrounding downstream area is essential (especially in cold climates).

2.7 Remedial measures against scouring

In most cases, some form of bed protection is required for plunging jets below high-head dams. Only in some cases such as where the bedrock is competent, or the erosive forces are not of note, scour protection is not needed. Protection measures that are usually used to increase the strength of the bed material, or protection thereof, include the following - shifting the scour hole further away from the structure, changing the geometry of the flow or reducing the load of the plunging water [1,96].

When choosing a remedial method it has to be ensured that it is technically feasible (both objectively and subjectively), that it can be maintained (for effectiveness and longevity) and that it is economically feasible (long term and short term should be considered). The protection measure should also be compared to the scenario where the protection is not provided (the cost of the damages to both humans and infrastructure in comparison to the cost of the protection measure) [82,96,171].

2.7.1 Scour protection measures

Scour protection can be incorporated by using several methods of which some, as found in literature, are summarised below [1,6,24,69,96]:

- **Accommodating protection**

Accommodation protection allows for scouring to occur freely, but requires adjustment of the surrounding area (structures and community) to ensure their safety. Structures and the community are usually placed away from scour hole boundaries.

- **Flow boundary pre-forming**

Plunge pool pre-forming or pre-excavation increases the dissipation volume (water cushion) and thus reduces the scour potential [12]. This in turn reduces the turbulence at the boundaries (reduces pressure fluctuations) [1]. The water cushion is not the most effective remedial measure in terms of dissipation of energy, but can still have a large impact and should be used in conjunction with measures such as aeration for efficient dissipation of energy [82].

➢ **Hard protection**

Hard protection involves the hardening of the flow boundary by means of lining the boundary with concrete (see Figure 2-22), riprap, or other linings (apron). For rock of low mass strength, concrete with a higher mass strength can be used to cover it. The lining can also be used to reduce the pressure fluctuations in rock fissures. It, however, needs to be able to resist the uplift (needs to be heavy enough) and not be broken up by brittle and fatigue failure. Other methods include rock modification with the use of rock anchors [58].

➢ **Modification of flow**

The flow can be modified at issuance or in the plunge pool to increase energy dissipation.

At issuance:

Energy dissipation of the jet is caused due to spreading (atomisation and aeration in the air), air entrainment (in the air and at impact) and diffusion, as well as deflection in the plunge pool [31]. Jets can be aerated with careful spillway design and can reduce the required tailwater level to almost half of that, which was required for non-aerated jets [82]. The aeration and jet break-up in the air is responsible for some of the energy dissipation, but most of the energy has been found to be dissipated on impact and in the plunge pool [7]. The jet in the air can be broken up by spreading, by using splitters at spillways or spillway chutes:

- Flip bucket or ski jump - Some energy dissipation from bucket and air entrainment of free jet (increasing wetted impact area) or increasing throw distance (jet modification). Spray can be excessive from ski buckets.
- Splitters and nappe deflectors enhance spreading/ break-up (air entrainment) of the jet, reducing erosive capacity. Splitters are more efficient for smaller discharges. The effect of splitters for very large flows [Probable maximum flood (PMF)] is very small [70].

Studies have looked at reducing in the pressures at the plunge pool floor and found that, an increase in the drop height and tailwater level reduced the pressures significantly in comparison with increasing the width and the discharge of the jet at issuance [71].

In the case of adjacent jets, they can be separated by modification of a bucket lip [12].

Plunge pool:

The plunge pool or tailwater can be made deep enough so that the energy induced on the plunge pool floor does not scour the rock bed excessively, or at all through sufficient jet diffusion [12]. A stilling basin can also be implemented. The stilling basin employs the hydraulic jump formed downstream for energy dissipation in the plunge pool and confines it to a short distance. A stilling basin is not a cost effective solution for high flows and Froude numbers. Stilling basins are unreliable for high flow velocities as they are prone to cavitation (growth and collapse of air bubbles in water) and cause large spray action, unstable flow and wave generation in the tailwater.

- **Earth material strengthening**

Earth material strengthening is done by improving the earth material's scour resistance. In the case of rock beds, rock anchoring or bolting (see Figure 2-22) can be implemented for strengthening. In the case of rock anchoring, the mass strength of the rock needs to be high enough to be viable. Rock anchoring or bolting can be done by installing post-tensioned rock anchors and can be used to protect the dam's abutments. The anchors increase the resistance of the rock blocks by increasing the size of the blocks. This approach can be used when rock uplift is the main scour mechanism, and care should be taken when fatigue and brittle failure is present. Grouting of rock can also be used, but is only applicable to modest flows [18].

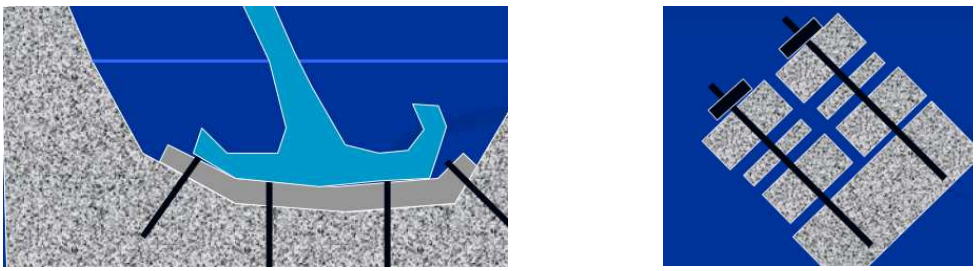

Figure 2-22 - Concrete lining (left) and rock anchoring (right) [64]

- **Combination**

Two or more of the protection measures mentioned above could be combined; for instance, the scour hole can be pre-formed and hard protection can be used for protection against future scouring. When considering the design of a plunge pool, the option of having a deep plunge pool (no concrete liner) and a shallower plunge pool (with concrete liner), is generally determined from the economic constraints [21]. During construction of the dam scouring can also occur if flood waters need to be spilled before completion, for example Calderwood dam in the USA ,and should thus be a point of consideration in the design stages [82].

3 Literature study, Part B: Scour prediction methods

Section 3 focuses on the relevant scour prediction techniques for rock scouring due to plunging jets as found in literature. Section 6 includes a discussion on the use of CFD in predicting rock scouring and is therefore not included in Section 3.

Due to the variability in boundary conditions (hydraulic, geotechnical and morphological) of each study area, there is no reliable method to predict the scour hole geometry due to the difficulty to assess these conditions theoretically and to reproduce them experimentally, especially for turbulent conditions. The main methods that have been used to assess the geometries of scour holes in the past have principally been physical laboratory models, but there have also been several empirical formulas and semi-empirical and physically based scour prediction methods. CFD (computational fluid dynamics) and other computer software, could also be used as an alternative or should rather be used in conjunction with physical laboratory models, but is subject to the available mathematical techniques.

3.1 Physical laboratory models

Physical laboratory models are a reliable method to demonstrate the scour hole formation, as well as modelling complicated three dimensional flow cases [17]. These models usually correspond to prototype conditions regarding their sediment transport, Froude number similarity and geometric conformity [34]. Where the gravitational and inertial forces are dominant, such as free surface flows (free falling jets) the models are generally modelled after Froude similarity. The main scaling relations of Froude similarity are shown in Table 3-1 and Eqn. 3-1 and Eqn. 3-2 respectively [17,72].

$$\boldsymbol{F_m = F_p} \qquad \text{Eqn. 3-1}$$

Thus:

$$\frac{V_m}{\sqrt{g_m L_m}} = \frac{V_p}{\sqrt{g_p L_p}} \qquad \text{Eqn. 3-2}$$

Where:

V	=	Mean flow velocity
L	=	Characteristic length
g	=	Gravitational acceleration
F	=	Froude number
Subscript m	=	Model
Subscript p	=	Prototype

Table 3-1 - Froude number similarity - Scale relationships [17]

Parameter	**Scale relationship or ratio**	**Equation number**
Length	$L_r = \frac{L_p}{L_m}$	Eqn. 3-3
Velocity	$V_r = {L_r}^{1/2}$	Eqn. 3-4
Discharge	$Q_r = {L_r}^{5/2}$	Eqn. 3-5
Pressure head	$h_r = L_r$	Eqn. 3-6
Time	$t_r = {L_r}^{1/2}$	Eqn. 3-7

Reynolds and Weber number similarities are also very important when trying to correctly simulate air entrainment of plunging jets as Froude similarity alone cannot simulate prototype aeration correctly and several of the plunging jet aspects such as lateral spreading and jet break-up, are also dependent on the Weber and Reynolds numbers [82]. The Weber, Froude and Reynolds numbers cannot, however, be satisfied simultaneously in physical laboratory models [73].

Physical laboratory models are limited to the physical resources (laboratory size and pump capacity), materials available to represent the bed material and structure, the cost or funding available for physical laboratory modelling, the amount of manpower available and the scale effects due to viscosity and surface tension [7,17]. Physical laboratory models, as with most other methods, cannot reproduce abrasion as the process takes very long and it is costly to reproduce [8]. The local topography and mechanism of scour are very important to model correctly in the physical laboratory modelling of scour holes [7].

The scour mechanisms of rock beds are very difficult to physically model in comparison to non-cohesive sediment. The modelling of the rock mass using non-cohesive bed material (gravel), that represents the broken up rock particles, has been found to give obscure results. Subsequent studies have alternatively used cohesive sediment to simulate the rock mass, as cohesive sediment can sustain steeper slopes, which are similar to prototype rock scour holes, rather than non-cohesive sediment (gravel) [7]. Non-cohesive sediment produces non-realistic scour holes due to the scour holes being too large and shallow. Firstly, it is due to the density and size of the particles, for example, gravel, which is scaled and represented incorrectly from prototype conditions and results in no transportation of particles. Secondly, the non-cohesive particles cannot sustain steep slopes due to the angle of repose. This, in turn, means that scour hole confinement cannot be simulated, including the enhancement of the erosive capacity of the water. In addition scouring occurs in the non-impingement areas due to the particles collapsing. The scour holes produced by the non-cohesive particles are more shallow and thus also distort the flow patterns as well as the lateral flow, and dissipation occurs freely as the boundary conditions differ from the prototype conditions of a rock bed [7,17]. Other studies have used cement mortar as a binder, in conjunction with non-cohesive particles for the bed material, but found when doing long term testing using cement mortar, that the characteristics of the material changed due to submergence. When using a binder, testing should thus occur in a short time-frame [17]. It should, however, be noted that when using a binder it may increase the strength of the bed extensively and scour may be reduced [7,17].

Due to the difficulty in reproducing the failure mechanisms of natural rock joints, artificial joint tests have been done experimentally by researchers such as Bollaert. 1D and 2D configurations of closed and open ended rock joints have been artificially created and tested using physical laboratory models by Bollaert (2002) by incorporating steel plates to determine the pressures in and around rock joints [36,117]. Bollaert (2002) stated that a scale of approximately 1:10 is required to correctly reproduce the pressure fluctuations and turbulent behaviour of the air-water jet impacting on the rock blocks. The pressure propagation in the joints and fractures also do not allow for any scaling [60]. Other studies suggested that when using a 1:20 scale, there are no scale effects on the aeration in the plunge pool, the jet's velocity and turbulence or the dynamic pressures. For scales of 1:100, however, Weber similarity is not guaranteed; thus the models may not account for the correct aeration effects [74].

3.2 Empirical formulas or relations

In literature there are several empirical formulas for both rock and sediment beds to estimate the scour hole depth at the centreline of the jet and to determine the scour hole geometry parameters. The empirical formulas are based on small-scale laboratory tests of scour holes, which were performed under idealised conditions. When applying the formulas to prototype conditions, care must be taken, as they may give a misrepresentation of the scour hole due to scaling complications, the formulas not taking into account all the prototype parameters as well as some of the variables of prototype conditions being averaged in the formulas. The formulas also generally perform their best when using corresponding or similar experimental data or study conditions (hydrological and geological) which make their application very limited due to the variability of the conditions, both hydraulic and geological/morphological, at each site. It is unrealistic for one formula to predict every case of scouring with accuracy [7,75,78,82].

When applying the formulas it should be noted that they were developed using a quasi-equilibrium depth in most instances, which means to a point where the scour hole changes a negligible amount with time, or becomes stable, and not to the point of no particle movement [76]. This becomes a concern when attempting to determine the ultimate scour depth with certainty, as the mechanisms of scour of rock and cohesive sediment are time dependant [7,8].

3.2.1 Empirical formulas

Mason and Arumugam (1985) [77] proposed a general empirical equation, taking into account the main scouring parameters (see Eqn. 3-8) for estimating the maximum scour depth below grade control structures such as dams that can be used for both rock and sediment [11,78] (see Figure 3-1 for clarification of variables).

$$y_s + y_o = k\frac{q^x y_0{}^w \Theta'^e H^y}{g^v d_s{}^z} \qquad \text{Eqn. 3-8}$$

Where:

q	=	Unit discharge or proportional discharge (at issuance) ($m^3/s/m$)
y_s	=	Scour depth (m)
y_0	=	Tailwater level (m)
Θ'	=	Angle of impact with plunge pool (β other literature)
d_s	=	Mean particle diameter (Studies have found that the use of the mean particle diameter is better that the median diameter (d_m) [1,35] (m)
H	=	Drop or fall height (Z in other literature) (m)
e,x,y,w,v,z and k	=	Empirical exponents of scour equation (dependent on author and model conditions)

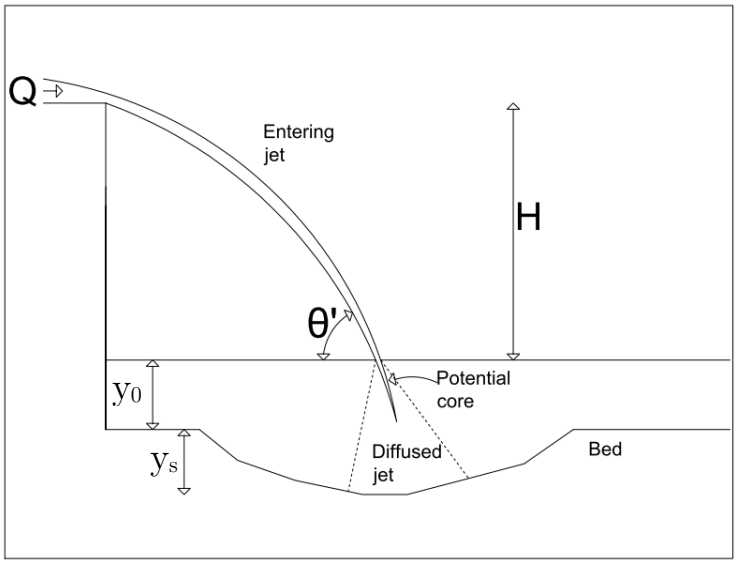

Figure 3-1 - Free falling jet

A pure empirical formula (see Eqn. 3-9), similar to equation Eqn. 3-8, was proposed by Liu (2005) for rock beds [79].

$$y_s + y_o = k_c\frac{q^x H^y}{d_r{}^z} \qquad \text{Eqn. 3-9}$$

Where:

x,y and z	=	Empirical exponents
d_r	=	Characteristic size of a mean/average rock block (the value of subscript r varies between researchers) (m)

Using a similar formula structure as that proposed by the two generalised equations above, researchers have developed several empirical (dimensional) equations for different physical laboratory model and prototype conditions. These formulas can be found in literature with a selected few, as found appropriate and shown in Table 3-2 and Table 3-3 [82].

Table 3-2 - Rock empirical formulas

Author	Formula (Empirical)	Equation number
Veronese (1937) [86]	$y_s + y_o = 3.68 \frac{H^{0.225} q^{0.54}}{{d_{90}}^{0.42}}$	Eqn. 3-10
Kotoulas (1967) [80]	$y_s + y_o = 0.78 \frac{H^{0.35} q^{0.7}}{{d_{95}}^{0.4}}$	Eqn. 3-11
	Scour length: $L_{sc} = 2.7 \frac{H^{0.45} q^{0.9}}{{d_{95}}^{0.8} g^{0.45}}$	Eqn. 3-12
	Horizontal distance where maximum scour occurs: $x_1 = 3.9 \frac{H^{0.27} q^{0.54}}{{d_{95}}^{0.27} g^{0.08}}$	Eqn. 3-13

Where:

d_s = Particle diameter representing a cumulative percentile (generally 90-95%) (m)
L_{sc} = Scour length (m)
x_1 = Horizontal distance to point of maximum scour (m)

Table 3-3 - Semi-empirical formulas

Author	Formula (semi empirical) - rectangular jet	Equation number
Mikhalev (1960) [81]	$y_s + y_o = \left[\frac{5.65q}{\sqrt{g d_{90}} \left(\frac{y_o}{d_{90}} \right)^{1/6}} - 9(B_u) \right] \frac{sin\theta'}{1 - 0.215 cot\theta'}$	Eqn. 3-14

Where:

B_u = Half of the thickness or diameter of the jet at impact with the plunge pool free surface (m)

For a more detailed literature review on physical laboratory model studies and related empirical formulas for rock and sediment scour refer to: Mason and Arumugam (1985) [77], Whittaker and Schleiss (1984) [82], Spurr (1985) [83], Bormann and Julien (1991) [84] and Sarkar and Dey (2004) [85]. For additional literature, regarding primarily sediment scouring studies, refer to [86,87,88,89,90,91].

3.3 Physically based scour prediction methods

Rock scouring is highly specialised and there is no general design relation to predict rock scour. Current numerical approaches for fractured rock beds predict the dynamic and fluctuating water pressures inside the fractures or joints. Scour evaluation is a combination of empirical equations and analytical or numerical methods [92]. For static (translation and rotation or roto-translation) and dynamic (flutter and divergence) failure modes, there is no perfect formulation for the general rock failure mechanisms and there is no specific method to determine the arbitrary or general loading (gravity, reinforcement and dam load) or the non-conservative plunge pool water pressures when evaluating scour. Present scour prediction methods still have numerous shortcomings [93,94].

There are currently two main or leading methods to determine the scour extent of rock beds, which take into account most of the variables concerning the rock scour mechanisms and erosive capacity of the jet [43]. The two leading methods are, the Erodibility Index Method (EIM) [95,96] and the Comprehensive Scour Method (CSM) [36] including the Quasi-Steady Impulsion Method. The two methods are semi-empirical and focus on rock scouring as a physical incident. Joint application of the two methods provides cross checking, and better understanding of the scour mechanisms, but the methods should also be checked against prototype and physical laboratory model studies [43]. These two methods are discussed in detail in Sections 3.3.1 and 3.3.2.

3.3.1 Erodibility Index Method (EIM)

The Erodibility Index Method (EIM), as proposed by Annandale (1995), compares the erosive capacity of the water in terms of stream power, to the resistive capacity of the rock mass or bed material [58,97]. The EIM is a scour threshold relationship, which was compiled from field data and near prototype validation [64]. If the erodibility threshold of the bed material is exceeded, erosion would occur [39]. The erodibility index is a replica of Kirstens's ripability index (1982) and is the product of the mass strength, particle/ block size, shape and orientation and the bond strength between particles (see Eqn. 3-15) [8,39,98]. The method can be applied to both rock and sediment.

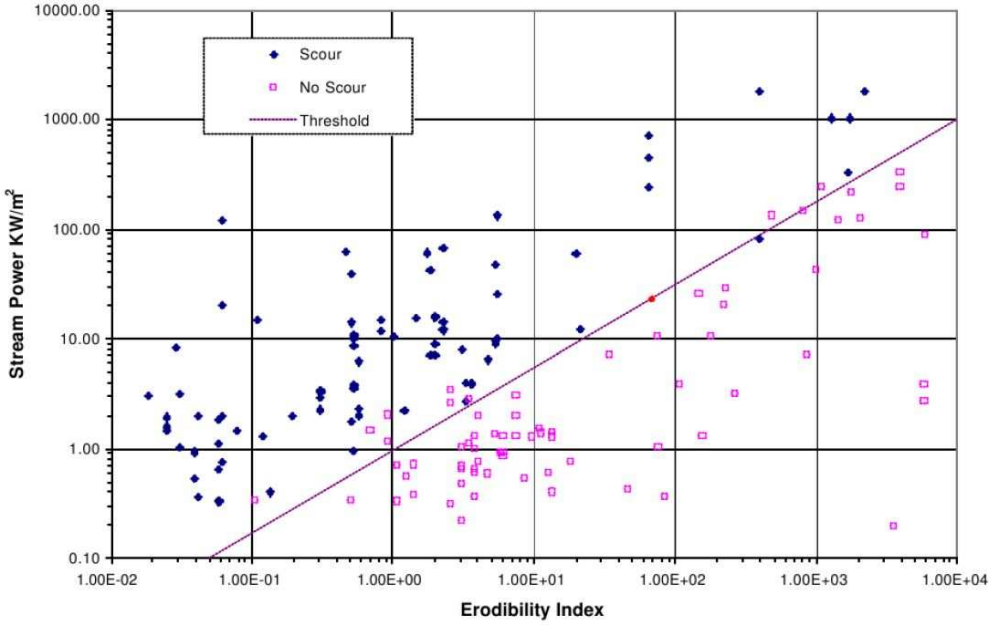

Figure 3-2 - Erodibility index threshold [99]

The erodibility index threshold is a graphical relationship of the rate of energy dissipation and the geomechanical classification of the rock or sediment (defined by the erodibility index) (refer to Figure 3-2) [8]. As it is a geomechanical method or classification (dimensionless), it does not account for the chemical processes, which directly affect the erosive resistance of the rock mass. To consider the chemical processes, the parameter values (see Eqn. 3-15) need to be taken at said conditions and adjusted accordingly. The EIM uses the rate of energy dissipation (stream power), rather than the velocity, when representing the erosive power of the water [99,100]. The EIM does not take into account all the mechanisms of rock scour and does not delineate between the different rock scour mechanisms [56].

3.3.1.1 *Erodibility index (K_h)*

The erodibility index (K_h) quantifies the earth or bed material's ability to resist erosion and can be calculated using Eqn. 3-15 as proposed by Annandale (1995).

$$K_h = K_m . K_b . K_d . K_s \qquad \text{Eqn. 3-15}$$

Where:

K_h = Erodibility index (EI)
K_m = Mass strength factor
K_b = Particle/block size factor
K_d = Interparticle bond (discontinuity shear) strength factor
K_s = Relative shape and orientation (ground shape) factor

The factors or parameters as contained in equation Eqn. 3-15 are determined from standard tables for both rock and sediment (cohesive and non-cohesive) as proposed by Kirsten (1982) (see Appendix B). The parameters were compiled from field measurements and rock/sediment property observations [100,101]. The parameters of Eqn. 3-15 are discussed individually in more detail below.

(i) Mass strength factor

The mass strength factor (K_m or M_s) is based on the strength of perfect earth material with no discontinuities [UCS (unconfined or uniaxial compressive strength of intact rock)] and the coefficient of the material's relative density (C_r) [134]. The factor is the ability and resistance of the rock to break-up into smaller pieces [96]. The mass strength values for rock are generally higher than that of cohesive and non-cohesive sediment and therefore offer higher resistance to scouring as the mass strength factor is a dominant factor in calculating the erosion resistance (Eqn. 3-15) [8,64,99]. Weathering affects the value, as it weakens the rock and thus needs to be taken into account [96].

The mass strength factor (M_s) can be calculated from tables (refer to Appendix B) or using Eqn. 3-16 and Eqn. 3-17 in Table 3-4 [96,134].

Table 3-4 - Mass strength factor [96]

Mass strength factor		
$UCS \leq 10\ MPa$	$\boldsymbol{M_s = C_r(0.78)(UCS)^{1.05}}$	Eqn. 3-16
$UCS > 10\ MPa$	$\boldsymbol{M_s = C_r.UCS}$	Eqn. 3-17

Where C_r is the coefficient of relative density and can be calculated using Eqn. 3-18 [96].

$$\boldsymbol{C_r = \frac{g\rho_s}{27 \times 10^3}} \qquad \text{Eqn. 3-18}$$

Where:

ρ_s = Masss density of rock (kg/m^3)

Other literature suggests the mass strength factor can be calculated using Eqn. 3-19 [134].

$$\boldsymbol{M_s = \lambda_b.\lambda_s.UCS} \qquad \text{Eqn. 3-19}$$

Where:

λ_b = Material unit weight (N/m^3)

λ_s = Unit weight of good quality material (rock) (N/m^3)

(ii) Particle/block size factor

The particle or block size factor (K_b) is based on the number of discontinuities or joint sets (J_n) as well as the rock quality designation (RQD) that defines the joint spacing for rock [96,99,101]. Larger rock blocks generally provide greater resistance and are harder to erode compared to smaller blocks (refer to Figure 3-3) [100]. The particle size factor (K_b) can be calculated using Eqn. 3-20 [96].

$$K_b = \frac{RQD}{J_n} \qquad \text{Eqn. 3-20}$$

Where:

RQD = Rock quality designation

J_n = Joint set number

Values for the joint set number can be calculated from a table (refer to Appendix B) or the formula shown in Table 3-5. The values for RQD can be calculated from formulas shown in Table 3-5. RQD values are generally between 5 and 100, while the joint set number values fall between 1 and 5. The particle size factor thus ranges between 1 and 100 for rock [96]. Some general RQD and joint set numbers, as proposed by Annandale, are shown in Table 3-6 [95,134].

Table 3-5 - RQD formulas [96]

RQD	
$RQD = (115 - 3.3J_c)$	Eqn. 3-21
$J_c = \left(\frac{3}{D}\right) + 3$	Eqn. 3-22
$RQD = \left(105 - \frac{10}{D}\right) = \left(105 - \frac{10}{(J_x \cdot J_y \cdot J_z)^{0.33}}\right)$	Eqn. 3-23

Where:

D = Mean block diameter (≥ 0.1m) (m)

$J_x \cdot J_y \cdot J_z$ = Average spacing of joint sets (in meters)

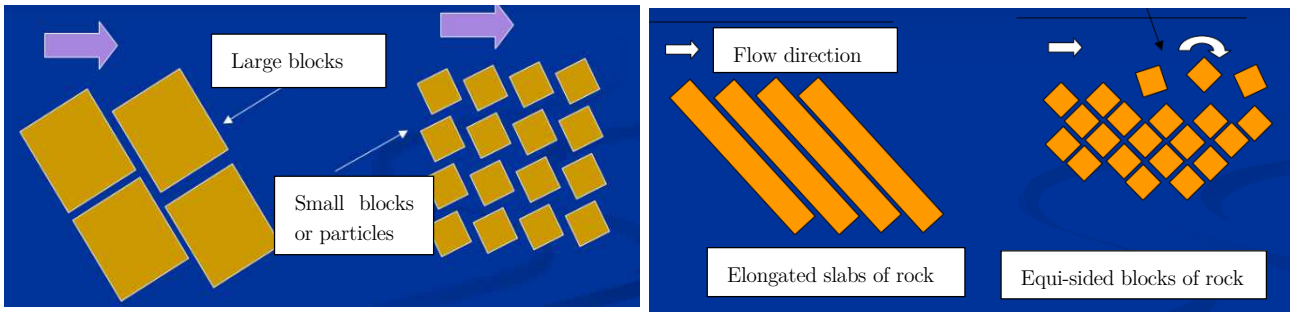

Figure 3-3 - Larger and elongated blocks are generally harder to erode than smaller and equi-sided blocks [64]

Table 3-6 - Joint roughness number and RQD [95,134]

Number of Joints Per Cubic Meter (Jc)	Ground Quality Designation (RQD)	Number of Joints Per Cubic Meter (Jc)	Ground Quality Designation (RQD)
33	5	18	55
32	10	17	60
30	15	15	65
29	20	14	70
27	25	12	75
26	30	11	80
24	35	9	85
23	40	8	90
21	45	6	95
20	50	5	100

(iii) Interparticle bond (discontinuity shear) strength factor

The interparticle bond (discontinuity shear) strength factor (K_d) and subsequently the strength of the joint interfaces in rock, are based on the joint alteration, edge spacing, fill material (between the cracks and joints) as well as rock edge roughness [100,101]. The rougher the edges and the closer together the blocks are to each other, the more difficult they are to erode [100]. The friction developed between the rock blocks determine the interparticle bond strength factor in rock beds. Cohesion is taken into account in the mass strength factor, as well as the interparticle bond strength factor [99]. The interparticle bond strength factor (K_d) can be calculated using Eqn. 3-24 [96].

$$K_d = \frac{J_r}{J_a} \qquad \text{Eqn. 3-24}$$

Where:

J_r = Joint roughness number

J_a = Joint alteration number

Values for the joint roughness number (J_r) and the joint alteration number (J_a) can be calculated using the tables in Appendix B. The joint roughness number (Jr) describes the degree of roughness of the rock discontinuity's opposing faces, while the joint alteration number (J_a) represents the degree of alteration

of the discontinuity faces. Joints with a spacing of 1mm are effectively in contact, while for a joint spacing of 5mm, the joints do not come into contact (upon shear) [96]. Typical interparticle bond (discontinuity shear) strength factors for various rock types are shown in Table 3-7 [98].

Table 3-7 - Interparticle bond (discontinuity shear) strength factor for various rock types

Rock type	Friction angle (degrees)	$J_r/J_a = \tan \Phi$
Quartzite	65	2
Sandstone	40-55	1
Dolerite (sound)	40	0.8
Dolerite (decomposed)	25	0.5
Shale	20-22	0.4

(iv) Relative shape and orientation (ground shape) factor

The relative shape and orientation (ground shape) factor (K_s or J_s) is applicable to the rock exposed to the erosive power of the water. The factor describes the resistance of the earth material based on the structure of the ground [96]. The factor is based on the dip and strike of discontinuities, relative to the flow direction. It is occasionally refered to as the "Real structure of soil/ rock layers" [99,101]. When the rock layers are orientated and dip in the direction of flow, they are prone to easier dislodgement (refer to Figure 3-4) [100]. Values of the relative shape and orientation (ground shape) factor can be determined from the tables in Appendix B.

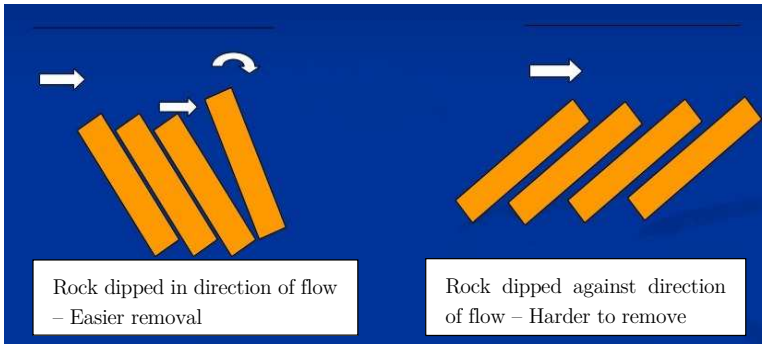

Figure 3-4 - Rock dipped in the direction of flow is generally more easily dislodged [64]

When examining the resistance of the rock mass, the particle/block size and the mass strength have been found to be the governing factors, while interparticle bond strength and relative shape and orientation are secondary factors in determining the resistance of the rock mass[58].

3.3.1.2 *Erosive power of the jet (Stream power)*

The EIM classifies the erosive power of the jet in terms of the rate of energy dissipation per unit area [stream power (P)]. Stream power is a product of shear, as well as the velocity and is representative of the fluctuating pressures as a scalar, to compare with the erodibility index (K_h), as opposed to velocity, shear stress and force which are vectors [99,100]. Eqn. 3-25 can be used to calculate the stream power for plunging jets and is visually represented in Figure 3-5 [39,64,95,101].

$$\boldsymbol{P = \frac{\alpha \rho_m g Q H}{A} = \frac{\gamma_m Q H}{A} = q \Delta E \gamma_m \ (in\ KW/m^2)} \qquad \text{Eqn. 3-25}$$

Where:

A	=	Plunging jet footprint at plunge pool free surface (impact area of jet) (m^2)
α	=	Adjustment factor (for air entrainment)
ΔE	=	Energy loss in terms of head per unit length of flow ($\Delta E = \frac{V^2}{2g}$) (m)
Q	=	Volumetric discharge of jet (m^3/s)
q	=	Unit discharge ($m^3/s/m$)

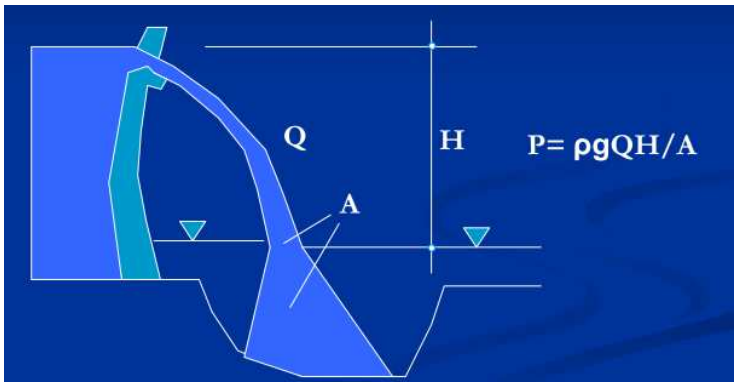

Figure 3-5 - Stream power of jet [64]

Eqn. 3-25 calculates stream power as it represents fluctuating pressures and energy loss [134,95]. The energy dissipation rates and fluctuating pressure magnitudes increase with an increase in turbulence intensity. The pressure fluctuations were found to be primarily responsible for dislodgement [8,134]. Eqn. 3-25, however, only calculates the average stream power per unit area of the jet as it impacts the plunge pool free surface and does not account for the diffusion in the plunge pool. Two methods are available, as proposed by Annandale (2007), to account for the diffusion in the plunge pool and are discussed below [96].

The first method (Approach 1) scales the stream power, by calculating the area of the water jet (jet footprint) at different depths using the methods, as proposed by Ervine and Falvey (1987), to account for jet expansion (see Section 2.5.1.2) and Eqn. 3-26.

$$P_{pool} = \frac{\gamma_m Q H}{A_i} \qquad \text{Eqn. 3-26}$$

Where:

A_i = Jet footprint (impact area of jet) at different elevations below water surface (m^2)
$\gamma_m QH$ = The power stays the same of that at impact with plunge pool free surface (W)
γ_m = Unit weight of the mixture (N/m^3)
H = Drop or fall height (m)
P_{pool} = Stream power in the pool at a certain depth (W/m^2)

Van Schalkwyk *et al.* as cited by Annandale (2007) [96], proposed that the area of a rectangular jet, at impact with the plunge pool free surface, can be approximated by using Eqn. 3-27. Eqn. 3-27 approximates the thickness of the jet at impact as a third of the drop height.

$$A = \frac{bH}{3} \qquad \text{Eqn. 3-27}$$

Where:

b = Jet or channel width at issuance (m)

The second method (Approach 2), to account for the diffusion in the plunge pool, uses fluctuating and mean pressure coefficients to estimate stream power similar to the methods proposed by Ervine and Falvey (1987), and Bollaert (2002), as discussed in the CSM section, outlined in Section 3.3.2. The variation in average stream power per unit area (P_{jet}), as a function of Y/D_j, can be determined using Eqn. 3-28 [96]. Where Y is the depth of the water cushion (plunge pool depth) and D_j is the diameter or thickness of the jet at impact with the plunge pool free surface.

$$P_{jet}\left(\frac{Y}{D_j}\right) = C_{sp}\left(\frac{Y}{D_j}\right)\frac{\gamma_m Q H}{A} \approx C_p\left(\frac{Y}{D_j}\right)\frac{\gamma_m Q H}{A} \qquad \text{Eqn. 3-28}$$

Where:

C_{sp} = Average stream power decay coefficient
C_p = Average dynamic pressure coefficient

Theoretically C_{sp} is smaller or equal to C_p but the average stream power decay coefficient (C_{sp}) is assumed equal to the average dynamic pressure coefficient (C_p) only when the velocity distribution plunge pool is

unknown or when the jet is undeveloped at impact (jet core still intact) as a conservative estimate [96]. If the velocity at a certain depth from the plunge pool free surface (V_z) is known, C_{sp} can be equated with Eqn. 3-29 [96]. Cp can be calculated using the

$$C_{sp} = C_p \frac{V_z}{V_j} = C_p \frac{J_p}{J} \qquad \text{Eqn. 3-29}$$

Where:

J = Jet length (m)
J_p = Length of jet core (m)
V_z = Jet velocity at depth z from the plunge pool free surface (m/s)

The fluctuating portion of stream power per unit area (P'_{jet}), as a function of Y/D_j, can be calculated using Eqn. 3-30 [96].

$$P'_{jet}\left(\frac{Y}{D_j}\right) = C'_p\left(\frac{Y}{D_j}\right)\frac{\gamma_m Q H}{A} \qquad \text{Eqn. 3-30}$$

Where:

C'_p = Fluctuating pressure coefficient

The sum of the mean and fluctuating portions equals the variation in total stream power per unit area (P_{total}), as a function of Y/D_j, (see Eqn. 3-31) [96].

$$P_{total}\left(\frac{Y}{D_j}\right) = P'_{jet}\left(\frac{Y}{D_j}\right) + P_{jet}\left(\frac{Y}{D_j}\right) \qquad \text{Eqn. 3-31}$$

The fluctuating pressure coefficient can be determined from the Section 3.3.2 (CSM) as proposed by Bollaert (2002), and Ervine and Falvey [96].

The erodibility threshold, as shown in Figure 3-2, occurs when the stream power is equal to the resistance of the bed material. The erodibility thresholds are shown in Table 3-8. The threshold stream power required, generally increases with depth, as it is a general assumption that rock strength increases with depth (see Figure 3-6) [64].

Table 3-8 - Erodibility threshold [39]

Erodibility threshold	
$P = f(K_h)$	Erodibility threshold
$P > f(K_h)$	Erosion occurs
$P < f(K_h)$	No erosion

Where:

$f(K_h)$ = Functional capacity of material to resist erosion

P = Magnitude of agitating agent (stream power)/ rate of energy dissipation

K_h = Erodibility index/ resistance of bed

The critical stream power equations, which relate to the stream power required to initiate scour or result in incipient motion, are shown in Table 3-9. The critical stream power is split into two categories, according to the bed material's resistance [96]. The formulas do not account for air entrainment. An adjustment factor can be applied to account for air entrainments effects on the jet break and amplification in closed rock joints [101].

Table 3-9 - Critical stream power [96]

Critical stream power		
$K_h \leq 0.1$	$\boldsymbol{P = 0.48(K_h)^{0.44}}$	Eqn. 3-32
$K_h > 0.1$	$\boldsymbol{P = {K_h}^{0.75}}$	Eqn. 3-33

The EIM erosion threshold graph (see Figure 3-2) is to be used for linear interpolation to find if erosion would occur or not. The critical stream power, as calculated using the formulas in Table 3-9, can also be used. Using the threshold stream power and the applied stream power, the critical sour depth can then be found, as shown in Figure 3-6.

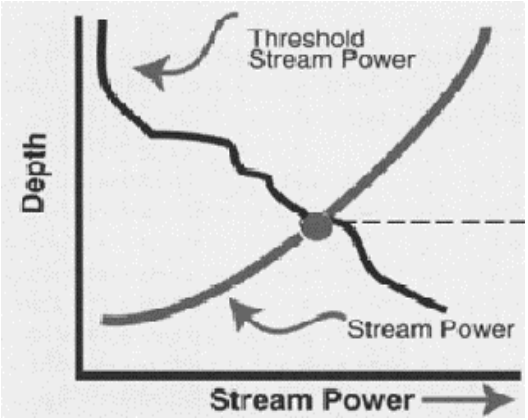

Figure 3-6 - Threshold stream power vs. applied stream power to calculate scour depth [100]

The erodibility index method does, however, have some uncertainties. The original graphical representation (Figure 3-2) shows some uncertainties at the threshold condition as some points are above the threshold condition - which showed no erosion, and other points are below the threshold and showed erosion. Researchers have suggested that two curves be introduced: a 0% erosion probability and a 100% erosion probability curve, as shown in Figure 3-7 to eliminate these uncertainties [101].

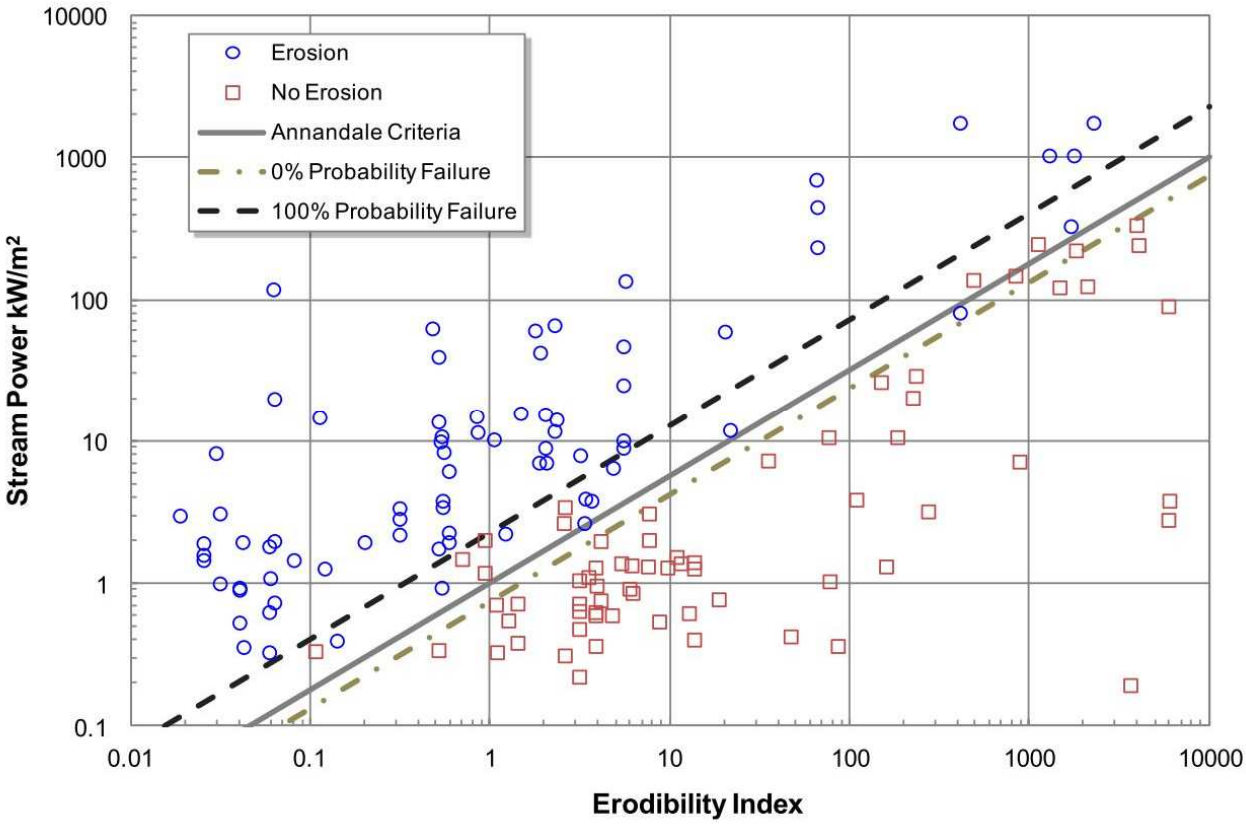

Figure 3-7 - EIM Scour threshold (with adjusted probabilities) [101]

EIM shortcomings

The EIM has several limitations and shortcomings, of which some are listed below, as found in literature.

- The EIM is sensitive to errors when the stream power required is relatively low.
- The vertical distribution of stream power available for scour in a plunge pool is dependent on the submerged velocity profile of the jet. The method generally calculates that the energy of the jet that is dissipated within a few metres of the plunge pool, which can be in error and it also does not take into account the change in discharge magnitude [8].
- The method is a classification method and not an analytical or a numerical method.
- The method was based on 150 observations of auxiliary earth spillways and not jet spillways [8]. Care should thus be taken when applying it to other spillway cases.
- The method can only give an indication if scour would occur, or not, and does not provide information on the shape of the scour hole that would form, or the evolution of the scour hole with time [102].
- EIM is a generalised evaluation of rock scour and does not explicitly consider the rock scour mechanisms, and due to the fact that the rock joint orientation is considered in 2D, 3D rock mass block removal cannot be captured [58]. It is applicable to the entire rock mass, but is not applicable to single rock blocks (individual rock block removal is a critical mechanism of scour). It also only approximately accounts for rock masses directionality [93,94].

3.3.2 Comprehensive scour model (CSM)

The comprehensive scour model (CSM), as developed by Bollaert (2002), is a physically based model and consists of three methods: direct impulsion (DI), quasi-steady impulsion (QSI) and comprehensive fracture mechanics (CFM). The specific method used is dependent on the type of rock discontinuities present. The CSM takes into account, both, the geomechanical properties of the bedrock, as well as describing the jet diffusion through the air and plunge pool. The CSM also allows the estimation of scour as a function of time. The CSM considers three modules as illustrated in Figure 3-10. The modules include the falling jet (from issuance to plunge pool free surface), plunge pool (jet traversing plunge pool) and rock mass (pressures and velocities at rock bottom) [41,54].

The CSM is based on near prototype scaled conditions to reproduce the turbulent flow and pressure fluctuations correctly. The jointed rock mass was modelled using steel plates. Figure 3-8 is a schematic illustration of the experimental facility, used to develop the CSM [36].

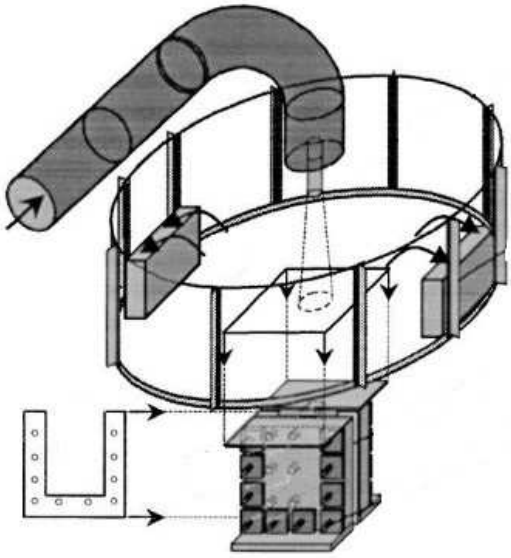

Figure 3-8 - Schematic of experimental setup used to develop the CSM [103]

CSM embraces linear elastic fracture mechanics principles to estimate brittle fracture and fatigue failure and considers block removal by net uplift force and dynamic impulsion [20,55,58]. The model is applicable to any brittle fractured medium, such as a fractured rock mass [55]. The method, however, does not fully describe the physical background of the scour phenomena and was primarily developed for circular jets. The scour hole computation is done on a block by block, or layer by layer basis, for each CSM methods [54].

3.3.2.1 *CSM methods*

3.3.2.1.1 Dynamic impulsion (DI) method

The dynamic impulsion (DI) method analyses sudden rock block ejection due to uplift pressures on individual rock blocks [36,41,103]. Uplift and impulsion is dependent on the rock block density, shape, dimensions, instantaneous forces on the blocks and their evolution [54]. The rock mass joint network is completely formed in this method [12].

Shortcomings:

The method analyses vertical translation failure of parallelepiped rock blocks, but does not take into account roto-translation which is a common failure mode of rock blocks. Uplift pressures for this method are estimated empirically or from curves and have estimation errors. The method also uses a scour threshold (height through which the block is lifted) that differs between researchers and is calibrated from experimental results [92,93,94]. The dynamic impulsion method (DI) uses fracture bounding orientations, which are still very simplistic in comparison to nature [58]. See Section 3.3.3 for alternative methods to the DI method.

3.3.2.1.2 Comprehensive fracture mechanics (CFM) method

The comprehensive fracture mechanics (CFM) method assesses the instantaneous or time dependant joint propagation due to joint water pressures (fatigue failure and brittle fracturing). The method can be used to determine the ultimate scour depth, as it is the only CSM method that allows time evolution of scour development [12]. The CFM method is dependent on the pressure fluctuations, fracture geometry and the rock bed's geomechanical properties [41,54]. In this method the rock mass joint network is not yet completely formed.

3.3.2.1.3 Quasi-steady impulsion (QSI) method

The Quasi-steady impulsion (QSI) method calculates the peeling of blocks along thin layers (see Figure 2-15 and Figure 3-9) in the wall jet region. The peeling of rock blocks can either occur instantaneously or be time dependant, but the QSI method only focuses on the instantaneous peeling of rock blocks. The method is dependent on the rock layer thickness, block dimensions and shape, protrusion and local flow velocities at the block boundaries [54]. This method allows the calculation of the extent of scour, whereas the above methods (CFM and DI) only determines scour in the impingement zone or at the centreline of the jet.

The DI, CFM and QSI methods are depicted graphically in Figure 3-9.

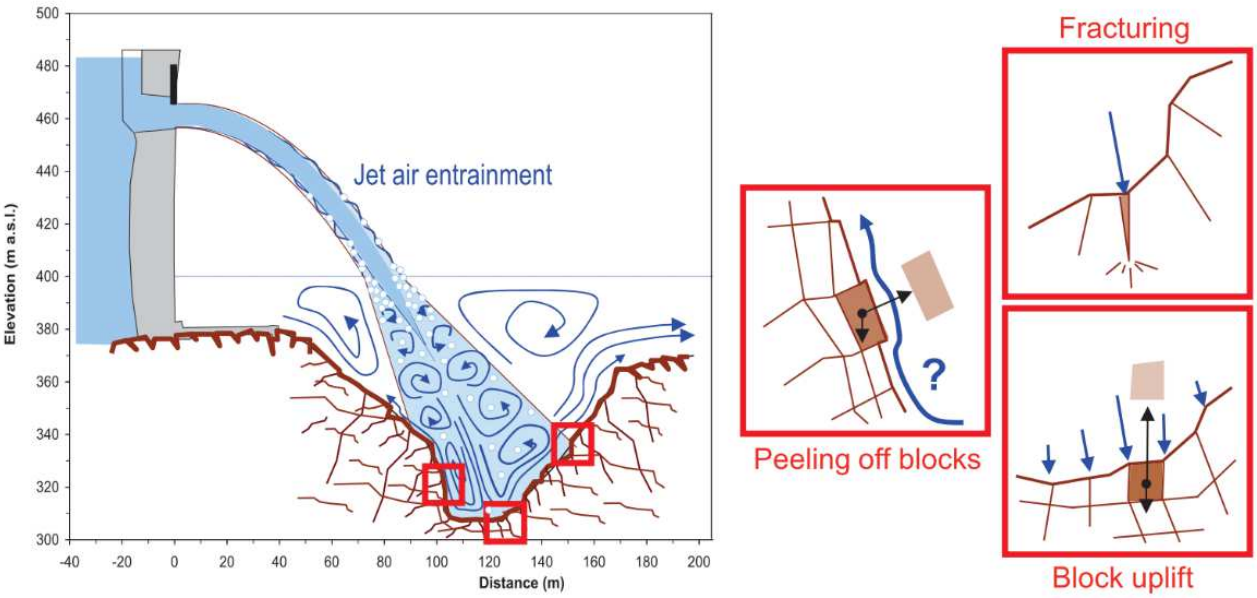

Figure 3-9 - CSM scour mechanisms (DI, CFM and QSI) [12]

Table 3-10 shows the use and purpose of each of the CSM models developed by Bollaert (2011) [104,105].

Table 3-10 - The use and function of each of the CSM models [104]

Mechanism	Symbol	Functioning	Validity	Output
Comprehensive Fracture Mechanics	CFM	Progressive break-up of existing rock joints due to jet impact	Area of turbulent jet impingement	Time evolution of scour development
Dynamic Impulsion	DI	Sudden vertical ejection of rock blocks generated by pressure differences over and under the block	Area of turbulent jet impingement	Ultimate scour depth
Quasi-Steady Impulsion impingement	QSI	Peeling off of protruding rock plates due to wall jet generated by turbulent impingement	Area between dam and location of turbulent jet	Ultimate scour depth

3.3.2.2 *CSM modules*

The calculation procedure of the CSM is split into three modules, which are explained in more detail below with their respective calculations also outlined where relevant. See Figure 3-10 for a visual representation of the CSM modules.

3.3.2.2.1 The falling jet module

The jet's behaviour in the air and plunge pool needs to be quantified, before the jet impact at the plunge pool bottom can be assessed. The falling jet module describes the jet geometry and hydraulic characteristics of the falling jet from dam issuance up until impact at the plunge pool free surface [38].

(i) Flow properties at issuance

The issuance velocity (V_i), initial turbulence (T_u) and initial jet diameter or thickness (D_i or B_i) are the main parameters describing the jet at issuance [36]. The issuance velocity and initial jet core diameter or thickness are dependent on the type of spillway and geometry of the issuance structure such as sluice gates. Refer to Section 2.3 for a detailed discussion on the initial turbulence.

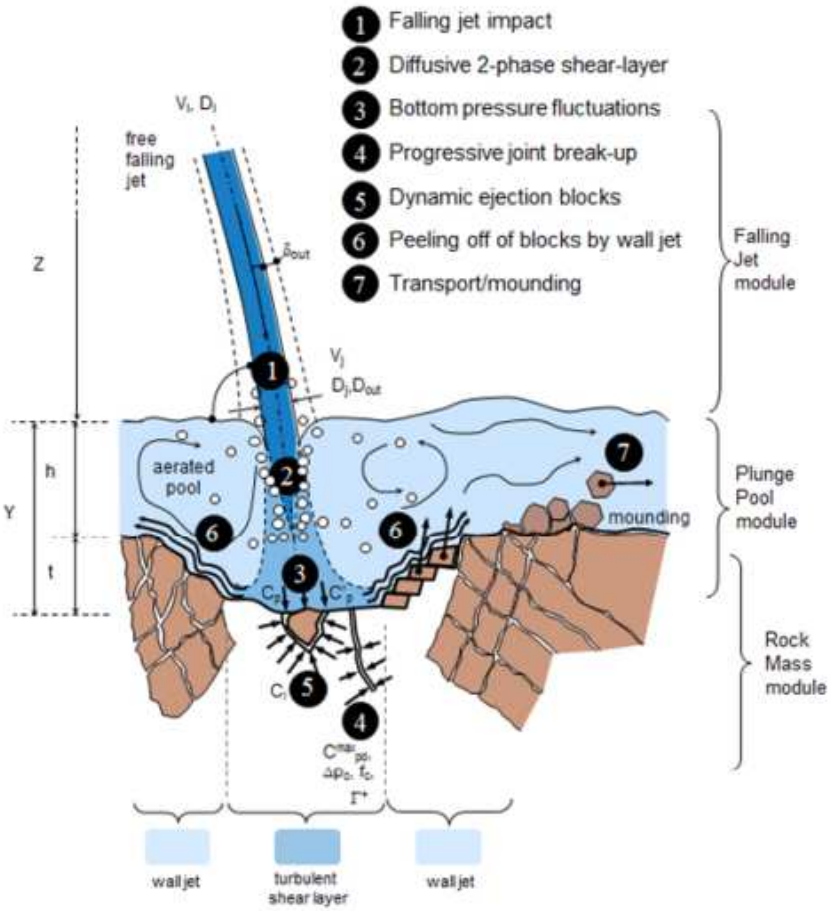

Figure 3-10 - CSM modules (Bollaert) [102]

(ii) Flow properties at impact with plunge pool free surface

Velocity at impact

The velocity at impact with the plunge pool free surface - if the jet is compact or undeveloped - can be calculated using Eqn. 3-34 [21,96].

$$V_j = \sqrt{V_i^2 + 2gH} \qquad \text{Eqn. 3-34}$$

Where:

V_i = Issuance velocity (U_0 or V_0 in some literature) (m/s)

V_j = Impact velocity with plunge pool free surface (m/s)

H = Vertical fall distance (see Figure 3-10) (Z in some literature). (m)

If the jet at impact with the plunge pool free surface is developed, the impact velocity can be calculated using Eqn. 3-35 (see Figure 3-11 for visual representation) [36,129]:

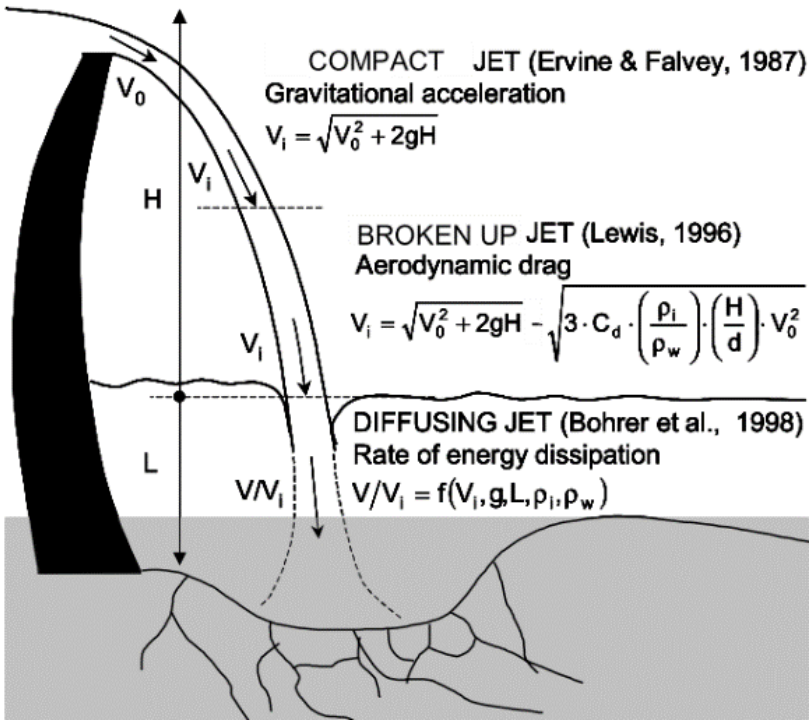

Figure 3-11 - Jet velocity at impact (Bollaert) [36]

$$V_j = \sqrt{V_i^2 + 2gH} - \sqrt{3C_d\left(\frac{\rho_a}{\rho}\right)\left(\frac{H}{d}\right)V_i^2} \qquad \text{Eqn. 3-35}$$

Where:

ρ_a = Density of air (1.29 kg/m^3) (kg/m^3)

d = Diameter of a sphere with the same volume as a water drop (m)

C_d = Drag coefficient of sphere [129].

Thickness or diameter of the jet core at impact

For circular jets, the diameter of the core of the jet at impact with the plunge pool free surface, due to gravity, can be calculated using Eqn. 3-36.

$$D_j = D_i\sqrt{\frac{V_i}{V_j}} \qquad \text{Eqn. 3-36}$$

Where:

D_i = Diameter of core/jet at issuance (m)

D_j = Diameter of core at impact with free surface of plunge pool (impact diameter) (m)

The inner diameter or minimum core diameter can be calculated using internal turbulence, instead of gravitational acceleration, as shown in Eqn. 3-37.

$$D_{in} = D_i - 2 \times (0.005\ to\ 0.01) \times L_j \qquad \text{Eqn. 3-37}$$

Where:

L_j = Trajectory length (m)

D_{in} = Minimum diameter of the core (m)

For rectangular jets, the width of the core can be calculated with Eqn. 3-38 [31,106]:

$$B_g = \frac{q}{\sqrt{2gH}} \qquad \text{Eqn. 3-38}$$

Where:

B_g = Core thickness of rectangular jet (m)

Trajectory length of a plunging jet

The trajectory length of the plunging jet can be determined from ballistics or kinematic theory, which neglects wind and jet breakup. The jet's trajectory can be calculated using Eqn. 3-39, by determining x and y coordinates of points along the trajectory [82,107,108]

$$y = x\tan\theta - \frac{gx^2}{2V_i^2\cos^2\theta} \qquad \text{Eqn. 3-39}$$

Where:

x = Horizontal distance along trajectory (m)

y = Vertical distance along trajectory (m)

θ = Initial angle of jet (positive if upwards and negative if downwards)

For a horizontal jet discharge condition at issuance, the above equation can be reduced to Eqn. 3-40 [107,108].

$$y = -\frac{gx^2}{2V_i^2} \qquad \text{Eqn. 3-40}$$

Eqn. 3-39 and Eqn. 3-40 relate to the trajectory of the bottom surface of the jet. By adding the initial thickness of the jet (D_i or B_i), the trajectory of the top surface of the jet can be also approximated. The actual horizontal distance (x) that the jet will travel to impact with the plunge pool free surface in reality will be shorter than calculated from Eqn. 3-40, due to jet break-up, aeration and air resistance, as the above formulas only describe the trajectory of an ideal jet [82,107]. The trajectory length for jets issuing from spillway chutes and deflector buckets, which can be used for prototype jet trajectory cases, have also been studied and can be calculated using Eqn. 3-41 [96,107].

$$y = x\tan\theta - \frac{x^2}{K_2[4(D_i + h_v)(\cos\theta)^2]} \qquad \text{Eqn. 3-41}$$

Where:

x = Horizontal distance travelled by the jet

θ = Issuance angle

K_2 = Coefficient allowing for air resistance

D_i = Thickness (B_i) or diameter (D_i) of jet at issuance

h_v = Velocity head ($h_v = \frac{V_i^2}{2g}$) (m)

The value of K_2 in Eqn. 3-41 is proposed to be taken between 0.75 to 0.9 but can be higher than 1 such as in the case of spillway chute where the value can be taken as 1.5, thus reducing the negative pressures and subsequent cavitation [107]. The trajectories calculated using Eqn. 3-41, however, have been found to be flatter in comparison to the trajectories calculated using the ballistics equation (Eqn. 3-39), because an extra depth term, D_i, is included in the formula. The horizontal distance travelled by the jet, is thus overestimated, due to the extra depth term. Various uncertainties pertaining to the values that should be taken for thickness of jet, or depth of flow at issuance (D_i) as well as the velocity head (h_v) and if the values should be added, are also present [107].

Ervine *et al.* (1997) proposed that the trajectory of the jet can be calculated in terms of the initial Froude number, by using Eqn. 3-42 [24].

$$\frac{L_j}{D_i {Fr_i}^2} = \frac{1}{2}\left[\left(\frac{V}{V_i}\right)^2 - 1\right] \qquad \text{Eqn. 3-42}$$

Where:

V = Velocity at the point (m/s)
V_i = Issuance velocity (m/s)
L_j = Trajectory length (L in some literature) (m)

In terms of the horizontal point of impact (X_n) of a plunging jet discharged over a weir, Stein and Julien (1993) suggested using Eqn. 3-43 to calculate its position [147].

$$X_n = V_i y_0 \sqrt{\frac{2}{g y_0}} \qquad \text{Eqn. 3-43}$$

Where:

y_0 = Flow depth over the structure i.e. overflow weir (critical depth) (m)

Angle of jet impact with the free surface

Eqn. 3-44 can be used to calculate the angle of impingement of the plunging jet, which was developed using the ballistics equation [96].

$$\xi(degrees) = \arctan\left[\tan\theta - \frac{x}{2K_2[(D_i + h_v)(\cos\theta)^2]}\right](-1) \qquad \text{Eqn. 3-44}$$

Where:

K_2 = Coefficient allowing for air resistance (normally set to 0.75)

For impingement angles of between 70 - 90 degrees, Bollaert (2002) suggests that it is reasonable to ignore their trivial impact on the travel distance of the jet in the plunge pool and the distance can be taken as the plunge pool depth. For smaller angles, the water depth should be redefined as the length of jet trajectory through plunge pool [38]. Correct estimation of the travel distance through the plunge pool becomes especially important where the calculations are dependent upon the Y/D_j ratio.

Impingement thickness/outer dimensions of plunging jet at impact with free surface

The outer diameter of a plunging jet, which includes the core diameter and the turbulent shear layer (lateral spread due to turbulence), for a circular jet at impact with the plunge pool free surface, can be calculated using the equations shown in Table 3-11. Most of the methods in Table 3-11 are in terms of gravitational acceleration, but some researchers, such as Davies [109], have suggested using the internal turbulence (Eqn. 3-49) [36].

Table 3-11 - Outer diameter of circular jets

Circular jets		
Author	**Outer diameter**	**Equation number**
Ervine and Falvey (1987) [27] and Ervine *et al.* (1997) [24]	$\boldsymbol{D_{out} = D_i + 2\frac{\delta_{out}}{X}L_j}$	Eqn. 3-45
	$\boldsymbol{D_{out} = D_i + 2 \times 0.38.Tu.L_j}$	Eqn. 3-46
Ervine *et al.* (1997) [24,96,115]	$\boldsymbol{D_{out} = D_i\sqrt{\frac{V_i}{V_j}} + 2\varepsilon}$ for $\boldsymbol{V_i \geq \frac{0.275}{Tu}}$	Eqn. 3-47
	$\boldsymbol{\varepsilon(jet\ spread) = \frac{1.14.Tu.{V_i}^2}{g}\left[\sqrt{\frac{2L_b}{D_i{Fr_i}^2} + 1} - 1\right]}$	Eqn. 3-48
Davies (1972) [109] and Ervine *et al.* [36] - Based on internal turbulence	$\boldsymbol{D_{out} = D_i + 2 \times (0.03\ to\ 0.04) \times L_j}$	Eqn. 3-49

Where:

D_{out} = Outer diameter of jet at impact with plunge pool free surface (m)

ε = Lateral spreading of the jet (m)

Castillo looked at the impingement thickness of a rectangular jet in terms of gravitational acceleration as discharged from an ogee spillway [31]. The proposed formulas are shown in Table 3-12.

Table 3-12 - Impingement jet thickness of rectangular jets [31,96,108,110]

Rectangular jets		
Author	**Outer Thickness**	**Equation number**
Castillo (1998) [31,96,108,111]	$\boldsymbol{B_j = B_g + 2\xi}$	Eqn. 3-50
	$\boldsymbol{\xi\ (Lateral\ spread) = 2\varphi\sqrt{h_0}\left(\sqrt{H} - \sqrt{h_0}\right)}$	Eqn. 3-51
	$\boldsymbol{B_j = \frac{q}{\sqrt{2gH}} + 4\varphi\sqrt{h_0}\left(\sqrt{H} - \sqrt{h_0}\right)}$	Eqn. 3-52
	$\boldsymbol{\varphi = 1.07Tu}$	Eqn. 3-53
	$\boldsymbol{h_0 = 2B_i \approx 2\left(\frac{q}{C_d}\right)^{\frac{2}{3}}}$	Eqn. 3-54

Where:

h_0 = Energy head at the crest of the weir (flow depth over weir) (see Figure 3-12). (m)

ξ = Jet lateral spread distance. (m)

B_j = Impingement thickness of the jet (m)

H = Drop height (m)

B_g = Core thickness of the rectangular jet at impact with the plunge pool free surface (m)

In subsequent studies the brink or overtopping depth (d_b) was proposed to be used in the equations, shown in Table 3-12, rather than the energy head (h_0), which is estimated as twice the overtopping depth ($2B_i$), as was initially specified by Castillo (1998)[108]. Davies (1972) suggested that the lateral spread can be approximated by using the square root of the fall distance [31,109].

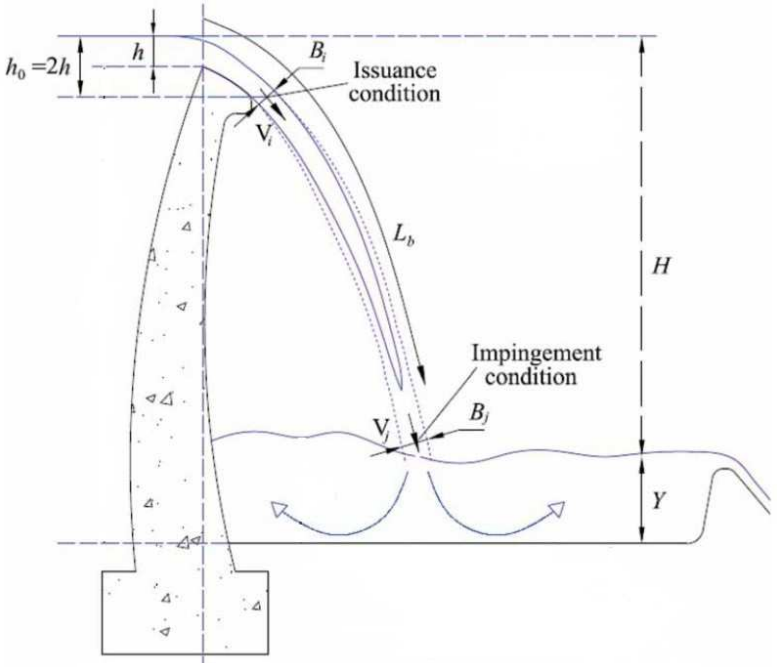

Figure 3-12 - Rectangular free falling jet [110]

3.3.2.2.2 The plunge pool module

This module defines the jet as it moves through plunge pool and impinges at the plunge pool bottom. The pressures at the bottom of the plunge pool are determined from this module.

(i) Mean dynamic pressures (2D)

Ervine *et al.* (1980) [27] developed formulas to calculate the dynamic and fluctuating pressure at the plunge pool bottom including air entrainment for plunging jets. The methods, summarised below, are adaptations of the methods proposed by Ervine *et al.* (1980) as developed by Bollaert (2002) and other researchers. The dynamic pressure coefficients describe the pressure field of the mean and fluctuating dynamic pressures. The formulas described in this section give the coefficients at the impingement zone, which include the jet centreline and the exponential decay radially outwards [113]. The plunge pool depth (Y), turbulence intensity (T_u) and jet impact diameter/thickness (D_j) are important factors as the ratio of Y/D_j is directly related to the diffusion of the jet and the subsequent pressures at the rock bed (see Figure 3-13).

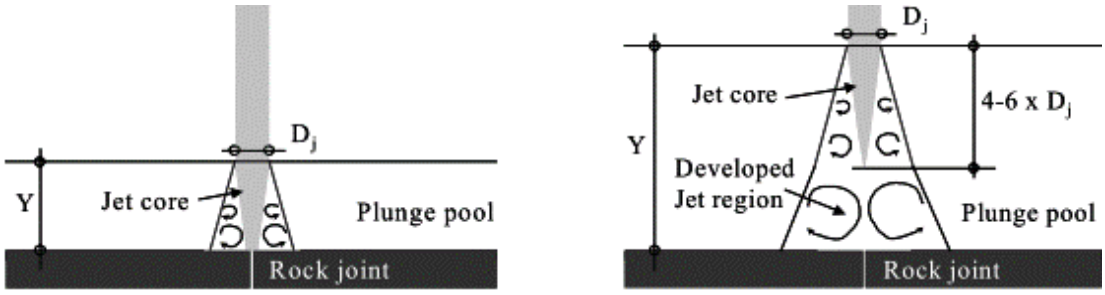

Figure 3-13 - Undeveloped (left) and developed jet (right) at impact with plunge pool floor [63]

Initially the water (plunge pool) depth equals the tailwater level but as scour occurs, or the discharge increases, the water depth increases to the sum of the tailwater and the scour depth [38]. In the case of jets impacting the plunge pool free surface at 70 - 90 degrees, the value of the plunge pool depth (Y), can be calculated as the vertical distance of the water cushion. In the case of jets with smaller impact angles (<70 degrees), the value of the plunge pool depth (Y) is calculated as the exact trajectory length of the jet, travelled in the plunge pool [103].

Total dynamic pressure [96]:

The total dynamic pressure can be calculated using Eqn. 3-55. The mean dynamic pressure coefficient (C_{pa}) and the root-mean-square (RMS) coefficient of fluctuating dynamic pressures (C'_{pa}), are measured under the centreline of the jet. The coefficients correspond with the ratio of pressure head to incoming kinetic energy [10,41,112,116].

$$P_{max} = (C_{pa} + C'_{pa})\gamma_m \emptyset \frac{V_j^2}{2g} \qquad \text{Eqn. 3-55}$$

Where:

Φ = Kinetic energy velocity coefficient (generally assumed as 1) - see Appendix A

V_j = Impact velocity with plunge pool free surface (m/s)

For the formulas proposed by Bollaert (2002), to determine the dynamic and fluctuating pressure coefficients as described below, no scaling effects are present, as velocities higher than 20m/s was used during the physical laboratory model tests to determine the pressure coefficients [115].

(ii) Mean dynamic pressure coefficient under the jet centreline (C_{pa})

The mean pressures at the plunge pool bottom have been studied extensively [21,24,36,63,113]. The mean dynamic pressure coefficient (C_{pa}) can be approximated in terms of the ratio of pressure head to incoming kinetic energy (see Eqn. 3-56).

$$C_{pa} = \frac{\frac{P_{mean}}{\gamma_m}}{\frac{V_j^2}{2g}} = \frac{Mean\ dynamic\ head}{Kinetic\ energy\ of\ jet\ at\ imapct} \qquad \text{Eqn. 3-56}$$

Where:

P_{mean} = Relative pressure or average dynamic pressure at the bottom of the pool (N/m^2)

γ_m = Unit weight of the fluid mixture (N/m^2)

Circular jets

Figure 3-14 graphically illustrates the mean pressure coefficients for different jets as studied by various researchers.

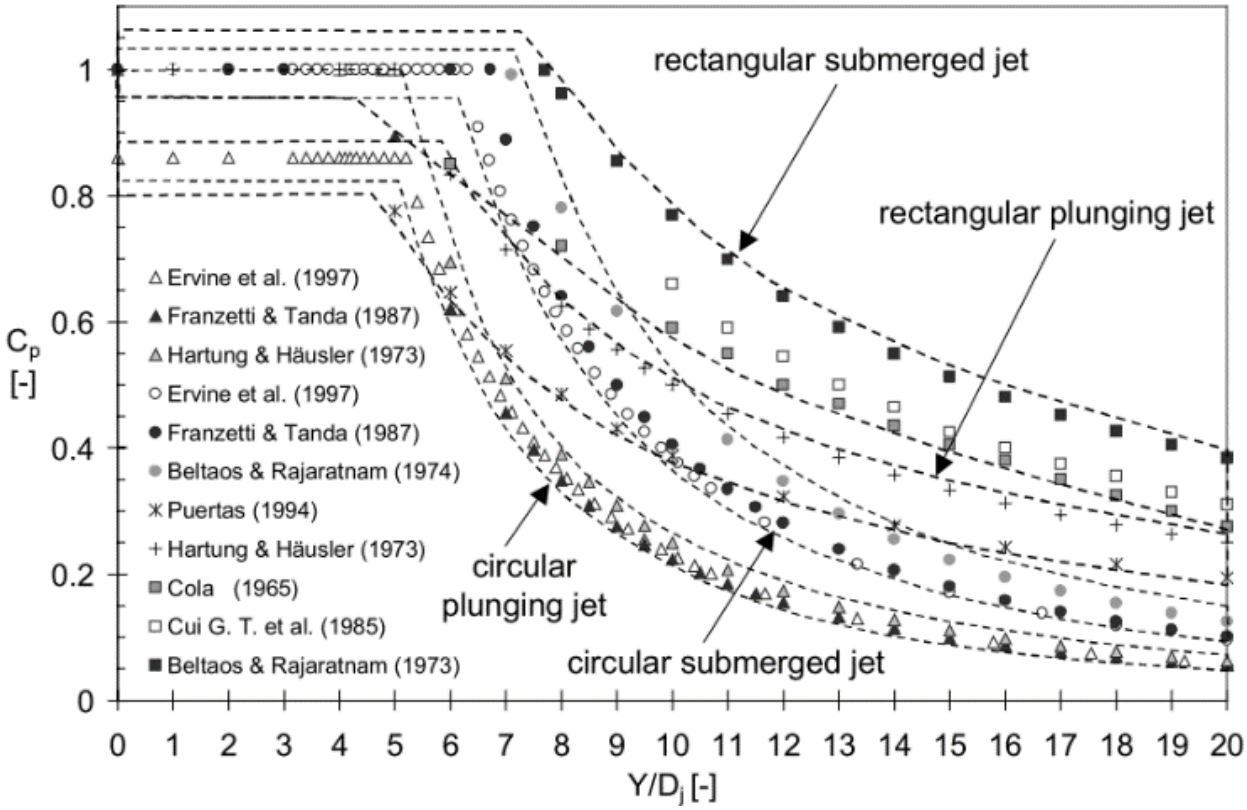

Figure 3-14 - Mean dynamic pressure coefficient [36]

For jets with a drop height (H) to break-up length (L_b) ratio of 0.5 (H/L_b), the mean pressure coefficient for circular jets can be calculated, as well as its spatial extent, using the formulas in Table 3-13 as proposed by Bollaert (2002), which is based on the methods proposed by Ervine *et al.* [96,24].

Table 3-13 - Mean pressure coefficient [24,96].

Mean Pressure Coefficients		
Undeveloped/core jet at impact with rock mass:		
$\frac{Y}{D_j} < 4 \text{ to } 6$	$\boldsymbol{C_{pa} = 0.85 \text{ or } 0.875}$	Eqn. 3-57
Spatial extent:	$\frac{C_{pr}}{C_{pa}} = e^{-K_2\left(\frac{r}{r_{max}}\right)^2}$ where $k_2 = 3$ $r_{max} = 0.5D_j + 0.25Y$ [96] or $r_{max} = Y$ [24]	Eqn. 3-58
Developed jet at impact with rock mass:		
$\frac{Y}{D_j} > 4 \text{ to } 6$	$C_{pa} = 38.4(1 - \alpha_i)\left(\frac{D_j}{Y}\right)^2$	Eqn. 3-59
Spatial extent:	$\frac{C_{pr}}{C_{pa}} = e^{-K_2\left(\frac{r}{r_{max}}\right)^2}$ where $k_2 = 6$	Eqn. 3-60

Where:

r = Radial distance from the centreline of the jet (m)

r_{max} = Maximum radial distance from centreline (m)

Y = Plunge pool depth (m)

α_i = Air concentration at impact (%)

D_j = Diameter (core) of the jet at impact with the plunge pool free surface (m)

For a developed jet it is necessary to determine the air concentration at impact (α_i), which can be calculated using Eqn. 3-61, to compute the mean pressure coefficient as proposed by Ervine and Falvey (1987) [21,36].

$$\alpha_i = \frac{\beta}{1 + \beta} \qquad \text{Eqn. 3-61}$$

Where:

β = Volumetric air-to-water ratio or free air content (-)

The free air content or volumetric air-to-water ratio (β) in water can be described by two ratios, as shown in Table 3-14, if the volumes and flows of the air and water are known [96]. Bollaert (2002) proposed plausible values of β of between one and two for prototype conditions [38].

Table 3-14 - Free air content ratios [96]

Free air content ratios	
$\boldsymbol{\beta = \frac{Volume\ of\ air\ (V_a)}{Volume\ of\ water\ (V_w)}}$	Eqn. 3-62
$\boldsymbol{\beta = \frac{Unit\ flow\ of\ air\ (q_a)}{Unit\ flow\ of\ water\ (q)}}$	Eqn. 3-63
Where: $\boldsymbol{q_a = 0.00002(V_j - 1)^3 + 0.0003(V_j - 1)^2 - 0.0058}$ For rectangular jets with thickness > 30mm and for velocities between 1.5 and 15m/s only	Eqn. 3-64

Free air content (β) can also be calculated using the formulas shown in Table 3-15 for different jet types, however, the formulas are still very ambiguous [11,29,96,114].

Table 3-15 - Free air content formulas [96]

Free air content formulas		
Circular jets	$\boldsymbol{\beta = K' \sqrt{\frac{L}{D_j}} \left(1 - \frac{V_o}{V_j}\right)}$ Where: K' = Empirical parameter see Table 3-16	Eqn. 3-65
Rectangular jets [11]	$\boldsymbol{\beta = 0.13 \sqrt{\frac{L}{B_j}}}$	Eqn. 3-66
	$\boldsymbol{\beta = 0.13 \left(1 - \frac{V_{air}}{V_j}\right) . (\frac{H}{B_j})^{0.446}}$	Eqn. 3-67

Where:

V_{air} = Minimum jet velocity required to entrain air (approximately 1 m/s) [11] (m/s)

Values for the empirical parameter K', as used in Eqn. 3-65, are shown in Table 3-16 [29]:

Table 3-16 - Empirical parameter K' values

Empirical parameter K'			
Turbulence	**Circular jets (K' values)**	**Rectangular jets (K' values)**	**Application limit**
Rough	0.4	0.2	$L/D_j \leq 50$
Moderate	0.3	0.15	$L/D_j \leq 100$
Smooth	0.2	0.1	$L/D_j \leq 100$

An initial velocity of 1m/s, is the minimum velocity needed to lead to aeration of the jet and the maximum air content that is expected to occur is between 65 - 70% [29,96]. The maximum value of the mean pressure coefficient (C_{pa}) is between 0.8 - 09 for plunging jets and not one due to the spreading and aeration of the jet. Bollaert (2002) found that the coefficient becomes insignificant for Y/D_j ratios above 10 - 12 [36,116].

Rectangular jets

Castillo (2006) looked at the mean pressure coefficients for rectangular jets [31,115]. Castillo found that one curve can be used for the values of the ratio of the head drop (H) to the break-up length (L_b), $H/L_b \leq 0.5$, but found several curves for values of $H/L_b > 0.5$ (aerated and developed jets). In a later study, Castillo (2014) updated the mean pressure coefficients to redefine them for both shallow and deep plunge pools [110]. Refer to Eqn. 3-68 - Eqn. 3-70 for the updated formulas, Table 3-17 for the constants and Figure 3-15 for a graphical representation. Castillo (2014) assumed the jet becomes developed for a Y/B_j ratio of 5.5 as opposed to a value of 4 as in his previous studies [31,110].

For $Y/B_j \leq 5.5$ (undeveloped jet):

For $H/L_b < 1$

$$C_p = 1 - 0.0014e^{5.755(\frac{H}{L_b})} \quad \text{Eqn. 3-68}$$

For $H/L_b \geq 1$

$$C_p = 14.643e^{-3.244(\frac{H}{L_b})} \quad \text{Eqn. 3-69}$$

For $Y/B_j > 5.5$ (developed jet):

$$C_p = \frac{H_m - Y}{\frac{V_j^2}{2g}} = ae^{-b\left(\frac{Y}{B_j}\right)} \quad \text{Eqn. 3-70}$$

Where:

H_m	=	Mean head at plunge pool (m)
a and b	=	Constants (see Table 3-17 for values)
L_b	=	Break-up length of the jet (m)

Table 3-17 - Constants a and b Castillo (2014) [110]

H/L_b	a	b
≤ 0.85	2.5	0.20
0.85-1.00	1.70	0.18
1.00-1.10	1.35	0.18
1.10-1.20	1.05	0.18
1.20-1.30	0.88	0.18
1.30-1.40	0.39	0.15
1.40-1.60	0.24	0.14
≥ 1.60	0.14	0.12

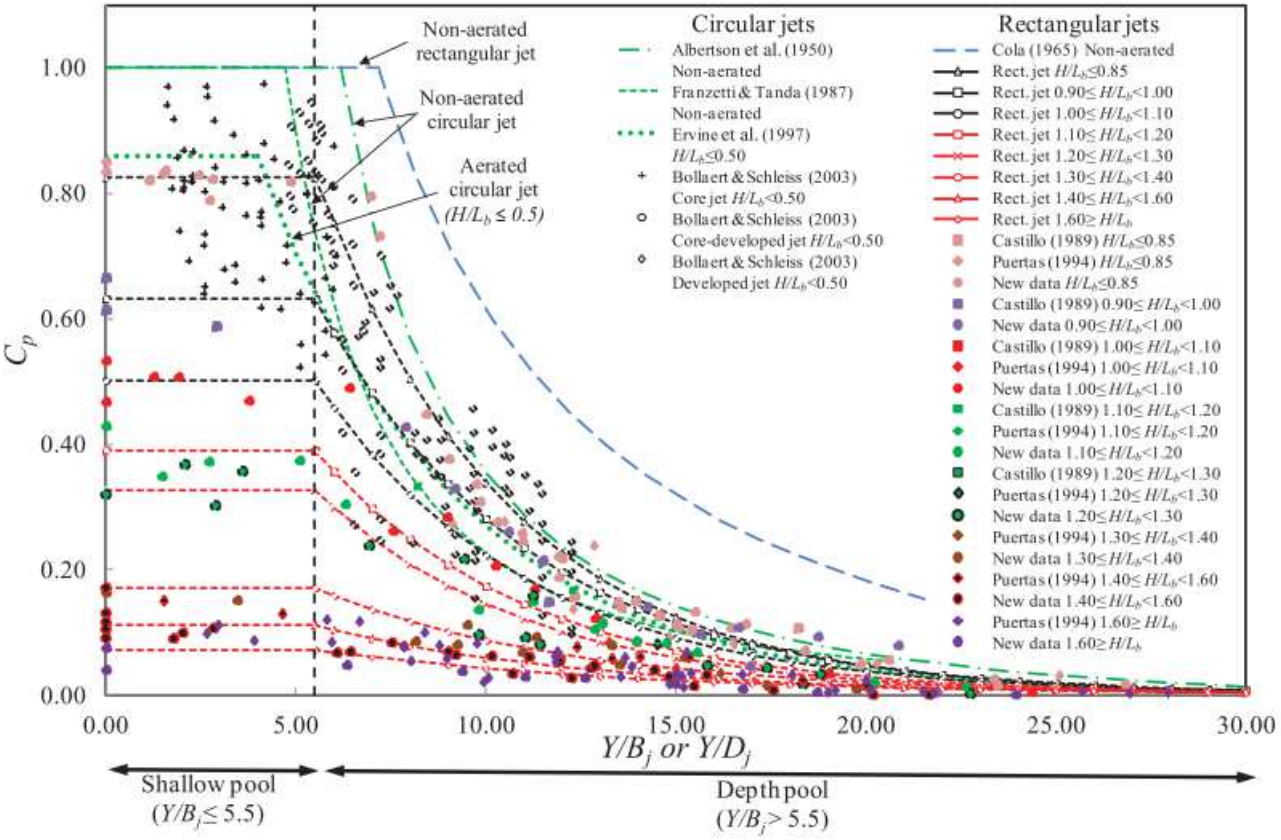

Figure 3-15 - Mean pressure coefficient of rectangular jets as proposed by Castillo [110]

(iii) RMS (Root-mean-square) dynamic pressure coefficient (C'_{pa})

The root-mean-square (RMS) or fluctuating dynamic pressure coefficient can also be written in terms of the ratio of pressure head to incoming kinetic energy and can be calculated using Eqn. 3-71. The fluctuating dynamic pressure coefficient values are dependent on turbulence intensity, as well as the jet break-up degree and aeration [36,63,116].

$$C'_{pa} = \frac{\frac{RMS}{\gamma_m}}{\frac{V_j^2}{2g}} = \frac{RMS\ of\ fluctating\ dynamic\ head}{Kinetic\ energy\ of\ jet\ at\ imapct} \qquad \text{Eqn. 3-71}$$

Circular jets:

Bollaert (2002) developed a third order polynomial function, Eqn. 3-72, to be able to determine the values of the fluctuating dynamic pressure coefficient (C'_{pa}) at the centreline of circular jets for Y/D_j ratio of up to 18-20 [36,63,116].

$$C'_{pa} = a_1\left(\frac{Y}{D_j}\right)^3 + a_2\left(\frac{Y}{D_j}\right)^2 + a_3\left(\frac{Y}{D_j}\right) + a_4 \qquad \text{Eqn. 3-72}$$

Where:

a_1, a_2, a_3, a_4 = Polynomial coefficients and regression coefficients for different turbulence intensities

As Eqn. 3-72 only calculates the coefficients at the centreline of the jet. Formulas were also proposed to calculate the spatial extent of C'_{pa}, which are shown in Table 3-18.

Table 3-18 - Spatial extent of the RMS dynamic pressure coefficient

Spatial extent of fluctuating pressure coefficient		
Developed jets (all r values)	$\frac{C'_{pr}}{C'_{pa}} = e^{-3\left(\frac{r}{r_{max}}\right)^2}$	Eqn. 3-73
Core jets ($r > 0.5r_{max}$)	$\frac{C'_{pr}}{C'_{pa}} = e^{-3\left(\frac{r}{r_{max}}-0.5\right)^2}$	Eqn. 3-74
Core jets ($r < 0.5r_{max}$)	$\frac{C'_{pr}}{C'_{pa}} = 1$	Eqn. 3-75

Where:

r = Radial distance from the centreline of the jet (m)

r_{max} = Maximum radial distance from centreline (m)

For values of the coefficients a_1-a_4, as used in Eqn. 3-72, see Table 3-19 below for different turbulence intensities.

Table 3-19 - Polynomial coefficients and regression coefficient for different turbulence intensities [63]

Tu [%]	a_1	a_2	a_3	a_4 (η - degree of jet stability)	Jet type
<1	0.000220	-0.0079	0.0716	0.000	Compact
1-3	0.000215	-0.0079	0.0716	0.05	Lowly turbulent/intermediate
3-5	0.000215	-0.0079	0.0716	0.1	Moderately turbulent/ undulating
>5	0.000215	-0.0079	0.0716	0.15	Highly/very turbulent

If the turbulence intensity is unknown, its value can be estimated using values as proposed by Bollaert (2002) as shown in Table 2-4 in Section 2.5.1.1 [36].

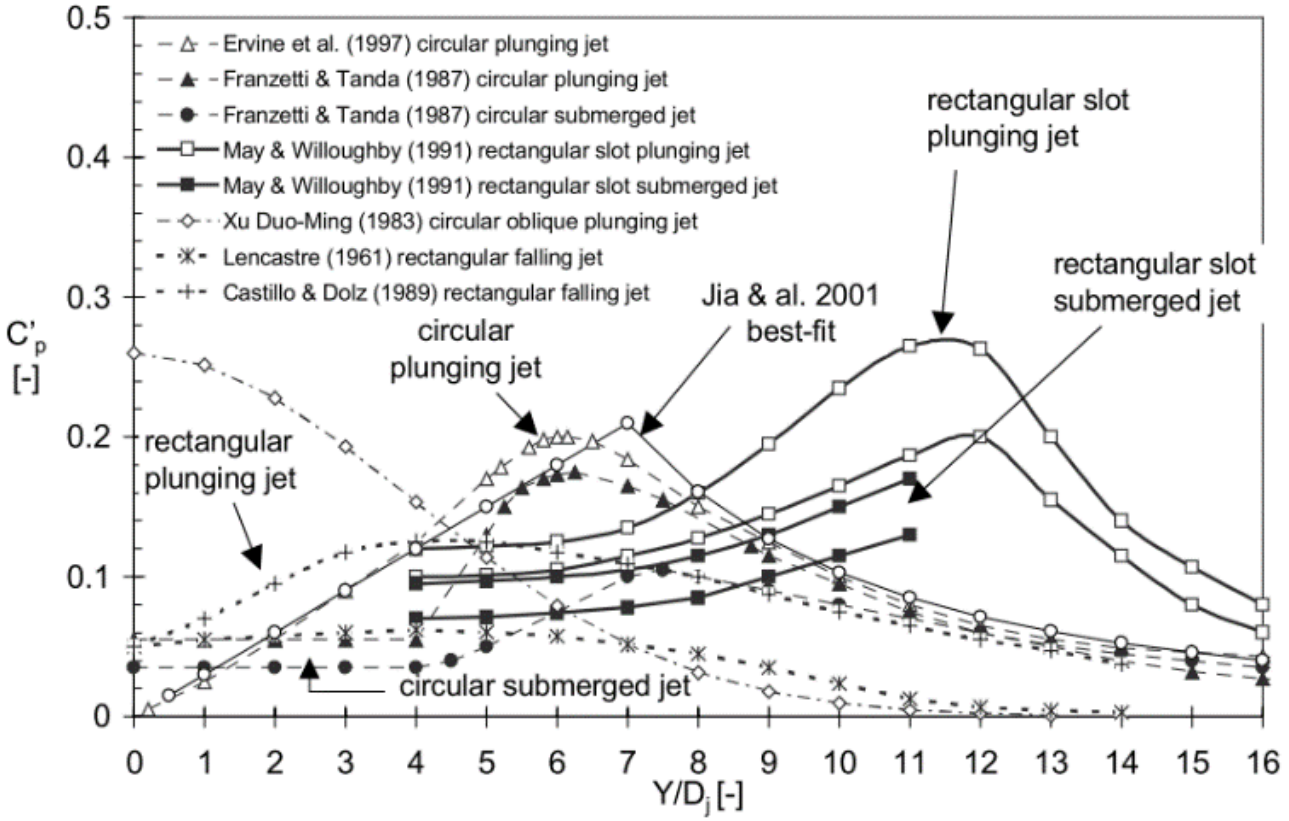

Figure 3-16 - Fluctuating pressure coefficient [36]

C'_{pa} values can be estimated up to values of Y/D_j of 18-20, thereafter a value of 0.05 is proposed by Bollaert (2002) [101,113]. It is important to note that turbulent jets produce low mean pressures, but high fluctuating pressures [63].

Rectangular jets

Castillo (2006) looked at the fluctuating dynamic pressure coefficients for rectangular jets [31,108,115]. Castillo (2006) found that the values for rectangular jets correspond reasonably well with those calculated by Bollaert (2002) for circular jets. Castillo (2006) suggested using the same form as the polynomial formula proposed by Bollaert (2002) (Eqn. 3-76) to calculate the fluctuating dynamic pressure coefficients, but by using different empirically derived constants for rectangular jets for plunge pools of Y/B_j smaller than 14.

$$C'_p = A\left(\frac{Y}{B_j}\right)^3 + B\left(\frac{Y}{B_j}\right)^2 + C\left(\frac{Y}{B_j}\right) + D \qquad \text{Eqn. 3-76}$$

In a later study Castillo (2014) [110] updated the fluctuating pressure coefficient constants, as for the dynamic pressure coefficients. Refer to Table 3-20, and for the refined constants and for a graphical representation, refer to Figure 3-17. The constants are shown in Table 3-20 for the ratio up to $Y/Bj \leq 14$ for different drop height (H) to break-up length (L_b) ratios (H/L_b).

Table 3-20 - Fluctuating pressure coefficient constants Y/Bj ≤ 14 (Castillo 2014) [110]

H/L_b	A	B	C	D
≤ 0.80	0.00030	− 0.01000	0.0815	0.080
0.80-1.00	0.00030	− 0.01000	0.0790	0.130
1.00-1.30	− 0.000005	− 0.00220	0.0160	0.350
1.30-1.60	0.00003	− 0.00180	0.0100	0.210
1.60-1.80	0.00005	− 0.00195	0.0098	0.160
≥ 1.80	0.00005	− 0.00190	0.0100	0.110

Castillo (2014) also proposed a potential fit for the values of Y/B_j >14 using Eqn. 3-77 and values of constants a and b in Table 3-21 [110]. Castillo (2014) found that for the ratio of H/L_b larger than two the fluctuating pressure coefficient becomes negligible [110].

$$C'_p = ae^{-b\left(\frac{Y}{B_j}\right)} \qquad \text{Eqn. 3-77}$$

Table 3-21- Fluctuating pressure coefficient constants for Y/Bj > 14 Castillo (2014) [110]

H/L_b	a	b
≤ 0.80	1.500	0.210
0.80-1.00	1.800	0.210
1.00-1.30	1.000	0.150
1.30-1.60	0.400	0.120
1.60-1.80	1.330	0.230
≥ 1.80	2.500	0.350

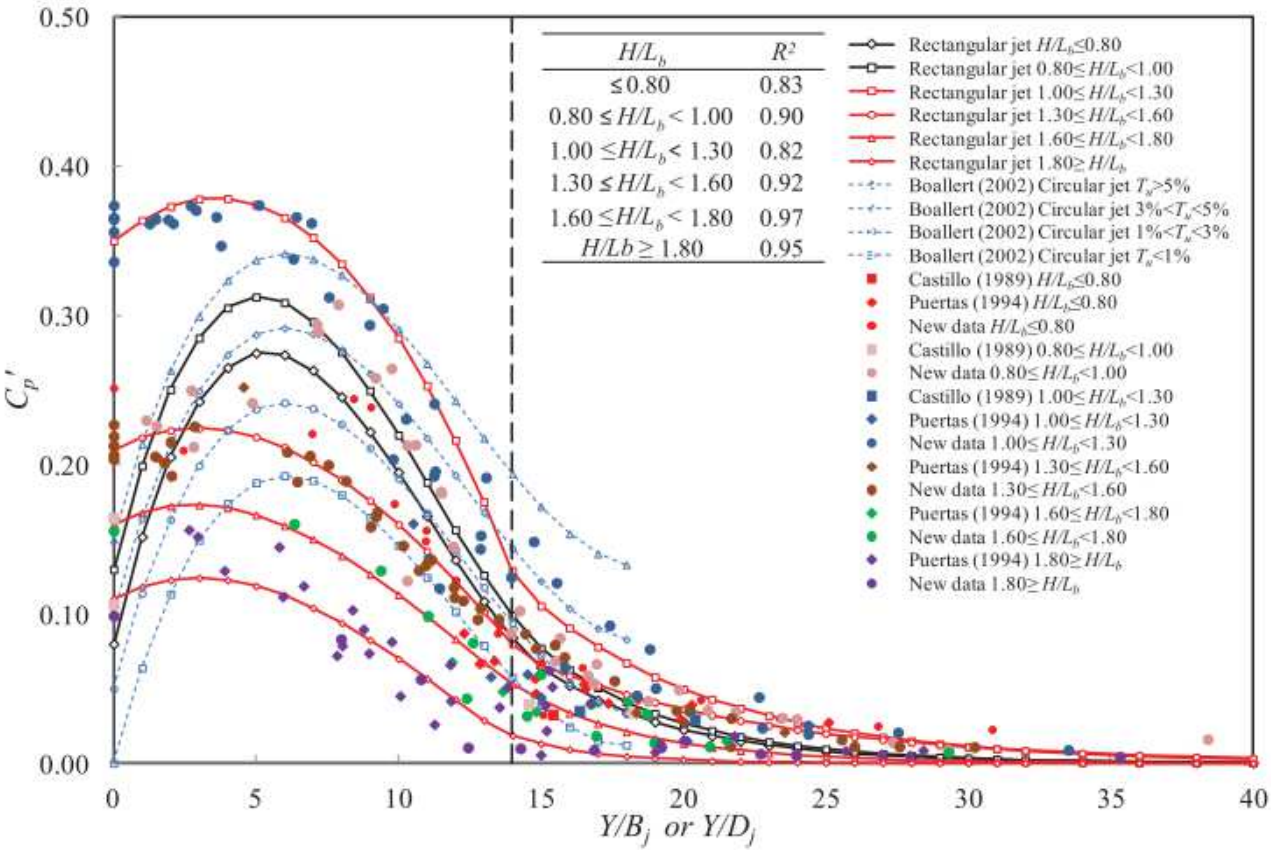

Figure 3-17 - Fluctuating pressure coefficient of rectangular jets as proposed by Castillo [110]

3.3.2.2.3 The rock bed module

The focus of this study was on the scour prediction methods after fracturing of the rock has occurred, such as rock block uplift and quasi-steady uplift. The CFM method was thus not considered, but for more information on the CFM method, please refer to the following literature [36,38,55,93,96, 103,116,117,118,119,120]. Both the dynamic impulsion and the quasi-steady impulsion methods are discussed in detail below.

(i) Dynamic impulsion method (block uplift)

The dynamic impulsion model is used when the rock mass joint network is completely formed (broken up rock mass). The fractures are in the form of open-ended discontinuities or joints. There are several forces acting on a particle under turbulent flow, namely the submerged weight of the particle (W_g), forces over and under rock block (F_o and F_u) and the shear forces/interlocking (F_{sh}) as shown in Figure 3-18 (in 2D) [96]. Due to the turbulent flow, these shear and lift forces act with different frequencies and induce pulses onto the particle. Uplift is said to occur if the upward pulses over the time period (Δt) are larger than the resisting forces [96]. The pressure field under the rock blocks is given by the transient pressures in open ended joints, while the pressure field above the rock blocks is given by the turbulent shear layer of the jet [103].

The lift forces on the rock blocks can be due to two factors: the pressure difference from the flow over the particle as well as the fluctuating pressures due to the turbulent flow (due to vortices in turbulent flow) - also known as the fluctuating and shear lift forces. The uplift caused by the flow over the particle occurs when the pressures above the particle are lower than those below the particle, while the uplift caused by the pressure fluctuating turbulent flow is due to pressure reduction (occurs suddenly or over a small time step) above the particle. Both these uplift scenarios cause the particle to be lifted out of the bed if they are higher than the submerged weight of the particle (friction should also be overcome) (refer to Figure 3-18) [96]. The net impulse or maximum dynamic impulsion on the individual rock blocks can be obtained by time integration of the net forces on the block shown in Eqn. 3-78 [38,55,96]. Eqn. 3-78 is discussed and explained in detail below in a systematic process.

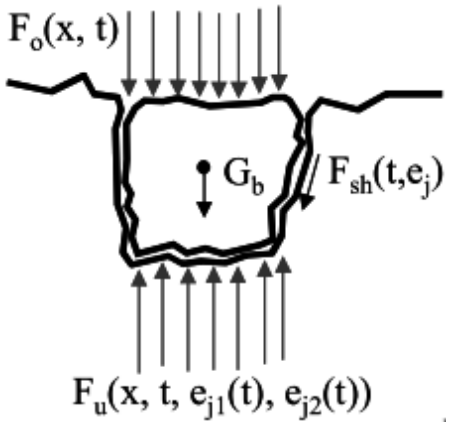

Figure 3-18 - Forces acting on a characteristic block in turbulent flow [117]

$$I_{\Delta t,pulse} = \int_{0}^{\Delta t,pulse} (F_u - F_0 - G_b - F_{sh})dt = mV_{\Delta t,pulse} \quad \text{Eqn. 3-78}$$

Where:

F_u	=	Total upward impulse due to transient pressure in joint (N)
F_0	=	Total downward impulse due to fluctuating pressure on the block (N)
W_g	=	Submerged weight of rock block (G_b some literature) (N)
F_{sh}	=	Total shear and interlocking forces - instantaneous (N)
m	=	Mass of the block (kg)
$V_{\Delta t,pulse}$	=	Average velocity experienced by rock block during time period Δt (m/s)
$\Delta t, pulse$	=	Time interval of certain pressure pulse (s)
$I_{\Delta t,pulse}$	=	Impulse on rock block (Ns)

1. Time interval of a certain pulse

The pressure amplifications in the joints and the wave celerity, depends on the air concentration in the joint (α_i) as well as the fracture length (L_f) and follows the assumption of a perfect resonator system. Meaning that the pressure amplifications occurs when jet excitation is close to resonance frequency [36,96]. Bollaert (2002) proposed that the time interval of a certain pulse ($\Delta t, pulse$) (see Eqn. 3-79) or persistence time, should be taken as the natural period or characteristic resonance frequency (f_{res}) of an open-ended joint pressure wave (see Eqn. 3-80) [117,118,121].

$$\Delta t, pulse = T_{res} = \frac{1}{f_{res}} \quad \text{Eqn. 3-79}$$

$$f_{res} = \frac{c_j}{2L_f} \quad \text{Eqn. 3-80}$$

Where:

C_j	=	Mean air-wave speed or wave celerity (m/s)
L_f	=	Joint or fracture length (m)

The fracture length of rock blocks (L_f) in Eqn. 3-80, assuming that the rock blocks are rectangular, can be calculated by using Eqn. 3-81 [36,96].

$$L_f = x_b + 2z_b \quad \text{Eqn. 3-81}$$

Where:

x_b	=	Length of the block (m)
z_b	=	Height of the block (m)

In the case of single-phase fluids, Eqn. 3-82 can be used to calculate the mean air-wave speed for a single-phase fluid as determined from continuity [36,96].

$$c = \sqrt{\frac{K}{\rho_0}} \qquad \text{Eqn. 3-82}$$

Where:

K = Bulk modulus of elasticity of mixed fluid (N/m^2)

ρ_0 = Density of fluid (kg/m^3)

An approximation of the pressure wave celerity was suggested by Bollaert for a constant temperature of 20^0C, atmospheric pressure and a free air content (β) of between 0 and 50%. The approximation of the wave celerity is given in Eqn. 3-83 [36,96].

$$c_{mix} = \sqrt{\frac{1}{\rho_{mix}} \frac{1}{\left(\frac{(1-\beta)}{\rho_{liq} \cdot c^2_{liq}} + \frac{\beta}{\rho_{air} \cdot c^2_{air}}\right)}} \qquad \text{Eqn. 3-83}$$

Where:

C_{liq} = Pressure wave celerity in water.

C_{air} = Pressure wave celerity in air [3 40m/s].

ρ_{air} = Density of air [1.29 kg/m^3]

ρ_{liq} = Density of the liquid (water) (kg/m^3)

ρ_{mix} = Density of the air water mixture (kg/m^3)

β = Percentage of free air content (%)

c_{mix} = Wave celerity of mixture (m/s)

In the case of pure water with no air content the pressure wave celerity in water can be taken between 1000-1440 m/s, while for water with 1% free air by volume, a value of 100 m/s is proposed [36]. Various formulas are available to determine the density of the air-water mixture. Eqn. 3-84 uses the percentage of free air content, while Eqn. 3-85 uses the volume of each phase to determine the density of the mixture [36,96].

$$\rho_{mix} = \rho_{air}\beta + \rho_{liq}(1-\beta) \quad \text{Eqn. 3-84}$$

$$\rho_{mix} = \rho_{air}\frac{V_{air}}{V} + \rho_{liq}\frac{V_{liq}}{V} \quad \text{Eqn. 3-85}$$

Where:

V_{air} = Volume of air (m^3)
V_{liq} = Volume of liquid (m^3)
V = Total volume (m^3)

The pressure wave travels slower in water with air, than in water without any air, as the air in the water reduces the pressure wave celerity, which is evident from Eqn. 3-83 and the relationship between wave celerity and air content, graphically illustrated in Figure 3-19 [36,96]. As a first hand estimation in practice, a wave celerity value of between 100 and 400 m/s was proposed (dependant on the mean pressure value) and the length of the fracture between 0.5 and 1m [38,103].

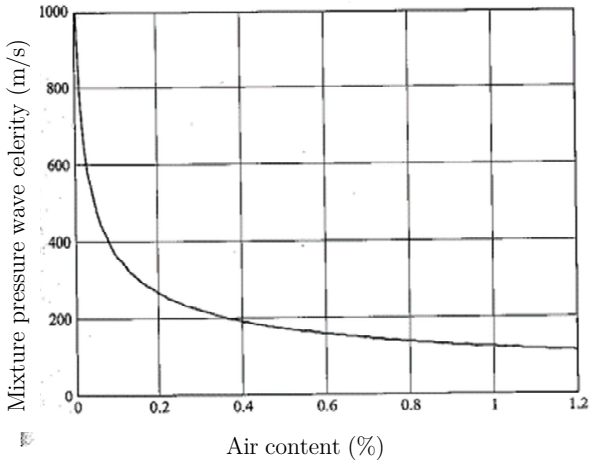

Figure 3-19 - Comparison between wave celerity and percentage of air content [96]

2. Uplift impulse

The first portion of Eqn. 3-78 defines the upward and downward impulses for a certain time interval (Eqn. 3-86).

$$I = \int_{0}^{\Delta t,pulse} (F_u - F_0)dt \quad \text{Eqn. 3-86}$$

Using the time interval, the net uplift pressure (difference between pressure on pool floor (P_{min}) and in the open-ended discontinuities) can then be calculated using Eqn. 3-87 [36,96].

$$P_{up} = C_I . \gamma_w \phi \frac{V_j^2}{2g} \quad \text{Eqn. 3-87}$$

Where:

C_I = Net upward pressure coefficient

P_{up} = Net uplift pressure

The dynamic impulsion coefficient (C_I) can be determined as the product between the time (C_T) and the dynamic pressure coefficients (C_p) [36,96].

$$C_T \times C_p = C_I \quad \text{Eqn. 3-88}$$

The time coefficient (C_T) can be calculated using Eqn. 3-89 or by using Figure 3-20 [36,96]. In most to all case studies done by Bollaert (2004) a C_T value of 1.5 was used [12,38].

$$C_T = \frac{\Delta t}{\left(\frac{2L_f}{c_j}\right)} \quad \text{Eqn. 3-89}$$

In addition, the dynamic pressure coefficient (C_p) is defined as (see Figure 3-21) [36,96].

$$C_p = \frac{\frac{P_{up}}{\gamma_m}}{\frac{\emptyset . V_j^2}{2g}} \quad \text{Eqn. 3-90}$$

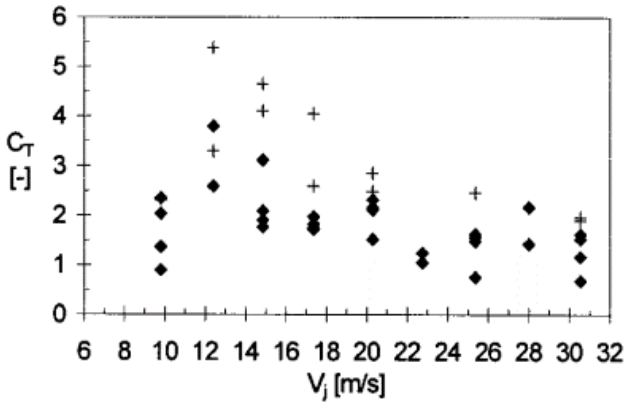

Figure 3-20 - C_T as a function of V_j (DI) [103]

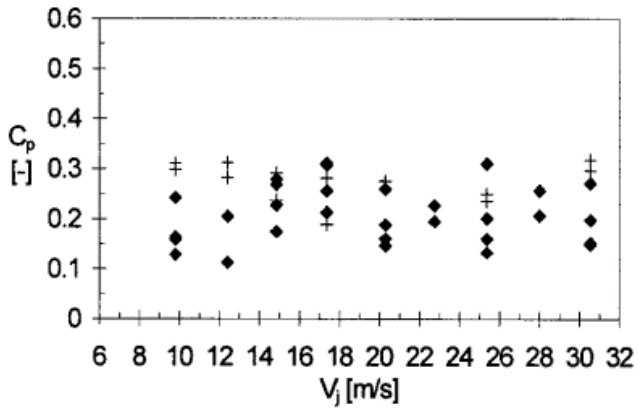

Figure 3-21 - C_P as a function of V_j (DI) [103]

Combining and rearranging the equations, Eqn. 3-79 to Eqn. 3-90, the net uplift pressure over a certain time step can be calculated using Eqn. 3-91 [36,96].

$$P_{up}.\Delta t = \gamma_m.C_I\left[\frac{\emptyset.V_j^{\,2}}{g}\times\frac{L_f}{c_j}\right] \qquad \text{Eqn. 3-91}$$

As the uplift forces are not constant in time due to the transient nature of the impulses, Bollaert proposed a second order polynomial function that was calculated experimentally, to determine the net dynamic impulsion coefficient (see Eqn. 3-92 and Figure 3-22) for Y/D_j values smaller than 18 [36,96].

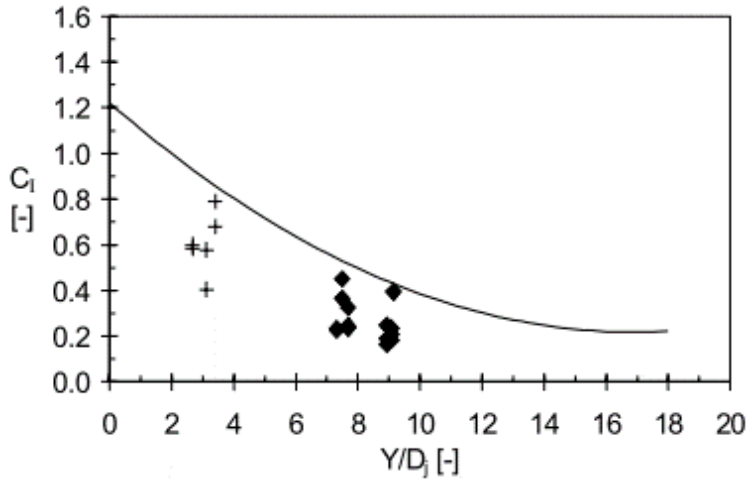

Figure 3-22 - Net upward pressure coefficient [36]

$$C_I = 0.0035\left(\frac{Y}{D_j}\right)^2 - 0.119\left(\frac{Y}{D_j}\right) + 1.22 \qquad \text{Eqn. 3-92}$$

Table 3-22 shows the typical value ranges of the net upward pressure coefficient (C_I) for developed and undeveloped jets at impact with the rock bed as determined by Bollaert (2002).

Table 3-22 - C_I coefficients for developed and undeveloped jets [36]

Net upward pressure coefficients (C_I)	
Jet type	**C_I range**
Developed jet	0.6 - 0.8
Undeveloped jet	0.2 - 0.5

From Eqn. 3-86 and Eqn. 3-91 the formula can then be written as [36,96]:

$$P_{up}.\Delta t = \frac{I_{\Delta t,pulse}}{A} = \frac{1}{A}\int_0^{\Delta t,pulse}(F_u - F_0)dt \qquad \text{Eqn. 3-93}$$

Where:

A = Surface area of the block impacted by the impulse force (m^2)

3. Submerged weight of the block

The second portion of Eqn. 3-78 is the submerged weight of the particle (W_g), which resists the uplift through gravity and can be calculated using Eqn. 3-94 [36,96]

$$\boldsymbol{W_g = V_b \times (\rho_s - \rho_m) g} \qquad \text{Eqn. 3-94}$$

Where:

V_b = Volume of the rock block (m^3)

ρ_s = Density of the solid (rock) (kg/m^3)

ρ_m = Density of the air-water mixture (kg/m^3)

The resistance offered by the block over the time period can consequently be calculated with Eqn. A3-95 [36,96]

$$\int_0^{\frac{2L_f}{c_j}} (\boldsymbol{W_g}) \boldsymbol{dt} = \boldsymbol{V_b \times (\rho_s - \rho_m) g \times \frac{2L_f}{c_j}} \qquad \text{Eqn. A3-95}$$

4. Shear and interlocking forces

The third portion of Eqn. 3-78 is the friction (shear and interlocking forces) from the surrounding particles or rock blocks (F_{sh}), which is dependent on the in situ stresses and joint pattern. The forces can be calculated using Eqn. 3-96, but can generally be neglected as a first approach [36,96,103,108].

$$\int_0^{\frac{2L_f}{c_j}} (\boldsymbol{F_{sh}}) \boldsymbol{dt} = \boldsymbol{F_{sh} \times \frac{2L_f}{c_j}} \qquad \text{Eqn. 3-96}$$

5. Net impulse

In case of a rectangular rock block, the net impulse, Eqn. 3-78, can subsequently be expressed as [36,96].

$$\boldsymbol{I_{\Delta t,pulse} = mV_{\Delta t,pulse} = \rho_s . V_b . V_{\Delta t,pulse} = \rho_s . A . z_b . V_{\Delta t,pulse}} \qquad \text{Eqn. 3-97}$$

6. Vertical displacement

Substituting equations Eqn. 3-91, Eqn. A3-95 and Eqn. 3-96 into Eqn. 3-78, the average velocity experienced by the rock block, during the time period, can consequently be calculated using Eqn. 3-98 [36,96].

$$V_{\Delta t,pulse} = \frac{1}{\rho_s . A . z_b}\left[\gamma_m . C_I . A . \emptyset\left[\frac{V_j^2 . L_f}{g . c_j}\right] - V_b \times (\rho_s - \rho_m) g \times \frac{2L_f}{c_j} - F_{sh} \times \frac{2L_f}{c_j}\right] \quad \text{Eqn. 3-98}$$

As the block is ejected out of the rock bed, the kinetic energy (velocity) applied to the block is transformed into potential energy. Bollaert (2002) proposed that the vertical distance through which the particle is lifted during the time period, due to the velocity applied to the block, can be calculated using Eqn. 3-99 [36,96].

$$h_{up} = \frac{V_{\Delta t,pulse}^2}{2g} \quad \text{Eqn. 3-99}$$

Where:

h_{up} = Height through which particle/rock block is lifted (m)

The vertical displacement distance can then be calculated, for a block with width and depth (x_b) and height (z_b) using Eqn. 3-100 [36,96].

$$h_{up} = \left[\frac{2(x_b + 2z_b)}{c_j}\right]^2 . \frac{1}{2g . \rho_s^2 . x_b^4 . z_b^2} . \left[\gamma_m . C_I . x_b^2 . \emptyset\left[\frac{V_j^2}{2g}\right] - x_b^2 . z_b \times (\rho_s - \rho_m) g - F_{sh}\right]^2 \quad \text{Eqn. 3-100}$$

If the height through which the block is lifted (h_{up}) during the time period (Δt), is high enough, the particle or rock block would be ejected out of the matrix and become mobilised, as shown in the Figure 3-23 [36,96].

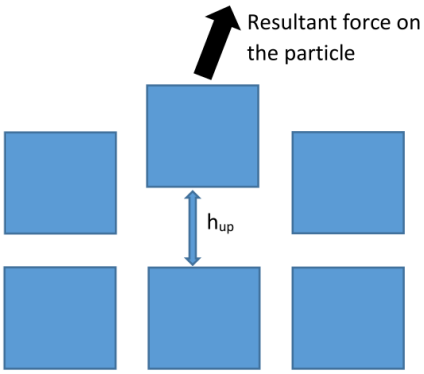

Figure 3-23 - Particle ejected out of matrix

The condition of the rock block for various h_{up}/z_b ratios is shown in Table 3-23 as given by Bollaert (2002) [96,103]. The values in Table 3-23 illustrate that the threshold condition of rock uplift thus lies between 0.5 and 1.0, but must be calibrated for the specific application of the model. Tightly jointed rock, as an example, would require a vertical displacement close to its height ($h_{up}/z_b \geq 1$) while rock, which is not as tightly jointed, would require a lower value of h_{up}/z_b [96,103].

Table 3-23 - Threshold conditions of rock block

Ratio	Rock block condition
$\frac{h_{up}}{z_b} \leq 0.1$	No movement
$0.1 < \frac{h_{up}}{z_b} < 0.5$	Vibration occurs
$0.5 < \frac{h_{up}}{z_b} < 1$	Vibration occurs and motion/removal likely to occur
$\frac{h_{up}}{z_b} \geq 1$	Block is removed from matrix

Bollaert (2002) initially stated that a rock block would be removed from the matrix if the ratio was $h_{up}/z_b > 1$, as given in Table 3-23, but further research found that to be an underestimation when calculating the maximum scour depth. Research now suggests that the rock block will be removed when $h_{up}/z_b > 0.2$ or 0.25 rather than 1 [36,96].

The ratio h_{up}/z_b is dependent on both the aspect ratio of the rock blocks and the pressure wave celerity. Bollaert found that for a higher air content and consequently lower wave celerities, the rock blocks are more likely to be removed than for low or no air content with higher wave celerities. Higher aspect ratios of the blocks were also found to be more difficult to remove than low aspect ratios [96].

The original CSM has been used relatively successfully on predicting the scour extent of prototype cases such as Kariba Dam (Zambia), as well as Srisailam Dam (India) by Bollaert [41]. Further research attempted to improve the original CSM (excluding the quasi-steady impulsion method) has also recently been completed. Manso [122] examined the effect of the plunge pool geometry, but primarily focused on the CFM model (mean and dynamic pressures) and focused on the effects on the persistence time of the pressure pulses regarding the dynamic impulsion method. Federspiel [123] determined the response of the jet impacting an embedded rock block at different locations along the block and the effect on the uplift

of the block. Duarte [124] studied the influence of air entrainment on the behaviour of the jet in the plunge pool and the subsequent effect on the CFM and DI models.

(ii) Quasi-steady impulsion method (QSI) - peeling

The quasi-steady impulsion (QSI) method should be used in conjunction with the conventional CSM to assess the regression towards the toe of the dam as well as further downstream, which the conventional CSM cannot assess, as the CSM is only applicable at the centreline of the jet. At the plunge pool floor, the jet is deflected upstream and downstream of the impingement zone in the form of wall jets. These wall jets interact with the plunge pool floor and are not considered in the conventional CSM. The conventional CSM is predominantly associated with the dynamic pressure fluctuations caused by the turbulent eddies in the turbulent shear layer (impingement area) and does not consider the wall jets, while the QSI method is more concerned with the sudden deviation of the flow parallel to the bottom, due to rock block protrusions [125].

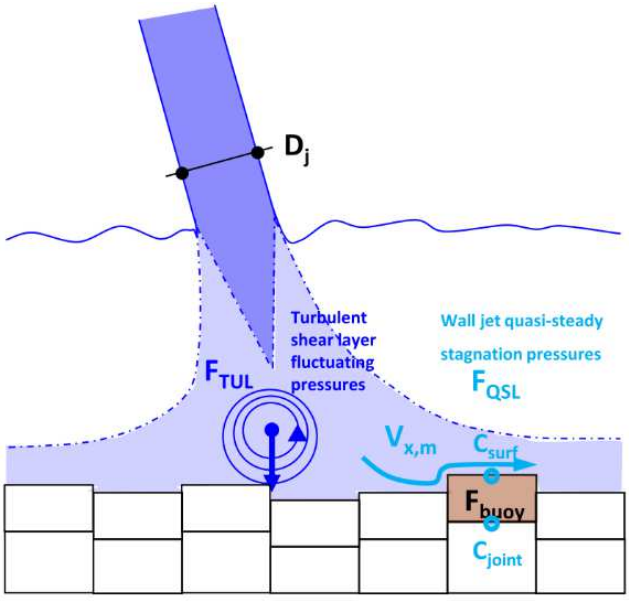

Figure 3-24 - Wall jet deflection [125]

The QSI method is dependent on the quasi-steady high-velocity wall jets parallel to the pool floor and the subsequent quasi-steady uplift forces on rock blocks, which are caused by the protrusions of the rock blocks (see Figure 3-24 and Figure 3-25) [125]. As the QSI method's name suggests, the method examines the instantaneous uplift and is not time dependant as with the dynamic impulsion method [126].

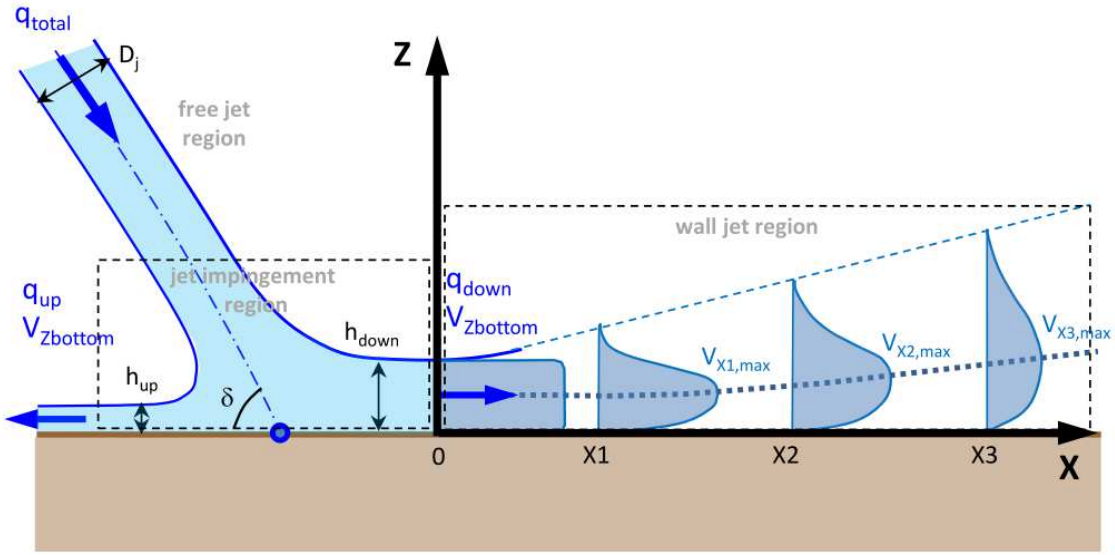

Figure 3-25 - Wall jet velocity profile and deflection [125]

1. Diffusion through pool:

The first step in the QSI method is to calculate the velocity at the plunge pool bottom or impingement region and wall jet region. As from the section above (Section 2.5.1.2), several researchers, such as Ervine and Falvey (1987), suggested that the velocity at the centreline of the jet for an undeveloped circular jet ($Y/D_j < 4$) is the same as that at impact with the plunge pool free surface until the jet becomes developed ($Y/D_j > 4$). Thus, the formulas that follow are predominantly to determine the velocity of the jet in the developed region. Hartung and Hausler (1973) proposed formulas that calculate the velocity decay in the plunge pool as well as at the plunge pool bottom which are shown in Table 3-24 [125,127].

Table 3-24 - Velocity decay in the plunge pool [125]

Velocity decay in the plunge pool		**Equation number**
Circular	$\frac{V(Z)}{V_j} = \frac{Z_{core}}{Z}$	Eqn. 3-101
Rectangular	$\frac{V(Z)}{V_j} = \sqrt{\frac{Z_{core}}{Z}}$	Eqn. 3-102

Where:

Z_{core}	=	Distance for jet to become developed or diffused generally taken as 4-5 times D_j (diameter of the core at impact) (m)
Z	=	Depth below plunge pool free surface (m)
V_j	=	Velocity at impact with plunge pool free surface (m/s)
V(Z)	=	Velocity at depth Z.

Beltaos and Rajaratnam (1973) also produced a formula to determine the velocity decay in the plunge pool, which was determined by experimental studies, which is shown in Eqn. 3-103 [36,128].

$$\frac{V(Z)}{V_j} = 0.508\left(\frac{B}{Z}\right)^{0.5} \quad \text{Eqn. 3-103}$$

Where:

B or D_j = Jet thickness at impact with free surface (m)

Ervine and Falvey proposed that the velocity decay in the developed region of the jet in the plunge pool can subsequently be calculated using Eqn. 3-104 [129].

$$V(Z) = \frac{4V_j D_j}{Z} \quad \text{Eqn. 3-104}$$

Bohrer *et al.* (1998) estimated the velocity decay of an undeveloped rectangular jet in the plunge pool using Eqn. 3-105, but only when Eqn. 3-106 is satisfied. The velocity decay approach is, however, only applicable after a certain minimum depth, which is calculated using Eqn. 3-108 [129]:

$$\frac{V(Z)}{V_i} = 0.0675\left[\left(\frac{\rho_i}{\rho_w}\right)\left(\frac{V_j^2}{gZ}\right)\right] + 0.1903 \quad \text{Eqn. 3-105}$$

Where:

ρ_i = Average density of the air entrained jet at impact with plunge pool free surface (see Eqn. 3-107) (kg/m^3)

ρ_w = Density of water (kg/m^3)

Z = Depth beneath water surface (referred to as L in literature) (m)

$$0.51 < \left(\frac{\rho_i}{\rho_w}\right)\left(\frac{V_j^2}{gZ}\right) < 5.76 \quad \text{Eqn. 3-106}$$

$$\rho_i = (1-\beta)\rho_w \quad \text{Eqn. 3-107}$$

$$\textit{Limiting depth}\ (m) = \frac{\left[\left(\frac{\rho_i}{\rho_w}\right)\left(\frac{V_j^2}{g}\right)\right]}{12} \quad \text{Eqn. 3-108}$$

Bohrer *et al.* (1998) also proposed an equation similar to Eqn. 3-105 to calculate the velocity decay in the plunge pool (see Eqn. 3-109) for a developed rectangular jet, but only when Eqn. 3-110 is satisfied. The velocity decay approach is, however, only applicable after a certain minimum depth, which is calculated using Eqn. 3-111 [129]:

$$-\ln\left(\frac{V(Z)}{V_i}\right) = -0.638ln\left[\left(\frac{\rho_i}{\rho_w}\right)\left(\frac{V_j^2}{gZ}\right)\right] + 1.848 \qquad \text{Eqn. 3-109}$$

$$-0.42 < ln\left[\left(\frac{\rho_i}{\rho_w}\right)\left(\frac{V_j^2}{gZ}\right)\right] < 2.05 \qquad \text{Eqn. 3-110}$$

$$\textbf{Limiting depth } (m) = \frac{\left[\left(\frac{\rho_i}{\rho_w}\right)\left(\frac{V_j^2}{g}\right)\right]}{18.1} \qquad \text{Eqn. 3-111}$$

Another approach calculating the velocity decay involves the use of the conservation of mass and the jet spreading angle (diffusion angle) [125]. A comparison between the velocity decay methods discussed above is shown in Figure 3-26, which indicates the variability in the methods found in literature.

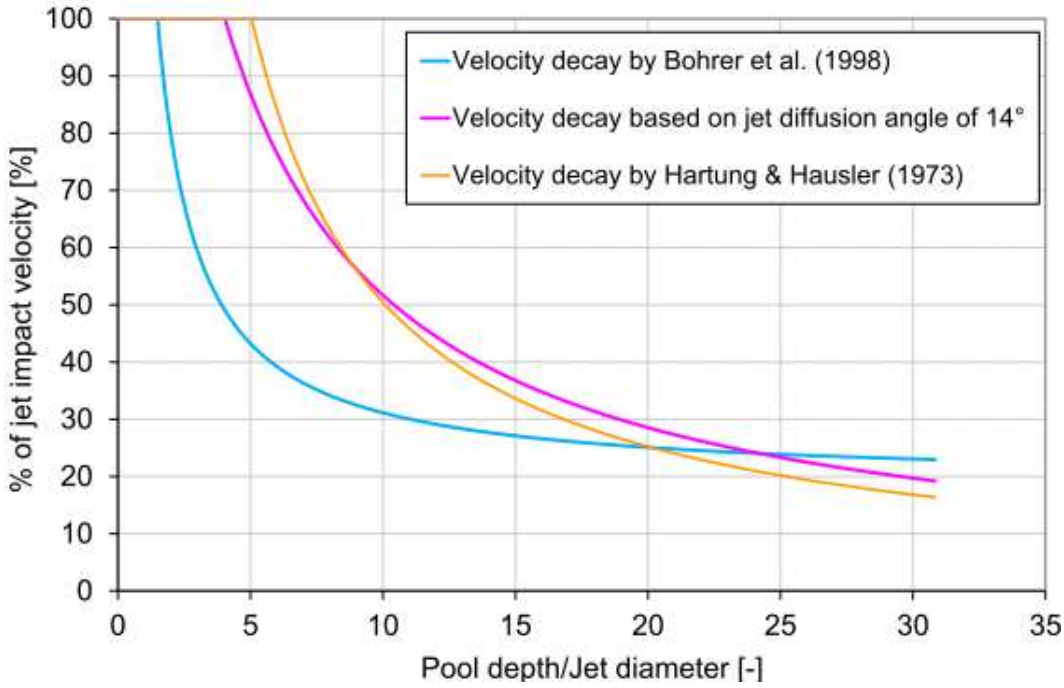

Figure 3-26 - Velocity decay of a jet with an impact angle of 60 degrees [125]

2. Wall jet region:

The wall jet region (refer to Figure 3-25) occurs outside the impingement region. Turbulent pressure fluctuations can be created if the parallel flow is deflected by protruding rock blocks. The deflection of flow can occur downstream, as well as upstream of the impingement region [125].

The deflection of jet flow is directly dependant on the angle of impingement at the plunge pool free surface (θ'), as the angle is proposed to remain the same through the plunge pool until impact with the rock bed. The relating up- and downstream wall jet thicknesses, h_{up} and h_{down} respectively, are calculated using the equations in Table 3-25 as proposed by Reich (1927) [125,130].

Table 3-25 - Upstream and downstream discharges from impingement region [125]

Upstream and downstream discharges from impingement region		Equation number
Upstream	$\frac{q_{up}}{q_{total}} = \frac{h_{up}}{D_j} = \frac{1}{2}(1 - cos\delta)$	Eqn. 3-112
Downstream	$\frac{q_{down}}{q_{total}} = \frac{h_{down}}{D_j} = \frac{1}{2}(1 + cos\delta)$	Eqn. 3-113

Where:

h_{up} and h_{down}	=	Upstream and downstream wall jet thickness
q_{total}	=	Initial discharge (before impact with bottom)
q_{up} and q_{down}	=	Up and downstream deflected discharges
δ	=	Angle of impact at the plunge pool bottom (Assumed equal to the angle of impact with the plunge pool free surface)

Table 3-26 shows the deflected discharge distribution for different impingement angles as applied in Eqn. 3-112 and Eqn. 3-113 [125,130].

Table 3-26 - Discharge distribution of wall [125]

Jet angle (θ')	10^0	20^0	30^0	40^0	90^0
q_{up}	1.5%	6.0%	7.0%	12.0%	50.0%
q_{down}	98.5%	94.0%	93.0%	88.0%	50.0%

The wall jet velocity at a horizontal distance, Xi, from the point of impingement (see Figure 3-25) can subsequently be calculated using the equations in Table 3-27 [125,128]. It should be noted that formulas to the wall jet velocities, in Table 3-27, were initially developed by analysing very small-scale jets impacting a flat plate [128].

Table 3-27 - Wall jet velocities [125]

Wall jet velocities		
Upstream	$\frac{V_{Xi,max}}{V_{Zbottom}} = \frac{3.5}{\sqrt{\frac{X_i}{h_{up}}}}$	Eqn. 3-114
Downstream	$\frac{V_{Xi,max}}{V_{Zbottom}} = \frac{3.5}{\sqrt{\frac{X_i}{h_{down}}}}$	Eqn. 3-115

Where:

$V_{Zbottom}$ = The average velocity at point of deflection or impact with plunge pool bottom. The value changes with scour formation (m/s)

3. Quasi-steady forces on protruding blocks

The next step is to calculate the quasi-steady lift force, due to the wall jet, on the protruding rock blocks which is calculated using Eqn. 3-116 [125,132].

$$F_{QSL} = (C_{uplift}).\rho_w.A_{exp}.\frac{V_{Xi,max}^2}{2} \quad \text{Eqn. 3-116}$$

$$C_{uplift} = C_{joint} - C_{surf} \quad \text{Eqn. 3-117}$$

Where:

C_{uplift} = Net uplift pressure coefficient
C_{joint} = Joint pressure coefficient
C_{surf} = Surface pressure coefficient
A_{exp} = Exposure area of rock block
F_{QSL} = Quasi-steady uplift force

Values of C_{surf}, C_{joint} and C_{uplift} are tabulated in Table 3-28 as was developed by Reinius (1986) from physical laboratory model studies [131,132]. Net uplift coefficient (C_{uplift}) values of between 0.1 - 0.2 are proposed for low to very low block protrusions and 0.3 - 0.5 for medium to large block protrusions. Bollaert (2012) suggests that the use of the latter values is more plausible for real life situations [125].

Table 3-28 - C_{surf}, C_{joint} and C_{uplift} values for different protrusion types [125].

	h_{block}/e_{block}	β_{block}	C_{surf}	C_{joint}	C_{uplift}	Comment
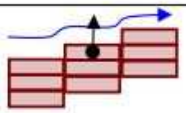	17-29	0°	0.030	0.250	**0.220**	
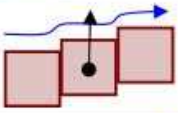	17-29	0°	0.030	0.250	**0.220**	
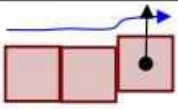	17-29	0°	0.020	0.105	**0.085**	
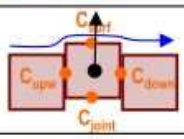	17-34	0°	-0.010	0.145	**0.155**	
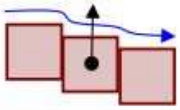	4-9	0°	0.075	-0.110	**-0.070**	block stabilizing forces
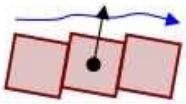	4-10	3°	0.030	0.350	**0.310**	
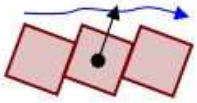	2-4	9°	-0.10-0.17	0.36-0.55	**0.37-0.47**	
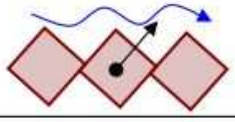	1.0-2.5	18°	-0.15-0.00	0.23-0.40	**0.25-0.45**	
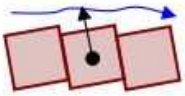	4.2-8.7	-3°	0.02-0.13	-0.105	**-0.070**	block stabilizing forces
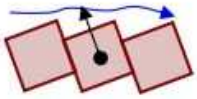	1.0-2.3	-18°	-0.10-0.16	-0.075	**-0.150**	block stabilizing forces

Computations are performed in a step or grid method (see Figure 3-27). The difference in the steps in the horizontal plane between X_i and X_{i+1} (Dx) is generally taken between 1 and 10 meters, while the difference in the steps in the vertical plane Z_i and Z_{i+1} (Dz) of 0.25 to 1 meter is taken [125]. The rock blocks are said to be plucked or peeled out due to the wall jet when the quasi-steady uplift force can overcome the buoyant weight (Eqn. 3-94) of the protruding rock blocks.

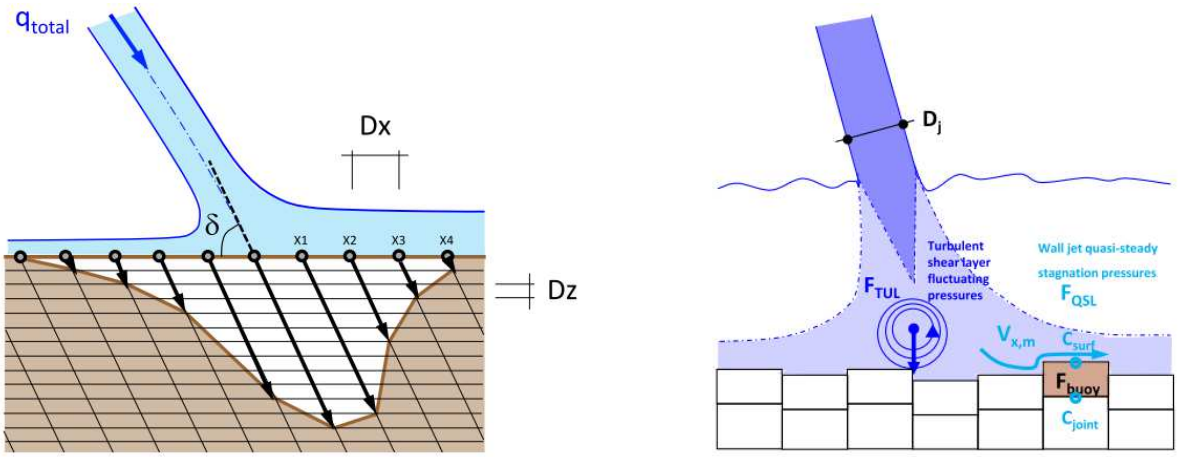

Figure 3-27 - Pressures on protruding rock blocks (left) and Grid method used for computation of QSI method (Left) [125]

The calculation process of both the CSM and QSI method is graphically presented in Figure 3-28.

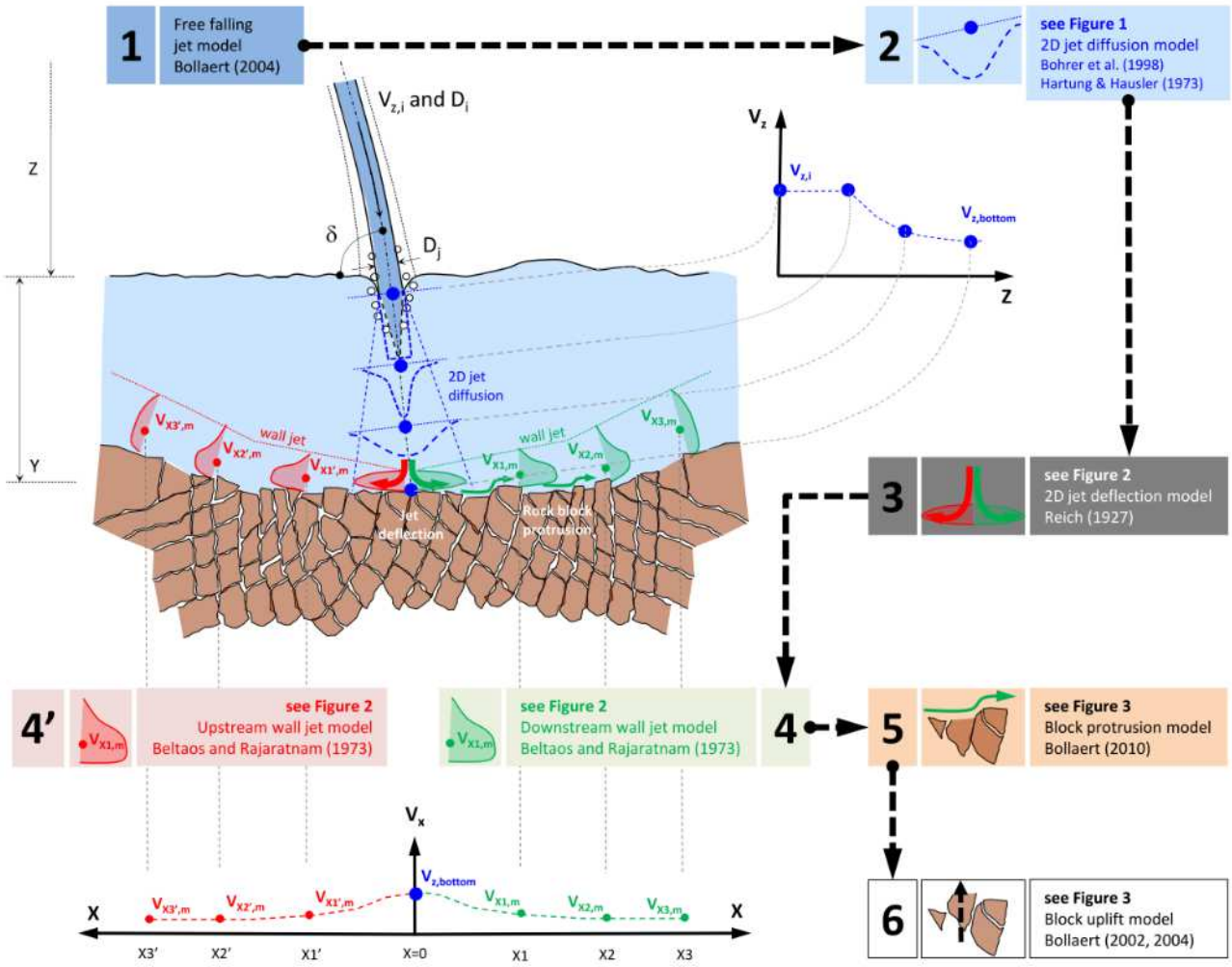

Figure 3-28 - CSM and QSI method calculation process [125].

3.3.3 *Alternative methods for calculating rock scour, primarily rock uplift*

Several of the alternative methods for calculating rock scour, predominantly rock block removal (uplift), are available in literature. The methods have, however, not been applied to prototype conditions with as much confidence as the EIM and CSM, and limited literature was available regarding the methods. A brief summary of each method is given below and for more information on the various methods refer to the applicable literature.

3.3.3.1 *BS3D - block stability (3D)*

The block stability 3D method (BS3D) considers the stability of single rock blocks, as is focused on in the DI method. The method also analyses the general failure modes of rock blocks due to arbitrary loading and water forces, as opposed to the DI method, which does not [93,94]. The method takes into account all failure modes of the rock blocks including roto-translation and general forces such as the non-conservative forces such as water pressure [29,92].

The net impulse and upward displacement calculations used by BS3D are similar to the DI method proposed by Bollaert [93,94]. The net impulse is calculated using Eqn. 3-118, which is similar to Eqn. 3-97 of the dynamic impulsion method, while the upward displacement is determined using Eqn. 3-119, which is similar to Eqn. 3-99 of the dynamic impulsion method proposed by Bollaert.

Net impulse

$$\boldsymbol{F_{\Delta t} = F\Delta t = mV_{\Delta t} = m.a.\Delta t} \qquad \text{Eqn. 3-118}$$

Where:

F	=	Unbalanced force due to maximum pressure fluctuation (N)
Δt	=	Maximum duration (s)
$F_{\Delta t}$	=	Net impulse on the block (BS3D) (N.s)
m	=	Mass of block (kg)
$V_{\Delta t}$	=	Initial velocity (m/s)
a	=	Acceleration of the block caused by the unbalanced force (m/s^2)

Upward displacement:

$$h_{up} = V_{\Delta t} . t_{up} - g \frac{t_{up}^{\ 2}}{2} \qquad \text{Eqn. 3-119}$$

Where:

h_{up} = Maximum upward displacement of block (m)

t_{up} = Duration of block movement due to initial velocity (s)

3.3.3.2 *Block scour spectrum*

The block scour spectrum (BSS) method is a 3D analytical method for determining the resistance of rock blocks. The method looks at the resistance offered by different rock block types comprising the rock mass and the direction and orientation of the resultant force or loading applied on a rock block. Both gravitational and hydrodynamic forces are considered in the method. The BSS comprises of a kinematic, stability and spectrum analysis module [58]. The method can be used to estimate potential locations where scouring is likely to occur and prioritize the rock blocks according to their resistance, thus allowing efficient scour remediation to be implemented.

3.3.3.3 *Statistical pattern recognition*

Statistical pattern recognition techniques have also been used to determine rock block removal similarly to the DI and BS3D techniques. The approach used in the statistical recognition techniques has been found to overestimate the scour depth by approximately 34%, which is conservative. The method is considerably simpler to apply in comparison to the BS3D and DI methods, as the technique estimates the scour depth with a simple formula show in Eqn. 3-120 [92].

$$y_s = \frac{-B + \sqrt{B^2 - 4C}}{2} \quad \text{Eqn. 3-120}$$

Where:

$$B = 0.57 \frac{V_j^2 \gamma_w D_j}{2 g \gamma_b a} - 8.02 D_j - 0.89 y_0 \quad \text{Eqn. 3-121}$$

$$C = -1.07 \frac{V_j^2 \gamma_w D_j}{2 g \gamma_b} \quad \text{Eqn. 3-122}$$

Where:

a	=	Size of rock blocks (m)
γ_b	=	Unit weight of rock blocks (N/m^3)
y_s	=	Scour depth (m)
y_0	=	Tailwater depth (m)

3.3.4 Incipient motion (sediment beds)

Sediment scouring prediction methods primarily focus on the incipient motion of sediment particles. This study focused on rock scouring methods and for literature regarding the scouring in sediment beds jets see [61, 76, 133, 134, 135, 136, 137, 138, 139, 140, 141, 142, 143, 144, 145, 146, 147, 148, 149, 150, 151].

4 Physical laboratory model investigation of rock scour due to rectangular plunging jets

The focus of this study was mainly on the analytical (CSM and EIM) and CFD analyses of the hydrodynamics of rectangular plunging jets and the subsequent rock scouring, rather than on the physical laboratory modelling thereof. The physical laboratory model was, however, required as a ccomparison and a basis on which the physically based methods and CFD analyses could be based. The physical laboratory model investigation also tried to establish if PVC blocks could be used to model scouring in a broken up rock bed. The following section contains a brief summary regarding the physical laboratory model and subsequent results.

4.1 Physical laboratory model setup

The 1:40 scale physical laboratory model used, was based on hypothetical conditions and not on a specific prototype case, or a previous study. The physical laboratory model consisted of a rectangular PVC issuance canal, which was supplied by water from a 110 mm diameter steel pipe. The issuance canal was situated above the plunge pool and could be situated at three different fixed heights and a steel frame was necessary to facilitate the issuance canal. A singular jet was discharged from the issuance canal as a free falling (plunging) jet. The plunge pool was constructed with masonry bricks and was painted with a resin to ensure no leakages could occur and was large enough in length and width as to ensure no large effects, due to confinement, occurred. A steel container was used to enclose the PVC blocks, that replicated the blocked up rock mass. The container could be repositioned to the impingement region of each of the different discharge heights. To ensure an adjustable tailwater depth and to create an outlet, a sluice gate was situated at the downstream end of the plunge pool. The dimensions of the physical laboratory model, as shown in Table 4-1, were calculated using empirical formulas found in literature and scaled using the results from an undergraduate level 1:100 scale scour hole study that used gravel to simulate the rock bed [214]. The physical laboratory model properties are shown graphically in Figure 4-1.

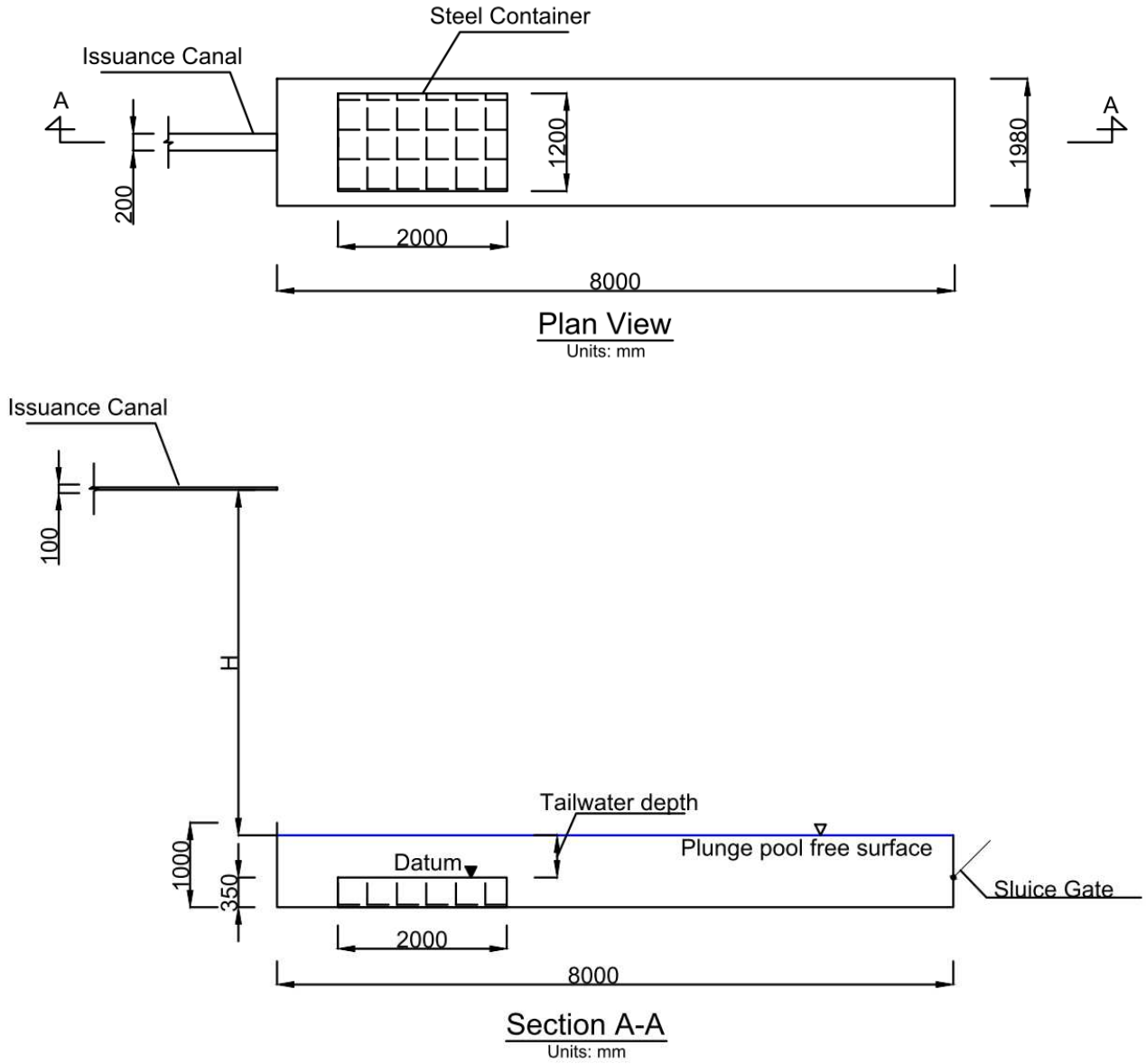

Figure 4-1 - Plan view and elevation of physical laboratory model setup

The physical laboratory model setup is shown in Figure 4-2.

Figure 4-2 - Complete physical laboratory model setup (left), issuance canal (bottom right) and the steel container containing the PVC blocks (top right)

4.2 Physical laboratory model properties

A 1:40 scale physical laboratory model was used to model the scouring of rock due to plunging jets for hypothetical high-head discharge conditions. A larger scale model was not possible, due to physical constraints (laboratory size and pump capacity) and financial restrictions (cost of PVC blocks). The properties of the physical laboratory model and the prototype, from which the properties were scaled, are given in Table 4-1. The prototype values were scaled using Froude number similarity, as discussed in Section 3.1 (geometric, kinematic and dynamic similarity laws). It should, however, be noted that Reynolds and Weber number similarities are also very important when trying to correctly simulate air entrainment of plunging jets, as Froude similarity alone cannot simulate prototype aeration correctly and several of the plunging jet aspects, such as lateral spreading and jet break-up, are also dependent on the Weber and Reynolds numbers [82]. All three similarity laws can, however, not be satisfied simultaneously

[73] and for this study the scaling was done according to Froude similarity only. Froude similarity was deemed acceptable, as the physical laboratory model was based on a hypothetical prototype case. The density, as given in Table 4-1, was determined using the Liu diagram, as contained in the SANRAL Drainage Manual [152], using the settling velocity of the PVC blocks and was not scaled from a prototype density. The prototype density corresponds to the scaled settling velocity of the PVC blocks.

Table 4-1 - Physical laboratory model properties

Model parameter	Model values	Prototype values
Drop heights (including tailwater depth) ($H + y_0$)	4m 3m 2m	120m 100m 80m
Tailwater levels (y_0)	0.5m 0.25m	20m 10m
Discharge (Q)	0.02 m^3/s (20l/s)	240 m^3/s
Rock block size (square blocks)	0.025m	1m
Density (ρ_s)	1527 kg/m^3	2700 kg/m^3*
Downstream dimensions of plunge pool		
Length	8m	224.7m
Width	1.98m	133.3m
Depth	1m	37.4m
Issuance canal dimensions		
Width	0.2m	8m
Depth	0.2m	8m

*The prototype rock type was assumed to be similar to Granite-Gneiss. Granite-Gneiss has a UCS between 128 (weathered) and 166 (un-weathered) and a density of 2699.2kg/m^3 (weathered) and 2709.7 kg/m^3 (un-weathered) [153].

The prototype scale values as given in Table 4-1 are only given for reference purposes as the study focused on the model scale analysis of the hydrodynamic of the jet and subsequent rock scouring and not on the prototype scale analysis thereof.The drop heights, as shown in Table 4-1, include the tailwater depth. The actual drop heights from the bottom of the issuance canal to the plunge pool free surface that were used in subsequent calculations, are shown in Table 4-2 for clarity.

Table 4-2 - Actual drop heights

Drop height (including tailwater) ($H + y_0$)	Tailwater depths (y_0)	Actual drop height modelled (H)
2m	0.25m	1.75m
2m	0.5m	1.5m
3m	0.5m	2.5m
4m	0.5m	3.5m

4.2.1 Issuance canal discharge considerations

The discharge at issuance of the physical laboratory model was restricted to a maximum of 20l/s. When a flow of 30l/s was tested, the water swirled inside the issuance canal, due to the large change in area between the pipe (circular), from which the water was pumped, and the issuance canal (rectangular) and created unstable and highly turbulent discharge conditions (non-uniform flow). The water that was discharged from the issuance canal at 30l/s, was also discharged as more than one column of water, which collided with each other in mid-air, causing the jet to break-up prematurely, due to the collisions mid-air (see circled area Figure 4-3).

Figure 4-3 - Highly turbulent flow at a discharge of 30l/s

From visual inspection, a discharge of 20l/s was the optimal discharge for the physical laboratory model. As for the 30l/s discharge, the water also swirled in the issuance canal, but to a lesser extent. At a lower

discharge of 10l/s, the jet was highly developed at impact with the plunge pool free surface, due to the low velocity and issuance depth, and due to the high drop heights tested. Flows larger than 30l/s were also not possible, due to pump capacity restrictions. Spillways or sluice gates operated at 100% capacity, which entails discharging at its maximum discharge, are generally the most harmful, due to the jet not being fully developed (jet core still intact) [185,186]. Due to the flow restrictions and the highly turbulent flow at higher discharges, this condition could not be tested.

An Endress-Hauser electromagnetic flow meter [154] was used to measure the flows in l/s in the issuance pipe (see Figure 4-4) and a valve was manually adjusted to ensure the correct issuance flows were supplied.

Figure 4-4 - Electromagnetic flow meter

Due to the change in area between the pipe and rectangular issuance canal, highly turbulent and irregular flow was produced (streamlines were not parallel to each other). A sluice gate was subsequently installed inside the issuance canal to ensure uniform flow at issuance (see Figure 4-5). The sluice gate restricted the flow to a depth of 0.1m, which was determined as the critical depth of the issuance canal (see Section 4.4.1.1).

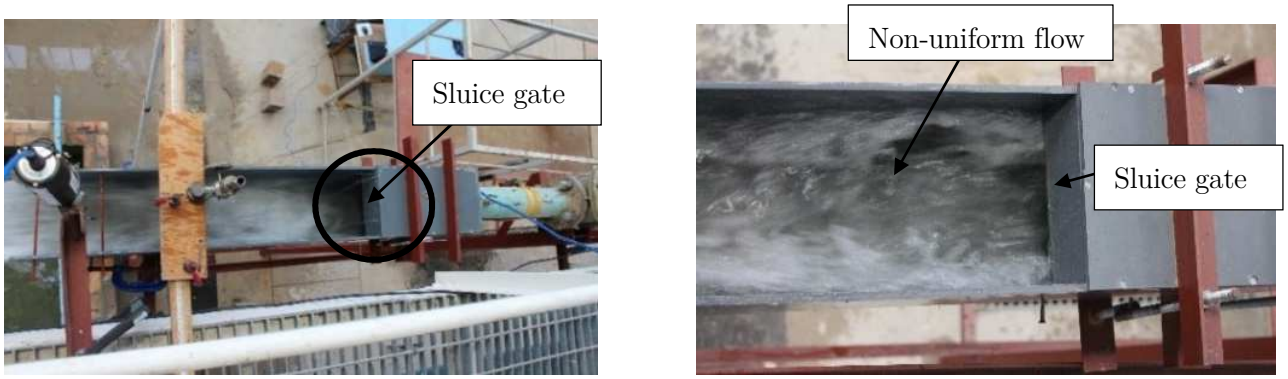

Figure 4-5 - Sluice gate installed in issuance canal (left) and non-uniform flow after sluice gate (right)

4.2.2 PVC block characteristics

The physical laboratory model used cubic PVC blocks to replicate rock blocks (Figure 4-6). These PVC blocks had dimensions of 25mm (height) x 25mm (breadth) x 25mm (width). Approximately 16 000 PVC blocks were used in total, to simulate the broken up rock bed, where the fracture network had already

Figure 4-6 - Typical PVC block used in physical laboratory model

completely been formed. Similar PVC blocks had been used in a previous study of scouring in unlined dam spillways, with relatively good results at the University of Stellenbosch, South Africa [134]. The fact that PVC blocks could sustain steeper scour hole slopes, that are generally visible in prototype rock scouring, which non-cohesive sediment (gravel) is unable to simulate, motivated the implementation of the PVC blocks in the physical laboratory model.

Due to the high cost involved in the use of the PVC blocks, a steel container was employed to enclose the blocks, which could be repositioned to the specific impingement region of each drop height tested. The inside dimensions of the steel container were 1.2m (width) x 1.2m (length) x 0.35m (depth) [Refer to the plan view in Figure 4-1]. Additionally, masonry bricks were implemented as a measure to minimize the amount of PVC blocks used. The masonry bricks were positioned inside the steel container in areas where no scouring was expected to occur. Some confinement effects on the flow were unavoidable, due to the masonry bricks and the steel container. During the manufacturing process of the PVC blocks, several distorted or malformed blocks arose during the moulding and drying process. As a consequence a discrepancy regarding the PVC block dimensions of approximately 3% (<1mm) was deemed acceptable.

Figure 4-7 - Weight of PVC blocks

The average density of the PVC blocks was physically calculated using the weight and volume of the blocks. The weight of the blocks was measured using an electronic scale and several different samples were tested for statistical accuracy (see Figure 4-7). The blocks weighed approximately 0.018 kg each and consequently the density of the blocks was calculated as being 1152 kg/m^3 (see Table 4-3).

Table 4-3 - Average density of PVC blocks

Property	Value
Weight of individual blocks	0.018 kg
Dimensions of blocks	0.025m x 0.025m x 0.025m
Average density of blocks	1152 kg/m^3

The author used the density as given in Table 4-3, which was physically calculated instead of the density which was determined using settling velocity and the Liu diagram (SANRAL Drainage manual [152]), given in Table 4-1. The settling velocity approach is generally the preferred approach, but due to the Liu diagram being developed for sediment and the rather consistant geometry and weight of the blocks, the density given in Table 4-3 was used. The density was also lower that the density determined from the Liu diagram, which ensured a more conservative density estimate, as it would provide lesser erosion resistance.

4.2.3 Velocity measurement

A Vectrino fixed probe was used to measure the flow velocities in the issuance canal and along the bottom of the scour hole. The probe measures the velocity at a distance of 0.05m from the probe head and the probe head needed to be submerged to measure the velocities [155,156]. As to ensure minimum influence on the flow profile, non-intrusive methods are generally preferred. Due to the probe head of the Vectrino probe being relatively small, as well as taking readings 0.05m away from the probe head, the interference

of the probe on the flow was deemed more acceptable in comparison to a traditional propeller velocity flowmeter.

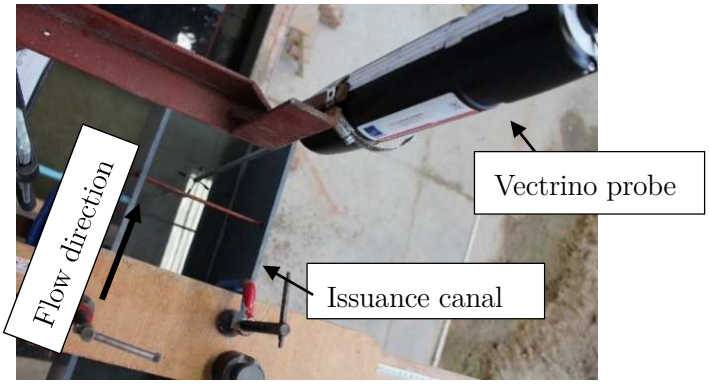

Figure 4-8 - Vectrino probe

4.2.4 Tailwater level

A sluice gate was located at the downstream end of the plunge pool, to ensure a constant tailwater level was maintained (see Figure 4-9). The plunge pool was filled using the plunging jet until the desired tailwater level was reached. The tailwater levels were monitored and established with a dimensioned cylindrical tube connected to the plunge pool, as shown in Figure 4-9. The cylindrical tube was used as it diminished the impeding effect of the fluctuating plunge pool free surface level, due to the plunging jet, on the measuring of the tailwater level and ensured a more accurate tailwater level was used.

Figure 4-9 - Tailwater measuring cylinder (left) and sluice gate (right)

4.3 Testing procedure

Before the physical test was run, the PVC blocks were placed into the steel container. The blocks were placed in the form of a planar joint network, as seen on Figure 4-2. Thereafter the steel container had to be moved to the correct impingement zone of each of the respective drop heights tested. The issuance canal was lifted to the required drop height using a crane. After the issuance canal and the steel container were moved into the correct positions, a valve was operated at the upstream end of the issuance canal until the desired flow was reached. A PVC board was placed at the front of the steel container as well as the issuance canal to minimise premature scouring of the PVC blocks, until the desired tailwater level was reached, which was controlled using the sluice gate. When the desired tailwater level was reached, the board was subsequently removed, thereafter the jet could impact the plunge pool and scouring could commence. The test was run until the equilibrium scour hole was reached (no more scouring was observed). A survey of the scour hole geometry was completed after the plunge pool was drained of water. The same procedure was used for each of the drop heights and tailwater levels tested as summarised in Table 4-1.

4.4 Physical laboratory model results

The results for the plunging jet's behaviour at issuance, in the air, at impact with the plunge pool's free surface, in the plunge pool and at the rock bed interface as determined from the physical laboratory model, are discussed in Sections 4.4 to 4.5.

4.4.1 Jet issuance conditions

The main aspects pertaining to the conditions of the jet at issuance are, the issuance flow depth or jet thickness (D_i), velocity (V_i) and turbulence intensity (T_u). Each of the respective factors, as calculated from the physical laboratory model, is discussed in this section.

4.4.1.1 *Issuance canal flow depth or jet thickness (D_i)*

A mechanical depth gauge was used to determine the depth of flow in the issuance canal (see Figure 4-10).

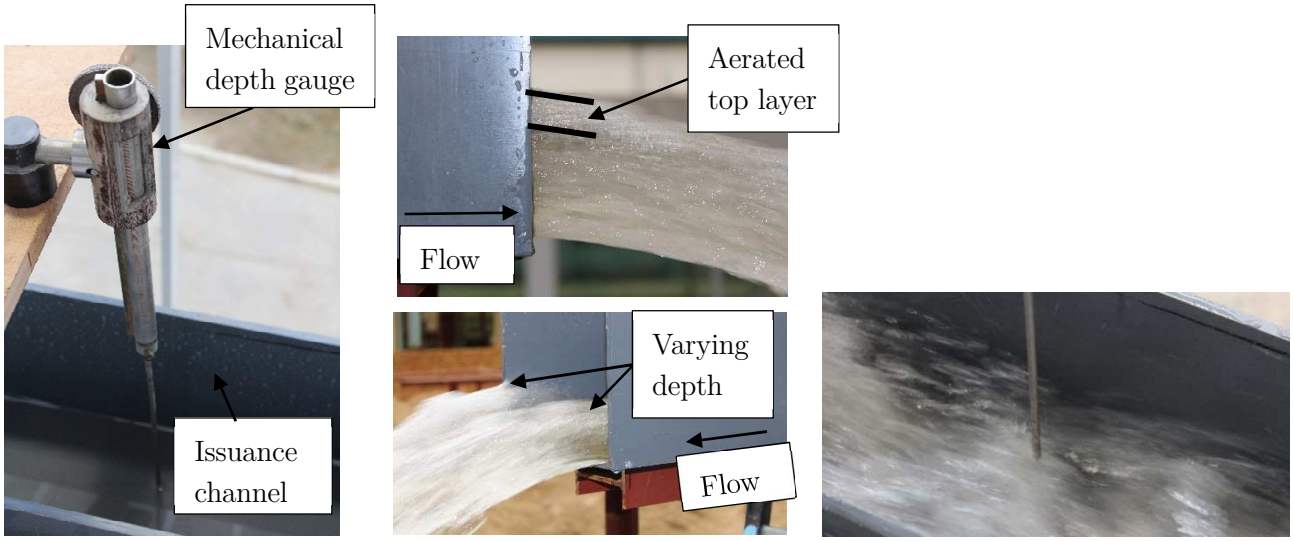

Figure 4-10 - Mechanical depth gauge (left), brink conditions (middle) and depth gauge at 20l/s (right)

Fully developed flow is generally preferred at depth measurement locations, as more accurate depth measurements can be taken due to the invariable velocity profile in the direction of flow, which reduces the magnitude of the fluctuations in the flow depth. Fully developed flow was, however, not reached in the issuance canal, due to the short issuance canal (approximately 1m) and the factors discussed in Section 4.2.1, as could be seen from the fluctuating flow depth that occurred in the issuance canal (see Figure 4-10). It was also observed that the depth of flow varied over the width of the issuance canal and that there was a turbulent aerated layer at the top of the flow (see Figure 4-10). For a rectangular weir, such as in the case of the physical laboratory model, the brink depth should be determined [157]. Due to the highly turbulent and variable flow, it was observed that there was no convincing difference in depths taken at the brink, or at a distance of 0.3m upstream from the end of the issuance canal.

Due to the variability in the depth, an averaged value was determined. The calculated mean flow depth, for the discharge of 20l/s, is shown in Table 4-4.

Table 4-4 - Issuance depth

Issuance flow rate (Q)	**Issuance depth (B_i)**
20l/s	≈ 0.05m

To determine the accuracy of the flow depth measured, the brink depth was calculated for an issuance discharge of 20l/s, using open channel flow formulas for a rectangular canal free over fall [158]. The critical depth in the issuance canal was calculated as 0.1m (Eqn. 4-1), which was the equal to the sluice gate opening in the issuance canal (see Figure 4-5). Having calculated the critical depth, the brink depth was subsequently calculated as 0.07m using the relation in Eqn. 4-2. The calculated depth was more than the measured depth of 0.05m, which was assumed to be due to the fact that the flow did not exit the sluice gate at 0.1m, as it was generally observed to be lower than the gate opening (see Figure 4-5), which would, in turn, reduce the brink depth. The depth of 0.07m did, however, correspond to the highest flow depth measured in the issuance canal at the brink, due to the non-uniform flow depth across the issuance canal. The measured depth was thus used in subsequent calculations in Section 5.

$$y_c = \sqrt[3]{\frac{q^2}{g}} \qquad \text{Eqn. 4-1}$$

$$\frac{y_c}{y_b} = 1.4 \qquad \text{Eqn. 4-2}$$

Where:

y_c = Critical depth (m)

y_b = Brink depth (m)

q = Unit discharge ($m^3/s/m$)

4.4.1.2 *Velocity (V_i) and turbulence intensity (T_u) at issuance*

Due to the low flow that could be accommodated at issuance, by the issuance pipe and pump capacity in the physical laboratory model, the Vectrino probe's head could not be submerged. The depth of flow at issuance was equal or lower than the required depth of 0.05m, to enable velocity readings to be taken. During the discharge of 30l /s, the probe head was slightly submerged, as can be seen from Figure 4-11, but due to the high turbulence, the submergence of the probe head was inconsistent and variable. To determine the turbulence intensity, velocity measurements were paramount as the turbulence intensity is determined from the ratio between the axial velocity fluctuations and the mean velocity (Eqn. 2-1) and could thus not be determined. The Vectrino probe's location, relative to the depth of flow in the issuance canal for various flows, is shown in Figure 4-11.

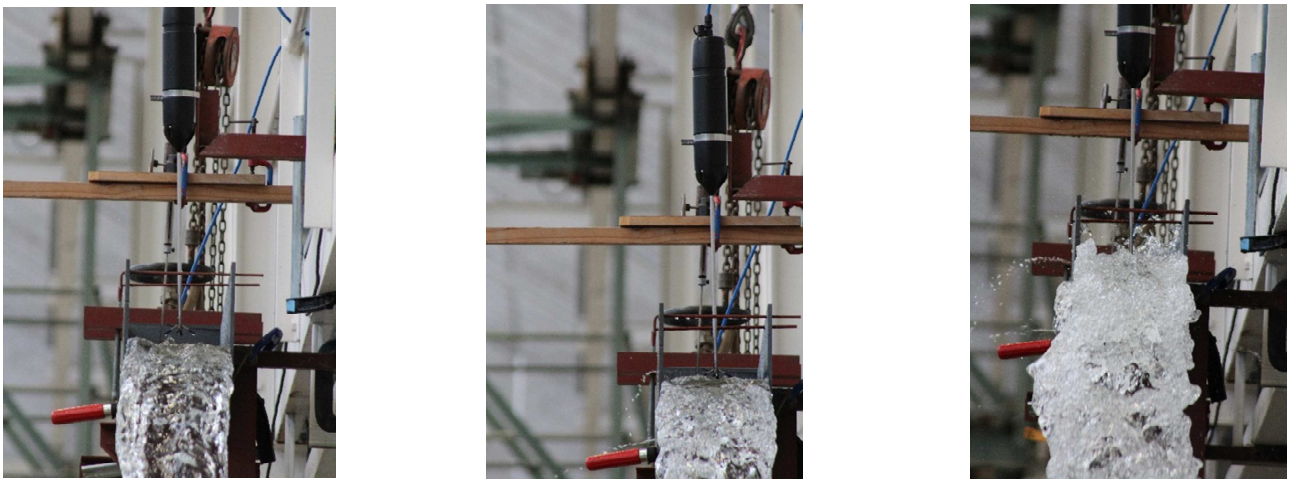

Figure 4-11 - Vectrino probe at 10l/s (left), 20l/s (middle) and 30l/s (right)

As the velocity at issuance could not be determined using the Vectrino probe, the general flow rate equation of Q (discharge) = V (velocity) × A (cross sectional area) was used to determine the issuance velocity using the flow depth as shown in Table 4-4. The calculated issuance velocity is shown in Table 4-5.

Table 4-5 - Issuance velocity

Issuance flow rate (Q)	**Issuance velocity (V_i)**
20l/s	≈ 2 m/s

The Vectrino probe could also not be used to measure the velocities along the bottom of the scour hole to compare to the velocities of the CFD model. The reason being that the depths at which the velocities had to be taken were too deep for the Vectrino probe used and the water impacted the region at which the probe had to be inserted, which would have jeopardised the instrument as it is not fully submersible. The total length of the instrument was approximately 0.65m, but the steel probe section was only 0.36m, which was insufficient to accommodate the 0.5m tailwater depth and could only accommodate the minor scour regions for the 0.25m tailwater depth.

A propeller velocity flowmeter can be used as an alternative, but as the focus of this study was not on the physical laboratory model itself, but rather the numerical simulation of the plunging jetfurther velocity measuring instruments were not explored. Time constraints also limited the use of alternatives.

4.4.1.3 *Conditions of flow at issuance*

From visual inspection, the conditions of the flow in the issuance canal were assumed supercritical and turbulent. To verify this observation, the Froude and Reynolds numbers of the issuance canal were determined. Eqn. 2-9 was used to calculate the Froude number, while Eqn. 4-3 was used to calculate the Reynolds number. The calculated values are shown in Table 4-6.

$$Re = \frac{V_i D_h}{\nu} \qquad \text{Eqn. 4-3}$$

Where:

ν = Kinematic viscosity (assumed at 10^{-6} for water at 20 degrees) (m^2/s)

D_h = Hydraulic radius (m)

V_i = Velocity at issuance (from Table 4-5) (m/s)

Table 4-6 - Froude and Reynolds number at issuance

Property	Value
Discharge	20l/s
Froude number (issuance)	2.86
Reynolds number (issuance)	3.42 x 10^6

The values in Table 4-6 agreed well with the observed flow conditions at issuance. The Froude number being more than one indicated supercritical flow, while the large Reynolds number indicated turbulent flow.

4.4.2 Jet spreading in the air

The spreading of the jet in the air was an important parameter to determine. The jet underwent spreading in both the lateral, as well as longitudinal directions. Longitudinal spreading was proposed as being the primary spreading direction as it is in the direction of flow, while the lateral spreading was the secondary spreading direction, as it is in the minor direction of flow for rectangular jets. Literature only refers to lateral spreading due to the fact that most of the studies were concentrated on circular jets impacting the plunge pool vertically or perpendicularly [21,36]. The respective spreading angles, which were determined, are shown in Table 4-7. The lateral and longitudinal angle of spreading of the jet is shown graphically in Figure 4-12.

Table 4-7 - Jet spreading angles

Spread direction	Angle
Longitudinal (primary)	2.1°
Lateral (secondary)	1.5°

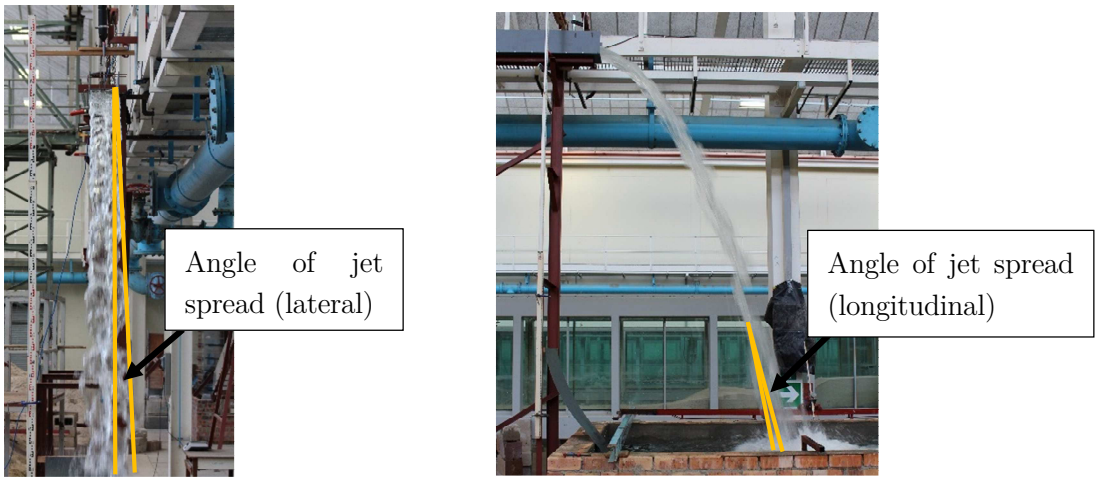

Figure 4-12 - Lateral (left) and longitudinal (right) spreading angle of the jet

The lateral and longitudinal angle of jet spreading, presented in Table 4-7, was determined by calculating the arctangent using the trajectory length and the outer thickness or width of the jet at impact with the free surface. From visual inspection, there was no major difference in jet spreading between the developed and undeveloped regions of the jet in the air as opposed to the jet spreading in the plunge pool (see Section 2.5.1.2). The total trajectory length was therefore used to determine the jet spreading angle. For the different physical laboratory model configurations, the spreading angles varied slightly and the author consequently proposed using the average of the different calculated angles, which are shown in Table 4-7. The longitudinal spreading angle was found to be slightly higher than the lateral spreading angle, which was expected, as it was in the direction of flow.

4.4.3 Behaviour of the jet at impact with plunge pool free surface

The properties of the jet at impact with the plunge pool free surface for a flow of 20l/s are shown in Table 4-8. One of the most important properties of the jet at impact with the plunge pool free surface, that was required, was if the jet was developed or undeveloped. From Figure 4-13, it is clear that the jet was developed (core broken up) at impact with the plunge pool for a drop height of 4m, which included

the tailwater level of 0.5m. From physical laboratory model observations, the jet became developed at a vertical distance approximately 1 to 2 m from issuance, but could not be determined with certainty.

Table 4-8 - Properties of the jet at impact with plunge pool

Property	Value			
Discharge (Q)	20l/s			
Drop height (including tailwater)	2m	3m	4m	2m
Tailwater (y_0)	0.5m			0.25m
Trajectory length (L)	1.87m	2.9m	4m	2.15m
Horizontal distance to impact (x)	1.13m	1.43m	1.73m	1.24m
Angle of impact (β)	69°	71°	75°	67°
Outer width of jet at impact	0.3m	0.36m	0.4m	0.32m
Outer thickness of jet at impact (B_{out})	0.21m	0.23m	0.3m	0.23m

Figure 4-13 - 20l/s discharge and 4m drop height including 0.5m tailwater. Lateral jet profile (left), longitudinal jet profile (middle) and plan view of jet (right)

The properties as calculated, in Table 4-8, were approximated using either the photos taken during the tests, or by taking actual measurements during the physical testing.

4.4.4 Behaviour of the jet in the plunge pool and at the rock bed

Due to the non-transparent nature of the plunge pool (masonry bricks), the diameter of the jet and the angle of jet spread in the plunge pool could not be determined from the physical laboratory model. The scour extent was, however, determined and is discussed in Section 4.4.4.1.

One of the major obstacles experienced during the physical testing, was to ensure that the correct tailwater level was obtained before scouring occurred. When the plunge pool was filled to the appropriate tailwater level, some premature scouring of the blocks occurred if the issuance flow was set too high (see Figure 4-14) as the plunge pool was filled using the plunging jet. To minimise the possibility of premature scouring, the issuance flow had to be maintained at a relatively low flow. At the lower head drops, this was, however, not possible and a PVC board (see Figure 4-14) was subsequently placed in front of the steel container and issuance canal to ensure that premature scouring was reduced to a minimum. The board allowed higher flows, which reduced the time to reach the required tailwater conditions and the board could be moved out of place with relative ease, when the desired tailwater was reached. Some form of premature scouring was, however, still present, even with the use of the PVC panel.

Initially the use of a water hose was aslo considered to fill the plunge pool to the appropriate level to reduce the effect of premature scouring. Due to the volume of the pool, the time required to fill the pool was rather excessive in comparison with using the issuance canal. Some premature scouring still occurred when the water level reached that of the container. The use of the issuance canal was thus the preffered option in filling the plunge pool.

Figure 4-14 - Premature scouring due to large flow during the filling of the plunge pool (left) and PVC board used to control flow (right)

4.4.4.1 *Scour extent*

The scour hole geometry was determined for all the physical laboratory model configurations as shown in Table 4-1 and are summarised below for each configuration tested and the scour hole cross sections for

each of the tests are compared in Section 4.4.4.2. From preliminary testing, it was observed that after approximately 30 minutes the scour hole reached a quasi-steady state, with the majority of scouring occurring in the first 15 minutes. Subsequent tests were, thus, run for approximately 30 minutes until insignificant to no scouring occurred. A grid was used to measure the scour depths. The grid consisted of 0.1m x 0.1m squares covering the whole container and the measurements were taken at the centre of each of the squares. Measurements were taken using a ruler connected to a spirit level to ensure relative accuracy (see Figure 4-15).

Figure 4-15 - Scour hole depth measuring instrument (left) and measuring grid (right)

With the complete number of 16 000 PVC blocks present, the container could not be filled entirely. The top two layers of the container were partially filled as can be seen in Figure 4-7. Due to the cost constraints, this was unavoidable. The author thus anticipated where scouring would occur and ensured that sufficient blocks were present so that satisfactory results could be obtained. The fact that the top edge of the container and the bottom of the plunge pool floor were not aligned, as well as the blocks not being able to fill the container to its top, creating an edge, inevitably also had an effect on the flow profile as shown in Figure 4-16.

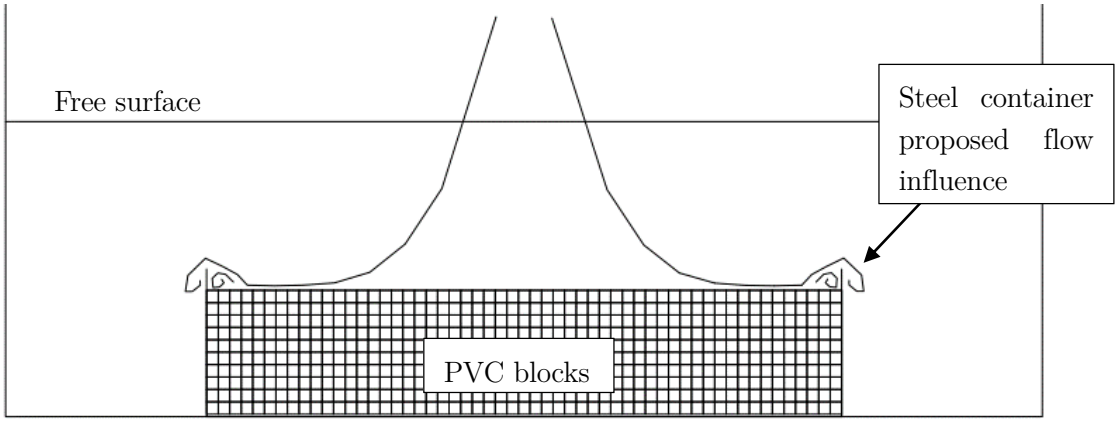

Figure 4-16 - Steel container flow profile effects

(i) 4m drop height with 0.5m tailwater

The scour profile of the 4m drop height, with a 0.5m tailwater depth physical laboratory model test, is shown in Figure 4-17. The jet was found to be developed at impact with the plunge pool free surface, as can be seen from the broken up nature of the jet in Figure 4-18. The scour hole was located closer to the upstream side of the container. From Figure 4-13, it is evident that the jet did not impact the steel container perfectly in the middle, but more to the upstream side of the container, which consequently caused the scour hole to shift upstream.

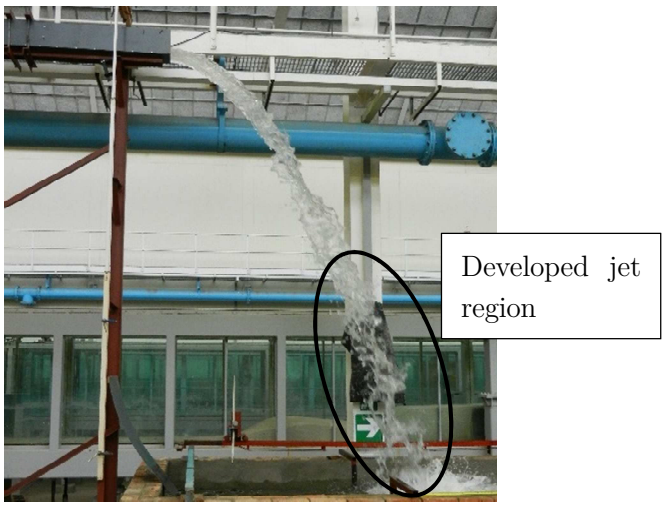

Figure 4-18 - Developed jet at impact for 4m drop height including 0.5m tailwater (physical laboratory model)

Figure 4-17 - Scour profile for the 4m drop height with a 0.5m tailwater

Only a small amount of the PVC blocks was removed from the bed and very few of the removed blocks were transported out of the steel container, as can be seen in Figure 4-17. The most pronounced scouring occurred in the impingement region, with the maximum scouring depth occurring at the jet centreline.

The majority of the uplifted blocks were transported in the form of bed load, while a selected few were carried as suspended load, subsequently being transported and deposited downstream. The steel container was positioned approximately 1.56m horizontally from the end of the issuance canal to the upstream edge of the steel container as shown in Figure 4-19.

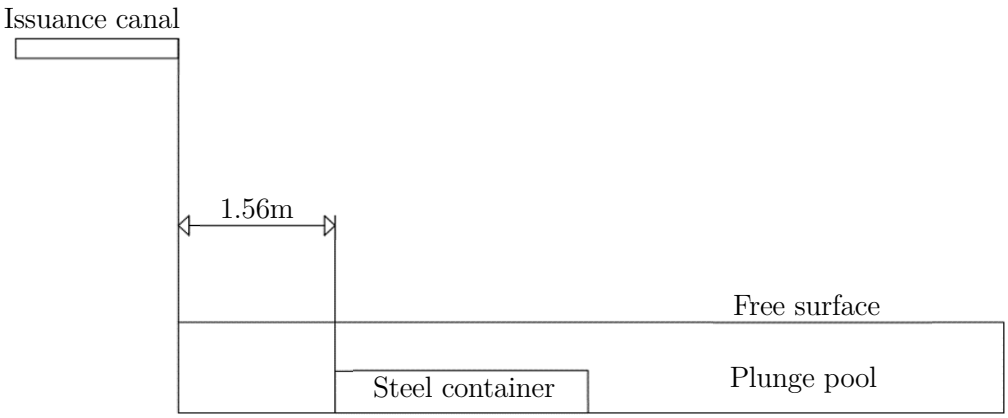

Figure 4-19 - Location of steel container

(ii) 3m drop height with 0.5m tailwater

The scour profile of the 3m drop height, with a 0.5m tailwater depth physical laboratory model test, is shown in Figure 4-20. The jet was thought to be in transition between being developed and undeveloped at impact from visual inspection during the physical laboratory model test as the jet lost coherence. From Figure 4-21 it was, however, clear that the jet was tending to be more developed than undeveloped at impact with the plunge pool free surface. The scour hole was located closer to the upstream side of the container, as was seen in the 4m test, which was again thought to be due to premature scouring and due to the jet not impacting the container exactly in the centre (see Figure 4-22).

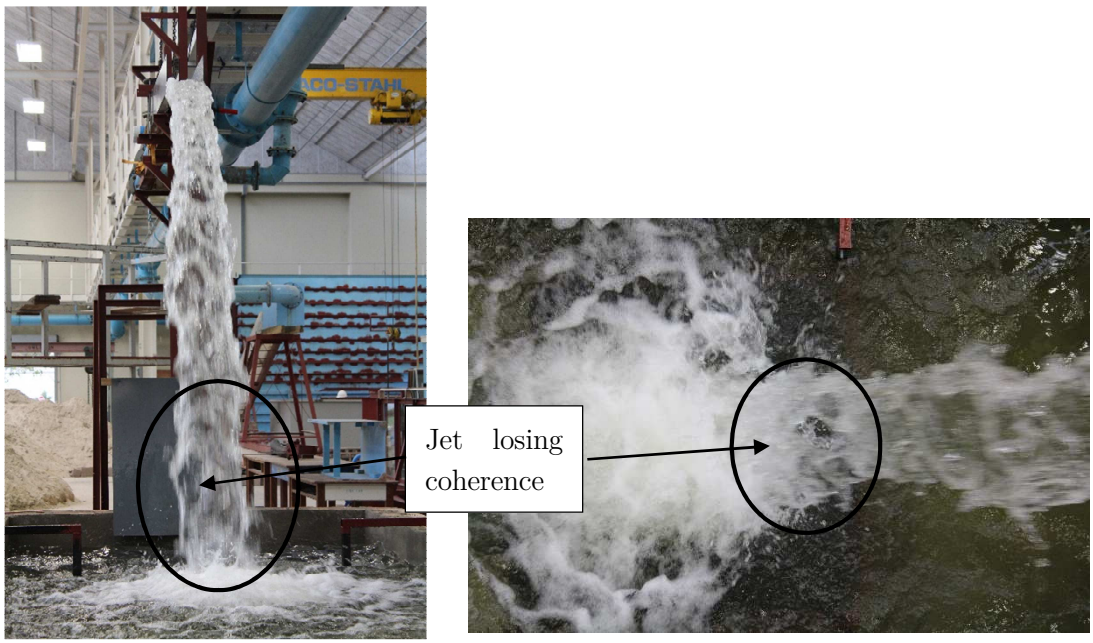

Figure 4-21 - Jet conditions at impact (3m drop height and 0.5m tailwater)

A large amount of the PVC blocks was removed from the bed. Of the blocks removed, the minority were transported out of the steel container, as can be seen in Figure 4-17. The majority of the uplifted blocks were transported in the form of bed and suspended load and deposited downstream, forming a mound, as is generally seen in the scouring of non-cohesive (gravel) beds. The steel container was positioned approximately 1.29m horizontally from the end of the issuance canal to the upstream edge of the steel container.

Figure 4-20 - Scour profile for the 3m drop height with 0.5m tailwater

Figure 4-22 - Plan view of jet impacting plunge pool free surface

(iii) 2m drop height with 0.5m tailwater

The scour profile of the 2m drop height, with a 0.5m tailwater depth physical laboratory model test, is shown in Figure 4-25. The jet was thought to be undeveloped at impact and the jet impacted the steel container almost perfectly in its centre as shown in Figure 4-23. The scour hole was located almost perfectly in the centre of the container.

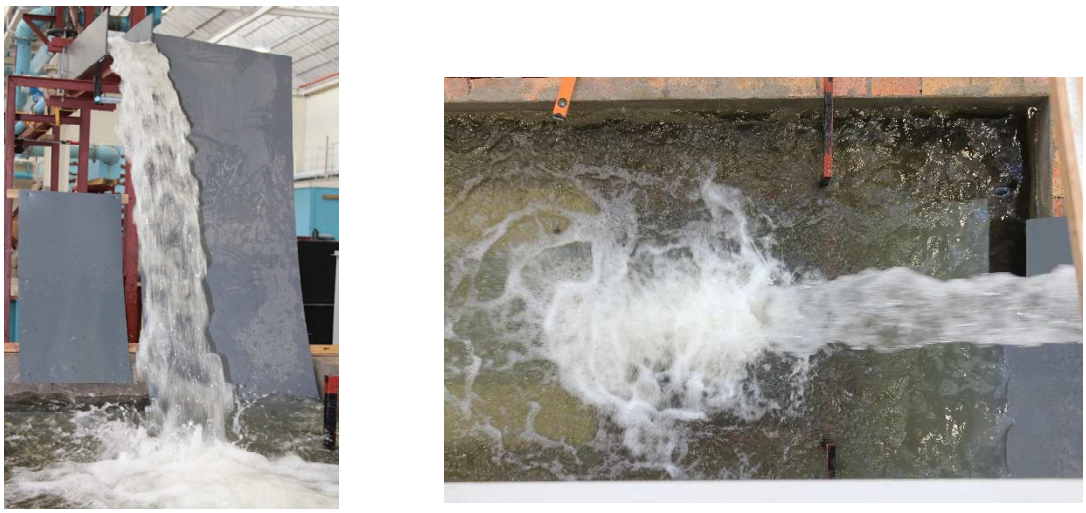

Figure 4-23 - Jet impact conditions for 2m drop height including 0.5m tailwater

A large amount of the PVC blocks was removed from the bed. Of the blocks removed, the minority were transported out of the steel container, as can be seen in Figure 4-25. The majority of the uplifted blocks were transported in the form of bed and suspended load and deposited downstream, forming a mound. The scour hole that formed was almost symmetrical in shape. The steel container was positioned approximately 0.99m horizontally from the end of the issuance canal to the upstream edge of the steel container.

Figure 4-25 - Scour profile for the 2m drop height with 0.5m tailwater

Due to the large mound that formed downstream, the author suspected that the mound reduced the scouring potential. Previous studies using non-cohesive sediment (gravel), suggested that the critical scour depth can only be formed when the mound is removed [7,62].The author thus predefined the scour hole, as shown in Figure 4-24, using similar scour hole dimensions to those of the original test (Figure 4-25) and repeated the test. The predefined scour hole test also served as a repeatability check of the scour hole results. The resultant scour hole is shown in Figure 4-24. The mound produced downstream was lower than the original test, but the shape and extent of the scour hole remained the same, which indicated that the mound formed downstream had no major influence on the scour hole using PVC blocks and that repeatability of the results was not a concern.

Figure 4-24 - Scour profile using predefined scour hole shape for the 2m drop height including 0.5m tailwater

(iv) 2m drop height with 0.25m tailwater

The scour profile of the 2m drop height, with a 0.25m tailwater depth physical laboratory model test, is shown in Figure 4-26. As for the 2m drop height including 0.5m tailwater, the jet was found to be undeveloped at impact with the plunge pool free surface and impacted the container near perfectly. The

scour hole was located almost perfectly in the centre of the container. The majority of the PVC blocks were removed from the bed. Of the blocks removed, more than half were transported out of the steel container, as can be seen in Figure 4-26. The majority of the uplifted blocks were transported in the form of bed and suspended load and deposited downstream, forming a mound or being transported further downstream outside the steel container. The steel container was found to be too small for the test conditions, as the blocks were almost completely removed from the container with only the masonry bricks and the minority of the blocks still present in the container. The steel container was positioned approximately 0.99m horizontally from the end of the issuance canal to the upstream edge of the steel container.

Figure 4-26 - Scour profile for the 2m drop height with 0.25m tailwater

4.4.4.2 *Longitudinal and lateral scour hole cross sections*

The lateral and longitudinal cross sections of the scour holes for the various physical laboratory model configurations are shown graphically in Figure 4-27 and Figure 4-28 for comparative purposes. The location of the cross sections for each test was taken at the location of the critical scour depth; this meant for the 3m and 4m cases, the lateral cross section was located upstream, while for the 2m tests, the lateral cross section was located in the middle of the container. The location of the longitudinal cross section was located in the middle of the container for all tests, as the jet impacted the container at the same position for all the test conditions laterally, as the issuance structure's location was fixed. The depths and distances as given in Figure 4-27 and Figure 4-28 were taken from the top edge and anterior of the steel container. As the blocks did not fill the container to the top edge, the measured depth was never zero, even in areas of no scouring.

From Figure 4-27 and Figure 4-28, the maximum scour depth for each drop height and tailwater level was determined and is shown in Table 4-9.

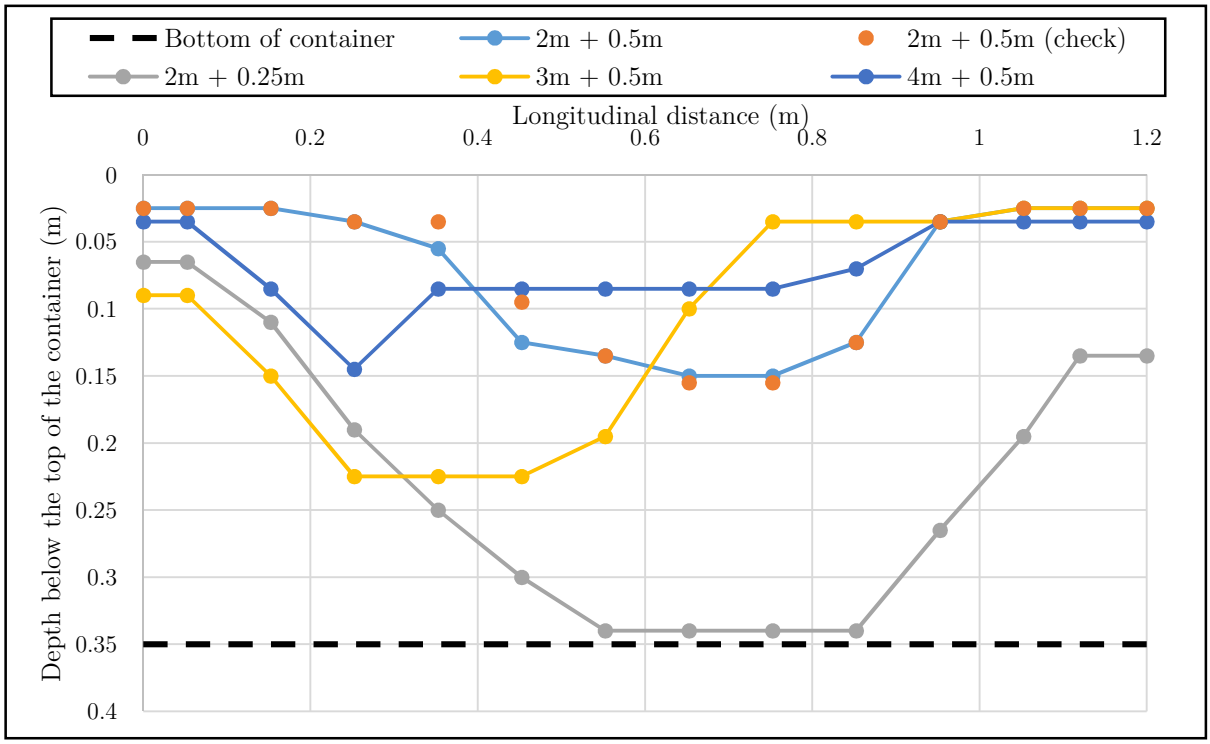

Figure 4-27 - Longitudinal cross section of scour hole

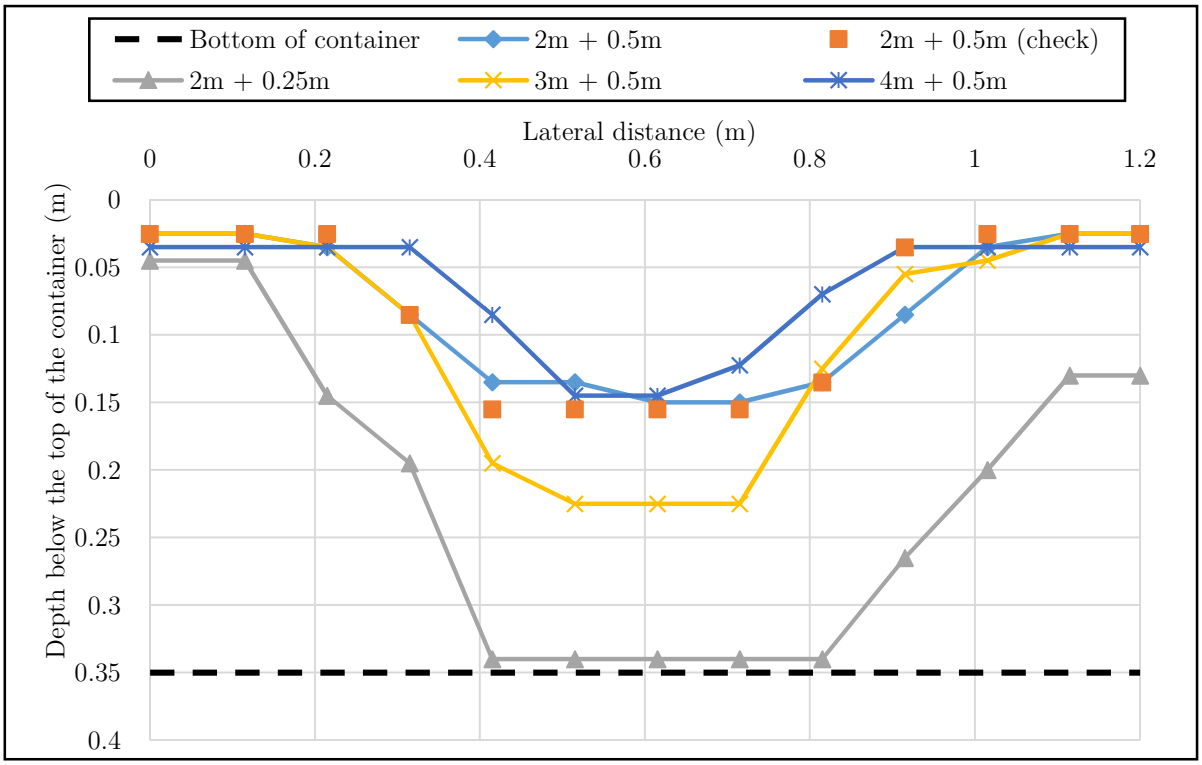

Figure 4-28 - Lateral cross section of scour hole

Table 4-9 - Physical laboratory model maximum scour depths

Property	Value			
Discharge (Q)	20l/s			
Tailwater (y_0)	0.5m			0.25m
Drop height (including tailwater)	2m	3m	4m	2m
Physical laboratory model scour depth (y_s)	0.155m	0.225m	0.145m	>0.35m

4.5 Discussion of results

The physical laboratory model scour hole results given in Section 4.4.4 indicated that the blocks could sustain relatively steep slopes as is generally seen in prototype rock beds (see Figure 2-17). This indicated that the use of the PVC blocks in physical laboratory models can serve as a more accurate alternative to model the steeper scour hole slopes of rock beds, in comparison to the originally used cohesive and non-cohesive sediments.

From the test results the deepest scour hole depth occurred in the case of the lowest tailwater depth of 0.25m. The 0.25m tailwater depth provided less energy dissipation in comparison to the 0.5m tailwater depth and subsequently caused the jet to have a higher erosive capacity at the rock bed. From previous studies, it was found that an increase in the tailwater depth decreased the scour hole depth as it increased energy dissipation and was also clear from the physical laboratory model results in this study. The exact depth could, however, not be determined for the 0.25m tailwater depth conditions, due to the depth of scouring being deeper than the depth allowed by the container used in the physical laboratory model (additional blocks were required).

For the 0.5m tailwater depth physical laboratory model tests, the 3m drop height showed the deepest scour hole depth and extent. This was presumed to be due to the jet being relatively compact (partly developed) at impact with the plunge pool free surface. Initially it was presumed that the 2m drop height would yield the largest and deepest scour hole, due to the jet being the most compact (undeveloped), but was thus found to not be the case. The jet's scouring potential was thus not only dependant on the compactness of the jet, but also on the velocity of the jet at impact with the plunge pool free surface. This was due to the magnitude of the velocity being directly related to the drop height, unless the jet is developed where the effect of air drag on the conglomeration of water droplets becomes a factor. From

the physical laboratory model results, it was found that the scour hole was the smallest and shallowest for the 4m drop height. This was presumed to be due to the jet being highly developed which significantly reduced the erosive capacity of the jet.

The scour profiles in the longitudinal direction, in Figure 4-27, showed that the scour profile tended to be more pronounced to the upstream side of the container for the 3m and 4m cases, but symmetrical for the 2m cases. The location of the scour hole was thought to be influenced by the presence of premature scouring and the location at which the jet impacted the steel container. The scour hole profiles (shape and depth), as depicted in Figure 4-28, showed that the scour hole profile (shape and depth) was almost symmetrical in the lateral direction for all the physical laboratory model configurations tested. The predefined (check) and original scour profile for the 2m drop height with 0.5m tailwater depth showed almost no difference in both the lateral and longitudinal directions, which illustrated that the downstream mound that formed did not have a significant effect on the scour hole, as opposed to what was found in previous studies using non-cohesive sediment (gravel) [7,63]. The scour hole produced for the 2m drop height including 0.25m tailwater depth was not representative of the actual scour hole that could have been produced as the container was too small for the scouring that occurred.

To further investigate the above results, CFD models, empirical formulas and physically based (analytical) prediction techniques were used to determine and validate the scour hole geometries found in the physical laboratory model test.

5 Comparison of physical laboratory model results with that obtained from empirical formulae and physically based methods

This section contains the results of the physically based (EIM and CSM) and empirical methods, as explained in Section 3, on predicting rock scour using the physical laboratory model setup conditions, as discussed in Section 4. The hydrodynamic characteristics of the plunging jet in the air and plunge pool are also calculated in this section. The physical laboratory model setup conditions limited the jet to being predominantly developed at impact with the plunge pool free surface, due the high drop heights and the low allowable flow from the pumps. The lower drop heights, however, enabled undeveloped jet conditions at impact with the plunge pool to be tested, which was previously found to have more scouring potential.

The empirical formulae and physically based methods (EIM and CSM) were used to verify the physical laboratory model scour hole results, but also to compare with the CFD simulations. Due to the fact that no prototype or previously used model setup conditions were used in this study, the use of the empirically and physically based methods to verify the results, of both the physical laboratory model and CFD simulations, were further motivated.

5.1 Hydraulic behaviour of the jet

The hydraulic behaviour of the jet in the air and plunge pool, as calculated for the physical laboratory model setup conditions, is described below. The behaviour of the jet in both the air and plunge pool was calculated using the methods, as explained in Section 3.3.

5.1.1 Behaviour of the jet in the air

The trajectory of the jet was calculated using the ballistics equation (Eqn. 3-39) and by using the properties of the physical laboratory model, as given in Table 4-1. The horizontal distance from the point of issuance to impact with the plunge pool free surface, and the angle of impact with the free surface,

was also calculated from the trajectory calculation. The angle of impact was calculated using the tangent of the segments (x and y), to determine the trajectory length (refer to Eqn. 3-39 and Figure 5-1), and by using Eqn. 3-44. The issuance angle was 0 degrees (horizontal discharge) and the value of K_2, was assumed as being 0.75 as proposed by Wahl *et al.* (2008) [107].

Castillo (2007) [31,110,111] proposed that an initial turbulence value of 1.2% should be used for nappe spillways (rectangular jets). Due to the high turbulence at issuance in the physical laboratory model, the author proposed that a value of 3% should rather be used, as was proposed by Bollaert (2002) for nappe spillways [36].

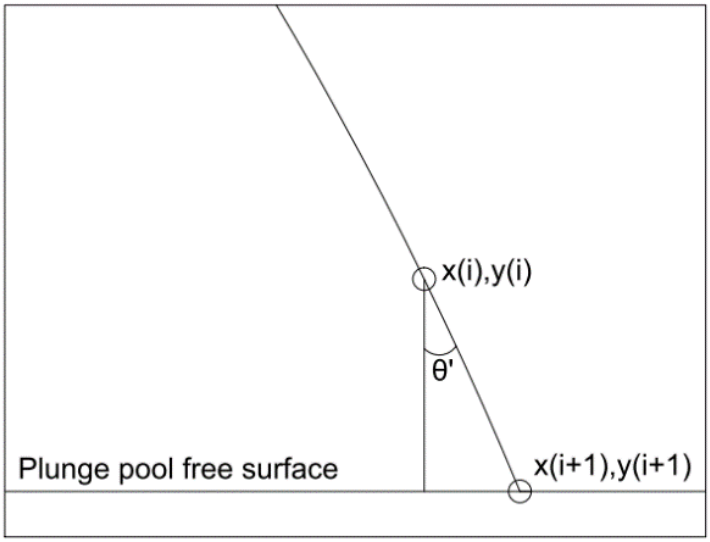

Figure 5-1 - Angle of impact using trajectory segments

The lateral spread of circular jets was studied by Ervine and Falvey (1987) [21], which was discussed in Section 2.5.1.1. The angles of lateral spread (δ_{out}) that were proposed by Ervine and Falvey (1987) falls between 1.7° - 2.3°, which were calculated using the turbulence intensity and the distance along the trajectory. Comparing the lateral spread angle proposed by Ervine and Falvey (1987) to the physical laboratory model's estimated angle of lateral (1.5°) and longitudinal (2.1°) spread in Table 4-7, the two compared relatively well. The discrepancies were deemed acceptable, as Ervine and Falvey (1987) developed the angles for circular jets and the measurements of the physical laboratory model could have incurred some form of human error. For subsequent calculations, the spreading angles as calculated from the physical laboratory model were used.

The break-up length (L_b) was calculated using the methods proposed by Castillo (2007) [31,110,111] and Horeni (1956) [30] (see Eqn. 2-5 and Eqn. 2-6 in Section 2.5.1.1). As the flow at issuance was lower than 0.25m^3/s (0.02m^3/s for 20l/s), the method, as proposed by Horeni (1956), could be used to determine the break-up length. The calculated values are shown in Table 5-1.

Table 5-1 - Behaviour of the jet in the air - calculated values

Property	**Value**			
Discharge (Q)	20l/s			
Tailwater (y_0)	0.5m			0.25m
Drop height (including tailwater) ($H+y_0$)	2m	3m	4m	2m
Horizontal distance to impact (x)	1.11m	1.43m	1.69m	1.19m
Angle of impact (Tangent) (θ')	70	74	76	71
Angle of impact (Eqn. 3-44) (θ')	71	75	77	72
Trajectory length (L)	1.95m	3m	4.03m	2.22m
Turbulence intensity (T_u)	3%	3%	3%	3%
Break-up length (Castillo, 2007) (L_b)	1.04m	1.04m	1.04m	1.04m
Break-up length (Horeni, 1956) (L_b)	2.87m	2.87m	2.87m	2.87m

The empirically calculated values of the properties of the jet in the air, shown in Table 5-1 agreed well with the measured values determined from the physical laboratory model in Table 4-8. The impact angles from the physical laboratory model were slightly lower than those calculated using the tangent of the segments, which were used in determining the trajectory of the jet, but they did not differ considerably. The theoretical angles of impact with the free surface using Eqn. 3-44, varied slightly from those calculated, using the tangent of the trajectory segments. The values of the trajectory length, as well as the horizontal distance to impact with the plunge pool free surface, compared very well between the physical laboratory model and the theoretical values. As the measurements of the physical laboratory model were done using photos taken and physical measurements, the difference in the values was thought to be acceptable, as some discrepancies were inevitable. The trajectory of the jet is given graphically in Figure 5-2, for both the physical laboratory model and the theoretical values for the 20l/s discharge, 4m drop height and 0.5m tailwater depth. The trajectory profiles differed slightly, but there was still a good correlation between the two profiles. As the trajectory of the lower drop heights are essentially identical to the highest drop in theory, due to the trajectory being dependent on the issuance conditions, which was identical for all the tests, only the highest drop height trajectory was given graphically. From

Table 5-1 it is clear that the different tailwater levels tested had no major effect and only affected the trajectory length of the jets, but only slightly.

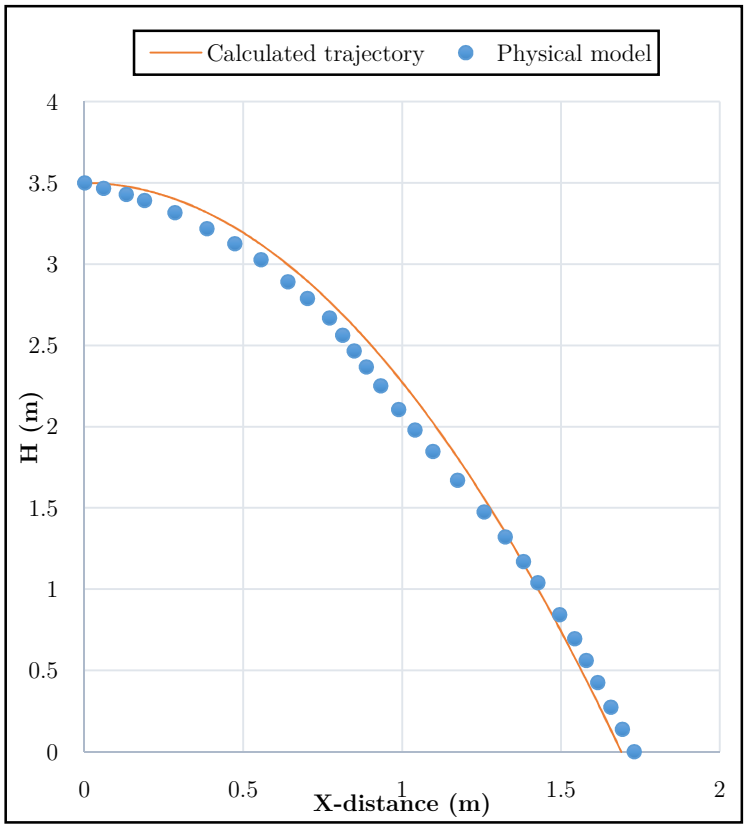

Figure 5-2 - Calculated and physically modelled jet trajectories

The different break-up lengths calculated from the equations proposed by Horeni (1956) (Eqn. 2-5) and Castillo (2007) (Eqn. 2-6) varied quite significantly, as can be seen from Table 5-1. The jet was always developed at impact when using Castillo's equation, while the equation, as proposed by Horeni (1956), indicated that the jet was undeveloped at impact with the plunge pool free surface for the lower drop heights (refer to Table 5-2). Both the equations (Eqn. 2-5 and Eqn. 2-6) are directly related to the discharge at issuance, as well as the drop height. For the calculations that followed, the break-up lengths as calculated using the equation proposed by Horeni (1956), were used as a conservative approach, due to a more compact (undeveloped) jet present at impact with the plunge pool free surface, which had higher scouring potential. The break-up length calculated using Eqn. 2-5, proposed by Horeni (1956), also compared better to the estimated break-up length from the physical laboratory model that was presumed to fall between 1 and 2m.

A comparison between the two approaches was, however, still included to illustrate the difference and impact of using the different break-up length methods for the 2m drop height, 20l/s and 0.25m tailwater depth case in determining the pressure coefficients and the subsequent pressures at the centreline of the jet in the plunge pool (see Section 5.1.3.1).

Table 5-2 - Jet condition at impact (developed or undeveloped)

Property	**Value**			
Discharge (Q)	20l/s			
Tailwater (y_0)	0.5m			0.25m
Drop height (including tailwater)	2m	3m	4m	2m
Jet condition (H /L_b) (Castillo, 2007)	D	D	D	D
H/L_b	1.4	2.4	3.4	1.7
Jet condition (H /L_b) (Horeni, 1956)	UD	UD	D	UD
H/L_b	0.52	0.87	1.22	0.61
Jet condition (L_j/L_b) (Horeni, 1956)	UD	D	D	UD
L_j/L_b (Horeni)	0.7	1.0	1.4	0.8

Where:

D = Developed jet

UD = Undeveloped jet

Literature suggested that the beak-up length should be compared to the drop height to determine if the jet was developed or not, as shown in Table 5-2 [31,36,110]. The author, however, suggests that the break-up length should rather be compared with the trajectory length, as it represents the actual distance the jet has travelled through the air. The formulas to determine the properties of the rectangular jet at impact with the plunge pool free surface (jet thickness and velocity), as proposed by Castillo (2007), however, used the drop height and not the trajectory length, which may be the reason for using the drop height and not the trajectory length in determining the jet's condition at impact. The formulas to determine the diameter for circular jets at impact, with the plunge pool free surface, however, used the trajectory length. Using the trajectory lengths, as shown in Table 5-1, rather than the drop height, the jet was developed for 75% of the physical laboratory model configurations, rather than 25% of the test configurations when using the drop height as calculated using the formula proposed by Horeni (1956), as shown in Table 5-2.

5.1.2 Jet at impact with plunge pool free surface

Using the approaches, as was explained in Section 3.3.2.2.1, the behaviour of the jet at impact with the plunge pool free surface could be determined. The velocity, at impact, was calculated using the equation, as proposed by Ervine and Falvey (1987) [21], for a compact jet due to gravitational acceleration (Eqn. 3-34). The thickness of the core and the outer thickness of the jet were calculated using the equations, as proposed by Castillo (2007) [31,110,111] (Eqn. 3-38 and Eqn. 3-50 to Eqn. 3-54) for rectangular jets. The overtopping depth was used in Eqn. 3-52, as was suggested by other researchers, rather than the energy head, as was originally proposed by Castillo (2007) [108]. The calculated values are shown in Table 5-3.

Table 5-3 - Properties of the jet at impact with the plunge pool free surface

Property	Value			
Discharge (Q)	20l/s			
Tailwater (y_0)	0.5m			0.25m
Drop height (including tailwater)	2m	3m	4m	2m
Thickness of the core at impact (B_g)	0.018m	0.014m	0.012m	0.017m
Later spread distance (ξ)	0.006m	0.008m	0.014m	0.007m
Impingement thickness (B_j)	0.03m	0.03m	0.04m	0.03m
Impact velocity (V_j)	5.78m/s	7.28m/s	8.52m/s	6.19m/s

From Table 5-3, it appeared that the inner jet core was intact for all the model conditions tested; however, from the break-up length calculations (Table 5-2) and from inspection of the physical laboratory model, this was not possible. For the developed jet cases, the presence of the core from calculation was ignored.

To determine the value of the impingement thickness of the jet (B_j) in Table 5-3, a discharge coefficient (C_d) of 2.1 and a value of 0.85 for K were used, as was proposed by Castillo (2007), to determine lateral spreading of the jet (ξ). The calculation of the impingement thickness (B_j) includes the spreading of the jet, which is not included in the calculation of the impact, or core diameter (D_j), in circular jets, as proposed by Ervine and Falvey (1987) [21]. The calculated values of the impingement thickness (B_j), were found to be lower than the issuance thickness, as Eqn. 3-50 uses the thickness of the core, as opposed to the equation for the outer diameter of circular jets. This was proposed by Ervine and Falvey (1987) (Eqn. 3-46), which uses the issuance diameter (D_i) to determine the outer diameter (D_{out}). The author found no formulation to determine the outer dimensions of a rectangular jet at impact with the plunge

pool free surface. It is therefore proposed to use similar formulations; Eqn. 5-1 and Eqn. 5-2, which were available for circular jets, as was proposed by Ervine and Falvey (see Table 3-11). Eqn. 5-1 was based on the equation to calculate the outer diameter of a circular jet (Eqn. 3-46), while Eqn. 5-2 determined the outer dimensions using the lateral and longitudinal spread angles calculated from the physical laboratory model and the trajectory length. The dimensions calculated using Eqn. 5-2 compared very well with the dimensions measured in the physical laboratory model, while Eqn. 5-1 underestimated the outer thickness of the jet as shown in Table 5-4.

$$\textbf{\textit{Outer impact thickness}} = B_i + 2\xi \qquad \text{Eqn. 5-1}$$

$$\textbf{\textit{Outer impact thickness and width}} = B_i + 2(\tan(\delta_{out}) \times L_j) \qquad \text{Eqn. 5-2}$$

Where:

δ_{out} = Lateral and longitudinal outer spread angle

L_j = Trajectory length (m)

B_i = Issuance thickness of the jet (m)

The calculated impact velocities as shown in Table 5-3 were not applicable for the developed jets. For the developed jets, as indicated in Table 5-2, Eqn. 3-35 should be used as the formula was developed for developed jets. The calculated developed jet velocities are shown in Table 5-5. A value of 0.5 was assumed for the drag coefficient of a sphere [159] and a diameter of 5mm for the water droplet was assumed [160]. The size of the water droplets varied considerably over the width and thickness of the jet in the physical laboratory model, as can be seen from Figure 5-3. For an accurate estimation of the developed jet velocity, accurate determination of droplet size is essential, which was impeded by the variability in the droplet size in the physical laboratory model.

Table 5-4 - Jet footprint at impact (proposed methods)

Property	Value			
Discharge (Q)	20l/s			
Tailwater (y_0)	0.5m			0.25m
Drop height (including tailwater)	2m	3m	4m	2m
Impingement thickness (B_j)	0.03m	0.03m	0.04m	0.03m
Outer impact thickness (using B_i)	0.057m	0.060m	0.062m	0.058m
Outer thickness at impact (using angle)	0.19m	0.27m	0.35m	0.21m
Outer width at impact (using angle)	0.30m	0.36m	0.41m	0.32m

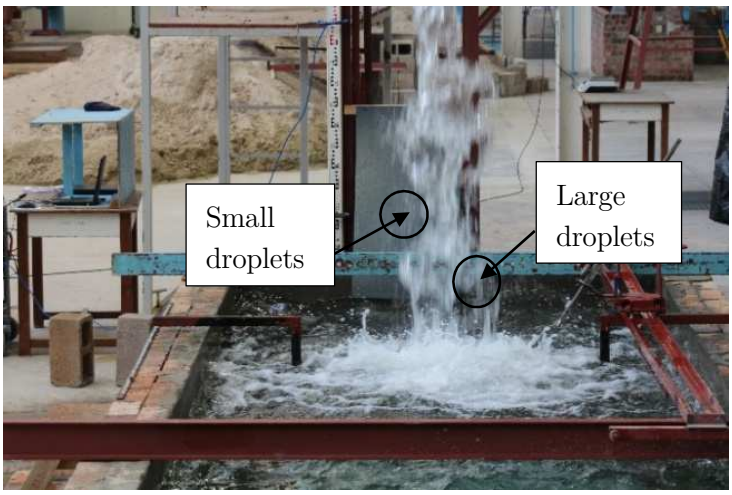

Figure 5-3 - Variable water droplet diameter

Due to the uncertainty regarding whether the jet was developed or undeveloped at impact, the velocities using the developed jet formula was calculated for all the physical laboratory model configurations (see Table 5-5). As no velocity measurements at impact with the plunge pool free surface were taken, due to instrument restrictions, the velocities could not be verified or compared with the physical laboratory model, but they were compared to the CFD models in Section 6. The calculated velocities of the developed jets were lower than those of the compact jets, as would be expected, due to the inclusion of air drag on the individual water droplets. For the calculations that followed, the velocities as highlighted in Table 5-5 were used. The velocities were chosen based on the nature of the jet, developed or undeveloped, from Table 5-2, as was determined using the equation proposed by Horeni (1956).

Table 5-5 - Developed jets velocities at impact with plunge pool free surface

Property	**Value**			
Discharge (Q)	20l/s			
Tailwater (y_0)	0.5m			0.25m
Drop height (including tailwater)	2m	3m	4m	2m
Impact velocity (V_j) - undeveloped	5.78m/s	7.28m/s	8.52m/s	6.19m/s
Impact velocity (V_j) - developed	4.26m/s	5.32m/s	6.2m/s	4.55m/s

5.1.3 Jet behaviour in the plunge pool

The behaviour of the jet for the different physical laboratory model configurations was determined using the methods as explained in Sections 3.3.2.2.2 and (ii).

Due to the rectangular nature of the jet, the depth of the jet to become developed and lose its core was assumed, as 5.5B_j as was proposed by Castillo (2007) [31,110,111] (see Section 2.5.1.2). The spreading of the jet in the plunge pool was assumed similar to that of circular jets, as was proposed by Ervine and other researchers (see Section 2.5.1.2 and Table 2-7). Rough turbulent conditions were assumed at impact with the plunge pool free surface. From Table 2-7, for rough turbulent conditions, it was assumed that an outer jet boundary expansion angle of 13-14 degrees was present in the undeveloped region, with an outer spread angle of 14-15 degrees when the jet was developed. See Figure 5-4 for a visual representation of the above assumptions.

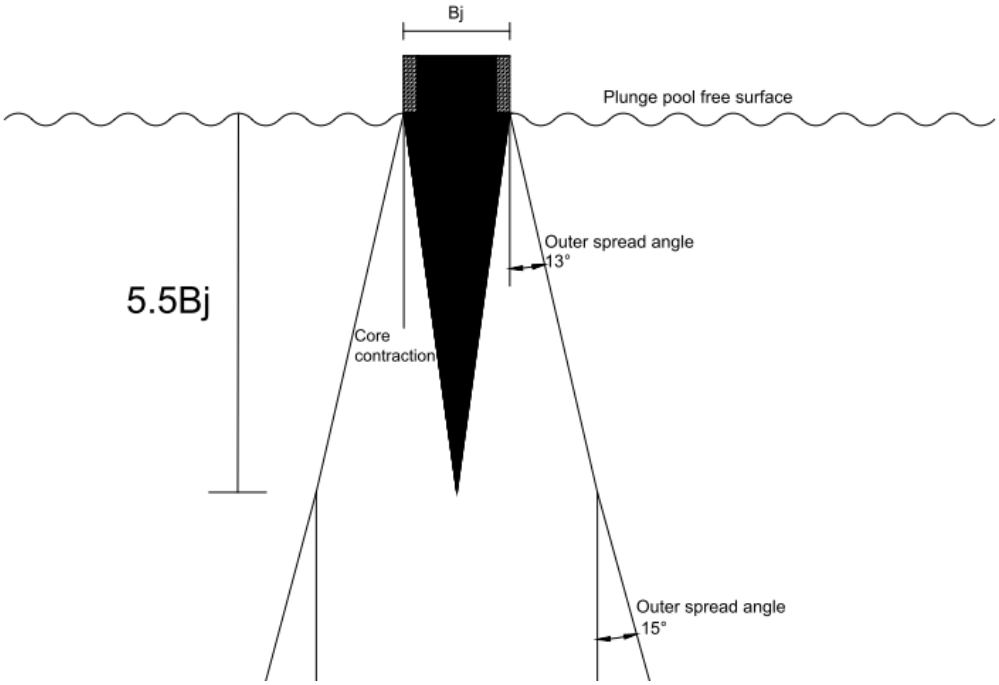

Figure 5-4 - Jet behaviour in plunge pool

5.1.3.1 *Pressures in the plunge pool*

The fluctuating pressure coefficients and subsequently the maximum pressures in the plunge pool, at the centreline of the jet, were determined using the methods as developed by Castillo (2014) [31,110,111] for rectangular jets, as was explained in Section 3.3.2.2.2. As no pressure measurements were taken in the plunge pool during physical laboratory model testing, the pressures were compared to those calculated in the CFD model in Section 6. The pressure coefficients also needed to be calculated, as they were required in calculating the stream power using the EIM as discussed in Section 5.2.2.

(i) Mean dynamic pressure coefficient

The mean dynamic pressure coefficients (C_{pa}) were calculated using Eqn. 3-68 to Eqn. 3-70 that were discussed in Section 3.3.2.2.2. A graphical representation of the calculated mean dynamic coefficient (C_{pa}) values in comparison to the Y/B_j ratio is shown in Figure 5-5. The depth of the water cushion (Y) was calculated as the tailwater level in addition to the scour hole depth (not the exact trajectory), due to the plunge pool free surface impact angles being above 60 degrees, as was proposed by Bollaert (2002) [36]. The break-up lengths used to determine the coefficients were calculated using the equation as proposed by Horeni (1956) (Table 5-2).

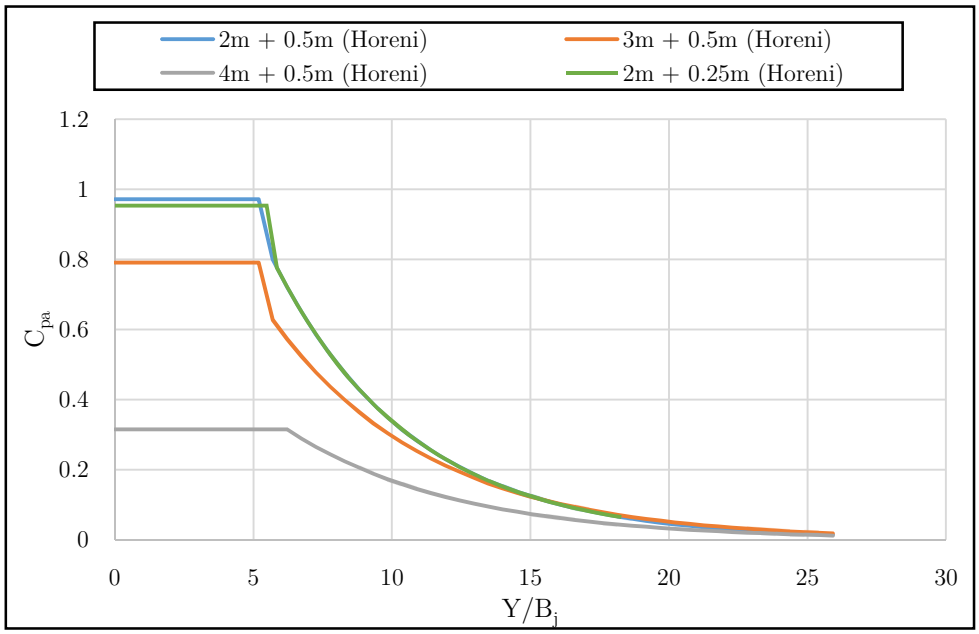

Figure 5-5 - Mean dynamic pressure coefficient for the different tested tailwater levels and drop heights

From Figure 5-5, it was clear that the lowest drop height produced the highest mean dynamic pressure coefficients, while the highest drop height produced the lowest dynamic pressure coefficients. Due to the compactness of the undeveloped jets produced at the lower drop heights (see Table 5-2), the mean pressure coefficients were higher, compared with the more developed jets from the higher drop heights.

As discussed in Section 5.1.1, for comparative purposes, the mean pressure coefficients were calculated for the worst case tested (2m drop height and 0.25m tailwater depth), using the break-up lengths determined from the equations proposed by Horeni (1956) and Castillo (2007) (see Table 5-2). As can be seen from Figure 5-6, the coefficients, as calculated using the break-up length from Castillo, were

considerably less than the coefficients as calculated using the break-up length from Horeni (1956). This was due to the jet being highly developed for all the physical laboratory model configurations tested, using the break-up lengths calculated from Castillo (2014) ($H/L_b > 1$) shown in Table 5-2, because the mean dynamic pressure coefficient is directly related to the break-up length (Eqn. 3-68 to Eqn. 3-70).

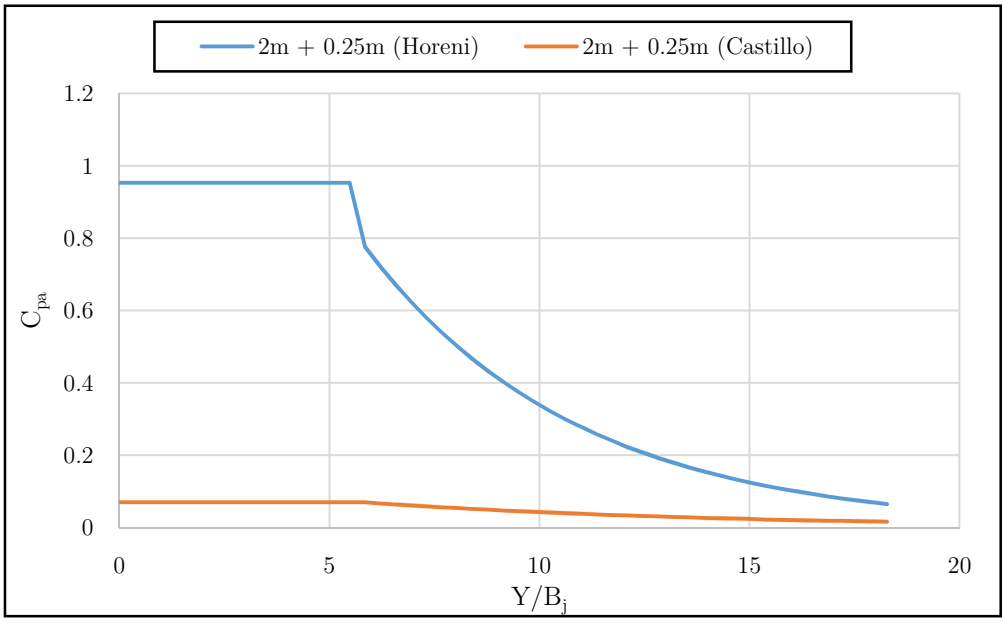

Figure 5-6 - Mean dynamic pressure coefficient using H/L_b values from Horeni (1956) and Castillo (2014)

(ii) Fluctuating pressure coefficient

The fluctuating dynamic pressure coefficients (C'_{pa}) were calculated using Eqn. 3-76 and Eqn. 3-77 that were discussed in Section 3.3.2.2.2. A graphical representation of the calculated fluctuating dynamic pressure coefficients in comparison to the Y/B_j ratio, is shown in Figure 5-8. The break-up lengths used to determine the coefficients were calculated using the equation as proposed by Horeni (1956).

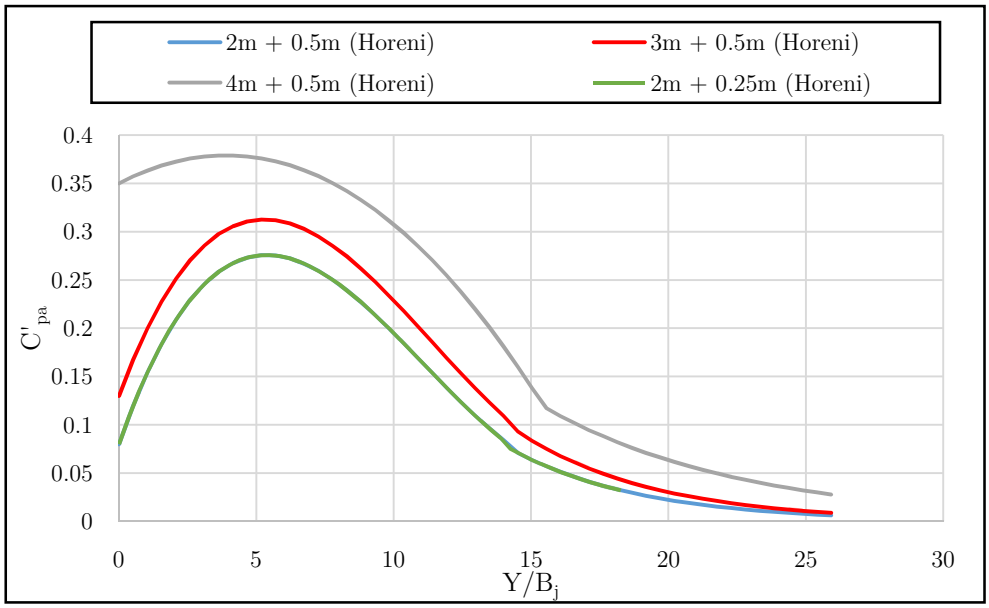

Figure 5-7 - Fluctuating dynamic pressure coefficient

From Figure 5-7, it was construed that the highest fluctuating pressure coefficients (C'_{pa}) occurred at the drop height of 4m, as opposed to 2m, as found for the mean pressure coefficient (C_{pa}). Of the conditions tested, the 2m drop height produced the lowest fluctuating pressure coefficients. In contrast to the mean pressure coefficients, the developed nature of the jet at the higher drop heights, produced higher pressure fluctuations in comparison to the compact nature of the undeveloped jet at impact with the plunge pool free surface at the lower drop heights.

As for the mean dynamic pressure coefficient (C_{pa}), the mean fluctuating coefficients (C'_{pa}) were calculated for the worst case tested, by using the break-up lengths determined by the equations proposed by Horeni (1956), as well as Castillo (2007), for comparison. The mean fluctuating coefficients, calculated using the break-up lengths (determined using the equation of Castillo (2007)), were considerably less than the coefficients calculated using the equation of Horeni (1956). This was due to the jet being highly developed for all the physical laboratory model configurations tested ($H/L_b > 1$), which was similar to the results of the mean dynamic pressure coefficient (see Figure 5-8).

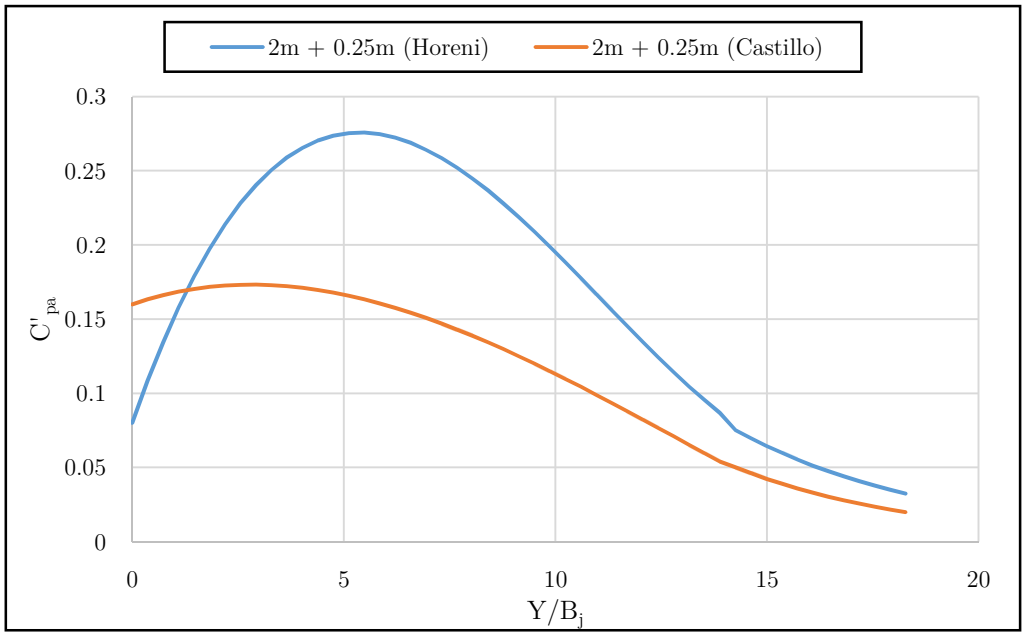

Figure 5-8 - Fluctuating dynamic pressure coefficients using H/L_b values from Horeni (1956) and Castillo (2007)

(iii) Total dynamic pressure

Using the calculated mean and fluctuating dynamic pressure coefficients, the total dynamic pressure was calculated using Eqn. 3-55, including the velocities as calculated and capsulated in Table 5-5. A graphical representation of the calculated total dynamic pressure values in comparison with the depth below the plunge pool free surface is shown in Figure 5-9.

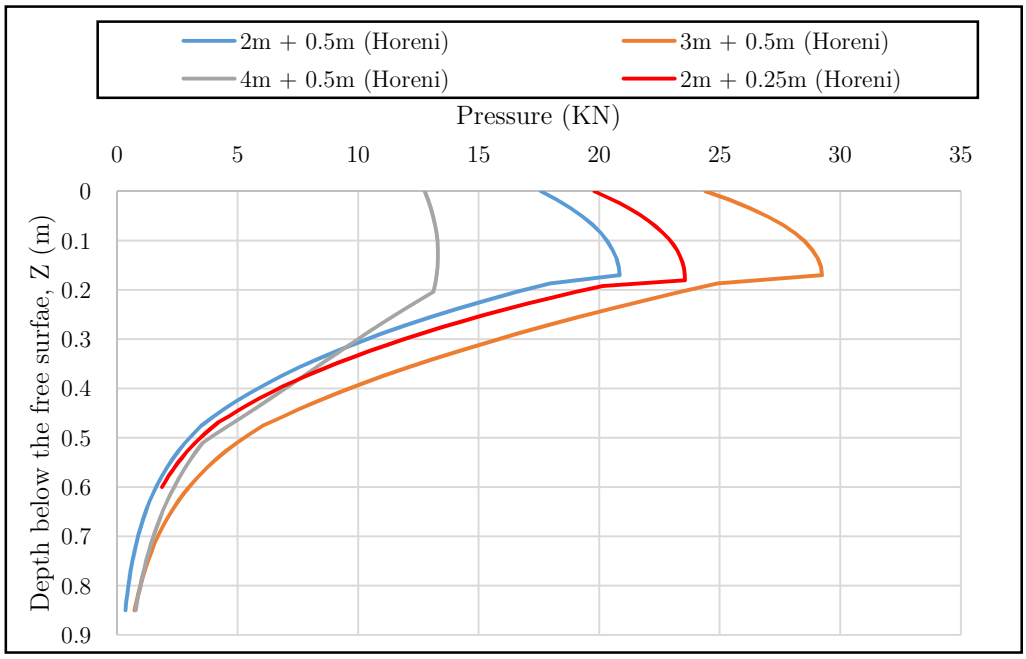

Figure 5-9 - Total dynamic pressure values for the different physical laboratory model

From Figure 5-9 it was clear that the highest dynamic pressures were experienced for the drop height of 3m (including tailwater depth of 0.5m), which was due to the fact that the jet was undeveloped at impact, while the lowest pressures occurred at the highest drop height (4m), due to the developed jet at impact with the free surface. The highest pressures did not occur at the lowest drop height (2m), due to the lower velocity at impact at the free surface, in comparison to the 3m drop height, as the total dynamic pressure is directly related to the velocity at impact (Eqn. 3-55). The velocity at impact is directly related to the drop height, and if the jet is undeveloped at impact. As the jet was still undeveloped at impact for the 3m drop height including 0.5m tailwater depth (Table 5-2) and the drop height was higher than for the 2m case, as well as the velocity (Table 5-5), the total dynamic pressures were subsequently also higher.

As for the mean and fluctuating dynamic pressure coefficients, the total dynamic pressure was calculated for the worst case tested, by using the break-up lengths determined from the equations proposed by Horeni (1956) and Castillo (2007), to illustrate the difference in results of the different methods available. The effect of using the velocities of an undeveloped or developed jet at impact with the plunge pool free surface

(Figure 5-10) was also explored. From Figure 5-10, it was apparent that it is paramount to correctly ascertain if the jet is developed or undeveloped at impact with the free surface and that the correct break-up length formula should be used. There was a substantial difference in pressures when using the break-up lengths, as calculated by the equation proposed by Horeni (1956), in comparison with the one proposed by Castillo (2007), as was found for the mean and fluctuating pressure coefficients. The total dynamic pressure calculated using the break-up length formula proposed by Horeni (1956) was found to be much higher than the total dynamic pressure calculated using the formula proposed by Castillo (2007). From Figure 5-10, it was also apparent that there was a large difference in the pressures calculated, when the impact velocity was that of a developed or undeveloped jet at impact with the plunge pool free surface, due to the influence of air drag on the developed jet velocity (see Table 5-5 and Eqn. 3-55). Both the mean and fluctuating pressure coefficients are directly related to the impact velocity and subsequently also the total dynamic pressure.

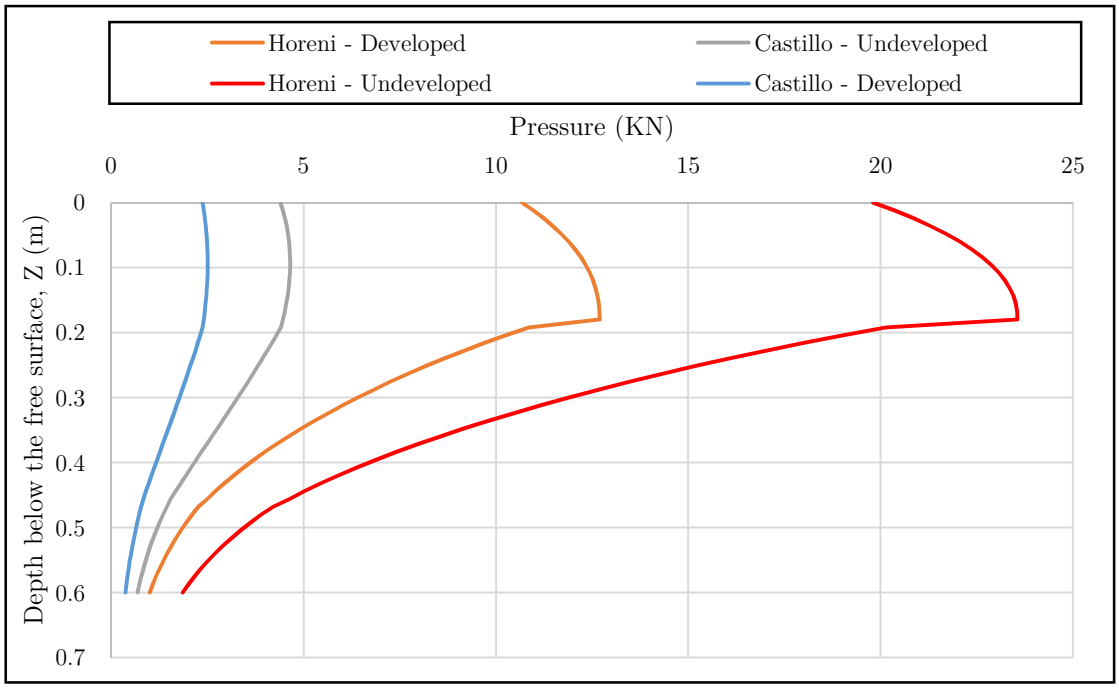

Figure 5-10 - Total dynamic pressure values for an undeveloped and developed jet at impact with the free surface using L_b values as calculated using equations from both Castillo (2007) and Horeni (1956) and using developed and undeveloped velocities at impact with the plunge pool free surface

5.1.3.2 *Velocity decay in the plunge pool*

The velocity decay in the plunge pool was calculated using the methods as proposed in Section 5.2.3.2. Four approaches were available as found in literature [21,36,125,127,128,129] to calculate the velocity decay of the jet in the plunge pool and were all heavily dependent on the impact thickness or diameter and the velocity of the jet at impact with the plunge pool free surface. From first assessment, the approach, as proposed by Bohrer (1998) [129] (Eqn. 3-105 to Eqn. 3-111), produced significantly larger velocities compared with the other three approaches. The minimum depth restriction also reduced the applicability of using the velocity profile for all the model setup configurations, because, whilst using the 0.25m tailwater depth condition, the approach could not be used, since the minimum depth (≈0.65m) fell below the maximum depth of the physical laboratory model (0.6m) and the method was thus not considered for this study. The method, as proposed by Beltaos (1973) [36,128] in contrast produced rather low velocities in comparison to the other methods and was disregarded for this study. Only the methods proposed by, Ervine and Falvey (1987) [21,125] and Hartung and Hausler (1973) [125,127] was thus considered for this study. See Figure 5-11 for a visual representation of the velocity decay in the plunge pool, using the four different methods.

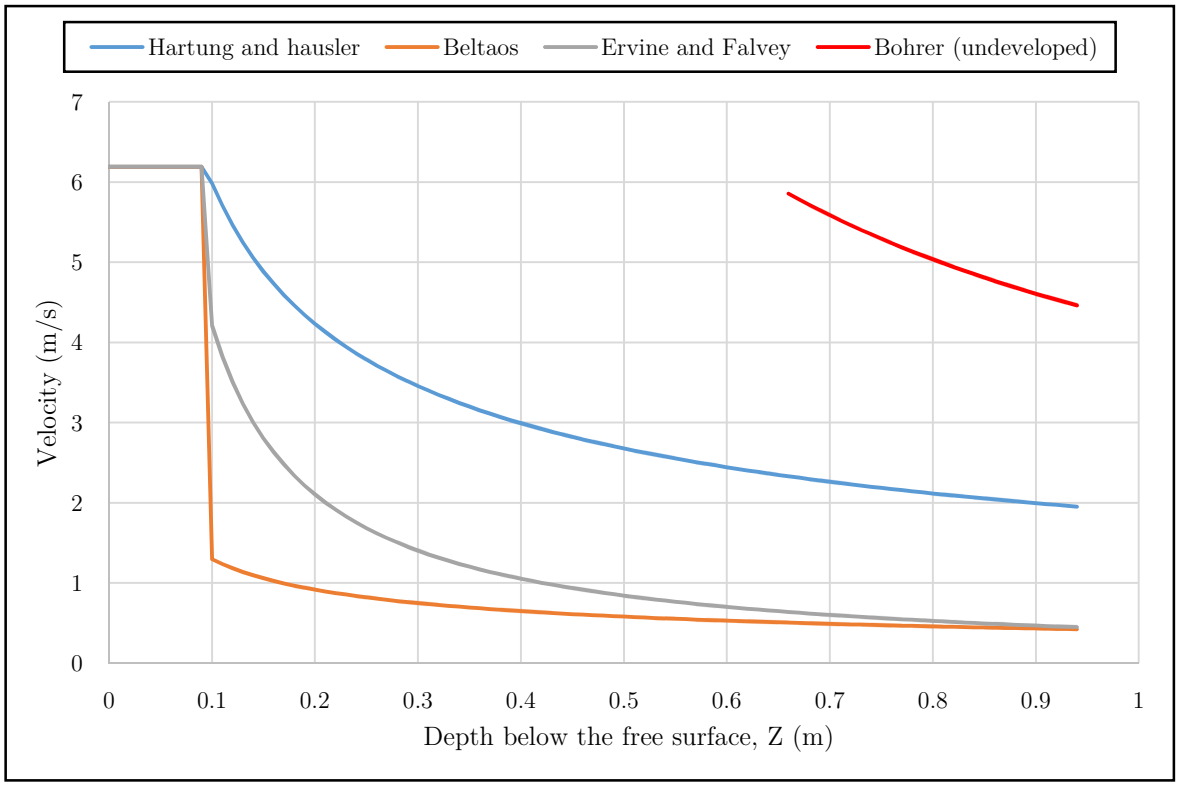

Figure 5-11 - Velocity decay using the four available velocity decay methods

The methods considered, were originally developed for undeveloped circular jets and not undeveloped and developed rectangular jets, which were the focus of this study. The impact velocities, as shown in Table 5-5, were used, while the thickness of the jet at impact with the free surface was taken as B_j (Table 5-3). The author used the impingement thickness (B_j) as previous studies done by Castillo (2014) suggested the value of B_j was comparable to the value of impingement diameter (D_j) of circular jets. It should be noted that the value of impingement thickness (B_j) takes into account some of the lateral spread, while the value of the impact diameter (D_j), which the methods were developed for, disregards any of the lateral spread of the jet and only takes into account the diameter of the core. Ervine and Falvey (1987) [21] proposed that where the jet was undeveloped at impact with the free surface, the velocity in the plunge pool up to a depth of four times D_j, or in this case four times B_j, can be taken as the same as the impact velocity. Studies by Castillo (2014), however, showed that the core remains up to a distance of 5.5 times B_j for rectangular jets [110]. Subsequently, the author assumed the core would remain up to a distance of 5.5 times B_j for consistency.

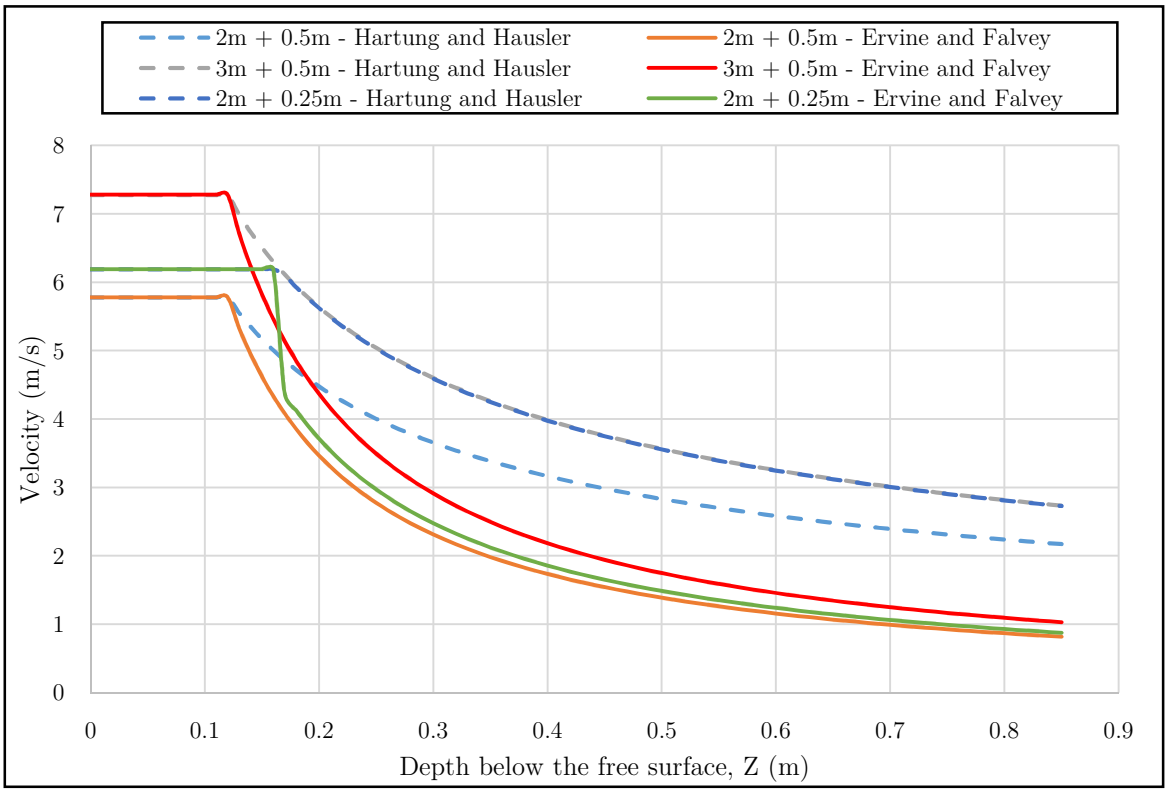

Figure 5-12 - Velocity decay for the different physical laboratory model configurations

It could be observed from Figure 5-12, that the velocity decay in the plunge pool did not change considerably change with the change in drop height, tailwater level, as well as discharge. There was, however, still a slight difference between the different model configurations used, which influenced the calculations when the quasi-steady impulsion method was used (see Section 5.2.3.2). A considerable disparity was visible, between the method proposed by Ervine and Falvey (1987) [21,125], as well as the approach by Hartung and Hausler (1973) [125,127], with the latter producing higher velocities as can be seen in Figure 5-12. The applicability of the different methods is further investigated in Section 3.3.2.1.3.

One important aspect to take into consideration, is that the velocity decay for the developed jets could not be calculated using the methods available in literature for this study. The methods proposed by Bohrer (1998) could be applied to developed jets, but were limited to certain criteria (limiting depth), which could not be satisfied by the model configurations, and the velocities calculated using the proposed method was much higher than the other methods (see Figure 5-11). Thus, only the velocity decay of the undeveloped jets could be determined. This subsequently meant that the velocity decay of the 4m drop height including 0.5m tailwater depth could not be determined.

5.2 Scour hole depth and extent calculation

5.2.1 Empirical formulas

The physical laboratory model properties, as outlined in Section 4, were used in empirical formulas to calculate the scour depths of the physical laboratory models. This study only included the scour depths as calculated from empirical formulas for reference and only two of the formulas were applied as was explained in Section 3.2. The formulas, as proposed by Veronese (1937) [86] (Eqn. 3-10) and Kotoulas (1967) [80] (Eqn. 3-11), were used. From initial inspection the formula, as proposed by Veronese (1937), presented scour depths that were much deeper than those of Kotoulas (1967) (refer to Table 5-6). A limiting equation of the Veronese (1937) equation (Eqn. 5-3) was, however, also available. It was developed for scour hole depth calculations, which were independent of particle size. Care should, however, be taken in using this formula, as it was developed for particle sizes smaller than 5mm [82].

$$y_s + y_o = 1.9H^{0.225}q^{0.54} \qquad \text{Eqn. 5-3}$$

Where:

H	=	Drop height (m)
q	=	Unit discharge ($m^3/s/m$)
y_0	=	Tailwater depth (m)
y_s	=	Scour depth (m)

It should be noted that the formulas, as proposed by Kotoulas (1967) and Veronese (1937), were developed for free falling jets impacting non-cohesive sediment beds, as is the case with most empirical formulas, and care must be taken when applying them to scouring of rock beds and in this study, when using PVC blocks.

Table 5-6 - Empirical formulas scour hole depth (y_S) results

Property	**Value**			
Discharge (Q)	20l/s			
Tailwater (y_0)	0.5m			0.25m
Drop height (including tailwater)	2m	3m	4m	2m
Author/formula	**Scour depth (y_s)**			
Kotoulas, (1967) (Eqn. 3-11)	0.24m	0.4m	0.53m	0.58m
Veronese, (1937) (Eqn. 3-10)	4.75m	5.5m	6.01m	5.42m
Veronese (limiting formula) (Eqn. 5-3)	0.08m	0.16m	0.21m	0.37m
Physical laboratory model scour depth (m)	0.155m	0.225m	0.145m	>0.35m

From Table 5-6 it is evident that larger scour depths occurred at higher drop heights (larger erosive capacity) and lower tailwater levels (lower energy dissipation capacity). The difference margin between the calculated scour depths using the empirical formulas and the physical laboratory model results, shown in Table 5-6, illustrated one of the major drawbacks in using empirical formulas, which is that the formulas explicitly perform satisfactorily in similar or the same setup conditions as which they were developed for. The formulas used in this study did not account for the condition of the jet at impact with the plunge pool free surface (undeveloped and developed). The depths, as calculated using the formula of Kotoulas 1967) and the original Veronese (1937) formula, overestimated the scour hole depths. The limiting formula, proposed by Veronese (1937), overestimated, as well as underestimated the scour depths. It was deduced that none of the proposed formulas were adequate at predicting the scour depths for the physical laboratory model conditions used. The depths, produced by the formula proposed by Kotoulas (1967), were, however, thought to be the most applicable and viable as the depths were slightly overestimated and compared the best.

5.2.2 Erodibility index method

The erodibility index method, as explained in Section 3.3.1, was used to calculate the scour depths, for the physical laboratory models configurations. The calculation of the erodibility index, stream power and scour depths is summarised in Sections 5.2.2.1 to 5.2.2.2.

5.2.2.1 *Erodibility index and required stream power*

Mass strength factor (M_s)

The UCS of the PVC blocks used to model the rock in the physical laboratory model was not physically determined. The mass strength factor could thus not be determined with certainty using equations Eqn. 3-16 to Eqn. 3-19 in Section 3.3.1.1. Five different mass strength values were, therefore, tested (refer to Table 5-7 and Appendix B) as to ascertain in which rock type the modelled PVC blocks fell. Using the scour depths, as calculated, from the physical laboratory models, the approximate stream power was calculated for each of the five rock types, from which the block type could then be determined (refer to Section 5.2.2.2).

Particle/block size factor (K_b)

To determine the particle or block size number, using Eqn. 3-20, both the rock quality designation (RQD) and joint set number (J_n) had to be determined first:

- The RQD was unknown for the PVC blocks. Using equations Eqn. 3-21 and Eqn. 3-22, the value of RQD could, however, be determined. Care should, however, be taken as Eqn. 3-22 was developed for blocks with a length larger than 0.1m, while the square PVC blocks had a side length of only 0.025m. Using the equations, a negative RQD value was calculated using a side length of 0.025m, which was incorrect. The prototype conditions would, however, represent very good quality rock as the length of the sound core of the rock core sample (core sections larger than 0.1m) would represent the total length of the core sample (uniform 1m rock blocks), thus representing an RQD value of 100 (maximum value). The PVC blocks were, thus, assumed to have an RQD of 100.
- The square blocks represented already broken up rock, with three joints sets, uniform in length, width and depth. From Table B-2 in Appendix B a joint set value (J_n) of 2.73 was subsequently assumed.

Having calculated both the values of RQD and the joint set number, the value of the particle or block size number could be determined using Eqn. A2-2 (refer to Table 5-7).

Interparticle bond strength factor (K_d)

The interparticle bond strength factor was calculated using Eqn. 3-24. For the square PVC blocks used to represent the rock bed, a joint alteration number (J_a) of 1 was assumed from Table B-4 in Appendix B. The joints of the PVC blocks were effectively in contact, with a joint separation of approximately 1mm. A joint roughness number (J_r) of 1 was assumed from Table B-3 in Appendix B, as the joints were assumed to be smooth planar. During the filling of the steel container with PVC blocks, it was found that the blocks did not form a completely planar joint network as originally thought. Stepping in the joint network occurred, due to the uneven shape of the masonry bricks, which caused the PVC blocks not to fit as perfectly, as was numerically calculated. To account for the non-planarity as well as the stepping in the joint network, the author proposed using a joint roughness number of 4.

The erodibility index and required stream power of both joint set numbers (1 and 4) were subsequently calculated for verification of the physical laboratory model scour hole depths, as the UCS of the PVC blocks was unknown. Both joint set numbers were used to illustrate the sensitivity of the EIM to the parameters pertaining to the erodibility index (EI).

Relative shape and orientation factor (J_s)

The relative shape and orientation factor was assumed as 1.14 from the Table B-6 in Appendix B. The packed square PVC blocks representing the rock bed, effectively had a 90-degree dip, vertically and a 0 degree dip, horizontally.

Erodibility Index (EI)

Having calculated all the required parameters, the erodibility index was calculated using Eqn. 3-15. The erodibility index for five different rock types is shown in Table 5-7. From Table 5-7 it was evident that the erodibility index is heavily dependent on the mass strength number, in addition to the particle or block size factor, as has been established by previous researchers, such as Annandale (2007) [36,96]. The EI is consequently heavily reliant on defining the correct geomechanical properties of the rock mass.

Table 5-7 - Erodibility index of different rock types

	Rock type				
Property	**Very soft**	**Soft**	**Hard**	**Very hard**	**Extremely hard**
M_s	3.3	13	26	106	280
RQD	100	100	100	100	100
J_n	2.73	2.73	2.73	2.73	2.73
K_b	36.6	36.6	36.6	36.6	36.6
J_r	1	1	1	1	1
J_a	1	1	1	1	1
K_d	1.00	1.00	1.00	1.00	1.00
J_s	1.14	1.14	1.14	1.14	1.14
Erodibility index (K_h) with $J_r = 1$	137.8	542.9	1085.7	4426.4	11692.3
Erodibility index (K_h) with $J_r = 4$	550.8	2169.6	4339.3	17691.0	46730.9

Having determined the EI, the required or critical stream power could be determined, which defines the threshold stream power using Eqn. 3-32 or Eqn. 3-33. As the erodibility index calculated was more than 0.1, Eqn. 3-33 was used to determine the required stream power. The required stream power for each of the different rock types, is shown in Table 5-8.

Table 5-8 - Required stream power

Rock type	Very soft	Soft	Hard	Very hard	Extremely hard
Stream power required with $J_r = 1$ (W/m^2)	40.22	112.46	189.14	542.67	1124.41
Stream power required with $J_r = 4$ (W/m^2)	113.69	317.90	534.64	1533.96	3178.36

From Table 5-7 and Table 5-8 it is evident that there is a large effect on the required stream power and the erodibility index, due to the interparticle bond factor and the mass strength factor. As there was still no clear indication as to which rock type or joint roughness number (J_r) value was the most applicable for the PVC blocks, the upper (extremely hard rock) and the lower (very soft rock) values were compared to find the most appropriate conditions that compared the best to the PVC blocks.

It should be noted that the geotechnical properties of the PVC blocks did not change with depth, which is generally not the case in prototype rock beds [18]. Due to the unchanging properties of the PVC blocks, a constant EI value could subsequently be applied over the full depth in the scour hole depth prediction.

5.2.2.2 *Applied stream power and scour depth*

As discussed in Section 3.3.1.2, there are two approaches available to calculate the applied stream power with depth, in the plunge pool, that takes into account the jet diffusion. Both the approaches used and the results, are discussed below for the physical laboratory model setup conditions.

(i) Approach 1

The first approach uses Eqn. 3-26, as was proposed by Annandale (2007), to calculate the stream power at different elevations below the plunge pool free surface. The approach uses the area of the jet, calculated using the outer area of the jet at impact with the free surface (see Table 5-4) and the lateral spreading

angles of the jet in the plunge pool (see Figure 5-4), to determine jet footprint at different elevations below the free surface of the plunge pool. The spreading angles of the jet in the lateral and longitudinal direction in the plunge pool were assumed equal. The stream power calculated was then subsequently plotted against the threshold stream power, as was determined in Table 5-8 and is shown graphically in Figure 5-13. The black dots in Figure 5-13 indicate the critical scour depths, which is defined by interception points between the threshold stream power and the applied stream power.

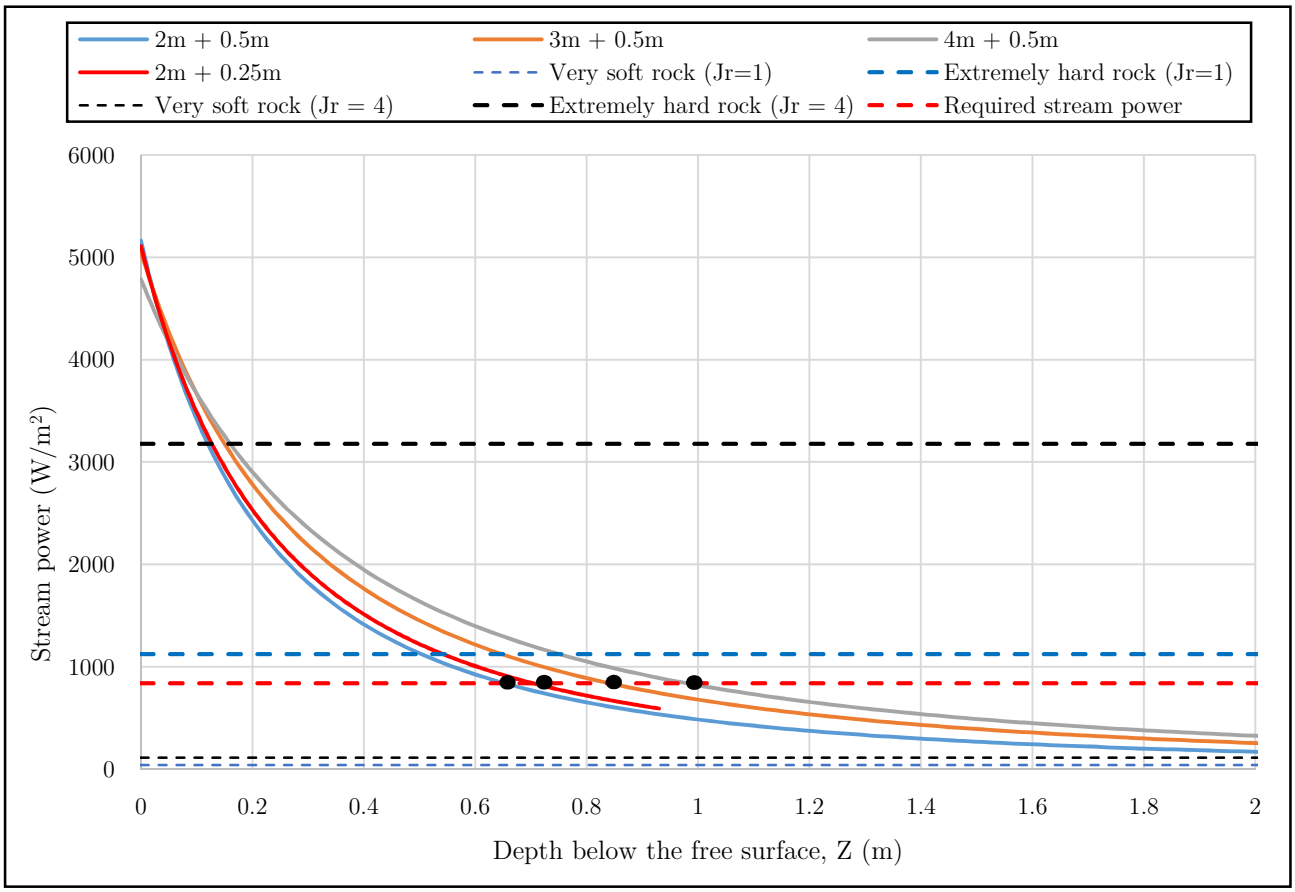

Figure 5-13 - Comparison between stream power and scour threshold (Approach 1)

The type of the rock had a significant effect on the scour threshold, as can be seen from Figure 5-13. Due to the EIM's dependence on the spreading of the jet in Approach 1, accurate estimation of the spreading angle is paramount. Due to the UCS of the PVC blocks being unknown, it was proposed using the physical laboratory model's scour depths, as shown in Table 4-9, to determine the most suitable rock type. Using the depths in Table 4-9, it was found that the stream power required to produce the scour depths, ranged between 840 – 1305 (W/m^2), using Figure 5-13. As a conservative approach, the lower value of 840(W/m^2) was used to ensure that the scour hole depth was not underestimated. The PVC

blocks were thus representative of very hard to extremely hard rock with a mass strength number of 190 when $J_r = 1$ and 47 when $J_r = 4$, which is representative of hard to very hard rock. The new required stream power that was applied (840 W/m^2), is indicated with the red dashed line in Figure 5-13. Having calculated the most suitable rock type for Approach 1, the estimated scour depths, using the EIM, are shown in Table 5-9. It should be noted that the depths given in Figure 5-13 were determined from the free surface level of the plunge pool. To determine the scour depths as given in Table 5-9 the respective tailwater depths were subtracted.

Table 5-9 - Scour depths (Approach 1)

Property	Value			
Discharge (Q)	20l/s			
Tailwater (y_0)	0.5m			0.25m
Drop height (including tailwater)	2m	3m	4m	2m
Scour depth (y_s) (m) (EIM Approach 1)	≈0.16m	≈0.35m	≈0.49m	≈0.46m
Physical laboratory model scour depths (m)	0.155m	0.225m	0.145m	>0.35m
% difference	3%	56%	238%	-

As a conservative value of the mass strength number (M_s) was applied, the calculated scour depth values in Table 5-9 were found to be higher than the scour hole depths found in the physical laboratory model.

To compare the scour depths calculated using EIM Approach 1 and the physical laboratory model depths, a percentage difference was calculated, as shown in Table 5-9. The 4m drop height showed the highest percentage difference, which was thought to be due to the formula (Eqn. 3-26), used to calculate the stream power, not taking into account the developed nature of the jet, thus causing a gross overestimation of the scour depth. Approach 1 is also highly dependent on calculating the correct spreading angles.

(ii) Approach 2

The second approach used Eqn. 3-28 to Eqn. 3-31 and the pressure coefficients, as calculated in Section 5.1.3.1, to calculate the stream power at different elevations below the plunge pool free surface. The stream power calculated was consequently plotted against the threshold stream power, as was determined in Table 5-8 and is shown graphically in Figure 5-14.

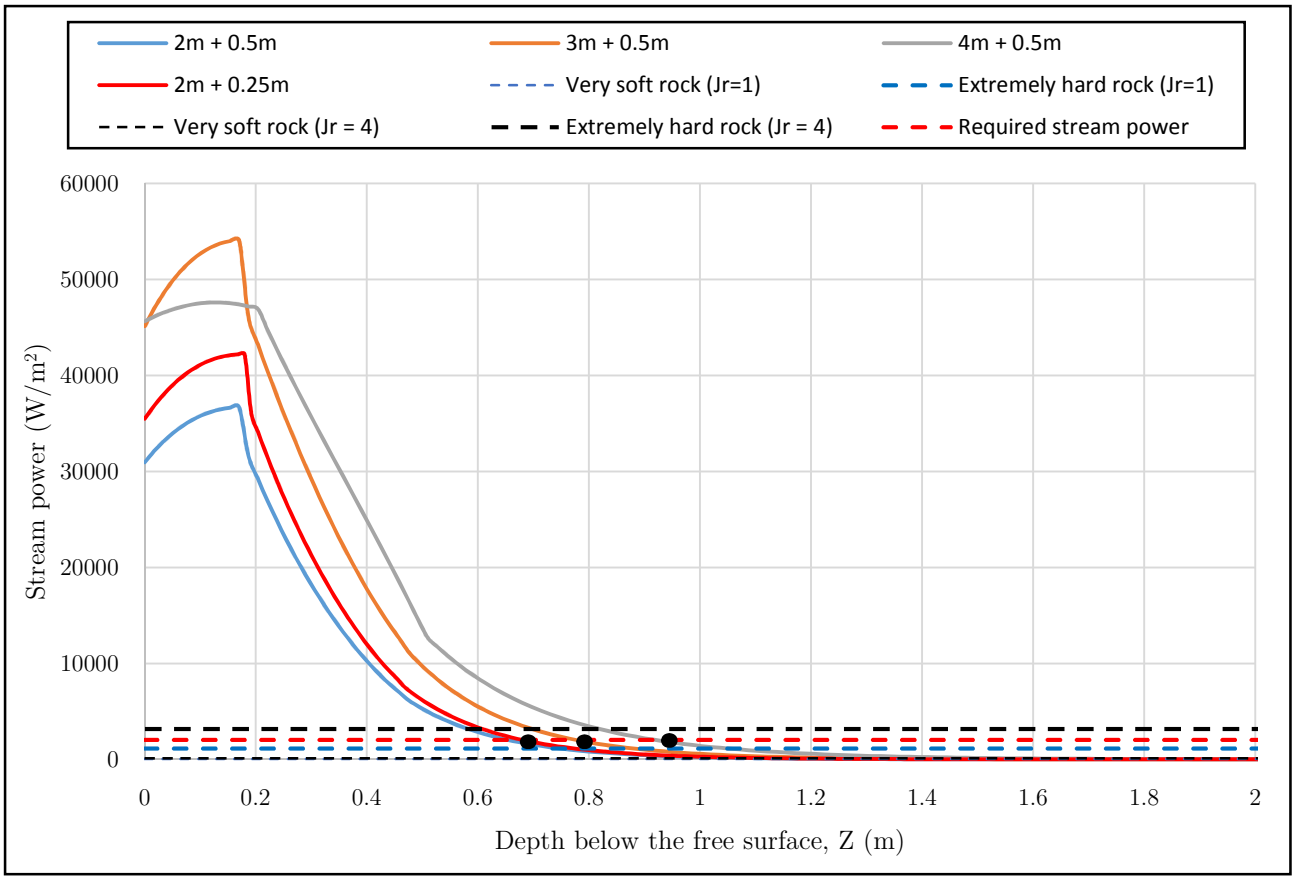

Figure 5-14 - Comparison between stream power and scour threshold (Approach 2)

A similar method to the one applied in Approach 1 was adopted to calculate the rock type in Approach 2. The physical laboratory model scour depths in Table 4-9 were used to determine the stream power required. A stream power required of between 2020 – 6902 (W/m^2) was calculated using Figure 5-14. As a conservative approach, the lower value of 2020 (W/m^2) was used to ensure that the scour hole depth was not underestimated. The PVC blocks were representative of extremely hard rock (refer to Table 5-7) with a mass strength number of 152 when $J_r = 4$. For $J_r = 1$. None of the proposed rock types provided the required resistance to correspond to the scour depths calculated in the physical laboratory model and a Ms number of more than 280 for the PVC blocks was unrealistic. The red dashed line in Figure 5-14 illustrates the adopted critical stream power of 2020 W/m^2. Having calculated the most suitable rock type, the estimated scour depths using the EIM, were calculated and are shown in Table 5-10.

Table 5-10 - Scour depths (Approach 2)

Property	Value			
Discharge (Q)	20l/s			
Tailwater (y_0)	0.5m			0.25m
Drop height (including tailwater)	2m	3m	4m	2m
Scour depth (y_s) (m) (EIM Approach 2)	≈0.16m	≈0.28m	≈0.43m	≈0.44m
Physical laboratory model scour depths (m)	0.155m	0.225m	0.145m	>0.35m
% difference	3%	25%	197%	-

The applied stream power for the 4m drop height, including 0.5m tailwater depth, followed a different pattern to the other setup conditions as can be seen in Figure 5-14. As the jet was highly developed at impact for the 4m drop height the values of the mean dynamic pressure coefficient (C_{pa}), as depicted in Figure 5-5, were significantly lower, which in turn directly influenced the applied stream power calculated in Approach 2, which caused the difference in stream power profile.

As for Approach 1, a percentage difference was calculated to compare the scour depths. The 4m drop height showed a significant percentage difference, which was also thought to be due to the formula used (Eqn. 3-31), not taking into account the developed nature of the jet, as was also found to be the case in Approach 1.

The calculated applied stream power from Approach 2 (see Figure 5-14), was significantly higher than the applied stream power from Approach 1 (Figure 5-13), at lower depths, but lesser than Approach 1 at deeper depths. Even though the applied stream power varied quite significantly between the two approaches, the calculated scour depths were very similar (see Table 5-9 and Table 5-10). Heed should, however, be taken, as the mass strength number of the PVC blocks varied significantly between the two approaches, with the second approach having rock with a much larger mass strength number than for Approach 1 and the second approach only being applicable to stepped joints (Jr = 4). This illustrated the importance of identifying the correct geotechnical properties of the rock mass when using the EIM and the sensitivity of the method to the properties of the rock mass.

Comparing the scour depths in Table 5-9 and Table 5-10 to the scour depths calculated from the physical laboratory model, the calculated depths compared relatively well, but for the 4m drop height including 0.5m tailwater depth test, the depth was much larger than that of the physical laboratory model. It

should be noted that the physical laboratory model scour hole depths were used to calibrate the mass strength and the subsequent scour hole depth and the values could thus not be compared. As the actual scour depth of the 2m drop height including 0.25m tailwater was unknown for the physical laboratory model, its depth could not be compared to that of the EIM.

5.2.3 Comprehensive scour model (CSM)

The results, as calculated using the CSM method, which include the dynamic impulsion method (DI) and the quasi-steady impulsion method (QSI), are summarised in Sections 5.2.3.1 and 5.2.3.2 respectively. The CFM method was not applied, as the rock mass already comprised of a fully formed mass joint network. As the CSM was developed for prototype conditions, the applicability of using the method on the small scale model was questionable, but due to the physical laboratory model being developed from hypothetical prototype conditions and the only results being model scale based, the model scale conditions were used in the scour hole analysis. The CSM was additionally developed for undeveloped circular jets with a breakup-up length ratio (H/L_b) of 0.5, which was far less than the break-up length ratios as calculated for the physical laboratory model conditions (see Table 5-2). In addition, the jets of the physical laboratory model were rectangular rather than circular, as was used to develop the CSM [36]. The reason for applying the QSI method in this study was because, the method was the only approach found to study the extent of scouring, due to the wall jets. The QSI method could also be used to verify the velocities in the scour hole of the CFD model to determine if the ultimate scour hole was reached during the physical laboratory model tests (see Section 6). At the centreline of the jet, the DI method was used to determine the depth of scouring, due to the uplift of the PVC blocks, as the QSI method is only applicable outside the impingement region.

5.2.3.1 *Dynamic impulsion method (DI)*

The dynamic impulsion method was applied to determine the scour depths at the centreline of the jet using Eqn. 3-78 to Eqn. 3-100, as discussed in Section 3.3.2.2.3. The time interval ($\Delta t, pulse$), over which a pulse acts to lift the rock block out of the rock bed, was calculated using Eqn. 3-79 and is shown in Table 5-11. A wave celerity (c_{mix}) of 100m/s was assumed for this study, as proposed by Bollaert (2002)

in previous studies and the total length of the joint under the rock (fracture length (L_f)) was determined using Eqn. 3-81 [36].

Table 5-11 - Time interval of pulse

Property	Value
Wave celerity (c_{mix})	100m/s
Fracture length (L_f)	0.075m
Time interval ($\Delta t, pulse$)	0.0015s

In determining the dynamic impulsion, the effect of interlocking and shear forces was ignored. The assumption of ignoring the interlocking and shear forces was conservative, as the forces aid in resisting uplift, but the main reason for ignoring the forces was that the forces were not measured to give an indication to their magnitude. From the physical laboratory model there was a clear indication that shear and interlocking between the blocks were present in areas where the blocks were tightly packed, but in other areas, due to the loose packing of the blocks, null to insignificant shear and interlocking forces were thought to be present. Only the resisting force, due to the submerged weight of the PVC blocks, was subsequently considered and was calculated using Eqn. 3-94. The density of the PVC blocks was determined as 1152kg/m^3 (Table 4-3) and the density of water was assumed as 1000kg/m^3.

As the dynamic impulsion coefficient (C_I) equation was developed for undeveloped jets (Eqn. 3-92), the DI method could only be applied to the physical laboratory model cases where the jet was undeveloped at impact with the plunge pool free surface (see Table 5-2). The dynamic impulsion coefficients, at different Y/D_j ratios, were calculated using Eqn. 3-92. Furthermore, the jets in the physical laboratory model were rectangular, while the coefficient was developed for circular jets.

The value of the diameter at impact (D_j) in the Y/D_j ratio was taken as the impact thickness (B_j) when calculating the values of C_I. Uplift was said to occur when the vertical height through which the block was lifted (h_{up}) was equal to the height of the block (z_b). Bollaert (2002) [36,96] suggested that a ratio of h_{up}/z_b bigger than 0.25 indicated scouring. Due to the tightly packed nature of the PVC blocks in the steel container, it was assumed that uplift will occur only when the ratio is equal to one, or when the block is lifted though the height of the block, rather than using the proposed ratio of h_{up}/z_b bigger than 0.25. Due to the equation of C_I being restricted to a ratio Y/D_j value of 17, the full extent of scouring

could originally not be determined due to the ratio of Y/D_j being larger than 17 for the physical laboratory model conditions. To overcome this limitation, it was proposed that an exponential function be superimposed on the original function to determine a potential fit for values of C_I larger than 17. The trendline function in Excel was used to determine the potential fit exponential function using the values calculated from the original function proposed by Bollaert (2002) (Eqn. 3-92). The function was, however, developed for a ratio of Y/D_j larger than 15 and not up to 17, as the value of C_I started to flatten out at Y/D_j >15. The new function was then used to crudely estimate the values of C_I for the ratio of Y/D_j larger than 15 and Eqn. 3-92 was used to estimate the values of CI for the ratio of Y/D_j smaller than 15. The proposed formula is shown in Eqn. 5-4 and is graphically represented in Figure 5-15.

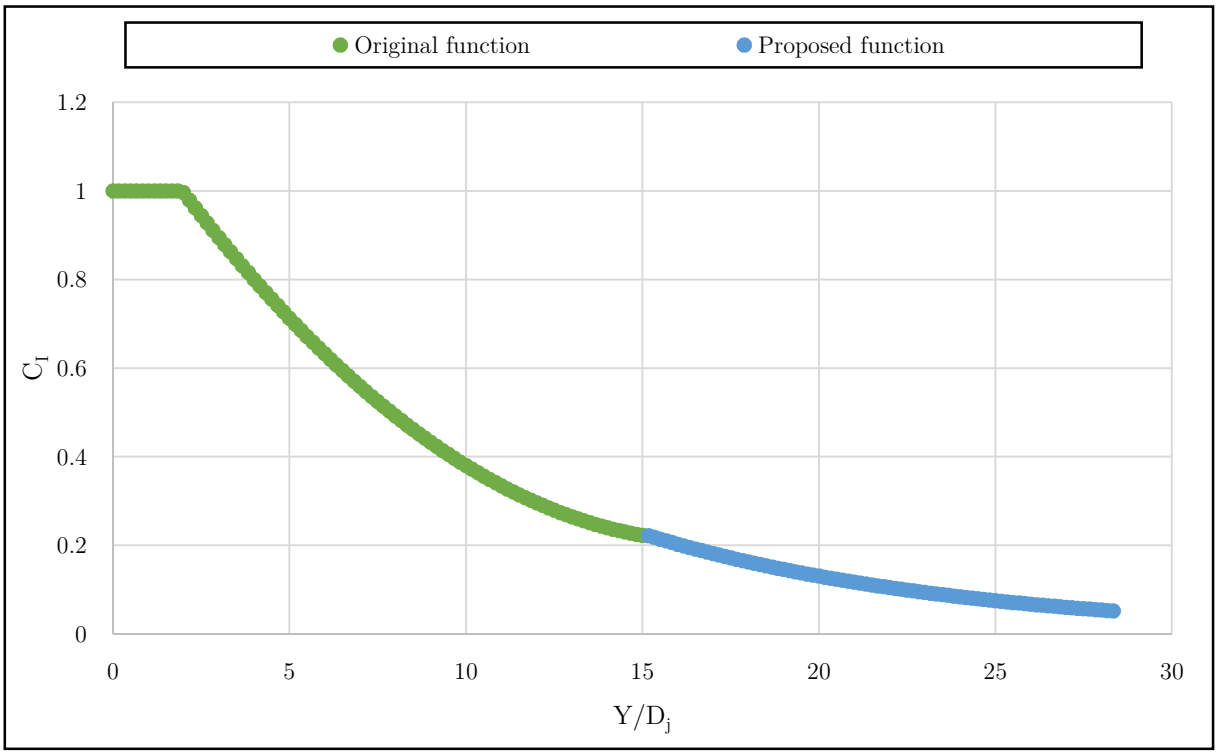

Figure 5-15 - Proposed function for C_I values of $Y/D_j > 15$

$$C_I = 1.2028e^{-0.114\left[\frac{Y}{D_j}\right]} \quad for\ Y/D_j > 15 \qquad \text{Eqn. 5-4}$$

The calculated scour depths using the DI method is shown in Table 5-12. For the 4m drop height, including 0.5m tailwater, the scour depth was not determined, as the DI method is only applicable to undeveloped jets and not developed jets, as is the case for the 4m drop height.

Table 5-12 - Scour depths using DI method

Property	Value			
Discharge (Q)	20l/s			
Tailwater (y_0)	0.5m			0.25m
Drop height (including tailwater)	2m	3m	4m	2m
Scour depth (y_s) (m) (DI method)	0.15m	0.28m	-	0.44m
Physical laboratory model scour depths	0.155m	0.225m	0.145m	>0.35m
% difference	3%	24%	-	-

The values of the scour depths in Table 5-12, as calculated using the DI method, compared favourably to the scour depths as calculated for the physical laboratory model in Table 4-9. The DI method produced scour holes, which were deeper than the physical laboratory model results (3 – 24% deeper) and more conservative. Due to the very good comparison in results, the potential fit of the C_I values for $Y/D_j >$ 15, as proposed by the author, was thought to have been adequate for this study.

5.2.3.2 *Quasi-steady impulsion method (QSI)*

The scour hole extent was calculated for all the relevant physical laboratory model configurations (undeveloped jets only) using the quasi-steady impulsion method. Eqn. 3-101 to Eqn. 3-117, as discussed in Section 3.3.2.2.3, were used to determine the scour hole extent. As the velocity decay in the plunge pool, as well as the methods to calculate the wall jet, was dependent on the fact that the jet needed to be undeveloped at impact with the plunge pool free surface, the QSI method could only be applied to the physical laboratory model cases, which had an undeveloped jet at impact with the plunge pool free surface.

The velocity decay, as was calculated in Section 5.1.3.2, was used in the determination of the wall jet velocities using the approach discussed in Section (ii). For comparison, the author plotted the scour hole profiles (shape and depth) as produced from the different velocity decay methods are plotted in Figure 5-16. The velocity decay profiles calculated using the approaches of Ervine and Falvey (1987), and Hartung and Hausler (1973), as calculated in Section 5.1.3.2, were initially considered in the calculation of the scour hole profiles (shape and depth). However, the velocity decay profile using the approach proposed by Hartung and Hausler (1973), produced unrealistically large scour hole profiles (shape and depth) and required underestimation of the net uplift coefficients to produce reasonable scour hole profiles

(shape and depth). When using the velocity decay approach as proposed by Beltaos and rajaratnam (1973), discussed in Section 5.1.3.2, the scour hole was largely underestimated, depicted in Figure 5-16, and the approach was therefore not considered. Subsequently, the velocity decay profiles were calculated by using the approach proposed by Ervine and Falvey, as the scour hole profiles (shape and depth) compared substantially better to those produced in the physical laboratory model tests.

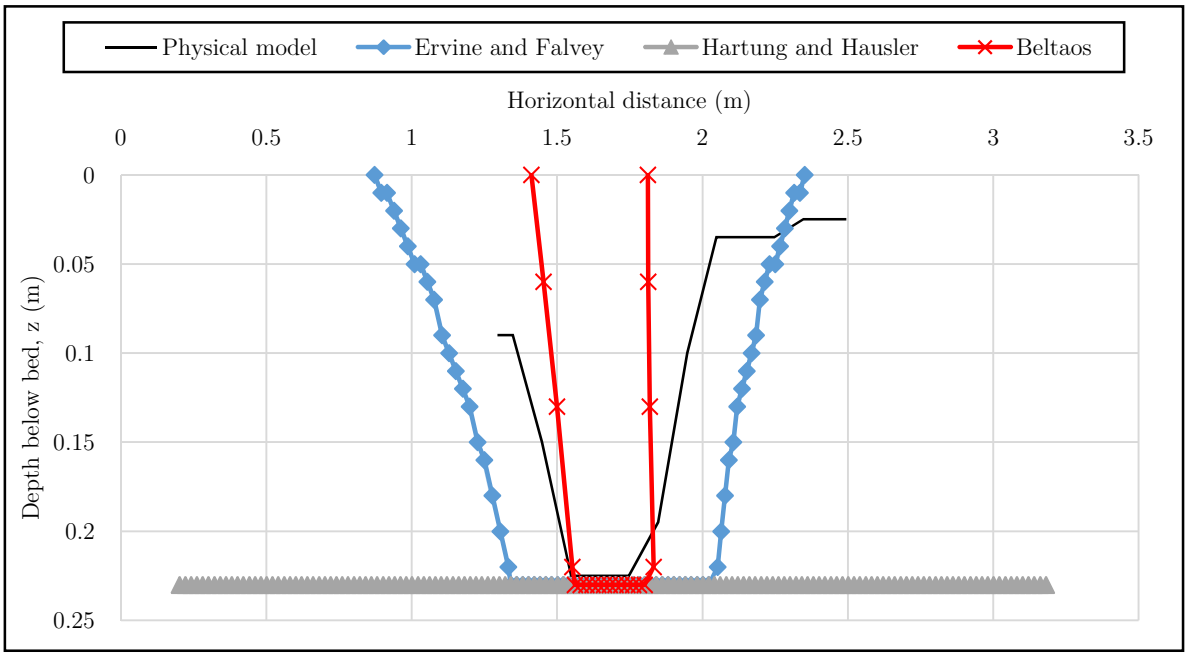

Figure 5-16 - Scour profile produced from different velocity decay methods (3m drop height and 0.5m tailwater)

Due to the symmetrical nature of the scour holes produced from the physical laboratory model, a symmetrical (50%) distribution was assumed between the upstream and downstream wall jet thickness, instead of using the impact angles, determined in Table 5-1, to calculate the upstream and downstream wall jet thicknesses through interpolation. The wall jet velocities were calculated using Eqn. 3-115.

In the determination of the net uplift coefficient (C_{uplift}), the author determined the scour hole profiles (shape and depth) using various net uplift coefficients, which were determined from the characteristic block uplift profiles from the physical laboratory model, as shown in Figure 5-18, which were calculated from Table 3-28. Due to the equal shape of the PVC blocks, as well as the packed block structure having very low to no block protrusions affecting the flow, the net uplift coefficients proposed were reasonably small.

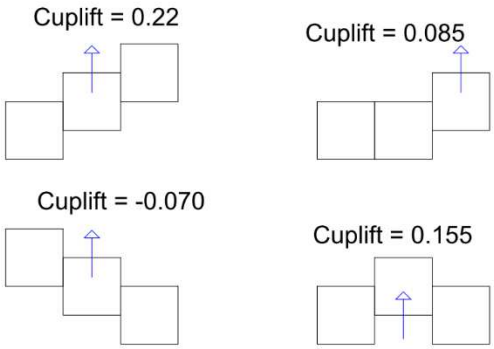

Figure 5-18 - C_{uplift} of characteristic block uplift profiles of physical laboratory model

Plotting the calculated scour hole profiles (shape and depth) against the profile determined from the physical laboratory model, the most appropriate net uplift could be determined (see Figure 5-17). As can be seen from Figure 5-17, the net uplift coefficient of 0.1 produced scour hole profiles (shape and depth), which compared the best to those found in the physical laboratory model tests.

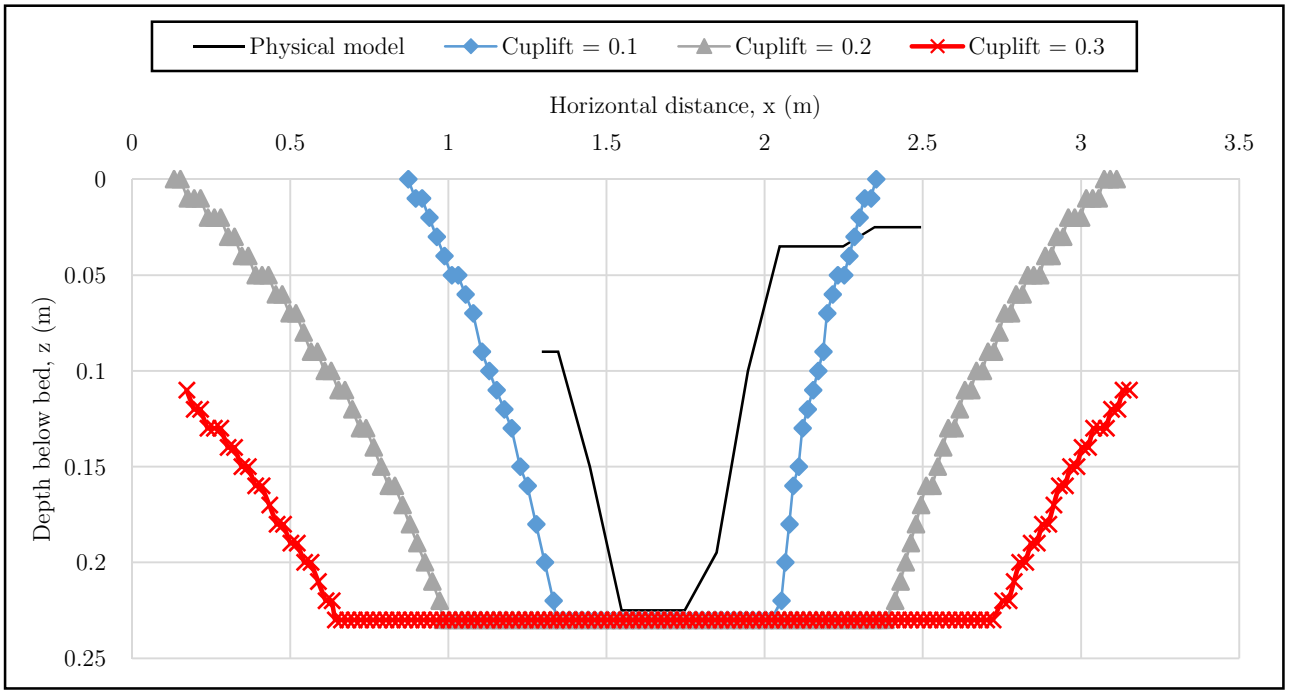

Figure 5-17 - Scour hole profiles (shape and depth) calculated using C_{uplift} of 0.1, 0.2 and 0.3 (3m drop height and 0.5m tailwater)

Bollaert [125] suggested using a grid size of between 1m and 10m for the horizontal plane segments and 0.25m to 1m for the vertical plane segments, as the computations are completed in a grid like fashion (see Section (ii)). Due to the small-scale test, these values could not be used and values of 0.01m for the vertical plane and 0.02m for the horizontal plane were used instead. Uplift of the blocks was said to occur when the quasi-steady uplift force on the blocks was higher than the submerged weight of the blocks,

which was calculated as being 0.023N, using the density of the PVC blocks as calculated in Table 4-3. The scour depth values at the impingement zone were taken as those calculated using the DI method, as shown in Table 5-12, as the QSI model exclusively determines the scouring, due to the wall jet, which is beyond the impingement region. As the method is quasi-steady, no time step is applied. The calculated scour hole profiles (shape and depth), using the quasi-steady impulsion method and the DI method, are shown graphically in Figure 5-19 (a-c), in conjunction with the scour hole profiles produced from the physical laboratory model.

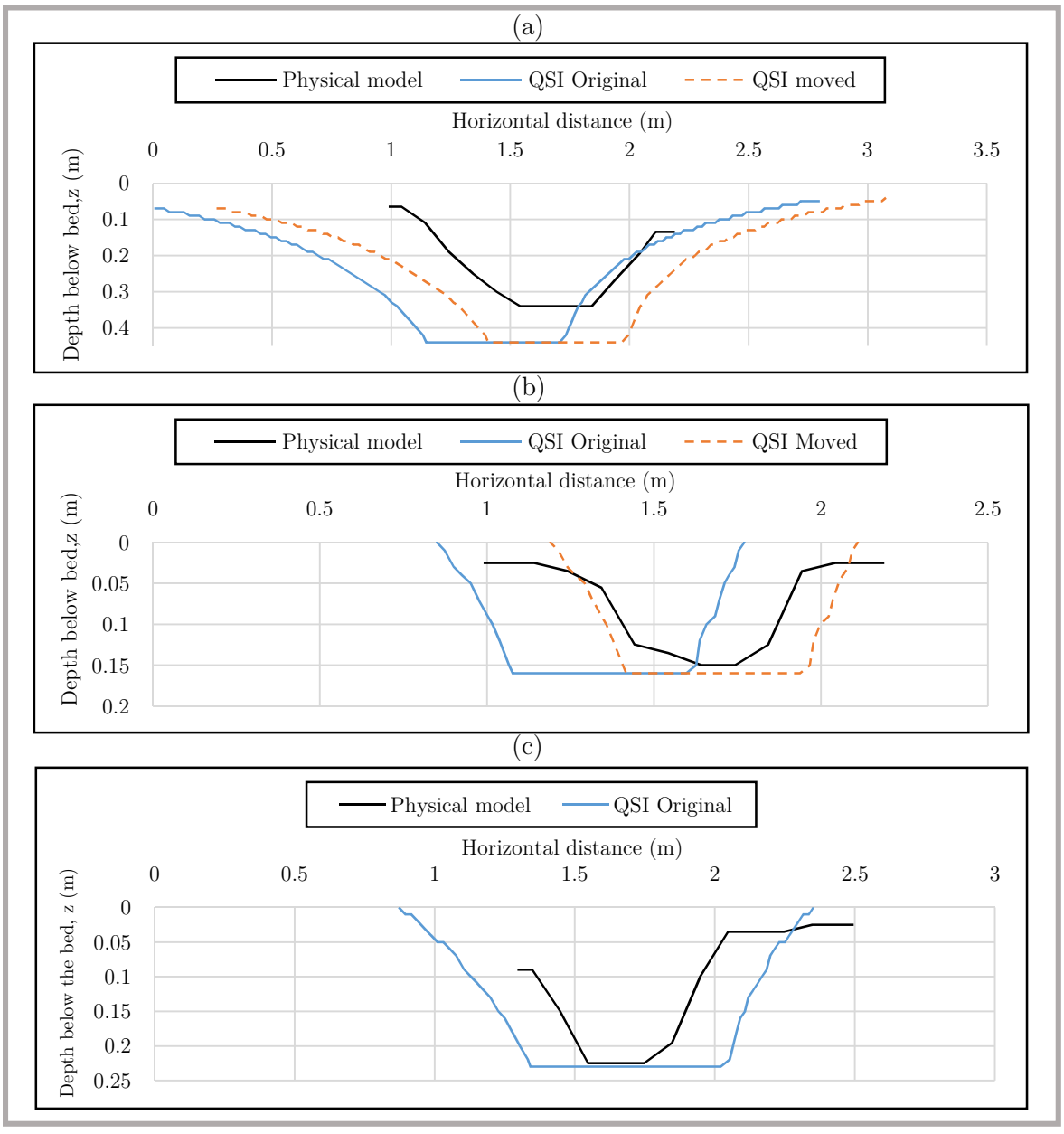

Figure 5-19 - Scour hole profiles (shape and depth) determined using the QSI and DI methods for:
a) 2m drop height including 0.25m tailwater
b) 2m drop height including 0.5m tailwater
c) 3m drop height including 0.5m tailwater

The scour holes produced using the QSI and DI methods compared relatively well to those of the physical laboratory model, as shown in Figure 5-19 (a-c). For the 2m drop height (including tailwater of 0.25m and 0.5m) cases, the calculated scour holes were observed to be displaced to the left of the location of the scour holes of the physical laboratory model. The displacement might have been to be due to the QSI method being dependant on correctly determining the horizontal distance at impact, as well as presuming the jet follows the same angle in the plunge pool as the angle at impact, as was proposed by Bollaert (2014) [125]. As the scour holes calculated were located closer to the issuance structure, it was assumed that the displacement was conservative, as the likelihood of endangering the foundations due to regression was higher.

As the scour hole location calculated from using the DI and QSI methods did not correspond to the physical laboratory model, the position of the calculated scour hole was repositioned 0.3m upstream (QSI moved - Figure 5-19). The repositioning was done to better correlate to the physical laboratory model results and for comparative purposes. Further investigations into the position of the scour hole are included in Section 6.5.1.3.

For the 3m drop height (including tailwater), the scour hole was located similarly to that of the physical laboratory model. Each of the scour hole profiles (shape and depth) compared relatively well to the physical laboratory model. In general, the author found that the QSI and DI methods performed relatively well in predicting the scour hole profiles (shape and depth). As the position of the scour hole correlated favourably with the physical laboratory model, the position of the scour hole for the 3m drop height was not adjusted.

Due to the large difference in the velocity decay profiles of the different methods, as well as the dependence of the QSI method on the velocity decay profile and subsequent wall jet velocities, the author proposed that the velocity required to uplift the blocks, using the QSI method, be used to verify if the scour hole profiles (shape and depth) used in the CFD models reached their equilibrium stage of scouring. The velocity required to uplift the PVC blocks was calculated using a net uplift coefficient of 0.1 and the submerged weight of the PVC blocks, which is shown in Table 5-13.

Table 5-13 - Velocity required to uplift block using QSI method

C_{uplift}	**Velocity required**
0.1	0.86m/s

The required velocity (Table 5-13) was compared to those calculated in the CFD models as discussed in Section 6.5.

5.3 Summary

The EIM and empirical formulas overestimated the scour hole depth in comparison to the physical laboratory models. Both the empirical and semi-empirical EIM did not account for the developed jet for the 4m (0.5m tailwater) dropheight.The EIM is also sensitive to both the mass strength number and the joint set number. The accuracy of the method depends heavily on determining the correct geotechnical properties of the rock mass.

The CSM (DI and QSI) overestimated the scour hole profile (depth and extent), but the shape of the scour hole compared well with the physical laboratory model scour hole shapes.

In summary, the current preferred scour hole prediction methods can be used with relative success to determine a conservative scour hole profile (depth and extent). The use of the current predictions methods for use in small-scale physical laboratory conditions was also confirmed.

6 Computational fluid dynamics simulations of the hydraulics of a rectangular plunging jet with the boundary conditions of physical laboratory model

Computational fluid dynamics (CFD) solve the fluid flow and the associated phenomena numerically, and should be used in conjunction with physical laboratory models or prototype cases for verification and calibration [2,175]. Physical laboratory models can form the basis on which the CFD modelling is based, as was done in this study, and vice versa.

This section contains the results of the CFD simulations using the scour holes determined from the physical laboratory model and the calculated profiles using the physically based methods (CSM including QSI). The simulated hydrodynamic properties of the rectangular plunging jet was compared with the empirically calculated values in Section 5 to determine if CFD simulations can be used as an alternative.

CFD codes; ANSYS FLUENT and FLOW-3D, were originally considered in conjunction with distinct element codes such UDEC for this study. Distinct element codes can be used for the simulation of a discontinuous or broken up rock mass, as the CFD codes are not capable of simulating the rock scour mechanisms. ANSYS FLUENT was used in this study, as it was readily available, as opposed to FLOW-3D that had to be purchased and ANSYS FLUENT had been used on similar studies. Due to the physical mechanisms of rock scouring being very complex, the use of empirical and physically based methods were used in this study instead of distinct element codes in [171]. Pertaining to more information regarding FLOW-3D [2,3,161,162,163,164,165] and distinct element codes [93,166,167,168,169,170] as well as their capabilities, other literature should be consulted.

6.1 Similar studies

Various researchers, as shown in Table 6-1, have used CFD and other mathematical codes, such as MATLAB, to simulate scour processes and the hydrodynamics of water jets. Similar studies are summarised in Table 6-1 as found in literature.

Table 6-1 - Similar CFD studies

Author	Simulation description
Karim and Ali (2002) [171]	Simulation of submerged turbulent horizontal jets using FLUENT to determine the validity of using FLUENT to simulate the flow patterns of turbulent flow.
Johnson and Savage (2001)[172]	Simulation of flow over an ogee spillway using FLOW-3D examining the pressure distribution and discharge characteristics.
Adduce and Sciortino (2006) [173]	Simulation of submerged horizontal turbulent jets scouring sediment beds using numerical methods. Mathematical models were developed that can be used in CFD packages.
Boroomand *et al.* (2007) [190]	Simulated submerged horizontal offset jets using FLUENT and sediment transport was modelled using a movable mesh.
Avila *et al.* (2008) [195] and Avila [139]	Simulation of scouring of non-cohesive sediment in catch basin sumps due to a vertical water jet using FLOW-3D and FLUENT.
Chanel and Doering (2007) [193]	Spillway modelling using FLOW-3D to check the validity of using CFD to simulate flow over a spillway in terms of the flow profile, velocities and pressures and comparing it to physical laboratory models.
Dey and Eldho (2009) [13]	Simulation of multiple vertical offset jets and scouring in sediment beds using FLUENT.
Neyshabouri *et al.* (2003) [75]	Numerical simulation of a free falling jet and scouring of a sediment bed.
Dasgupta *et al.* (2011) [174]	FLUENT and UDEC simulation of rock scouring at Kariba dam.
WenXin *et al.* (2011) [148]	Submerged 2D vertical jet numerical simulation and scouring of a sand bed.
Kamanbedast and Aghamajidi (2013) [175]	Simulating the length of the jet issuing from a ski jump using FLOW-3D.
Jia *et al.* (2001) [76]	Simulation of a plunging jet and the scour process of loose bed material (sediment) using CCHE3D.
Epely-Chauvin *et al.* (2014) [176]	Simulation of plunge pool scour evolution in non-cohesive sediment due to plunging jets using FLOW-3D.
Weidner (2012) [177]	FLUENT was used to simulate the erosion of a cohesive sediment bed due an undeveloped submerged water jet.

6.2 Limitations and advantages of using CFD

CFD, as with any other modelling technique, has certain limitations and advantages of which some, as found in literature, are summarised below [183,208].

6.2.1 Limitations and risks of CFD

The limitations and risks of using CFD are namely:

- The solutions of CFD are only as accurate as the set of governing equations, adjustable parameters and predefined boundary conditions they are based on.
- For accurate simulation of the problem the initial and boundary conditions are very important to input correctly as the mathematical solution methods in CFD are very sensitive to the boundary and initial input values [183].
- Simplifications of the problem as well as parameter and model assumptions are still required in CFD to overcome computational demand [2,195].
- There are limitations in the available models to simulate the physical or real conditions [195].
- Numerical simulations generally go hand in hand with some numerical errors such as round-off and truncation errors. Round-off errors cannot be avoided due to the finite word size (number of digits) available on computers. The truncation errors are due to numerical model approximations and can be reduced or avoided by refining the mesh.
- The construction of the grid can take up large amounts of time when simulating complex problems to ensure accurate simulation of the problem. There is a direct relationship pertaining to the time spent on CFD models and the experience of the modeller or engineer. It should also be noted that there is a direct correlation between the increase in complexity of the problem and the engineering expertise required to solve the problem as well as solving or understanding the errors that may arise [178].
- The accuracy of the solution depends on the grid resolution.
- CFD is still not capable of representing or mimicking the turbulent flow patterns in most cases realistically. It can, however, give an indication of the mean dynamic pressures [74].

- CFD software still has limitations in accurately modelling the velocity gradients in the boundary layer (water/solid interface) which is critical in scour estimation [2].
- CFD software is limited to only analysing simplified phenomena for which it has the mathematical equations. User defined functions do, however, allow the user to input equations for which the software does not have the built-in mathematical equations to analyse more complex problems.

The above risks and uncertainties become more pronounced when no experimental or similar simulations are available for comparison or validation [195].

6.2.2 Advantages of using CFD

The advantages of using CFD are namely:

- Numerical simulations generally have a small timeframe and a low cost in comparison to physical laboratory models. The calculation and modelling time of CFD should, however, be taken into consideration as it consumes considerable amounts of time for complex problems.
- Physical laboratory models require expensive and sophisticated measuring instrumentation for turbulent flow, which is not the case in CFD. Most CFD software has appropriate turbulent models and monitoring can be applied to the appropriate areas of interest with relative ease. Information regarding the fluid flow can be extracted without impeding the fluid motion at any location in the simulation domain [171].
- There are physical laboratory model data of several different types and in large quantities available in literature for the validation of various CFD simulations.
- CFD has enormous numerical simulation potential and room for improvement with the advancements in computer potential. Various different geometries, boundary conditions as well as design options, can furthermore be simulated with relative ease [171].
- CFD allows prototype scale models to be simulated, thus real scale models can be simulated and are thus not subject to scale effects as with physical laboratory models [179,180].

Due to the developments in computational power, CFD simulations have become a promising alternative to physical laboratory model studies; but nonetheless, they require calibration and verification using physical laboratory model or prototype studies. In the case of rock scouring the understanding of the

scouring processes is, however, very limited and is tailored to equations as discussed in Section 3 [3]. CFD models can nevertheless aid in the modelling of the hydraulic processes of the plunging jet in the air and plunge pool, as was done in this particular study.

6.3 Ansys FLUENT Background

ANSYS FLUENT is a general-purpose code, which has a comparably low cost, good software support, excellent user interface (GUI) in addition to being flexible (allows for user-defined functions). ANSYS FLUENT was originally not intended for open channel flow simulations, but has been adapted to handle open channel simulations and could therefore be used in this study [2]. A summary of the CFD modelling procedure is shown in Figure 6-6.

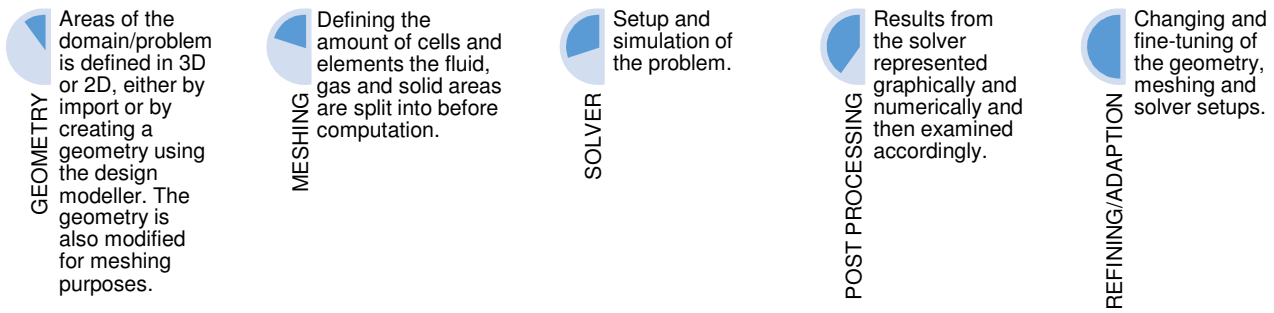

Figure 6-1 - CFD modelling process

Before the above steps are attempted, the problem needs to be well defined and a domain needs to be identified from a physical laboratory model or prototype case. For this study the physical laboratory model configurations, as defined in Section 4, served as the basis from which the CFD models were created. ANSYS FLUENT v16 was used in this study.

6.3.1 Geometry

The first step in the CFD modelling process is to create the geometry (2D or 3D), which needs to be defined correctly, as it represents the shape of the flow domain and its extent to be solved by the CFD solver. Geometry files can be imported into the design modeller from software such as AutoCAD or can be created in the design modeller itself, which is the CAD package of ANSYS Workbench. Before the domain can be meshed, the geometry needs to be modified appropriately to ensure the different fluid and

solid regions are quantified correctly. The geometry should be simplified at the boundaries, where possible, to avoid unnecessary complexities. After the necessary geometry modifications have been completed, the design modeller can be used to create the surfaces and in turn create the respective bodies and parts required for meshing.

It is extremely important to allow large enough portions upstream and downstream of the area of interest, in the fluid flow domain, to avoid boundary effects and to ensure any inadequacies in the fluid flow (flow lines) are smoothed out [2]. 2D CFD models can be used as an initial approach to identify relevant parameters, as well as the capabilities and limitations of 2D modelling. 3D CFD models, on the other hand, are calibrated and validated from experimental data and can be used to model the scenarios that were not able to be modelled physically [195]. 3D models also simulate fluid motion in all directions and capture flow patterns, while 1D and 2D models do not capture flow in all the directions [181].

The empirically based methods used to determine the hydrodynamic parameters of the plunging jet for this study, such as the diffusion of the jet, were developed for 2D (refer to Section 3.3). 2D CFD models were subsequently proposed for comparative purposes. As a number of various model configurations were tested, as shown in Table 4-1 in Section 4, the use of 2D models was also preferred, as 3D models have significantly higher computational cost. It should be noted that possible confinement effects, due to the plunge pool and steel container, were neglected due to the use of the 2D models. The scour profiles in 2D were manually drawn using the design modeller. The geometry of the domain was split into three sections, but maintained as one part to ensure conformal mesh at the surface boundaries, namely issuance canal, free falling jet (air body), as well as the plunge pool (water body) (refer to Figure 6-2).

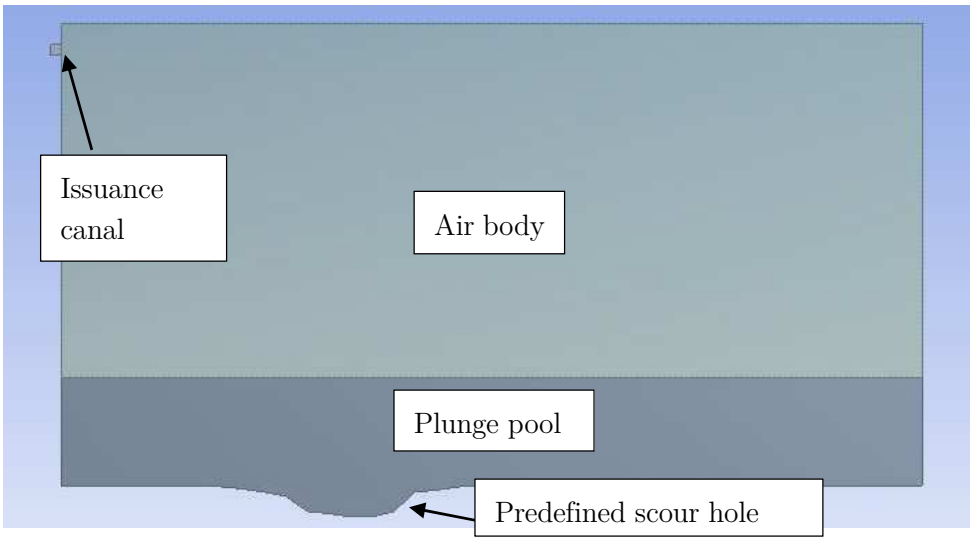

Figure 6-2 - Numerical domain geometry

6.3.2 Meshing

The numerical domain that is solved by FLUENT, is made up of a grid or mesh formed from elements or cells that define the control volumes over which the equations of the fluid flow are solved [162,178,182]. The built-in function in ANSYS Workbench, or other software such as GAMBIT, can be used for meshing. The meshing function provided in ANSYS Workbench was used to generate the mesh for this study.

The shape of the cells dictates the stability and accuracy of the solution. Several cell shapes are available, some of which are shown in Figure 6-4. The chosen cell type depends on the domain geometry. A number of the main uses of the different cell shapes are summarised below [183]:

- Tri/tetrahedron mesh can be used for more complex geometries, as the quad/hexahedron cells do not offer any numerical advantage for complex geometries and the tri/tetrahedron cells require less effort to apply.
- Quad/hexahedron mesh is predominantly used for simple geometries as they can provide a higher quality mesh for fewer cells, as compared to tri/tetrahedron cells.
- Hybrid mesh utilises the efficiency and accuracy of both the quad/hexahedron and tri/tetrahedron meshes. Specific regions can be meshed with different mesh types according to the required need such as accuracy.

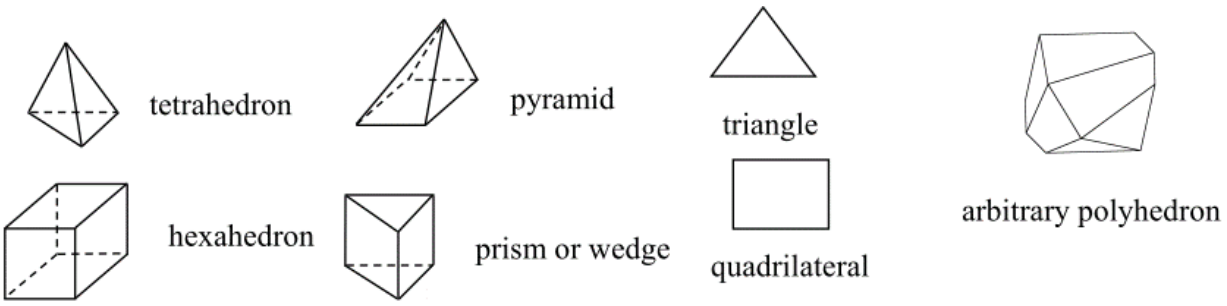

Figure 6-4 - Shape of cells [183]

Not only is the shape of the cells important, but also the degree of meshing resolution, the size of the cells, geometrical similarity, as well as the number of cells. If the cells are too large, the solution can become dependent on the cell size, rather than the boundary and input conditions. When using larger cells, convergence does, however, occur earlier, as there are fewer cells in the domain [171]. High resolution meshes are more accurate than coarse meshes, but are computationally more intensive and time consuming and should therefore be used near solid boundaries, where fine details in the geometry are present, for example at the air-water surface and where output is required [2,184]. The degree of mesh refinement primarily depends on the accuracy of the output values required [171,195]. A large change in adjacent cell size should be avoided as it can reduce the numerical accuracy. In some cases, a second order accuracy numerical solution can be reduced to a first order accuracy solution, just by using a bad mesh [162,172]. Uniform and geometrically similar meshes are also generally used instead of a variable mesh, to avoid increased numerical diffusion in the lower mesh density areas of the domain [74]. Two important parameters to check are the skewness, as well as orthogonal quality. Ranges of appropriate skewness and orthogonal quality values are shown in Figure 6-3 [183].

Skewness mesh metrics spectrum

Excellent	Very good	Good	Acceptable	Bad	Unacceptable
0-0.25	0.25-0.50	0.50-0.80	0.80-0.94	0.95-0.97	0.98-1.00

Orthogonal Quality mesh metrics spectrum

Unacceptable	Bad	Acceptable	Good	Very good	Excellent
0-0.001	0.001-0.14	0.15-0.20	0.20-0.69	0.70-0.95	0.95-1.00

Figure 6-3 - Skewness and orthogonal quality desired ranges [183]

Due to the simplicity of the geometry of the physical laboratory model (Figure 6-2), including the scour profile, a conformal hexagonal mesh was used to define the numerical domain for this study. Further mesh refinement methods used in the study are discussed in Section 6.5.1.

6.3.3 Solver (FLUENT)

The solver (FLUENT) is used to solve steady and transient flow problems mathematically and the initial and boundary conditions need to be specified correctly to provide accurate results. In addition, simplifications and assumptions regarding the flow are made in the solver in order to make the problem more manageable [183].

6.3.3.1 *Numerical solution techniques*

Different CFD packages solve the fluid domain in different ways. There are three main numerical solution techniques that are generally used by the CFD packages to solve the flow field, namely [183,184]:

- **Finite difference method (FDM)** - Equations that govern the flow are approximated from Taylor series expansion [2,178]. The linear functions resulting from the Taylor series expansion are then solved iteratively or directly. This is the oldest method of the three.
- **Finite volume method (FVM)** - The partial differential equations, which are non-linear, governing the fluid flow are integrated over the control volumes representing the domain. These integral equations are discretised to convert them into simple algebraic equations that can be solved numerically by using the adjacent cells through iteration in time and space. They can also be solved directly. Energy, mass, momentum and any other quantities that may be relevant are conserved for each cell [2,178]. This method is used by FLUENT and is a modified form of the finite difference method. The method is better suited for flow past more complex geometries than the finite difference method [178].
- **Spectral method** - Harmonics is used to approximate the solution.

Most CFD codes, such as ANSYS FLUENT, use the finite volume method as there is a clear relationship between the numerical algorithms and the underlying physical conservation principles [2]. A well-defined and accurate mesh is thus required for an accurate simulation of flow problems using the finite volume

method as the flow field is rendered from the solved equations over the control volumes [2,201]. A detailed discussion of the above methods and other available methods is beyond the scope of this study and other literature should be referred to for a more detailed discussion [2,178,184].

6.3.3.2 *Fundamental equations for fluid flow*

The fundamental equations for fluid flow (laminar and turbulent) are based on the fundamental conservation principles of fluid dynamics, which are defined below [2,171]:

1. **Conservation of mass** (continuity): "The rate of increase of mass in the fluid element is equal to the net rate of flow of mass into the fluid element."
2. **Conservation of momentum** (Newton's second law): "The rate of increase of momentum of fluid particles is equal to the sum of the forces on the fluid particle."
3. **Conservation of energy** (First law of thermodynamics): "The rate of change of energy of a fluid particle is equal to the rate of heat transfer to the fluid particle plus the rate of work done on the particle."

The above conservation laws must be satisfied throughout the flow region that is being modelled and which is of interest [183]. The general conservation or transport equations are solved for the control volumes of the domain defined by the mesh [175,185,186]. These equations are solved iteratively or directly until the solution converges.

The general conservation equation (standard transient convection-diffusion transport equation) for a general scalar quantity (ϕ) which is integrated and discretised into algebraic equations is shown in Eqn. 6-1. Each of the conservation scalar quantities to be solved, is defined in Table 6-2 for a three dimensional domain [2,184].

$$\frac{\partial(\rho\phi)}{\partial t} + \nabla.\left(\rho\phi\underline{u}\right) = \nabla.(\Gamma\nabla\phi) + S_\phi \qquad \text{Eqn. 6-1}$$

Where:

Γ = Diffusion coefficient
S = Source term
ϕ = Dependent variable (scalar quantity)

Table 6-2 - Conservation laws scalar quantities [183]

Φ	Scalar quantity
1	Continuity/mass
U	X momentum
V	Y momentum
W	Z momentum
H	Energy

Each of the parts of Eqn. 6-1 is described in words in Figure 6-5 [184].

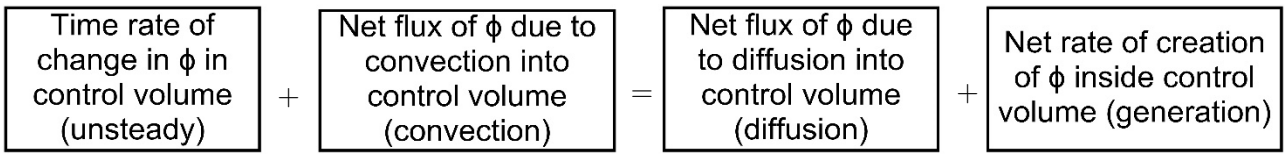

Figure 6-5 - General conservation equation

Two particle tracking approaches or flow specification methods are available that influence the form of the differential equations to be solved, namely Eulerian and Lagrangian specifications [183,184].

- Eulerian specification is where the fluid moves through the finite control volume or infinitely small element, which is fixed in space. The conservation form of equations is solved.
- Lagrangian specification is where the finite control volume or an infinitely small element moves with the fluid flow and the particles stay in control volume. Non-conservation form of the equations is solved.

For an in-detail description and explanation regarding the finite volume method such as discretisation and other aspects, Malalasekera and Versteeg [184] or the FLUENT theory guide [187], should be consulted.

The Eulerian flow specification was used in this study. The conservation form of the continuity and momentum equations was thus used to integrate over the control volumes, and is shown below for turbulent flow.

(i) Continuity equation

The conservation form of the time-averaged continuity equation is given by Eqn. 6-2 for turbulent flow [187,200].

$$\frac{\partial \rho}{\partial t} + \frac{\partial U_i}{\partial x_i} = 0 \qquad \text{Eqn. 6-2}$$

Where:

U_i	=	Mean velocity (ith direction fluid velocity component)
x_i	=	Coordinate component
ρ	=	Fluid mixture density (see Eqn. 6-5 for multiphase density)
t	=	Time

(ii) Momentum equation

Eqn. 6-3 is the conservation form of the time averaged momentum equation for turbulent flow [75,187,188,200].

$$\rho \frac{\partial U_i}{\partial t} + \rho \frac{\partial (U_i U_j)}{\partial x_j} = -\frac{\partial P}{\partial x_i} + \frac{\partial}{\partial x_j}\left(\mu\left(\frac{\partial U_i}{\partial x_j} + \frac{\partial U_j}{\partial x_i} - \frac{2}{3}\frac{\partial U_k}{\partial x_k}\delta_{ij}\right) - \rho\overline{u_i' u_j'}\right) + \rho g_i + F_i \qquad \text{Eqn. 6-3}$$

Where:

μ	=	Dynamic molecular viscosity (see Eqn. 6-6 for multiphase dynamic viscosity)
u_i'	=	Axial velocity fluctuations
P	=	Mean pressure (dynamic)
$-\overline{u_i' u_j'}$	=	Specific Reynolds stress tensor (turbulence stresses)
ρg_i	=	Gravitational body force
F_i	=	External body forces and other source terms
δ_{ij}	=	Kronecker delta

The Boussinesq approximation is used to model the turbulence stresses with the use of an eddy viscosity in the two equation turbulence models (i.e. SST k-ω) and is defined by Eqn. 6-4 [189,187].

$$-\rho\overline{u_i' u_j'} = \mu_T\left(\frac{\partial U_i}{\partial x_j} + \frac{\partial U_j}{\partial x_i}\right) - \frac{2}{3}\rho k \delta_{ij} \qquad \text{Eqn. 6-4}$$

Where:

μ_T	=	Turbulent or eddy viscosity
k	=	Turbulent kinetic energy

Eqn. 6-2 and Eqn. 6-3 are referred to as the Reynolds-Averaged Navier-Stokes equations (RANS). To compute the Reynolds stresses in Eqn. 6-3, turbulent closure models are required, which are discussed in Section 6.4.1. The difference between the conservation equations above and the original conservation equations is that the time-averaged variables (velocity, pressure etc.) instead of the instantaneous variables are computed and that other terms, such as the specific Reynolds stress tensor, are included to account for the turbulent effects.

6.3.3.3 *Solution process*

The solution process of the solver (FLUENT) is shown grammatically in Figure 6-6.

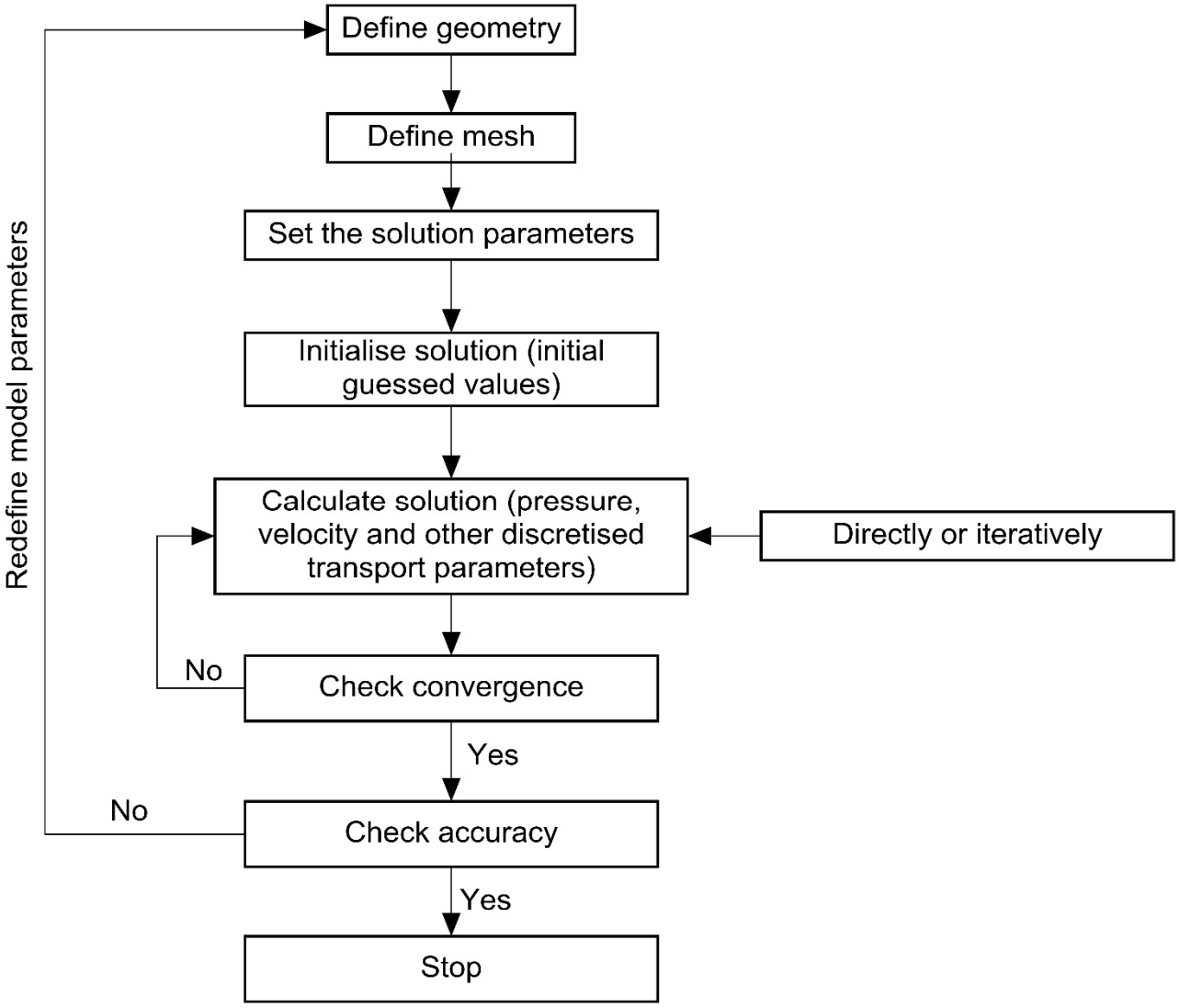

Figure 6-6 - Solver procedure flow chart

6.4 Solver (FLUENT) setup

FLUENT allows the simulation of both steady and transient flows. In the case of a plunging jet, transient flow was selected as the flow changed irregularly with time. Gravitational acceleration was also activated with the value set at -9.81m/s^2. A negative value was used due to the default coordinate system used by FLUENT. The sub-sections below (Sections 6.4.1 to 6.4.6), describe the solver setup as was used to solve the fluid flow of the plunging jet with some background information regarding each step of the setup procedure.

6.4.1 Computational models

The appropriate computational (physical) models in FLUENT need to be selected for the problem that is being simulated to ensure the physical conditions are represented correctly. In the case of a plunging jet, the two computational models that needed to be selected were the multiphase and turbulence physical laboratory models.

(i) Multiphase flow

A multiphase flow model needs to be selected when more than one material (fluid/solid/gas) is modelled simultaneously in the numerical domain. The materials can be different substances, or different phases of the same substance such as water liquid and water vapour. In the case of plunging jets, the materials are air and water. Multiphase flow can be calculated mathematically using one of two approaches, namely Euler-Langrange and Euler-Euler, which are summarised in Table 6-3 [187,190].

Table 6-3 - Multiphase approaches

Approach	Description
Euler-Langrange	The fluid phase is treated as a continuum and the dispersed phase is computed by tracking a large number of particles through the flow field. This makes it conceptually simple. Langrangian methods cannot be used in problems where very large deformations of the free boundaries (free surface) occur and the volume fraction of the second phase cannot be negligible [191].
Euler-Euler	The phases are treated as interpenetrating continua or continuous mediums mathematically (momentum and mass are exchanged). Phasic volume fraction concept is used due to the fact that one phase cannot be occupied by the others. Volume fractions are used to illustrate the volume or space used by each phase in the control volumes [172,192,201].

The Euler-Euler multiphase models were considered in this study. There are three different types of Euler-Euler multiphase models available in FLUENT that can be used to determine the interaction between the different phases as summarised in Table 6-4 [187,190].

Table 6-4 - Multiphase models

Model	Description
Volume of fluid (VOF)	The VOF model was developed by Hirt and Nichols [191]. The VOF model tracks and approximates the interface (free surface) between two or more immiscible fluids (no mixing/interpenetration of phases) with time, to determine its position (time dependant flow simulation). This model simultaneously solves the internal flow field, while calculating the profile of the free surface. Velocity and pressure fields are shared between phases, thus the equations used for one-phase flow can be used for two-phase flow conditions, as the model is a multi-fluid model [2,200]. The model allows for a sharp interface between the phases, which can change with space and time without the use of a fine mesh [193]. The model is used for gravity driven flows and is applicable to stratified or free surface flows [190]. The interface is related to the volume fraction of the fluid of the surrounding cells. Each cell contains only one fluid or the interface between the phases. For cells that are fully occupied by a liquid, a volume fraction of 1 is given, while the cells containing the interface have a value between 0 and 1 [172,191]. Due to the model being directly related to the size of the cells, the details at the interface can only be simulated to the resolution of the mesh. The model is known for not identifying the interface clearly and smearing the interface and is very computationally intensive when solving transient flow problems and is reasonably accurate [172,194].
Eulerian model	In the Eulerian model, the phases can be modelled to mix or exist simultaneously. The model does not allow immiscible water-air interface due to it being a mixture model [195]. The model solves the continuity and momentum equations for each phase individually. It is the most complex of the three available models. The model has been used for simulating scouring of non-cohesive sediment beds due to submerged water jets [190,196].
Mixture model	The mixture model is a popular air-water two-phase method as the model allows modelling of more than one phase as separate, yet interacting and treats phases as continuous mediums [201]. It is a simplified version of the Eulerian model. Continuity and momentum equations are solved for each phase and for the mixture, and relative velocities are given to describe the dispersed phases [74].

The multiphase models, as presented in Table 6-4 and used in FLUENT, are currently not capable of modelling air entrainment of a plunging jet, which is especially important in developed jet cases, which was present during the physical laboratory model tests [197]. Another concern with modelling the plunging jet in CFD was that multiple flow regimes had to be modelled. Both dispersed (developed jet) as well as stratified (free surface) flow are present. Currently none of the models in Table 6-4 can accurately model these conditions simultaneously.

The VOF multiphase model was used in this study, as the multiphase model was applied in similar studies previously. The VOF method was also the only method that allowed the modelling of open channel flow, which was a necessity, due to the plunge pool downstream. The VOF method was solved explicitly as it allowed for more accurate free surface tracking. The more accurate Geo-reconstruct discretisation scheme was also only available when using the explicit VOF solver. The implicit body force was enabled to improve convergence [208]. The conservation (continuity and momentum) and turbulence equations used in the VOF model, are still that of single phase flow, but the values of the density and the dynamic molecular viscosity of the cells, are dependent on the volume fraction of the secondary phase, which in this study was the air (refer to Eqn. 6-5 and Eqn. 6-6) [187].

$$\boldsymbol{\rho = \alpha_2 \rho_2 + (1 + \alpha_2)\rho_1} \qquad \text{Eqn. 6-5}$$

$$\boldsymbol{\mu = \alpha_2 \mu_2 + (1 + \alpha_2)\mu_1} \qquad \text{Eqn. 6-6}$$

Where:

$\boldsymbol{\alpha_2}$	=	Volume fraction of secondary phase
ρ	=	Density of the cell (subscript 1 and 2 refers to the phases)
μ	=	Dynamic molecular viscosity of cell (subscript 1 and 2 refer to the phases)

The interface between the phases is tracked by the continuity equation using the volume fraction of the secondary phase instead of its density (Eqn. 6-7), which is used on the conventional continuity equation (Eqn. 6-2) [183].

$$\boldsymbol{\frac{\partial \alpha_2}{\partial t} + u_i \frac{\partial \alpha_2}{\partial x_i} = 0} \qquad \text{Eqn. 6-7}$$

The double precision solver is generally recommended when multiphase flows are simulated, as the solver reduces round-off errors. The double precision solver was thus enabled for this study [198,199]. Open channel flow was also enabled to simulate the plunge pool.

(ii) Turbulence

Turbulent flow is very complex and variable. Turbulent flow is generally described as flow with large and random fluctuations in velocity and pressure in space and time and is generally characterised as flow with moderate to high Reynolds numbers (Eqn. 4-3). The conservation laws of mass, energy and momentum govern turbulent flow in CFD similarly to that of laminar flow. The effects of the turbulent fluctuations (velocity and scalar quantities) on the conservation equations of laminar flow are described by the turbulent models [171]. Due to turbulent nature of the plunging jet, a suitable turbulent model had to be selected. There are several turbulence models available in CFD. The turbulence model used is dependent on the computational power available and the accuracy required. More accurate turbulence models for solving the turbulent flow fields are available, but are used less frequently as they are generally too computationally expensive. Examples of the more accurate models are the direct numerical simulation (DNS) and large eddy simulation (LES) models and are summarised in short below.

- The direct numerical simulation (DNS) model can resolve even the smallest meaningful eddies. It is the most accurate model, but its computational cost, due to the model solving all the spatial and temporal fluctuations of the fluid flow (velocities and pressure), is excessive and impractical [178]. The method is therefore generally used for small Reynolds numbers and simple problems.
- The large eddy simulation (LES) and very large eddy simulation (VLES) models, simulate the eddies as individual units, but do not simulate the eddies at all scales, only the large eddies. The small scale turbulent effects are deduced from the larger scale eddies and as the scale of the eddies increases so too does the approximation degree. The model is still very computationally expensive, but less than the DNS model and a very fine grid is required to be able to model the eddies [2,180,195].

Due to the computational cost of the more accurate models (DNS and LES), researchers have preferred to use turbulence models (closure models) that use Reynolds averaged Navier-Stokes equations (RANS) to simulate the turbulent flow field [171,173]. These closure models make approximations and assumptions in regards to turbulence and describe an idealised turbulent fluid, rather than the real turbulent fluid to

solve the Reynolds stresses and close the system. The RANS turbulence models determine the time-averaged values of the pressure and velocities fields to describe the turbulent flow field. The idealised fluid is governed by the turbulence model chosen to solve the flow field and may thus not be realistic [2,50,171]. The RANS models are, however, limited in comparison to the more accurate models (DNS and LES), but are simple and effective for its computational time. Some of capabilities of the RANS turbulence models available in FLUENT are summarised in Table 6-5.

Table 6-5 - RANS turbulence models

Reynolds Averaged Navier Stokes (RANS) Turbulence Models	
Model	**Description**
k-ε	**Standard k-ε model** Turbulent kinetic energy (k) and rate of viscous dissipation (ε) equations are introduced, as well as an eddy viscosity to determine the Reynolds stresses with the use of the Boussinesq hypothesis (Eqn. 6-4), as is used in the other two equation models [178,200]. The model uses empirically derived constants to solve the introduced equations [2,50,163]. One of the major drawbacks of the simpler k-ε methods is that they are not able to resolve highly swirled flows and eddy structures completely [2]. In adverse pressure gradients and boundary layer separation, none of the k-ε models is recommended, due to their insensitivity (no viscosity corrections) [204,208]. The k-ε model does not differentiate between the spreading of plane and circular jets [204].
	Renormalisation group (RNG) k-ε model The model has improved accuracy over the standard k-ε model, simulates re-circulating and separated flows better than the standard k-ε model and has been found to converge almost twice as fast as the standard k-ε model [162,171,177,201]. The constants used in the formulas were not obtained empirically as with the standard k-ε, but from statistical analysis [148]. The standard k-ε and RNG k-ε models have been applied on similar flow problems and obtained comparably accurate results with no major difference in the calculated values at convergence [173] and the RNG k-ε model has been used to simulate a free falling jet [148,195].
	Realisable k-ε model The model is preferred above the other k-ε models, as it has the best performance for flows that are more complex [177]. In previous studies, the model has been found to perform better at simulating and representing high velocity free jets than the other turbulence models available (including k-ω and RSM) [189].

k-ω	**Standard k-ω model** The model replaces the dissipation rate equation (ε) with the specific dissipation rate equation (ω), which is defined as: $\omega = k/\varepsilon$ [202,203]. The model is sensitive to changes in boundary conditions (location of the wall shear layer) and the boundary values of k-ω, but generally performs better than the standard k-ε models especially for adverse pressure gradient flows [202,204]. The viscosity effects are, however, only modelled in the layers adjacent to the boundaries (near wall) and not in the main flow region (free stream) where the k-ε model performs better [180].
	SST (shear stress transport) k-ω model The model is a hybrid between the standard k-ω and k-ε models. The model is recommended above the standard k-ω model. The model uses the k-ω model at the near wall region (boundary layer) and the k-ε model outside this region (free stream) (see Figure 6-7) [177,205]. Due to the hybrid nature of the SST k-ω model, the flow in adverse pressure gradients and flow separation can be simulated more accurately, which the individual models cannot represent accurately independently [205].
Reynolds Stress Model	**Reynolds Stress model** This model differs from the two equation models as discussed above, as it calculates each of the Reynolds stresses (six in total for 3D flow and four in 2D) individually, as opposed to using the Boussinesq hypothesis to determine only one value (Eqn. 6-4). The RSM model is computationally more expensive than the two equation models (k-ω and k-ε), but is generally more accurate [187].

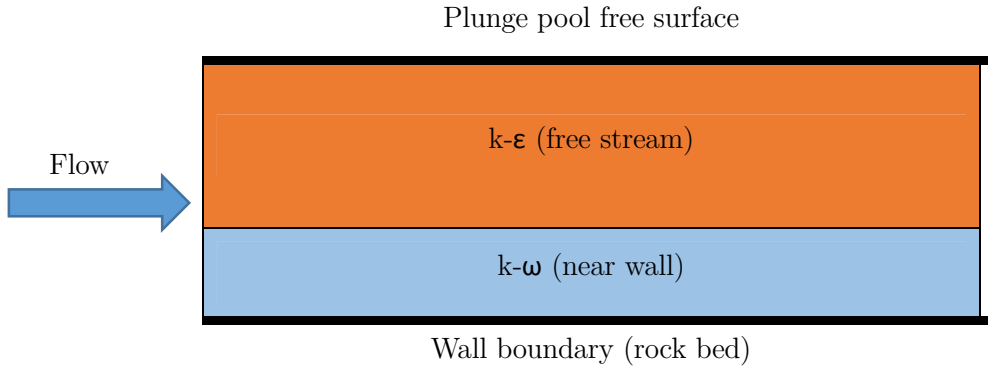

Figure 6-7 - SST (shear stress transport) k-ω model

For a more in-detail discussion on each of the turbulence models, other literature should be consulted, such as the FLUENT theory guide [187]. Turbulence and multiphase modelling go hand in hand and affect each other directly. The turbulence model affects the development of the free surface, while the free surface, in turn, affects the flow region in which the turbulence model is applied, which makes the tracking of the free surface very important [2,162]. The RANS turbulence models are only single-phase models and

are used to model the turbulence in the primary phase only. Additional terms are used in the turbulence equations to account for the turbulent effects of the secondary phase.

The SST k-ω turbulence model was applied in this particular study, as the model was used on other studies to model the turbulence effects of the plunging jet [174,177]. Turbulence damping was enabled to model the high turbulence generation at the interface between the immiscible phases correctly and was left at its default setting [187]. The equations of turbulent kinetic energy (k) and specific dissipation rate (ω) for the SST k-ω turbulence model, are shown in Eqn. 6-8 and Eqn. 6-9 [187,204,205,206]. Refer to the FLUENT theory guide [187] for a complete discussion of all the terms in the equations and their subsequent approximations.

$$\frac{\partial(\rho k)}{\partial t}+\frac{\partial(\rho k U_i)}{\partial x_i}=\frac{\partial}{\partial x_j}\left(\Gamma_k\frac{\partial k}{\partial x_j}\right)+\widetilde{G_k}-Y_k+S_k \qquad \text{Eqn. 6-8}$$

$$\frac{\partial(\rho\omega)}{\partial t}+\frac{\partial(\rho\omega U_j)}{\partial x_j}=\frac{\partial}{\partial x_j}\left(\Gamma_\omega\frac{\partial\omega}{\partial x_j}\right)+G_\omega-Y_\omega+S_\omega+D_\omega \qquad \text{Eqn. 6-9}$$

Where:

k	=	Turbulent kinetic energy
ω	=	Specific dissipation rate
$\widetilde{G_k}$	=	Generation of turbulent kinetic energy due to mean velocity gradients
G_ω	=	Generation of ω
D_ω	=	Cross-diffusion term
Γ_k and Γ_ω	=	Effective diffusivities
Y_k and Y_ω	=	Dissipation of k and ω
S_k and S_ω	=	Defined source terms

6.4.2 Materials (Fluids)

FLUENT has a database of materials with their respective material properties pre-defined, but user defined or custom materials as well as different material properties can be added. For multi-phase flows, the materials of each of the different phases need to be specified. In the case of the plunging jet, the material types selected were air and water and the material properties were selected from the default material database. It should be noted that both air and water, as well as real fluids, are incompressible which satisfy zero velocity at non-slip boundaries.

6.4.3 Phases

When using multiphase models the different phases need to be specified, as well as the interaction between the phases. For free surface flows, such as in the case of a plunging jet, both phases are treated as continuous and a distinct interphase is defined between the two phases. It should be noted that when using the other multiphase models (mixture or Eulerian multiphase models), the continuous phase needs to be specified as the primary phase, while the secondary phases are the phases dispersed in the primary phase [208]. In the case of the plunging jet, water and air needed to be specified for the different phases. Water was taken as the primary phase, while air was taken as the secondary phase. Interaction between the phases was defined by specifying the surface tension. Surface tension is an important parameter as both the Weber and Capillary numbers are directly related to it. A constant surface tension stress (σ) between water and air at 20 degrees was assumed as 0.0728 N/m [33]. Surface tension is modelled in the momentum equation by using an extra source term.

6.4.4 Boundary conditions

The domain boundaries are defined when either setting up the geometry or meshing by using named selections. The correct conditions (type and properties) at the domain boundaries need to be specified before the analysis can be run and need to represent what is physically occurring. The conditions of the boundaries can either be assigned explicitly, or defined by UDFs (user-defined functions) [162]. The accuracy and results of the equations solved that describe the flow field are directly related to the specified boundary conditions. There are several types of boundary conditions available in FLUENT and they in turn can be split into two sections, namely interior and exterior boundaries. The boundary conditions that were utilised in this study are discussed below [2, 184, 195].

6.4.4.1 *Velocity inlet boundary*

The condition at this boundary is set by specifying an inflow velocity (direction and magnitude) and the turbulence conditions, if known. For this study, the issuance velocity was normal to the specified boundary. The velocity magnitude and the turbulence parameters (turbulence intensity and hydraulic diameter) as shown in Table 6-6 were used. A uniform velocity profile was assumed, even though that

was not the case in the physical laboratory model due to the turbulent flow. As proper velocity measurements could not be taken in the issuance canal to determine the actual velocity profile during the physical laboratory model tests, a uniform velocity profile was assumed (see Section 4.2.3). A turbulence intensity, as well as a hydraulic diameter were specified to account for the turbulence at the inlet. The relevant values regarding the velocity inlet are shown in Table 6-6, which were taken from Section 4 and Section 5.

Table 6-6 - Velocity inlet boundary conditions

Parameter	Value
Turbulence intensity (T_u) (Bollaert, 2002)	3% (Table 5-1)
Velocity magnitude (x-direction) – from physical laboratory model	2m/s (Table 4-5)
Width of issuance canal (a) – from physical laboratory model	0.2m (Table 4-1)
Depth of flow (b) – from physical laboratory model	0.05m (Table 4-4)
Hydraulic diameter	0.04m

The hydraulic diameter, as shown in Table 6-6, was calculated using Eqn. 6-10, which is generally used to calculate the hydraulic diameter of rectangular canals [207].

$$D_h = \frac{ab}{a+b} \qquad \text{Eqn. 6-10}$$

Where:

a = Width of canal (see Figure 6-8) (m)

b = Height of canal (m)

D_h = Hydraulic diameter (m)

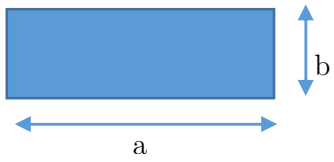

Figure 6-8 - Issuance canal cross-section

As the model had two phases (air and water), the specification of backflow of the secondary phase had to be specified. Due to the water being specified as the primary phase, no changes had to be made to the backflow at the velocity inlet for the primary phase and the volume fraction of the secondary phase (air)

was assumed as zero (default). This ensured that only the primary phase (water) was present at the velocity inlet.

6.4.4.2 *Pressure outlet boundary*

The pressure outlet requires the specification of the static (gauge) pressure at the boundaries for subsonic flows [208]. Two different pressure outlet conditions occurred in the numerical domain (see Figure 6-9), which are explained below. The pressure outlet configuration, as shown in Figure 6-9 for the 2D model, was used to ensure that there were no major impacts due to the boundaries on the flow profile of the jet.

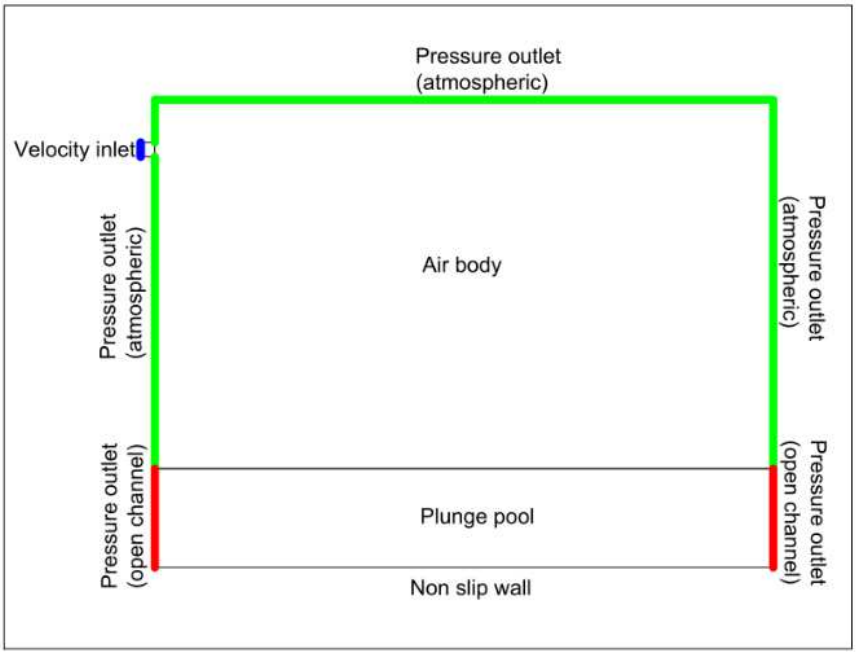

Figure 6-9 - 2D model boundary conditions

Plunge pool (water phase)

For the plunge pool pressure outlet, the open channel boundary of the VOF method was enabled. A free surface level (tailwater level) was specified, which defines the static hydraulic pressure at the boundary. For the study, a tailwater or free surface was used as a height of 0.25m and 0.5m respectively from the bottom level, which was taken as 0m. No backflow conditions had to be specified, as the open channel boundary condition was enabled.

For the density interpolation method at the boundary, the "From free surface level" method, rather than the default method ("From neighbouring cell"), was used. The particular interpolation method was chosen, due to the boundary being rather close to the impact area, especially the upstream boundary.

The latter method has been known to produce oscillations in the free surface at the upstream boundary, which was undesirable for the 2D simulations [208]. A limitation in using the open channel free surface boundary, is that the mass flow rate is not always conserved at the boundary, especially when using coarse meshes, which becomes noticeable when using the mass flow rate as a convergence monitor [208].

Air body

An atmospheric or gauge pressure of zero was used at all the pressure outlet boundaries for the air volume (see Figure 6-9). In the case of a plunging jet where there were two phases, to ensure backflow of the water did not occur into the air volume, the volume fraction of air (secondary phase) at the outlet of the air volume was set to one. Backflow conditions are important to specify correctly and realistically to ensure convergence. If and when backflow occurs, the outlet will act as an inlet [162,190,201].

6.4.4.3 *Wall boundary*

For viscous flows, the wall boundary is assumed to be a non-slip boundary condition, signifying that at solid boundaries the velocity of the fluid is equal to zero (velocity same as stationary wall). For this study, non-slip wall boundaries were specified at the rock bed and issuance canal as incompressible, real fluids were modelled (air and water).

6.4.4.4 *Operating conditions*

The operating density is mostly enabled for buoyant flow problems, but can be used for non-buoyant flow if the flow is governed by gravity, such as a plunging jet, and has a constant density. The operating density setting offsets the hydrostatic pressure from the domain to avoid round off errors. When using the VOF multiphase model, the operating density should also be enabled and the density should be set to the lightest phase [208]. For this study, the operating density was enabled and the operating density, as well as the operating pressure was kept at their default values.

6.4.5 Solution methods

The finite volume method has two methods for solving steady and unsteady flow problems. The solver can be either pressure-based or density-based. The pressure-based solver is the preferred and generally

more appropriate for most model scenarios, while the density-based solver is only generally used for higher Mach numbers (mostly aviation) and for specialised cases [184,171]. The pressure-based solver was thus used for this study. Several discretisation schemes are needed to solve the algebraic equations and subsequently the flow field. The various schemes available are discussed in Section 6.4.5.1 and Section 6.4.5.2 respectively.

6.4.5.1 *Pressure-velocity coupling scheme*

When using the pressure-based solver, a pressure-velocity coupling scheme needs to be specified. These schemes are used to derive equations, from the momentum and continuity equations, to calculate the pressure and velocity fields [202]. A staggered grid is used to calculate the velocities (vectors) and pressures (scalars). There are four main pressure-velocity coupling schemes, as summarised in Table 6-7 [2,190].

Table 6-7 - Pressure-velocity coupling schemes

Scheme	Description
SIMPLE	The Semi-implicit method for pressure-linked equations (SIMPLE) scheme is good for general cases. Primarily used for steady state calculations and low Froude numbers due to the scheme not being capable of handling large free surface changes near the structure [202]. The pressure field is calculated by applying a pressure correction at each iteration until continuity is satisfied [183]. The SIMPLE scheme has been used in similar plunging jet studies with relative success [75,174,177].
SIMPLEC	The SIMPLE and SIMPLEC (SIMPLE corrected/consistent) schemes have been found to give similar or identical results at convergence, but the convergence speed differs between schemes. The SIMPLEC scheme converges faster than the SIMPLE scheme [171].
PISO	The pressure implicit with splitting of operators (PISO) scheme is generally recommended for highly skewed meshes and transient calculations [187].
COUPLED	The COUPLED or pressure based coupled scheme (PBCS) is generally used where there are strong body forces due to buoyancy or rotation in incompressible flows or where the other schemes, such as SIMPLE, have convergence problems. The coupled scheme solves all the equations for all the variables for each of the cells individually, while the other schemes as mentioned above are generally termed segregated schemes, which solve the equations individually for each variable for all the cells of the numerical domain. The converged solution is generally reached significantly faster for the coupled scheme than for the segregated solvers [183].

The choice of which of the segregated schemes to use in Table 6-7, is dependent on speed and stability, as the converged solution is the same. The PISO and SIMPLEC schemes speed up convergence as they allow higher under-relaxation factors in comparison with the SIMPLE scheme. The COUPLED solver was applied in this study due to the high mesh density used, which increased the simulation time and due to the strong body forces present (gravity). The coupled solver also reaches a converged solution faster and is more robust than the segregated solvers.

6.4.5.2 *Spatial discretisation schemes*

There are several spatial discretisation schemes, which control the spatial discretisation of the convection terms in the partial differential equations and the gradients. The solvers and their respective spatial discretisation schemes, which were available in FLUENT, are shown in Table 6-8.

Table 6-8 - FLUENT spatial discretisation schemes

Solver	Discretisation schemes
Gradient	➢ Green-Gauss Cell-Based ➢ Green-Gauss Node-Based ➢ Least-Squares Cell-Based
Pressure (pressure based solver)	➢ PRESTO! ➢ Body forced weighted
Momentum, Turbulent kinetic energy and Specific dissipation rate	➢ First order upwind differencing scheme ➢ Hybrid differencing scheme ➢ Power-law differencing scheme ➢ Second order upwind differencing scheme ➢ Central differencing scheme ➢ QUICK (Quadratic Upwind Interpolation) scheme ➢ Third order MUSCL (Monotone Upstream-Centred Schemes for Conservation Laws)
Volume fraction	➢ First order upwind ➢ Second order upwind ➢ Compressive ➢ QUICK (Quadratic Upwind Interpolation for Convection Kinetics) ➢ Modified HRIC ➢ Geo reconstruct (explicit VOF only) ➢ CICSAM (explicit VOF only)
Transient formulation	➢ First order implicit ➢ Second order implicit (implicit VOF only) ➢ Bounded second order implicit (implicit VOF only)

As indicated in Table 6-8, several of the discretisation schemes were only available when a certain VOF scheme (explicit or implicit) is applied. Higher order schemes can be used to improve accuracy, as well as reduce the numerical diffusion. Numerical instability may, however, occur when using higher order schemes and care must be taken, as the lower order schemes may perform better [171]. The computational time will also increase when using higher order schemes. Higher order schemes were used for the spatial discretisation in this study. First order schemes were used as a first approach, but numerical diffusion occurred, as discussed in Section 6.5.1, and higher order schemes had to be applied**.** The respective spatial discretisation schemes used in the final simulations are shown in Table 6-9.

Table 6-9 - Spatial discretisation schemes used

Solver	Discretisation schemes
Gradient	**Least-Squares Cell-Based** Least-Squares Cell-Based method was used to solve the gradients of the solution variables. The Green-Gauss Cell-Based method has been used in a previous study [174], but due to the presence of numerical diffusion when applying the method in this study, the Least-Squares Cell-Based method was used instead.
Pressure	**Body forced weighted** Body force weighted discretisation scheme was used to solve the pressure gradient, rather than PRESTO! scheme, even though supersonic flow was not modelled. The body force weighted scheme gives a more stable solution for the VOF multiphase model, which motivated its use in this study [208].
Momentum, Turbulent kinetic energy and Specific dissipation rate	**Third order MUSCL (3rd order)** The third order accurate MUSCL scheme was used to calculate the Momentum, Turbulent kinetic energy and Specific dissipation rate terms as the scheme was used in a previous study for modelling plunging jets and the higher order schemes reduces the effects of numerical diffusion and is more accurate [174,208]. It should be noted that second order upwind and QUICK schemes have also been used in previous studies [177,76].
Volume fraction	**Geo-reconstruct** The Geo-reconstruct method was applied for the VOF discretisation scheme as to ensure that there was sharp interface between the two phases of air and water (VOF model) [208]. The Geo-reconstruct discretisation scheme was only available for the explicit VOF scheme.
Transient formulation	**First order implicit** The explicit VOF solver only allowed a first order transient formulation scheme. The first order implicit scheme is generally applied to unsteady simulations and is generally more stable than the higher order schemes, which also motivated its use [190].

Under-relaxation factors are specified primarily to relax: the velocity, pressure, eddy dissipation, as well as the turbulent kinetic energy. The under-relaxation factors speed up convergence and do not change the values of the final converged solutions and should be used with caution as sudden convergence can occur [171]. The factors have to be applied in some cases to stabilise the pressure-based solver, as some equations, such as the pressure-correction equation, are prone to divergence. For this study the under-relaxation factors were kept at their defaults [183].

6.4.6 Initialisation, time step and convergence of solution

6.4.6.1 *Initialisation*

Initialisation was required to start the calculation process. Initialisation entails that an initial guessed value for each variable is assigned to each of the cells in the numerical domain. Standard initialisation was used for this study using the default values. As the multiphase model was used, the fluid bodies had to be patched according to the volume fraction of each phase after initialisation. For this study, the solution was controlled for the pressure-based solver, by specifying a flow Courant number (CFL) of 20, due to difficulty of convergence of the multiphase conditions and for stability rather than using the default value of 200. The CFL value of 20 was estimated from discussion with more experienced modellers [210].

6.4.6.2 *Time step*

For the transient solver, a time step had to be specified, due to the simulation being time-dependent and had to be small enough to capture the transient flow behaviour. Smaller time steps improve convergence. The explicit solver required a small time step to accurately solve the fluid field. Similar studies have used relatively small time steps of 10^{-5}s [197] and $5\text{x}10^{-5}$s [163], as well as larger time steps such as $1\text{x}10^{-2}$s [174]. A general approximation of the time step is given by, Eqn. 6-11 [209].

$$\boldsymbol{Time\ step\ (s)} = \frac{\boldsymbol{\Delta x}}{\boldsymbol{u}} \qquad \text{Eqn. 6-11}$$

Where:

Δx = Smallest cell size in domain (m)

u = Characteristic velocity in domain (m/s)

Using Eqn. 6-11, a time step of between $1x10^{-3}$s and $3x10^{-4}$s was required using a minimum cell size of 0.0025m (Figure 6-14) and a velocity between 2m/s (issuance velocity) and 8m/s (maximum impact velocity). The author deemed a time step of $5x10^{-4}$s as adequate as a larger time step of $1x10^{-3}$s caused the simulation to diverge. The maximum number iterations per time step was taken as 30 to ensure an adequate solution was achieved per time step and that the residuals reduced by approximately three orders of magnitude per time step (refer to Figure 6-10).

6.4.6.3 *Converged solution*

Obtaining a converged solution is very important in any numerical simulation. Convergence is said to occur in transient simulations if the normalised residuals reach a specified tolerance, generally a decrease by 10^{-3} in one time step, and the residual plots show a repeating pattern of the fluctuation in the flow variables (see Figure 6-10). This is because convergence is not as clear in transient simulations, as in steady state simulations [171,183]. The residuals are dependent on the degree of satisfaction of the equations solved in the flow field. As the equations are solved iteratively by the Gauss-Seidel point-by-point iteration method in FLUENT, a number of iterations are usually required for a converged solution to occur. The model must converge, and if not, the model was not set up correctly and accurately [190]. The accuracy of the converged solution is only as good as the problem setup, meshing and the accuracy or appropriateness of the physical laboratory models used. To check if convergence occurs, surface monitors can be used to check certain quantities at various locations in the domain. The mass flow rate at the outlet was initially used as a surface monitor to compare to the flow rate at issuance, to check for convergence.

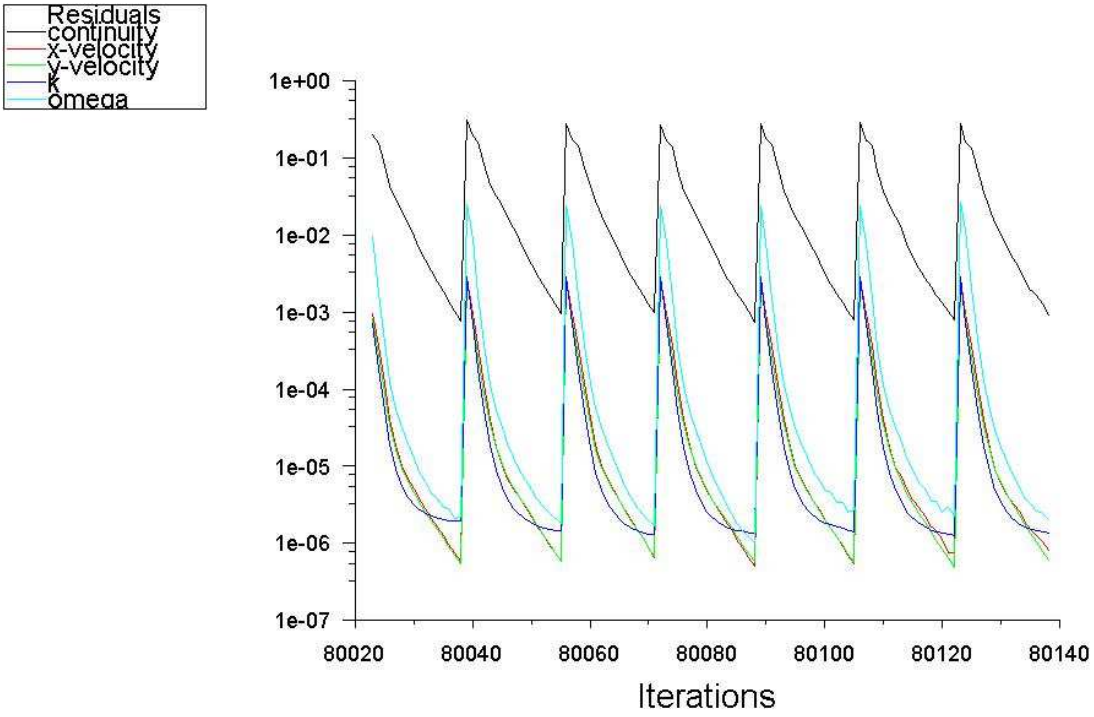

Figure 6-10 - Repeating pattern in residual plots with a 10^{-3} decrease in residuals over each time step

6.5 CFD modelling results

6.5.1 Preliminary simulation results

From the CFD modelling procedure, it was found that the model setup conditions, boundary conditions, geometry, as well as the mesh defined the accuracy and applicability of the simulation results. A short discussion follows regarding the preliminary simulation results and the subsequent adjustments made to improve the simulation validity.

6.5.1.1 *Discretisation schemes*

Lower order discretisation schemes were used as a first approach, as opposed to the higher order schemes shown in Table 6-9, which were used for the final simulations. Lower order discretisation schemes are generally used at the commencement of a CFD study, as the schemes are less computationally expensive and can give a good first approximation. When using lower order discretisation schemes with a relatively coarse mesh, numerical diffusion occurred, causing the jet to break-up prematurely as shown in

Figure 6-11. As the VOF method is highly dependent on the mesh size to track the free surface correctly, the mesh resolution was subsequently increased. Higher order discretisation schemes were subsequently applied on the higher resolution mesh, but the lower order VOF discretisation scheme (Modified HRIC) was, however, still used due to the uncertainty of the scheme's accuracy, as it is highly dependent on the grid size. Even with the higher grid resolution, the lower order VOF scheme simulated the jet behaviour in the plunge pool incorrectly (Figure 6-11). The simulated flow showed excessive splashing in the plunge pool. After the preliminary simulations and discussions with more experienced modellers [210], higher order discretisation schemes were applied, as given in Table 6-9, to reduce numerical diffusion and simulate the plunging jet more accurately.

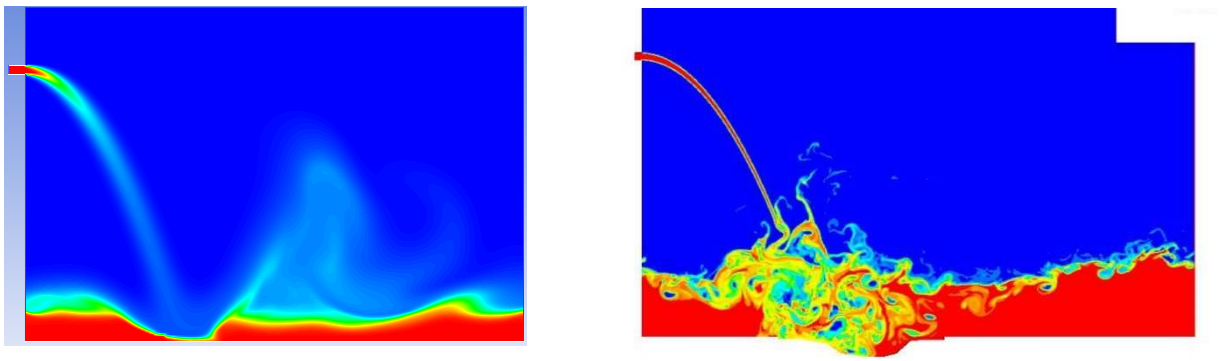

Figure 6-11 - Contour plots of volume fraction showing premature jet break-up (left) and incorrect plunge pool behaviour (right) due to numerical diffusion.

6.5.1.2 *Mesh refinement*

To determine the optimal mesh cell size for the numerical domain, three different mesh cell sizes were compared (see Table 6-10). Their applicability, in correctly simulating the plunging jet for the 2m drop height including 0.5m tailwater depth, was tested. The simulations were run for the same duration, 1.5 seconds, for each respective mesh cell size used and the subsequent results were compared (see Figure 6-12 (a-c)). Transient simulations generally require that the results of several time steps be compared, as the results at a certain time step may misrepresent the actual results. Due to the simulations compared having the exact same model setup and numerical domain, except for the mesh cell size, results taken at a single time step was, however, deemed acceptable. The mesh cell sizes, shown in Table 6-10, used in the

mesh refinement investigation, were estimated using the jet impact thicknesses at the plunge pool free surface, as presented in Table 5-3, as well as from the issuance thickness of the jet as reference.

Table 6-10 - Number of cells

Mesh cell size	Number of cells
0.05m	3 572
0.01m	88 793
0.005m	355 001

To ensure a good quality mesh was used to define the numerical domain, both the skewness and orthogonal quality of the different mesh cell sizes were determined and are shown in Table 6-11. Comparing the values to the optimal ranges, as depicted in Figure 6-3, it could be seen that the values of orthogonal quality and skewness fell in the desired ranges of a good to very good mesh. As a hexagonal grid was used for the rather simplistic domain, this was expected. The smallest mesh cell size considered of 0.005m produced the worst skewness and orthogonal quality; this was found to be due to the way in which the mesh was generated around the scour hole. This also illustrated that a high mesh density does not always ensure a good quality solution if the mesh is not checked and modified.

Table 6-11 - Skewness and orthogonal quality of mesh (different mesh cell sizes)

Mesh cell size	Skewness	Orthogonal quality
0.05m	0.22	0.78
0.01m	0.21	0.79
0.005m	0.31	0.58

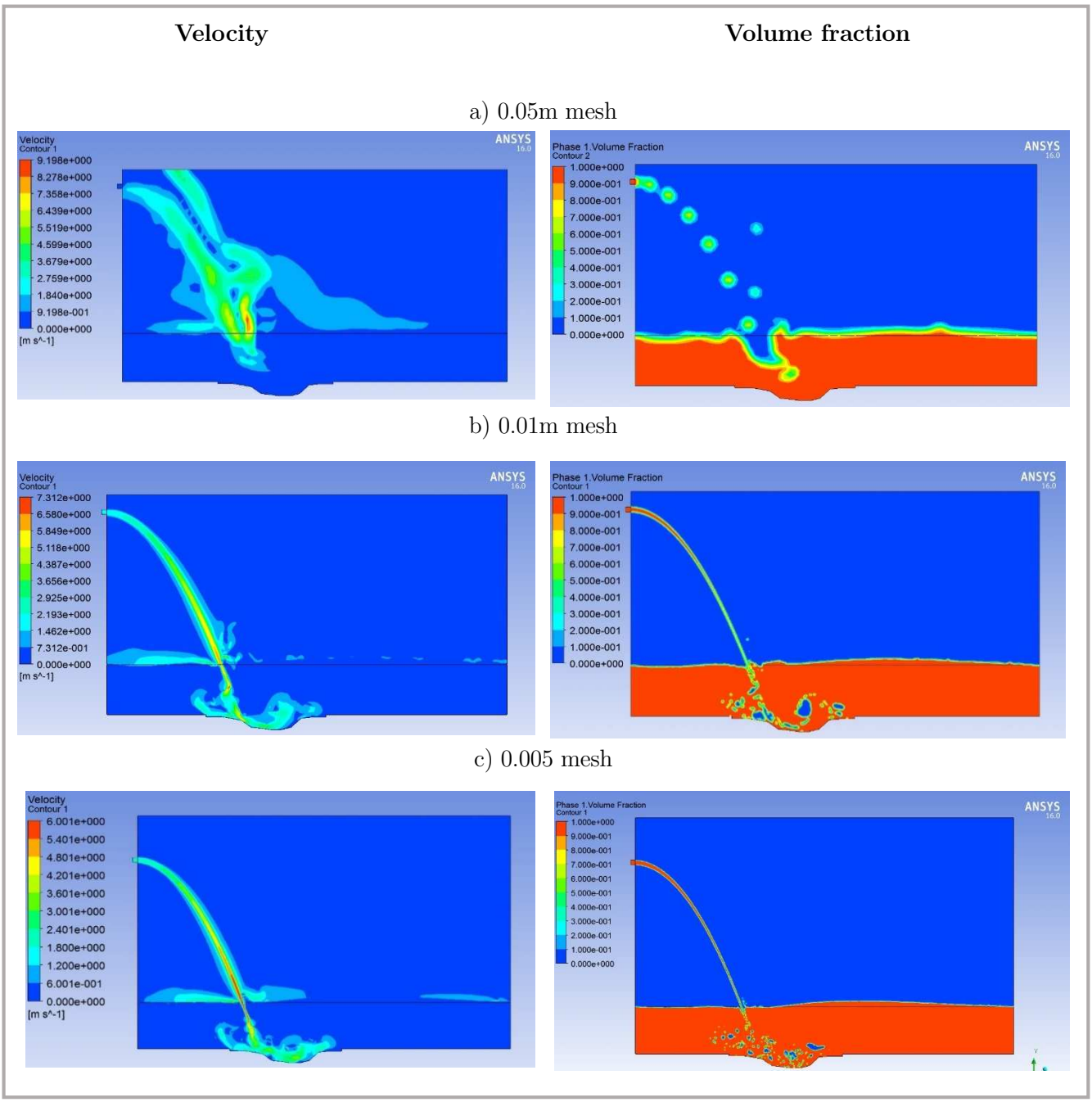

Figure 6-12 (a – c) - Velocity (left) and volume fraction (right) contour plots for the different mesh sizes tested

From the velocity and volume fraction contour plots, presented in Figure 6-12, the dependence of the VOF method on the cell size was apparent. For the lower resolution meshes (0.01m an 0.05m), the diffusion of the jet was more pronounced than for the higher resolution mesh (0.005m). For the 0.05m mesh, the simulation of the jet was completely misleading, as the mesh did not represent the physical behaviour correctly as observed during the physical laboratory model, which is clearly illustrated by

Figure 6-12. The number of cells, as well as the duration of the simulation increased exponentially, from a few hours to a number of days, as the cell size decreased, as shown in Table 6-10.

In subsequent simulations, a mesh cell size of 0.0075m was used. The reason being that the velocity plots between the 0.01m and 0.005m cell sizes did not differ considerably, as was confirmed when plotting the velocity profiles at the centreline of the jet for the different mesh cell sizes (Figure 6-13). As stated in Section 5.1.3.2 the velocity decay methods of both Ervine and Falvey (1987), as well as Hartung and Hausler (1973) were used to compare to the CFD results as shown in Figure 6-13. Furthermore, when using the 0.01m cell size, the core of the jet was not present at impact with the free surface, but when using a cell size of 0.0075m and 0.005m the core was still intact at impact with the plunge pool free surface (undeveloped jet). To reduce the amount of cells and the subsequent duration of the simulation, the 0.0075m mesh was used instead of the 0.005m mesh.

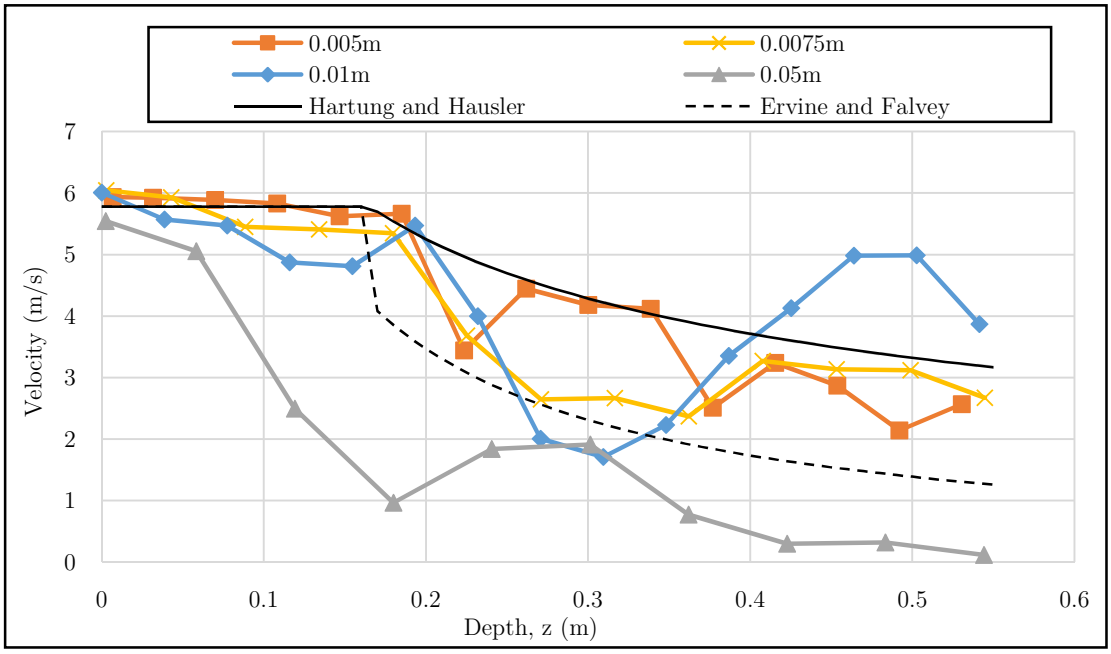

Figure 6-13 - Velocity profile at centreline of jet for different mesh sizes compared to literature

The mesh used in the issuance canal had to be relatively fine, as the jet underwent significant contraction when using larger cell sizes (see Figure 6-15). The contraction was presumed to be due to the process in which the VOF method solves the free surface boundary and only allowing one phase or the boundary to be present in a single cell. The contraction subsequently caused the core of the jet to contract prematurely causing the jet to become developed. The issuance canal was simulated as a closed conduit in the CFD

simulations. This was due to the short issuance canal and the fact that the water was discharged out of a pipe not representing the same flow conditions as general open channel conditions. For simplicity, a closed conduit was thus used. Even at moderately fine meshes, the core of the jet still suffered some minor contraction, as shown in Figure 6-15, but the slight contraction was assumed to have had a negligible effect. To minimise the contraction in the issuance canal a cell size of 0.0025m was subsequently used.

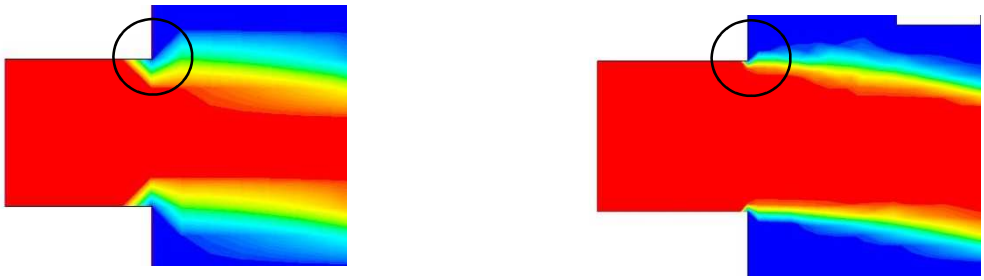

Figure 6-15 - Volume fraction contour plots illustrating jet core contraction at the end of the issuance canal (0.01m mesh (left) and 0.0025m mesh (right))

The mesh cell sizes used, in the respective areas of the numerical domain, is shown in Figure 6-14.

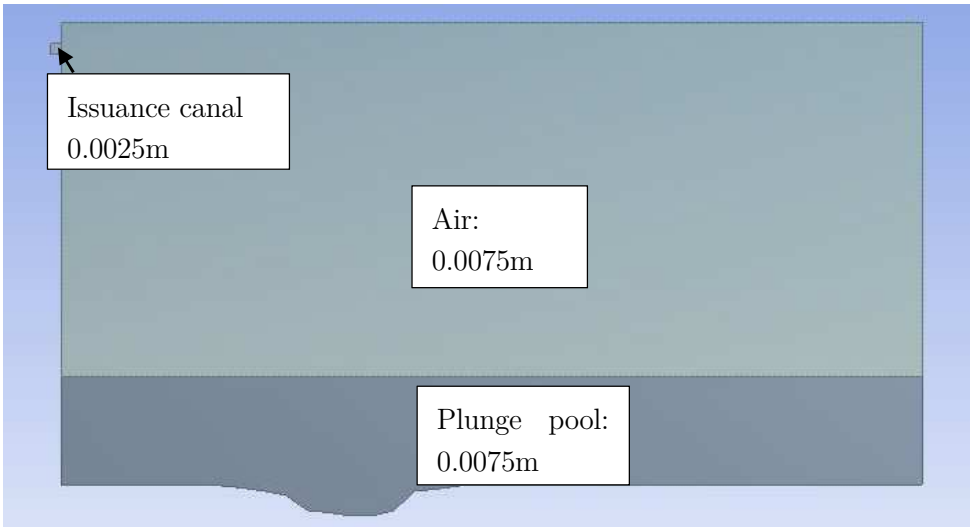

Figure 6-14 - Mesh cell sizes used in the numerical domain

As for the mesh refinement, the orthogonal quality and skewness values for the chosen mesh are shown in Table 6-12. The values fell in the good to very good ranges as indicated by Figure 6-3.

Table 6-12 - Skewness and orthogonal quality of mesh (final simulations)

Mesh cell size	Skewness	Orthogonal quality
0.0075m + 0.0025m (Figure 6-14)	0.25	0.75

6.5.1.3 *Scour hole repositioning*

From the initial simulations, it was found that for the 2m drop height simulations (including 0.25m and 0.5m tailwater depth), the jet impact location was offset from the location of the scour hole of the physical laboratory model by approximately 0.3m, as depicted in Figure 6-16. The position of the impacting jet, however, corresponded with the scour hole positions as calculated using the QSI and DI methods in Section 5.2.3, as opposed to the physical laboratory model results.

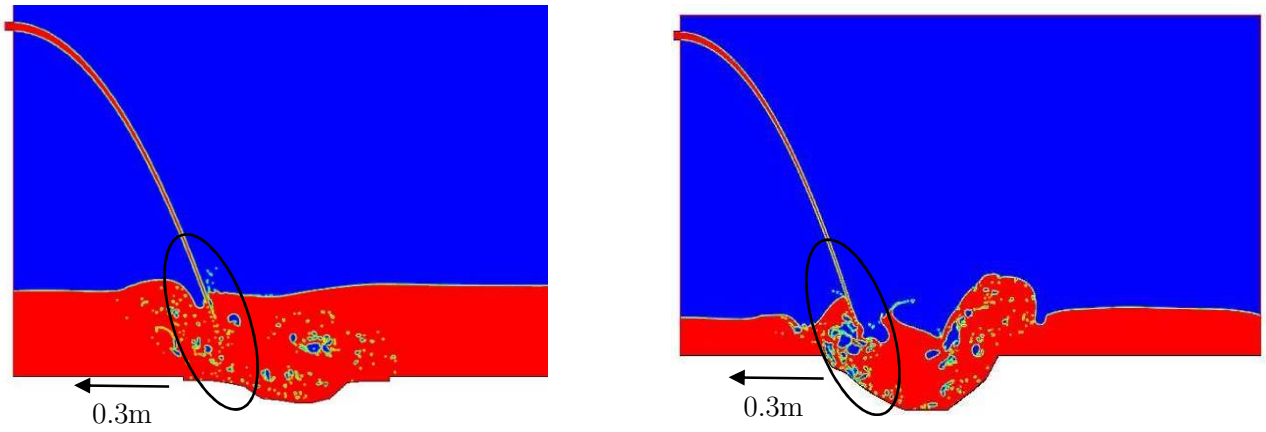

Figure 6-16 - Volume fraction contour plots illustrating offset jet impingement position for 2m + 0.5m (left) and 2m + 0.25m (right)

For the simulation results to agree with the physical laboratory model scour hole and impact location of the jet, the velocity at issuance had to be increased. The scour holes were subsequently relocated 0.3m upstream to ensure that the flow profile was not misrepresented in the scour hole by ensuring that the jet impacted the plunge pool correctly, rather than increasing the velocity. From further inspection it was found that the possible cause of the shifted scour hole position, could have been due to the pipe connection at issuance being bent at higher drop heights (Figure 6-17), but straight at the 2m drop height (0.25m and 0.5m tailwater depth), which changed the flow profile in the issuance canal. The straighter pipe was presumed to reduce the swirling flow, as well as the subsequent energy dissipation and turbulence intensity in the issuance canal, and thus allowing the jet to travel further downstream.

Figure 6-17 - Bended pipe connection at issuance

6.5.1.4 *Convergence*

Initially convergence was assumed to occur if the mass flow rate at the outlet coincided with the mass flow rate at issuance. The condition could, however, not be satisfied completely, due to the fluctuations in the plunge pool free surface level. As the velocities in the plunge pool were the most important variable required from the simulations, it was assumed that convergence occurred when the velocity profile and magnitudes at the centreline of the jet in the plunge pool reached a repeating pattern or did not change considerably over several time steps. A total duration of 3 seconds was subsequently determined for each of the simulations.

6.5.2 Final simulation results

The final simulations were run using the parameters and computational schemes which were determined from the preliminary simulations given in Section 6.5.1. The final simulations were run using the parameters and simulations schemes given in Table 6-13.

Table 6-13 - Final simulation parameters and schemes

Final simulations parameters	
Discretisation schemes	
Gradient	Least-Squares Cell-Based
Pressure (pressure based solver)	Body forced weighted
Momentum, Turbulent kinetic energy and Specific dissipation rate	Third order MUSCL (3rd order)
Volume fraction	Geo-reconstruct
Transient formulation	First order implicit
Computational models	
Turbulence	SST (shear stress transport) k-ω model
Multiphase	Volume of fluid (VOF)
Pressure-velocity coupling schemes	COUPLED
Mesh cell size	
Issuance canal	0.0025m
Air body	0.0075m
Plunge pool	0.0075m
Time step	
Time step	$5x10^{-4}$s

6.5.2.1 Behaviour of the jet in the air

(i) Trajectory

A comparison of the trajectory of the plunging jet for the 4m drop height, including 0.5m tailwater, as calculated using CFD, the ballistics equation, as well as the physical laboratory model, is presented in Figure 6-18. The trajectory as calculated using CFD and the ballistics equation (Eqn. 3-39) matched perfectly, as depicted in Figure 6-18 and compared well with the trajectory of the physical laboratory model.

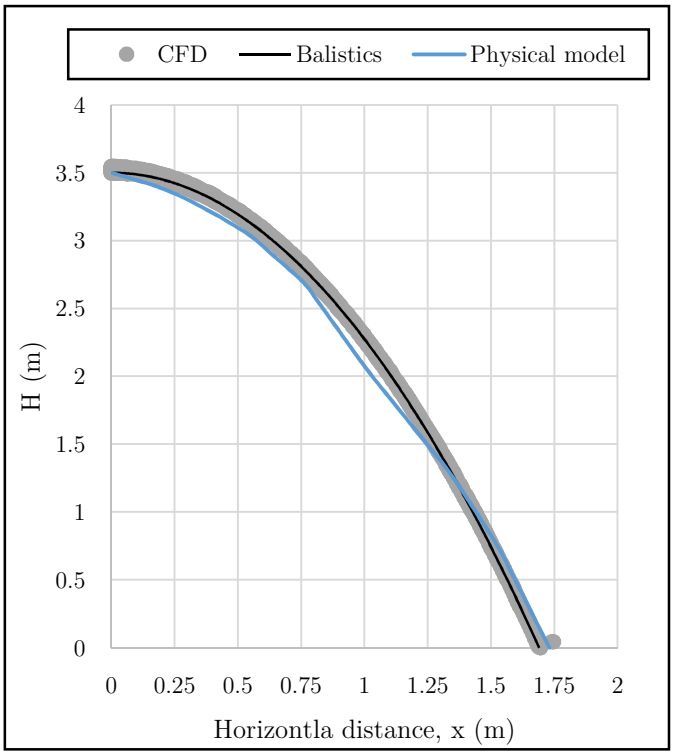

Figure 6-18 - Trajectory comparison (CFD, ballistics and physical laboratory model)

(ii) Condition of jet at impact

The condition of the jet at impact with the plunge pool free surface (developed or undeveloped) was determined by studying the volume fraction contour plots of the phases, specifically the primary phase (water), just before impact. From the volume fraction contour plots, it was established that the jet was developed at impact for all the conditions tested, except for the 2m drop height including 0.5m tailwater. A graphical representation of the disintegrated or developed jet at impact at the plunge pool free surface is presented in Figure 6-19 for the 2m drop height including 0.25m tailwater depth.

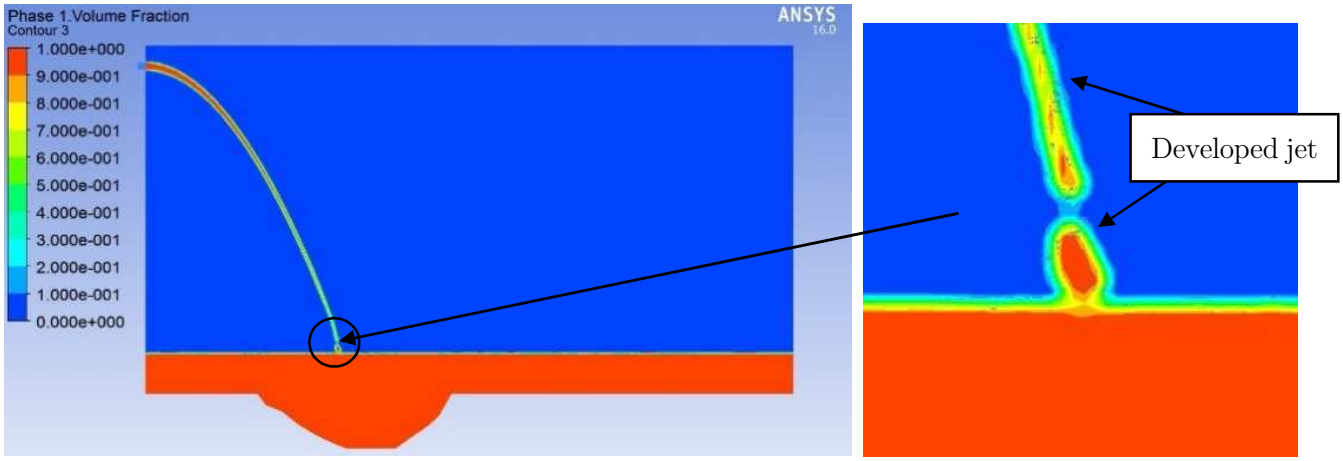

Figure 6-19 - Volume fraction contour plot of developed jet at impact (2m drop height including 0.25m tailwater) [red = water and blue = air]

The jet conditions compared relatively well to those determined from the physical laboratory model, as well as those calculated using the break-up length equation of Horeni (1956) (see Table 6-14). The break-up length calculated from using the formula proposed by Horeni (1956), however, indicated an undeveloped jet at the 3m drop height (0.5m tailwater depth), as well as the 2m drop height including 0.25m tailwater depth, whereas the numerical simulations indicated that a developed jet occurred at impact with the plunge pool free surface.

Table 6-14 - Jet core condition at impact with plunge pool free surface (CFD)

Property	**Value**			
Discharge (Q)	20l/s			
Tailwater (y_0)	0.5m			0.25m
Drop height (including tailwater)	2m	3m	4m	2m
Jet condition (Horeni)	UD	UD	D	UD
Jet condition (physical laboratory model)	UD	D	D	UD
Jet condition (CFD)	UD	D	D	D

Where:

UD = Undeveloped

D = Developed

The reason for the difference in jet condition might have been due to the dependency of the VOF method on the cell size to accurately simulate the boundary layer (free surface) of the plunging jet or due to the uncertainty regarding the applicability and accuracy of the break-up formulas, which were available.

6.5.2.2 *Properties of the jet at impact with the plunge pool free surface*

The properties of the jet at impact with the plunge pool free surface are shown in Table 6-15 as extracted from the simulations. The properties as calculated from the physical laboratory model (Section 4) and the calculated values (Section 5.1), using the approaches outlined in Section 3.3.2.2.1, are also included in Table 6-15, for comparison.

Table 6-15 - Jet properties at impact with plunge pool free surface (CFD)

Property	Value			
Discharge (Q)	20l/s			
Tailwater (y_0)	0.5m			0.25m
Drop height (including tailwater)	2m	3m	4m	2m
Velocity at impact (calculated)	5.78m/s	7.28m/s	6.2m/s	6.19m/s
Velocity at impact (CFD)	≈5.9m/s	≈7.3m/s	≈8.5m/s	≈6.25m/s
Impact thickness of the jet (calculated) (B_j)	0.03m	0.03m	0.04m	0.03m
Impact thickness of the jet (CFD)	≈0.03m	≈0.025m	≈0.02m	≈0.03m
Horizontal distance to impact (x) – physical laboratory model	1.13m	1.43m	1.73m	1.24m
Horizontal distance to impact (x) – calculated	1.11m	1.43m	1.69m	1.19m
Horizontal distance to impact (x) - CFD	≈1.1m	≈1.44m	≈1.69m	≈1.2m

Due to the similarity in trajectories, the horizontal distance to impact did not vary between the different approaches. The velocity at impact was similar to those calculated using the equation (Eqn. 3-34) proposed by Ervine and Falvey (1987) for compact jets. For the 4m drop height, including 0.5m tailwater depth, the velocity compared well to the velocity as calculated for a compact jet (Table 5-3) and not the velocity of a developed jet, as was proposed in Section 5.1.2.

The reason was presumed to be the manner in which the Eulerian model (VOF) interprets the solution in terms of a concentration field, as the phases are treated as a continuum (not individual particles), which is calculated from mass conservation principles [211,212]. The concentration field (volume fraction) as illustrated by Figure 6-19 clearly depicts that the model did not simulate small individual water droplets as was seen in the physical laboratory model. As the Eulerian model uses a concentration field (volume fraction), the areas where the jet was developed was illustrated as areas with the volume fraction of the primary phase (water) below one. The way in which the phases are treated as a continuum (air drag on individual particles ignored), was presumed to be the main reason why the velocity corresponded to the undeveloped (compact) jet impact velocity, rather than the developed jet impact velocity.

The impact thicknesses (B_j) of the jet from the CFD models compared relatively well to those calculated using the approach proposed by Castillo (2007) for the 2m drop height (0.25m and 0.5m tailwater depth), but for the 3m and 4m drop heights (0.5m tailwater depth), the thicknesses were found to be smaller than the thicknesses calculated. The reason was assumed to be due to the fact that the formula proposed

by Castillo (2007) (Eqn. 3-50) takes into account the spreading of the jet, while the CFD models did not. The difference in impact thickness might also have been due to the VOF method being highly dependent on the mesh cell size to accurately simulate the free surface of the plunging jet.

The simulated behaviour of the jet in the air and at impact with the plunge pool free surface, was thus found to compare favourably to the behaviour as calculated from the methods in literature (Ervine and Falvey), as well as the physical laboratory model results. This illustrated that CFD can be used as an alternative to accurately model the behaviour of the jet in the air.

6.5.2.3 *Behaviour of the jet in the plunge pool and at the scour hole bottom*

The behaviour of the jet in the plunge pool as well as at the scour hole bottom, was simulated using the scour hole profiles (shape and depth) as calculated from both the physical laboratory model as well as from using the QSI and DI methods. The simulation results are presented in Section 6.5.2.3.1 to Section 6.5.2.3.4 below.

6.5.2.3.1 Behaviour of the jet in the plunge pool – Physical laboratory model scour hole profiles (shape and depth)

This section includes the results of the simulations, which were run using the scour hole profiles (shape and depth) as calculated from the physical laboratory model. The velocity decay and pressure profiles at the centreline of the jet were extracted from the numerical domain using a line plotted along the centreline of the jet, as shown in Figure 6-20, for comparison with the values as calculated in Section 5.1.3.

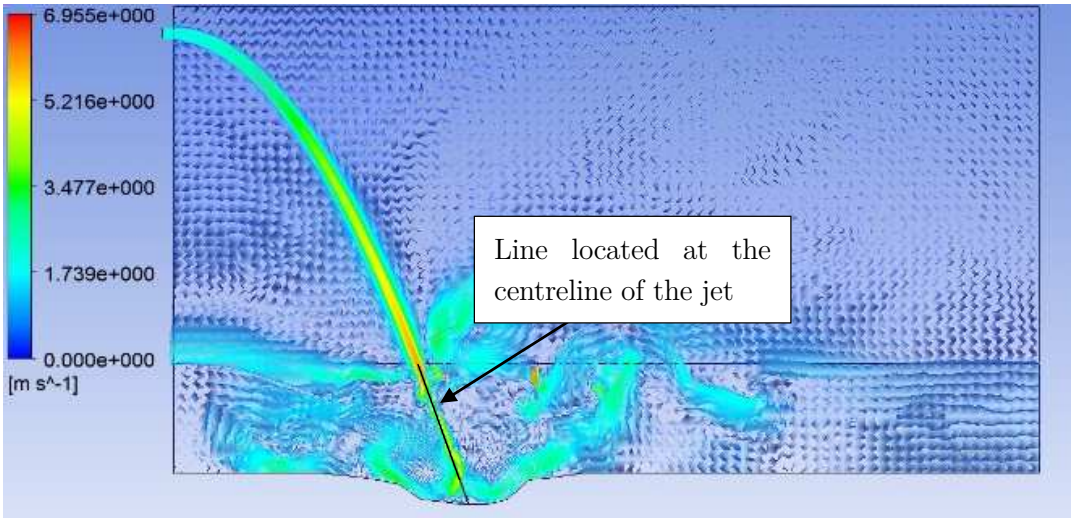

Figure 6-20 - Location of line at the centreline of the jet used for extraction of variables (velocity and pressure)

As the velocity and pressure profiles were different between time steps, the values were extracted at different time stages in the simulation for a more accurate assessment. The values were extracted using the post processor and the data files which were saved after a number of time steps for each simulation (100 time steps were used). The data, which corresponded with the approximate time of 1s, 1.5s, 2s, 2.5s, and 3s was subsequently assessed. For the pressures, the "Total pressure" values were extracted, which included the static, as well as the dynamic pressure at the centreline of the jet, while for the velocity the "Velocity" values were extracted. The velocitiues and pressures extracted were instantaneous. Generally mean velocities and pressures are determined for turbulent simulations. Due to the number of locations at which the velocities and pressures were taken and the number of simulations which were run, the instantaneous velocities and pressures taken at different timesteps were extracted for simplicity and plotted against the empirically calculated velocity and pressure decay profiles at the centreline of the jet.

(i) Velocity decay

The velocity decay profiles (instantaneous) at the centreline of the jet in the plunge pool are presented in Figure 6-21 (a-c) at five different time stages in the simulation for the different drop heights and tailwater levels tested. The velocity decay profiles, using the methods of Hartung and Hausler (1973), as well as Ervine and Falvey (1987) as calculated in Section 5.1.3.2 are also plotted for comparison. As the velocity profile was not determined during the physical laboratory modelling, the calculated velocity decay methods were used for comparison.

(a)

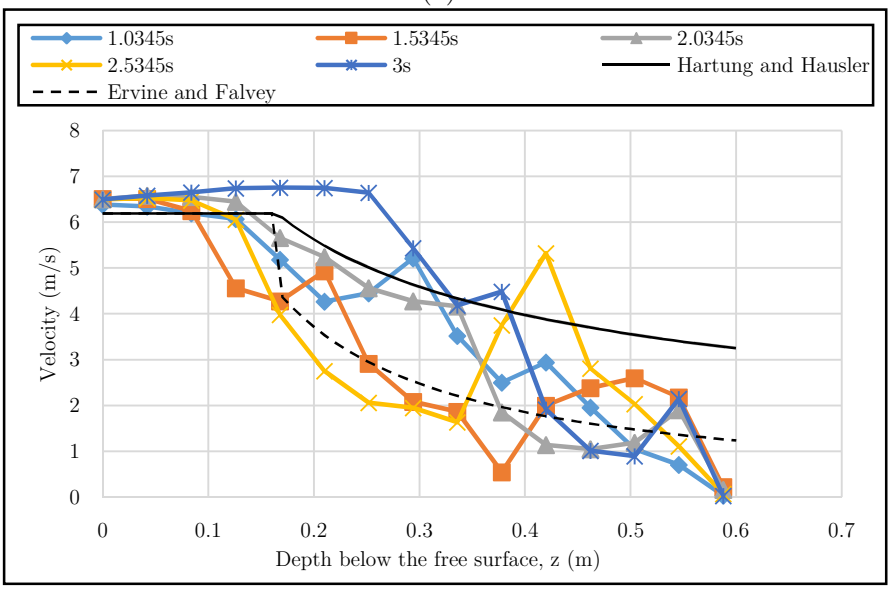

(b)

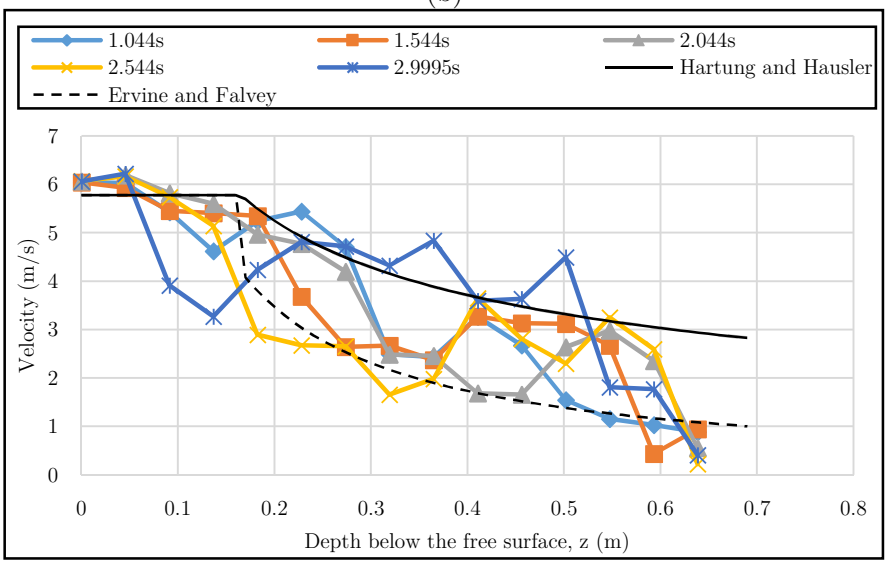

(c)

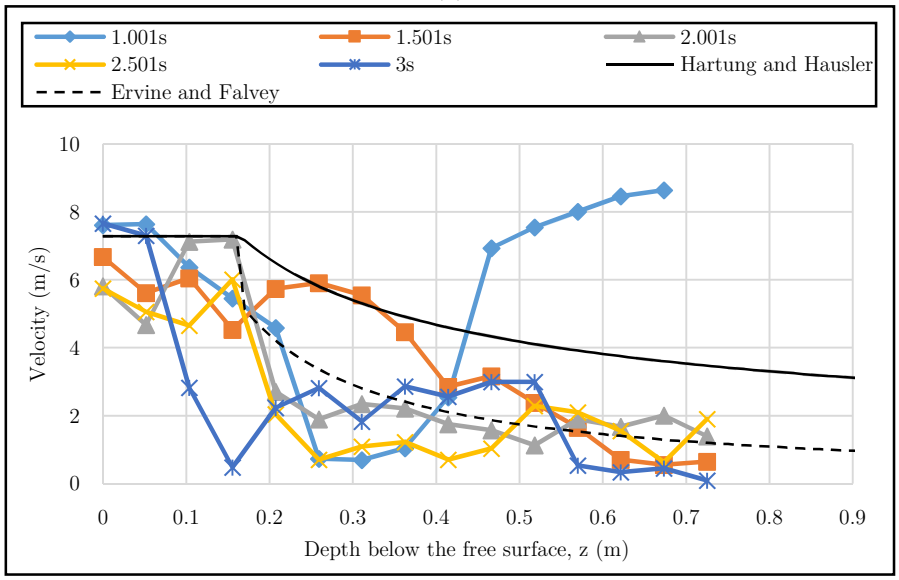

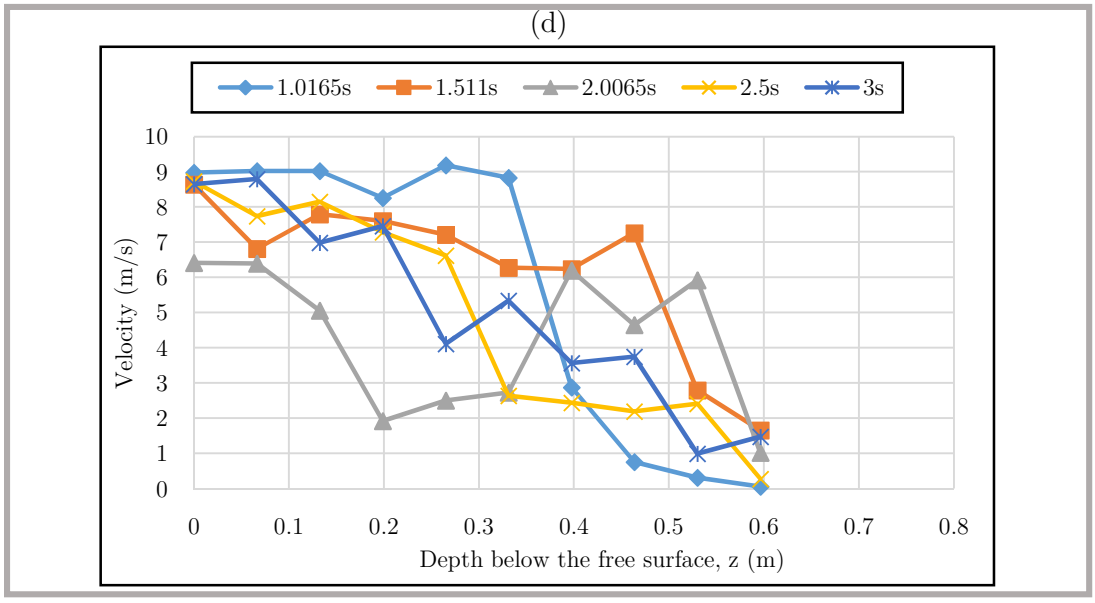

Figure 6-21 - Centreline velocity decay in the plunge pool
a) 2m drop height including 0.25m tailwater
b) 2m drop height including 0.5m tailwater
c) 3m drop height including 0.5m tailwater
d) 4m drop height including 0.5m tailwater

The velocities as extracted from the simulations, for all the undeveloped jet conditions tested, were scattered around the calculated velocity decay profiles. The velocities fluctuated between the two curves and there was no direct correlation to one specific velocity decay profile.

The large spike in the velocity profile for the simulation at 1.001s for the 3m drop height, including 0.5m tailwater, as highlighted in Figure 6-22, was due to the air entrained (developed) jet being separated from the plunge pool. This was presumed due to the process in which the VOF models immiscible (non-interpenetrating) fluids (water and air), as shown in Figure 6-22. Due to the flow separation, no energy dissipation in the plunge pool occurred and the velocity was thus higher than expected.

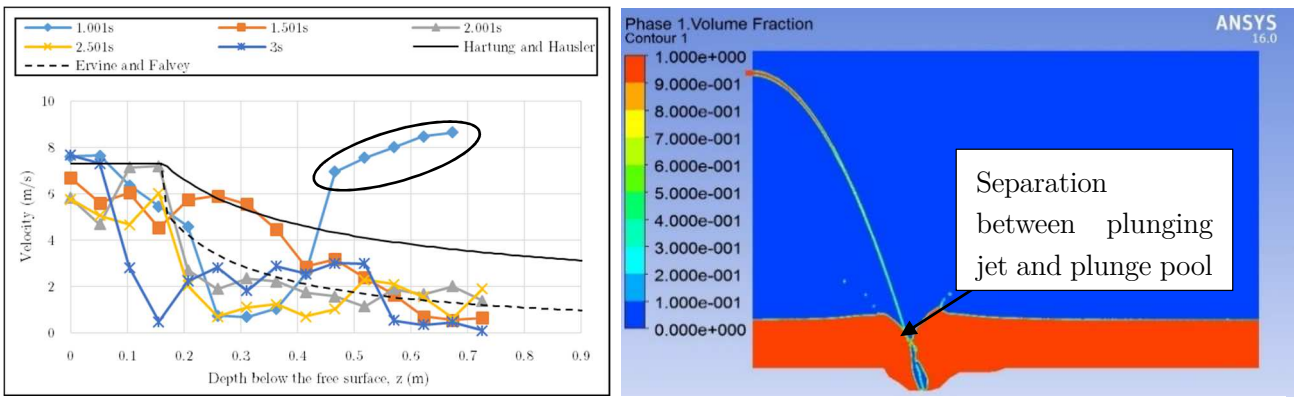

Figure 6-22 - Initial separation between developed jet and plunge pool causing spike in velocity decay profile.

Apart from the spike occurring due to flow separation (3m drop height), other spikes were also present in the velocity decay profiles. The spikes in the velocity profiles were initially presumed to be due to the entrained air present in the plunge pool, as the spikes correlated to the entrained air locations at some depths (Figure 6-23). The entrained air influenced the velocity profile in the plunge pool (vortices formed at entrained air locations), but was not the main reason for the spikes in the velocity decay profile.

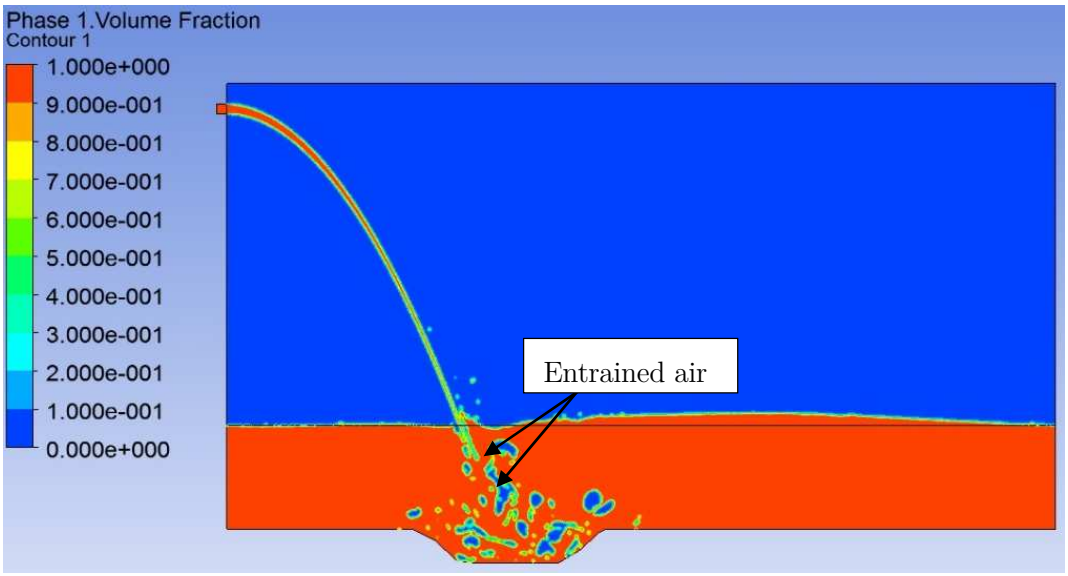

Figure 6-23 - Entrained air along the jet centreline in the plunge pool

From further inspection, the spikes were found to be primarily due to the scour hole deflecting the flow, and recirculation occurring, which subsequently increased the velocity. This is illustrated through the zoomed-in velocity plot in the plunge pool depicted in Figure 6-24.

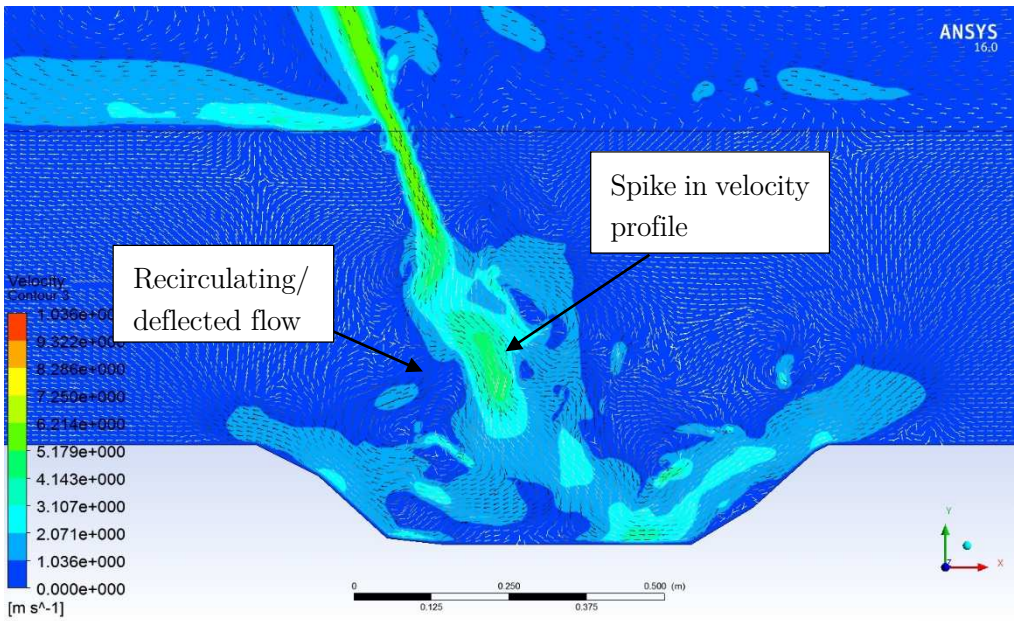

Figure 6-24 - Recirculating flow impacting the velocity profile

For the 4m drop height including 0.5m tailwater, the velocity decay profile could not be compared, due to the presence of a developed jet at impact.

(ii) Pressure

The pressures (instantaneous), as extracted from the numerical simulations, were plotted against the calculated pressures using the equations proposed by Castillo (2014) (see Section 5.1.3.1), as the pressures were not determined from the physical laboratory model. The pressure profiles, at the centreline of the jet, are shown graphically in Figure 6-25 (a-d) for the different drop heights and tailwater levels tested at different time stages in the simulation.

(a)

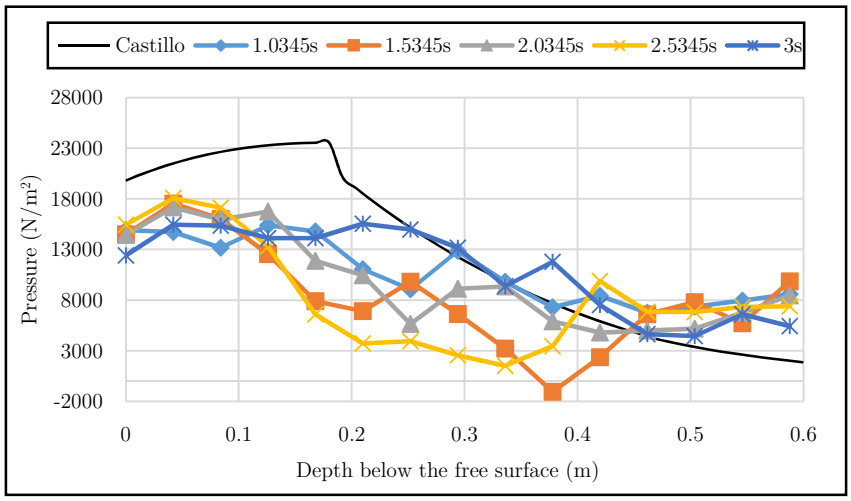

(b)

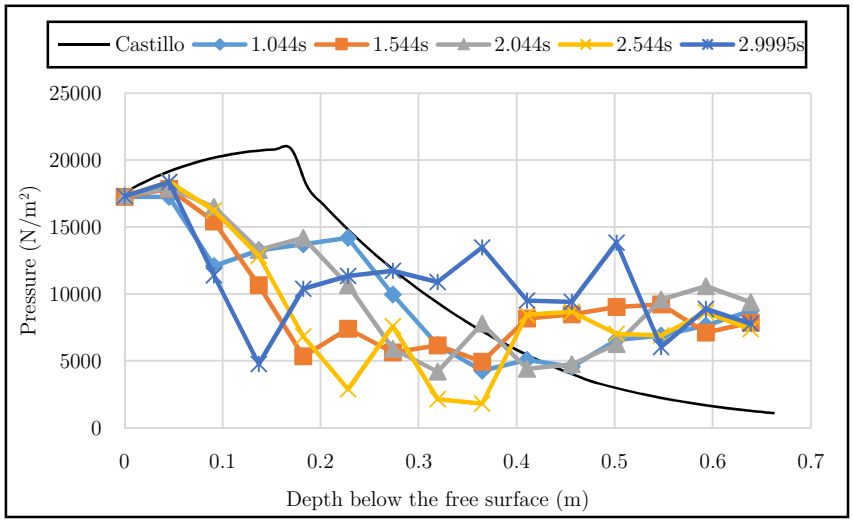

Figure 6-25 - Centreline pressure profile in the plunge pool
a) 2m drop height including 0.25m tailwater
b) 2m drop height including 0.5m tailwater
c) 3m drop height including 0.5m tailwater
d) 4m drop height including 0.5m tailwater

The extracted pressure profiles were found to be lower than the calculated profiles up to a depth of 0.3m to 0.4m ($Y/B_j < 10$ or 13), where after the extracted pressures were found to be higher than the calculated values. The pressure profile for the 4m drop height including 0.5m tailwater showed a more pronounced fluctuating profile as compared to the other pressure profiles. It was presumed to be due to the highly developed nature of the jet at impact, which influenced the flow profile in the plunge pool because of the

entrained air present. Due to the highly fluctuating pressure profile, both the pressure profile of the undeveloped, as well as developed jet was plotted on the same graph for comparison.

As for the velocity profile, the spike in pressure profile for the simulation at 1.001s for the 3m drop height including 0.5m tailwater, as shown in Figure 6-25, was due to VOF method initially separating the developed jet from the plunge pool, due to the process in which the VOF models immiscible fluids, as shown in Figure 6-22.

Similarly, to the spikes in the velocity profiles, the spikes in pressure profiles were presumed to be mainly due to the deflected and recirculated flow. The depths at which the spikes in the pressure profile occurred, corresponded to the depths below the free surface at which the spikes in the velocity profiles occurred, which motivated this assumption.

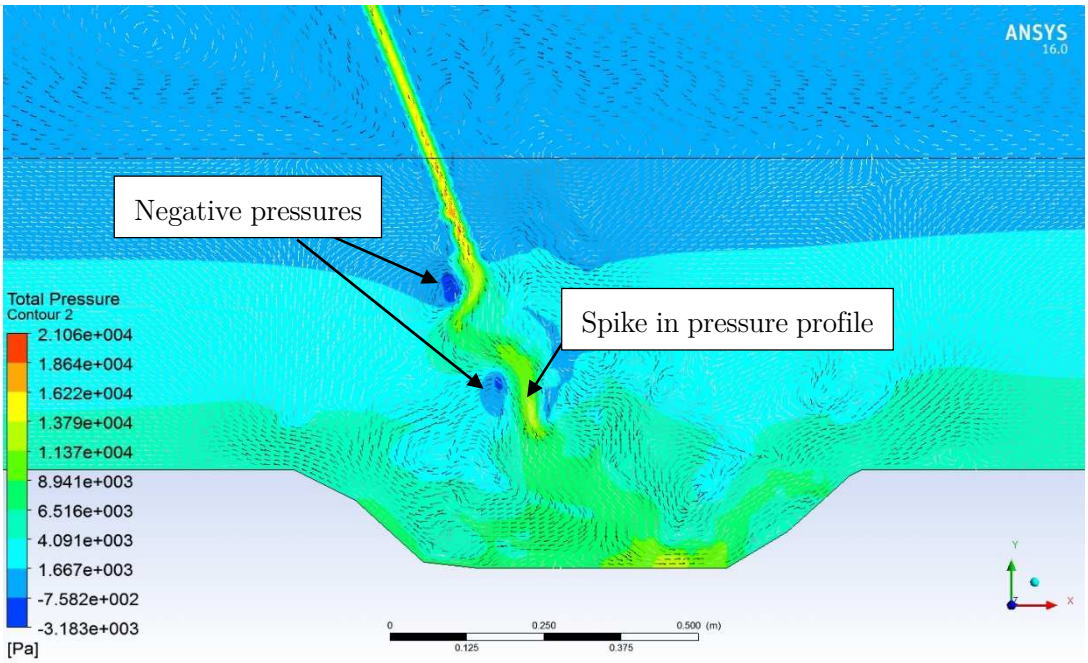

Figure 6-26 - Pressure profile in the plunge pool

There were negative pressures present in some of the simulations. Figure 6-26 shows the locations of the negative pressure regions, which correspond to the positions of the entrained air, depicted in Figure 6-23.

6.5.2.3.2 Behaviour of the jet at the scour hole bottom – Physical laboratory model scour hole profiles (shape and depth)

The deflected wall jet velocities (instantaneous) along the bottom of the scour hole were extracted from the CFD models to compare with the required velocity, as calculated using the Quasi-steady impulsion method given in Table 5-13. Points along the bottom of the scour hole were specified, as depicted in Figure 6-27, from which the velocities, at different time stages of the simulation, were extracted. The number and location of points between simulations varied as the shape of the scour hole was altered in accordance to the scour hole geometry calculated in the physical laboratory models.

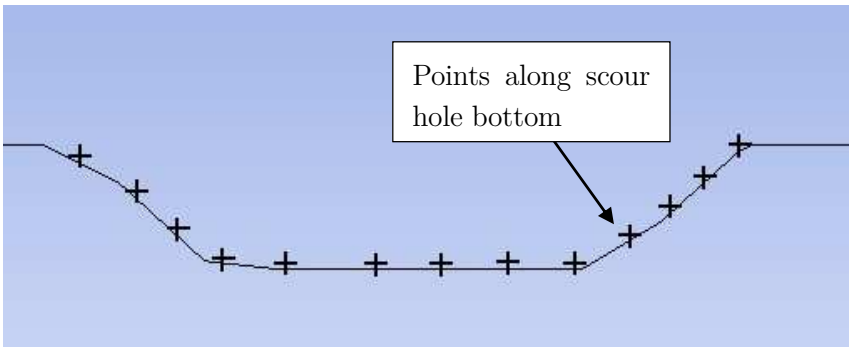

Figure 6-27 - Location of points along the bottom of the scour hole for velocity extraction

In previous studies (Section 3.3.2.2.3) a decreasing velocity profile was found to occur downstream and upstream from the point of impingement (jet centreline), as shown graphically in Figure 6-28 [128]. Previous studies used a flat plunge pool bottom, which was not the case in this study. A constant, or a velocity lower than the required velocity for uplift to take place (QSI method), was expected to occur along the bottom of the scour hole profile (shape and depth), if the scour hole had reached its equilibrium scour hole state.

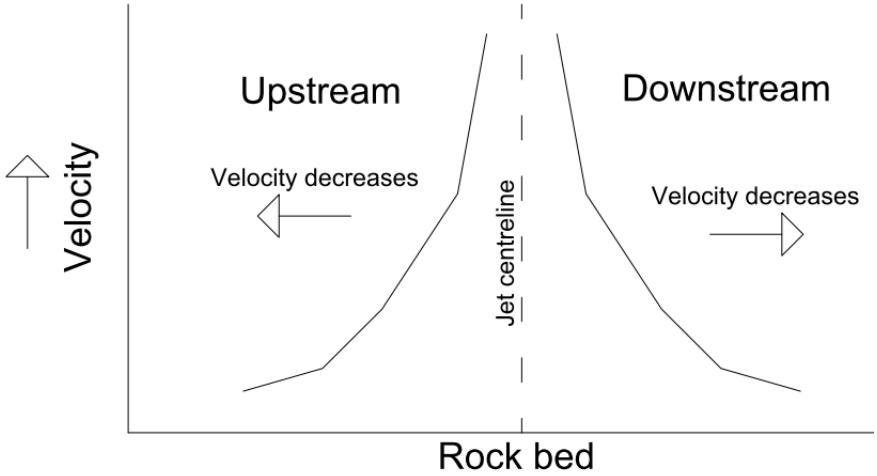

Figure 6-28 - Decreasing velocity profile upstream and downstream of point of impingement (centreline)

The extracted velocities were subsequently plotted against the required velocity for impulsion to occur, as shown graphically in Figure 6-29 (a-d). The horizontal distance in Figure 6-29 implied the horizontal distance from the issuance structure.

(a)

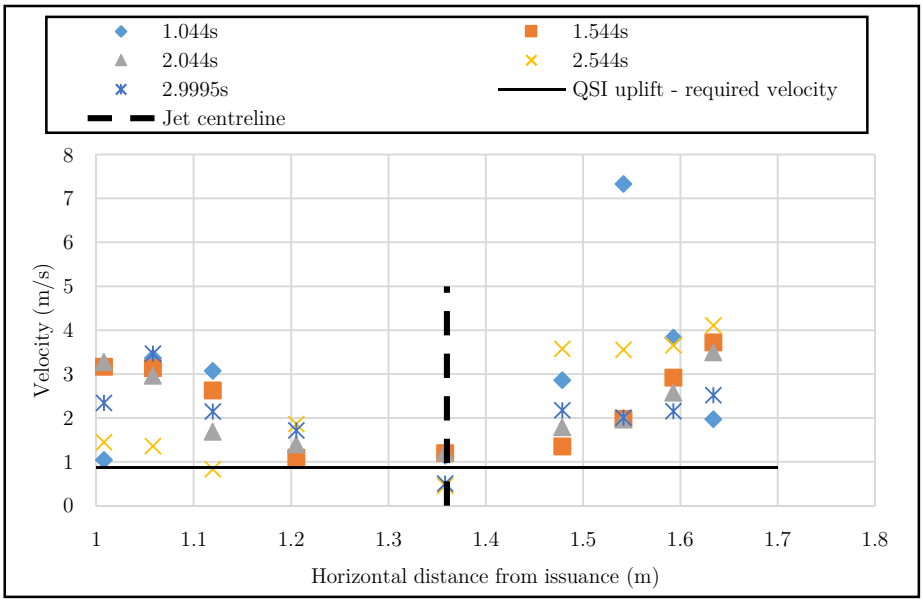

(b)

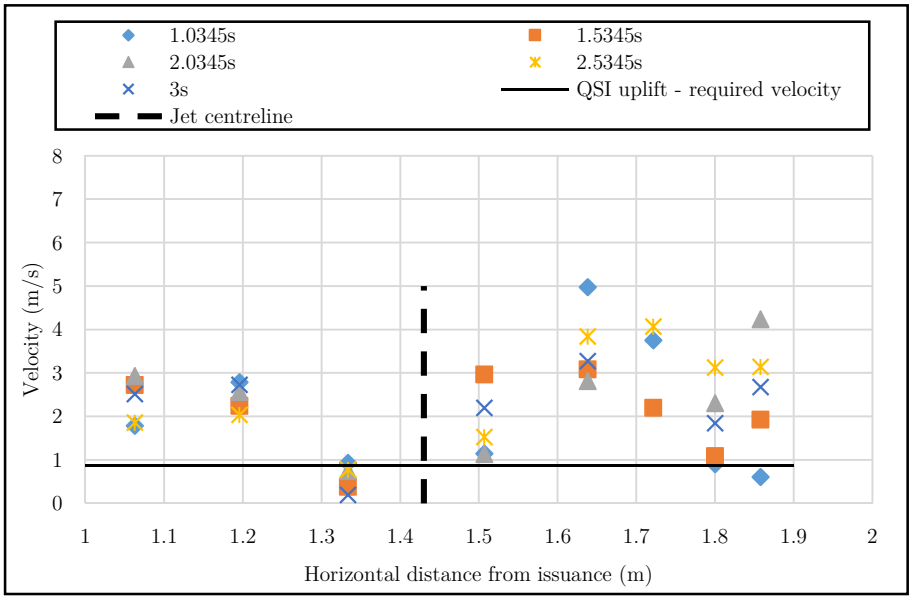

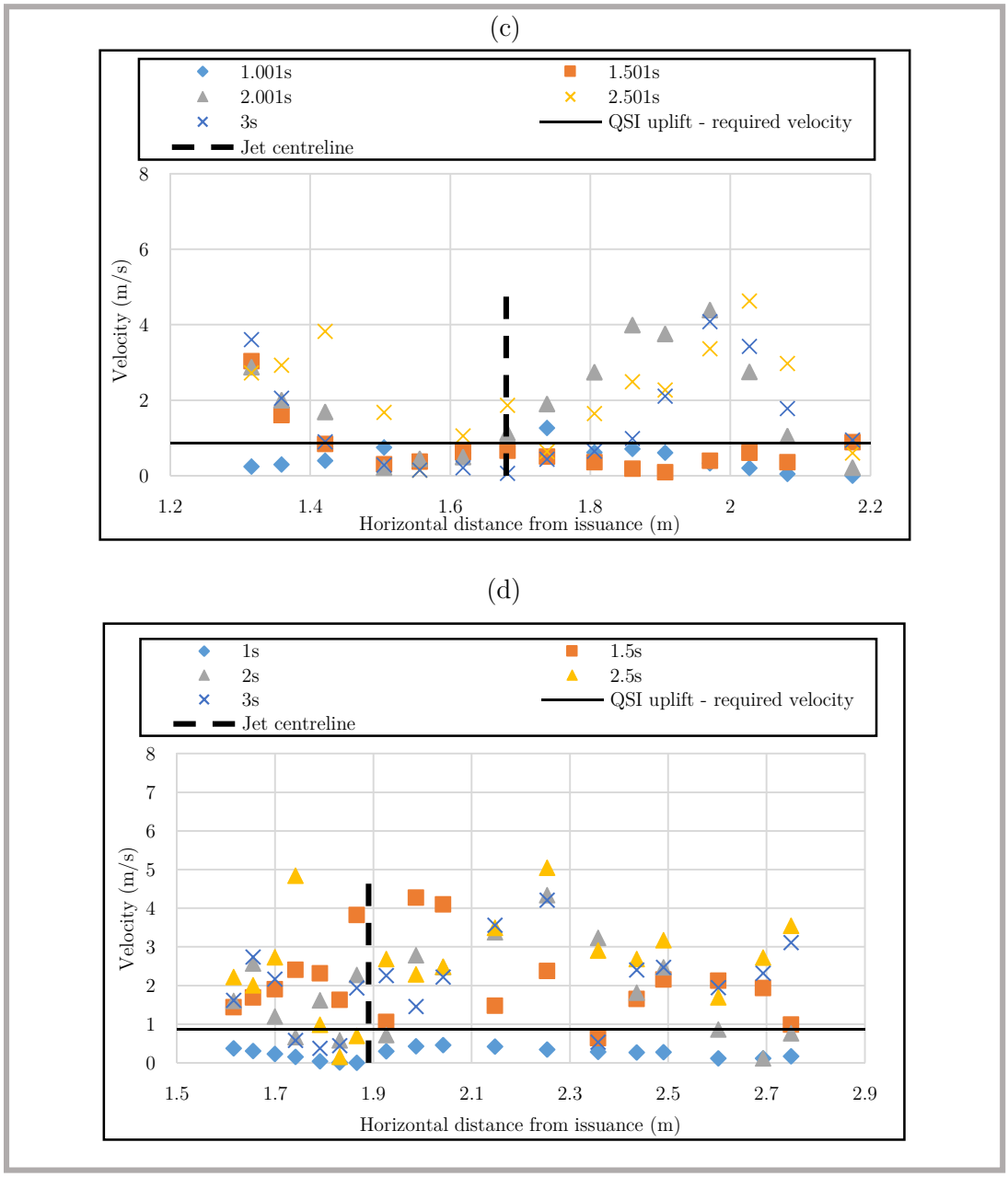

Figure 6-29 - Velocities along the bottom of the scour hole
a) 2m drop height including 0.25m tailwater
b) 2m drop height including 0.5m tailwater
c) 3m drop height including 0.5m tailwater
d) 4m drop height including 0.5m tailwater

From the graphs shown in Figure 6-29 (a-d), the velocity profiles along the scour hole bottom were fluctuating and the magnitude of the velocities from the CFD simulations were much higher than the required velocity, as calculated for quasi-steady uplift to occur. It should be noted that the velocities at the impingement region were ignored, as the QSI method is only applicable outside the impingement region [125].

From the extracted CFD velocity profiles shown in Figure 6-29 (a-d), it was clear that the physical laboratory model scour holes had not reached their equilibrium state, as the velocities were higher than the velocity required for uplift to occur. The velocities extracted along the bottom were found to be higher than, or in the same order of magnitude as, the impact velocity shown in Figure 6-21. This was assumed to be due to the confinement effects (recirculation and deflection), as well as the entrained air in the plunge pool.

6.5.2.3.3 Behaviour of the jet in the plunge pool – QSI and DI method scour hole profiles (shape and depth)

A similar procedure was implemented in simulating the plunging jet using the scour hole profiles (shape and depth) as calculated using the DI and QSI methods (Section 5.2.3) as was employed in the preceding section using the physically modelled scour hole profiles (shape and depth). Due to the similarity in numerical domains, apart from the scour hole profile (shape and depth), the interpolation function was used to initialise the solution up to where the jet was located just before impacting the plunge pool to reduce the run time required by using the solution files of the previous simulations. The velocity decay, as well as the pressure profile along the centreline of the jet in the plunge pool is presented in the subsequent sections below. Due to the presence of a developed jet at impact with the plunge pool free surface for the 4m drop height including 0.5m tailwater depth test, the simulation was excluded as no scour hole profile (shape and depth) could be calculated using the QSI and DI methods.

(i) Velocity decay

The velocity decay profiles as extracted at the centreline of the jet are shown in Figure 6-30 (a-c).

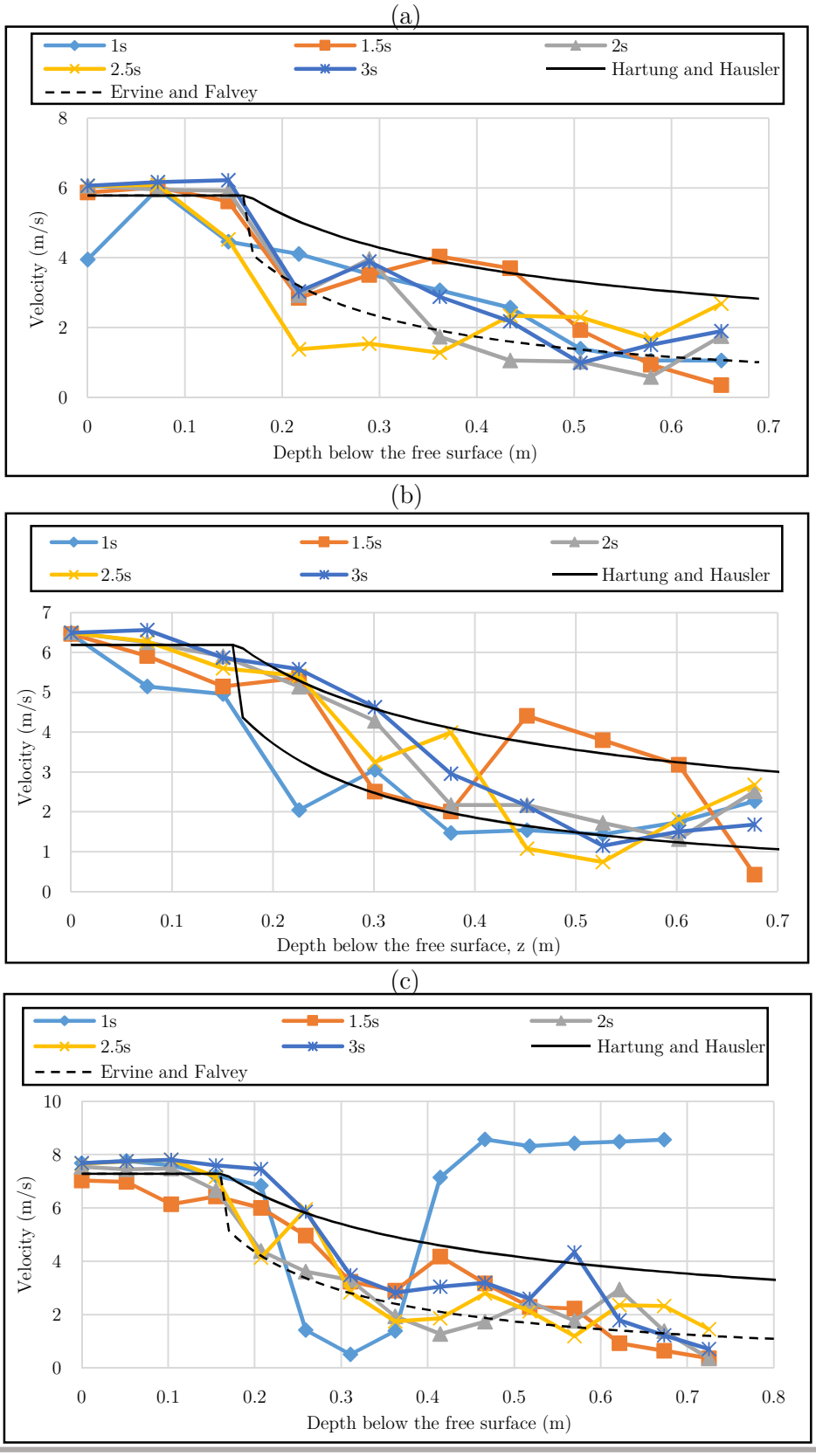

Figure 6-30 - Centreline velocity decay in the plunge pool

a) 2m drop height including 0.25m tailwater

b) 2m drop height including 0.5m tailwater

c) 3m drop height including 0.5m tailwater

The velocity decay profiles at the centreline of the jet, as extracted from the CFD models, were situated between the calculated velocity profiles (Ervine and Falvey (1987) and Hartung and Hausler (1973)), similarly to the velocity profiles extracted using the physical laboratory model scour hole profiles (shape and depth), as can be seen in Figure 6-30 (a-c). The extracted velocity profiles extracted correlated slightly better to the profiles, as calculated using the approach of Ervine and Falvey (1987), as can be seen in Figure 6-30 (a-c). This confirmed the assumption in Section 5.2.3 to use the method proposed by Ervine and Falvey (1987) to determine the scour hole profile (shape and depth). The larger and deeper scour hole profiles (shape and depth) were assumed to be the reason for the improved correlation between the calculated and simulated velocity decay profiles, as the effect of the wall boundaries (confinement – deflection and recirculation) on the flow was less profound.

(ii) Pressure

The pressure profiles, as extracted at the centreline of the jet, are shown in Figure 6-31 (a-c).

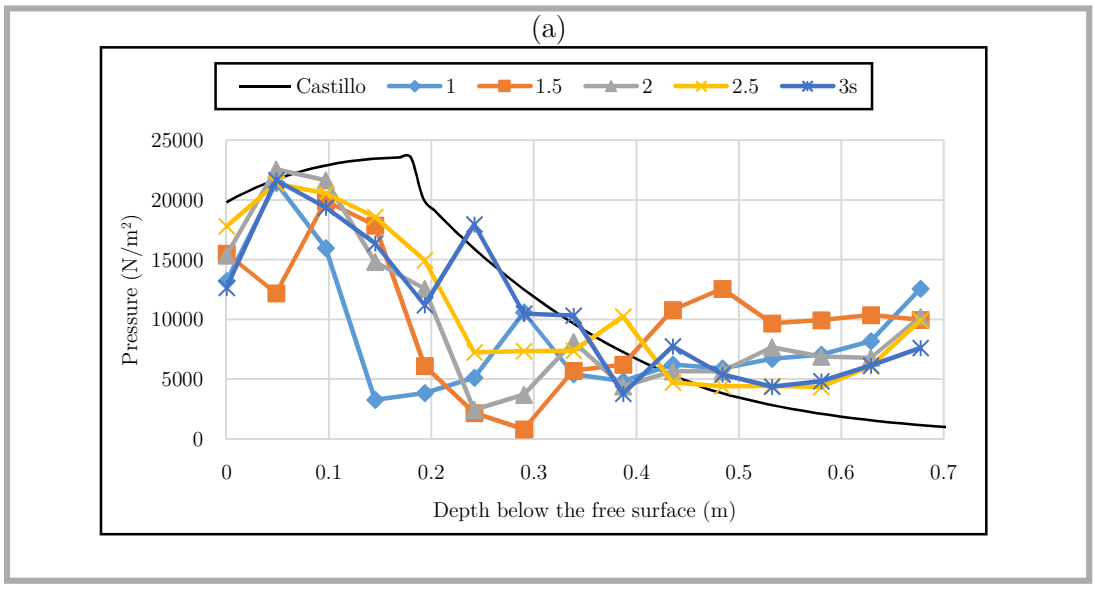

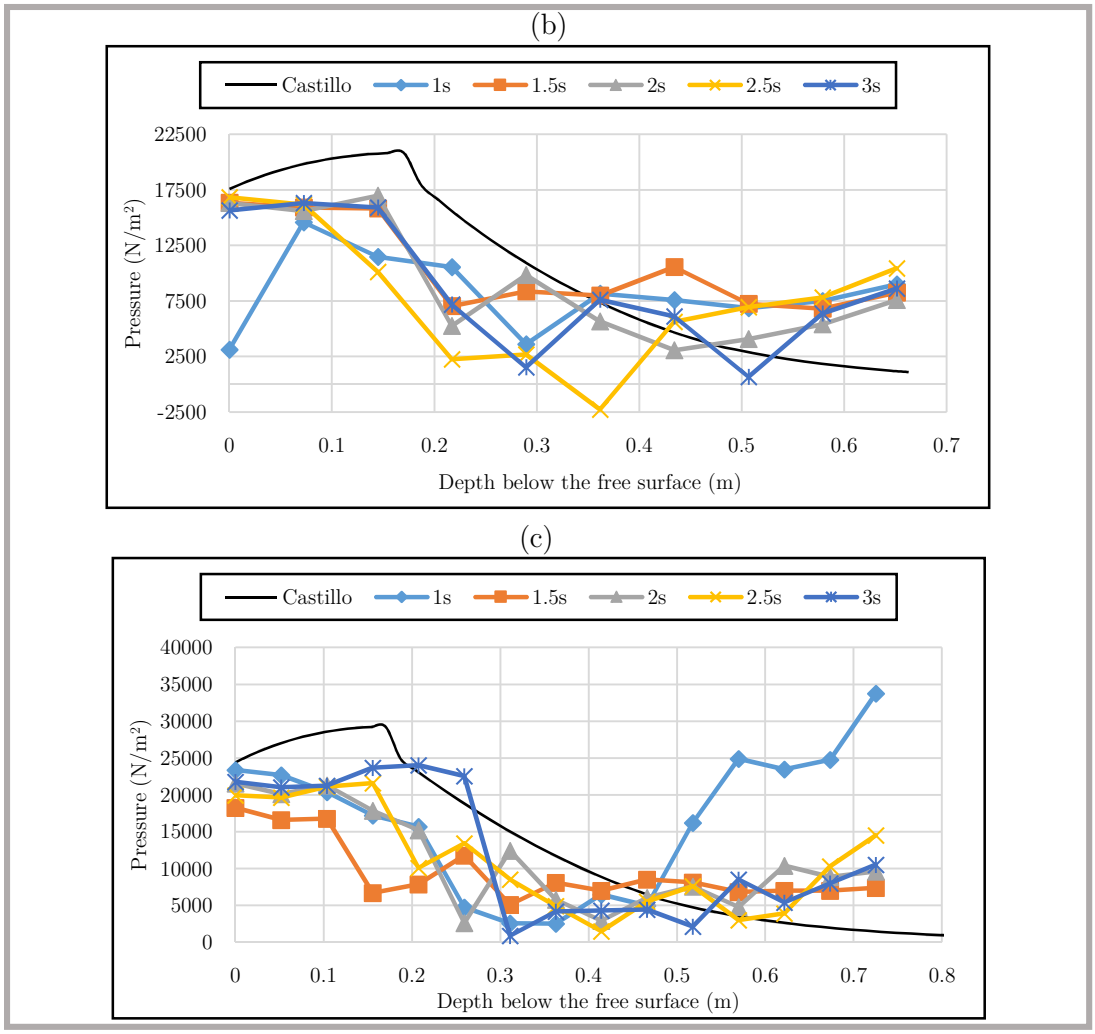

Figure 6-31 - Centreline pressure profile in the plunge pool
a) 2m drop height including 0.5m tailwater
b) 2m drop height including 0.25m tailwater
c) 3m drop height including 0.5m tailwater

A better correlation was found between the extracted CFD pressure profiles along the centreline of the jet and the calculated pressure profile (Castillo, 2014), using the calculated scour hole profiles (shape and depth) (QSI and DI methods), as opposed to using the physical laboratory model scour hole profiles (shape and depth), as can be seen in Figure 6-31 (a-c). As for the velocity profiles, the larger and deeper scour hole profiles (shape and depth) were assumed to be the reason for the improved correlation between the pressure profiles, as the effect of the wall boundary (confinement – deflection and recirculation) on the flow was less profound. The same reasons also hold true for the spikes in the pressure and velocity profiles and the negative pressures, as was determined in the preceding section (Section 6.5.2.3.1).

From the CFD results, it could be seen that, when using the scour hole geometry, as calculated using the DI and QSI methods (Bollaert, 2012), the velocity and pressure profiles at the centreline of the jet correlated better to empirically based methods (Castillo (2014) and Ervine and Falvey (1987)). The increase in the correlation was presumed to be due to the wall boundaries (rock bed) being situated further away and subsequently having a smaller effect on the flow profile. It should also be noted that the empirically based methods (Castillo (2014) and Ervine and Falvey (1987)) used in calculating the velocity and pressure profiles in the plunge pool were developed using a flat bottom and the confinement effects of the scour hole was not taken into account.

6.5.2.3.4 Behaviour of the jet at the scour hole bottom – QSI and DI method scour hole profiles (shape and depth)

The scour hole profiles (shape and depth) calculated using the QSI and DI methods were larger than the scour holes produced in the physical laboratory models. The velocities along the scour hole bottom were thus presumed to be lower than the velocities as calculated in the preceding section. The extracted velocities along the scour hole bottom were plotted against the required velocity for impulsion to occur, as shown graphically in Figure 6-32 (a-c).

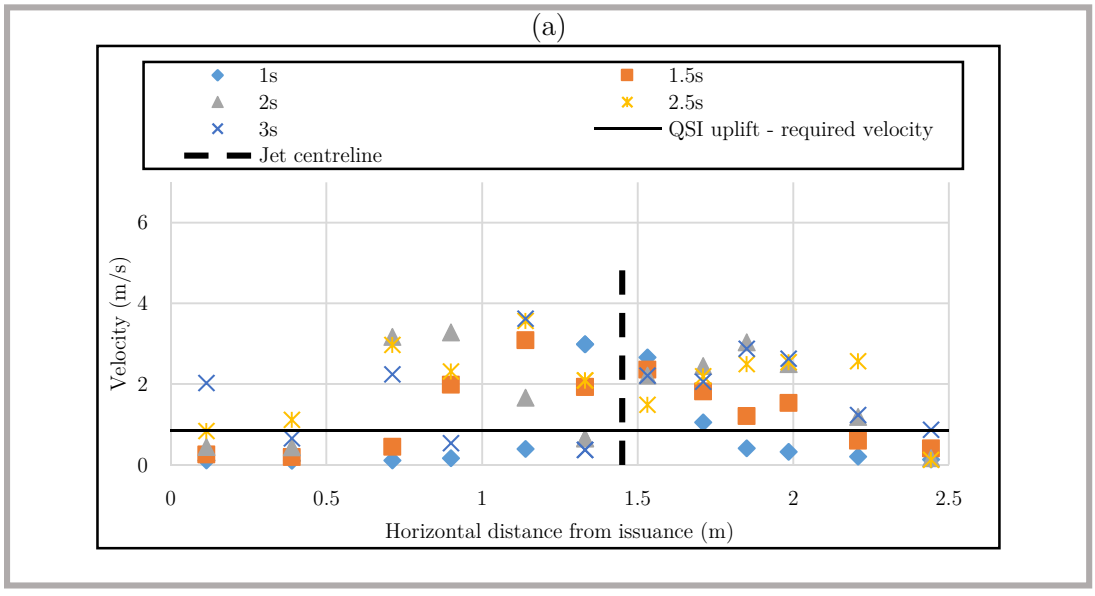

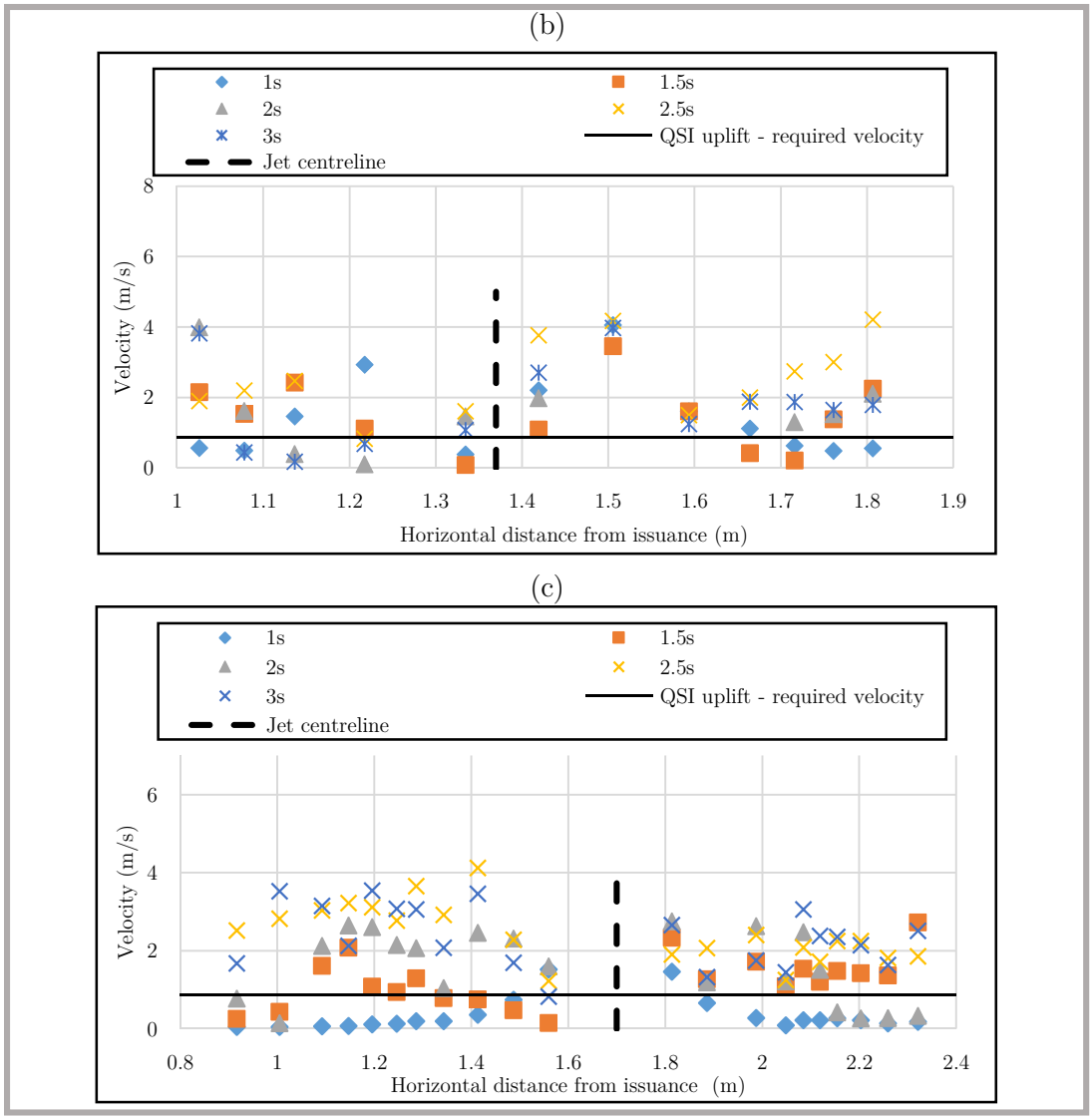

Figure 6-32 - Velocities along the bottom of the scour hole
a) 2m drop height including 0.25m tailwater
b) 2m drop height including 0.5m tailwater
c) 3m drop height including 0.5m tailwater

As for the physical laboratory model scour hole geometry simulations, the velocities along the bottom of the scour hole were found to be substantially higher than the velocity required for quasi-steady uplift to occur. A reduction in the velocity magnitude can, however, be seen when comparing the velocities along the scour hole bottom in Figure 6-32 (a-c) (QSI and DI method scour hole profiles (shape and depth)) to those shown in Figure 6-29 (a-c) (physical laboratory model scour hole profiles (shape and depth)). This was presumed to be due to the larger and deeper scour hole profile (shape and depth), which subsequently had a less profound effect on the flow profile in the plunge pool due to the wall boundary (confinement – deflection and recirculation).

Initially it was proposed that the velocity required to cause quasi-steady uplift should be used to determine if the calculated and physically modelled scour holes reached equilibrium. As the wall jet velocity profiles along the bottom of the scour holes, extracted from the CFD models, showed significantly higher velocity magnitudes than the calculated required velocity for quasi-steady uplift to occur, the equilibrium state was not reached according to the CFD results.

As the reduction in velocity along the bottom of the scour hole was not significant enough between the different scour holes (DI and QSI method calculated and physical laboratory model), as shown in Figure 6-33, it was deemed ineffective to increase the scour hole geometry in a trial and error basis until the scour hole reached an equilibrium state.

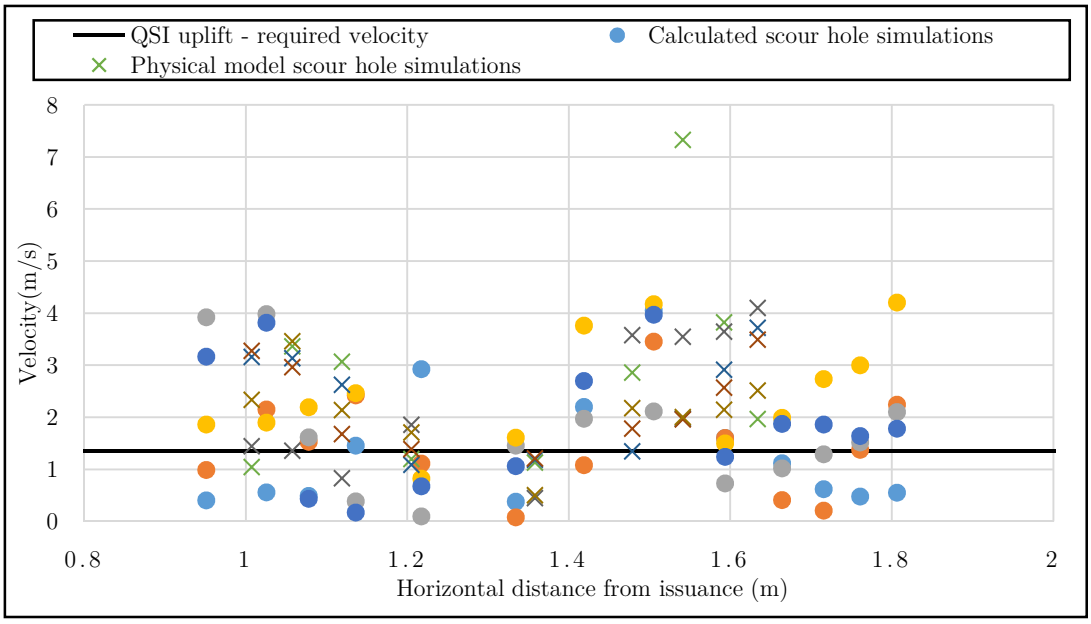

Figure 6-33 - Comparison between calculated scour hole velocities and physical laboratory model scour hole velocities as extracted from the CFD simulations (2m drop height including 0.5m tailwater depth)

The time required to complete a trial and error approach would also become excessive. Due to the wall boundary (scour hole) and the entrained air having a significant effect on the flow profile, which subsequently caused a misrepresentation of the flow in the scour hole, it was suggested that further research is required into using CFD modelling, especially 3D simulations as the flow influence may be negated. Additionally there were various uncertainties and simplifications regarding the current methods used to determine the required velocity for quasi-steady uplift to occur, which required further investigation.

7 Conclusions and Recommendations

7.1 Conclusions

The conclusions of each respective section (physical laboratory model, the prediction methods and CFD) are given below.

(i) Physical laboratory model

The secondary aim of the study was to attempt to replicate the scouring of rock blocks using PVC blocks in a scaled physical laboratory model. The study found that the use of the PVC blocks, instead of using a non-cohesive sediment such as gravel, produced scour holes, which could sustain steeper slopes as is expected for prototype rock scouring. The PVC blocks were, however, extremely expensive and the setup was time consuming due to the large amount of blocks required to be packed individually to form the broken up rock mass. The use of the PVC blocks can, however, serve as an alternative for non-cohesive sediment to replicate the scouring of rock blocks in physical laboratory model studies. As the physical laboratory model was not the primary focus of the study, because a parallel study was done focussing on the physical laboratory modelling, as well as due to time constraints, further research regarding both the physical laboratory model setup conditions and the PVC blocks is required.

(ii) Physically based prediction methods

Due to the hypothetical nature of the physical laboratory model conditions tested, no case study was available to verify and validate the results of the physical laboratory model. As an alternative, the use of physically based scour prediction methods (EIM and CSM) were used, as both methods have been used relatively successfully in past studies and are currently the leading methods when determining prototype rock scouring. The scour hole profiles (shape and depth) compared relatively well between the physical laboratory model and those calculated using the two methods. The CSM, including the QSI method, overestimated the scour hole profile (shape and depth), while the EIM method was very sensitive to the Mass strength number and the Interparticle bond strength factor applied. The two methods were originally developed for prototype scour prediction.

The CSM method was also developed using undeveloped circular jets, while the study focused on rectangular jets (undeveloped and developed). Due to the physically based methods' effectiveness in calculating the scour hole profiles (shape and depth) (shape and depth) in this study, it illustrated the robustness of their use in even small scale studies using rectangular jets. There were, however, numerous uncertainties and difficulties regarding several of the calculation parameters, such as the break-up length and the impact thickness, which require further study.

(iii) CFD analysis

Due to the advancements in computational power, the use of CFD software has become more desirable. As CFD was still not able to model the rock scour mechanisms, the commercial CFD code FLUENT was used to simulate the hydrodynamic characteristics of the rectangular plunging jet in the air and in the plunge pool.

The study looked at 2D simulations as opposed to 3D simulations for simplicity, and because the analytical and empirical methods against which they were compared against, were developed for 2D. The 2D simulations produced relatively accurate results and the velocity, as well as the pressure profiles, correlated to a certain extent. Due to the uncertainty regarding the analytical methods and their respective parameters, the results were concluded to be adequate. Additionally, the current multiphase models can simulate either the plunging jet in the air and the free surface profile (VOF method) or the jet behaviour in the plunge pool (Eulerian or Mixture model), with relative accuracy. Due to the variance between dispersed and stratified flow regimes when simulating plunging jets, especially developed jets, in the air as well as the plunge pool, the current methods cannot simulate the flow profiles correctly.

The velocities along the scour hole bottom were also compared to a required velocity for quasi-steady uplift to occur, as calculated using the QSI method. The velocities from the simulations, using both the physically modelled scour holes, as well as the calculated scour holes (CSM and QSI), were found to be much larger than the required velocity for uplift to occur. The entrained air and the confinement (deflection and recirculation), due to the scour hole, had a significant effect on the flow profile in the plunge pool and subsequently the wall and centreline velocity profiles. The wall jet velocity equations (Eqn. 3-112 to Eqn. 3-115) used for comparison were based on a very small-scale physical laboratory model that used a vertical jet impacting a flat plate, which was different to the conditions used in the

physical laboratory model. Further investigation was subsequently proposed to determine the applicability and accuracy of using the 2D CFD models, as well as the applicability of using 3D models, and using the required velocity for quasi-steady uplift to occur to determine if the equilibrium state of the scour hole was reached.

7.2 Recommendations

In order to improve accuracy of the physical laboratory model, scour prediction techniques and the CFD modelling in estimating rock scouring due to rectangular jets, it is recommended that the following adjustments and improvements be made:

(i) Physical laboratory model

Adjustments:

1. The length of the issuance canal should be increased to ensure fully developed flow occurs in the issuance canal for a more uniform jet profile, at issuance, for improved measurements and modelling (calibration). A closed conduit can also be used as an alternative to reduce air entrainment in the issuance canal and to remove the air entrainment effects due to the change in geometry.
2. The size of the pipes and pumps should be increased to allow for higher discharges, or lower drop heights should be tested to ensure the maximum scour potential of the jet is tested (undeveloped jets).
3. The area around the steel container should be made flush with the top of the container as to ensure no interference with the flow.
4. The depth of the steel container, as well as the number of PVC blocks should be increased to allow for higher flows and lower tailwater conditions to be tested.
5. Different size (volume) and density PVC blocks should be tested to verify their applicability to simulate rock scouring for various rock types and size rock blocks.
6. Due to the Vectrino probe not being the optimal measuring instrument for the physical laboratory model configurations, the use of a backflushing pitot tube (Bohrer [129]) or a laser Doppler

velocimeter (Ervine and Falvey [21]) to measure velocities in the plunge pool is suggested (other measures can also be used). These measurement instruments have been used in past studies to measure the velocities in the plunge pool.

7. Air entrainment at issuance, impact and in the plunge pool, as well as pressures in the plunge pool, should be measured and subsequently checked against other studies, as well as the CFD results.
8. The use of an acrylic issuance canal and plunge pool should be used to study the hydrodynamic characteristics of the jet.

Additional:

9. A case study should be modelled physically using the PVC blocks to determine their applicability in replicating prototype scour holes – for example Kariba Dam.

(ii) Physically based (analytical) prediction methods

1. The spreading angles (lateral and longitudinal) of the jet should be determined using more accurate measuring techniques, such as high-speed cameras, for rectangular jets in the air and the plunge pool.
2. The applicability of using trajectory length (L_j) instead of drop height (H), in the H/L_b ratio to determine if the jet is developed or undeveloped, should be explored using physical laboratory model or prototype studies.
3. A new break-up length approximation for rectangular jets should be developed and checked against current approaches, as the calculations of the break-up length vary considerably between the current approaches (Castillo (2007) [31] and Horeni (1956) [30]).
4. Experimental studies should be completed to determine the velocity decay profile of rectangular jets in the plunge pool. Current approaches are based on circular jets (Ervine and Falvey, 1987 [21]) or are very limiting to their application (Bohrer [129]).
5. The velocity at impact with the plunge pool free surface of developed jets (circular and rectangular jets), including the droplet diameter and drag coefficient of water droplets, should be studied physically.

6. An approach similar to the fluctuating and mean pressure coefficients for rectangular jets developed by Castillo (2014), should be developed for the net uplift coefficient (C_I) for various H/Lb ratios (undeveloped and developed jets). Ratios of Y/D and Y/B, which go up to values higher than 18 for circular and rectangular jets should be tested. Current approximation of C_I was developed using an H/Lb ratio less than 0.5 (undeveloped jet) and is only applicable to Y/D<18.
7. Determine a QSI based method to determine lateral scouring including the wall jet velocity profile (both lateral and longitudinal directions).
8. Conduct isolated studies of wall jets produced from plunging jets at a larger scale. The approach developed by Beltaos and Rajaratnam () was developed at a very small scale. The velocity profile of both circular and rectangular jets should be investigated.
9. Isolated physical laboratory models should be conducted which focus on wall jets and the effect of rock block protrusions, fixed and moving protrusions (PVC blocks), to verify the values of C_{uplift} as was developed by Reinius [131].

(iii) CFD analysis

1. Develop a mathematical model to be incorporated in CFD to calculate rock scour, similar to sediment transport modules currently available, for rectangular rock blocks similar to the QSI and DI approaches as was developed by Bollaert.
2. Develop a multi-phase open channel model that allows coarser grids. The new version of FLUENT (Ansys 16), has improved VOF capabilities allowing the use of larger cells, thus reducing the required amount of cells for accurate boundary tracking, but as was seen from the simulations it is still not ideal and still required a relatively fine mesh.
3. The use of FLOW-3D in modelling the plunging jet can be investigated. FLOW-3D tracks the free surface using TruVOF, not VOF as is used in FLUENT. TruVOF is a robust method for tracking the free surface and is more suitable for modelling free falling jets than FLUENT [2,213]. Air entrainment of the jet can be simulated using special physics packages included in FLOW-3D, as opposed to FLUENT which cannot simulate air entrainment.
4. The use of models using prototype conditions, such as Kariba Dam, to check the applicability of using the CSM and QSI method in conjunction with CFD techniques for prototype conditions.

5. 3D simulation should be run using the various setup configurations to study the flow profile in all three directions. Backflow, which is generally experienced upstream of the jet impact region, was not accounted for in the 2D models used. The effect of backflow was less critical for this study, as it is more important in sediment beds rather than rock beds. 3D models can, however, be used to study the effects of backflow and the possible scouring of the side channels.
6. An even finer mesh can be used to improve the accuracy of the models, as well as the free surface modelling of the VOF method.
7. A multiphase model or a combination of multiphase models should be investigated and developed to model both the dispersed, as well as the stratified flow regimes, and which can be applied to open channel flow simulations. Current multiphase models can only simulate one flow regime.

8 References

[1] **Hoffmans,** G.J.C.M. and **Verheij,** H.J. (1997): "*Scour manual.*" Balkema, Rotterdam.

[2] **Armitage,** N.; **Cunninghame,** M.; **Kabir** A.; and **Abban** B. (2007): "Local scour in rivers: The extent of the problem in South Africa, The state of the art of numerical modelling." WRC Report no. KV 185/07.

[3] **CUR** (1995): "*Manual on the use of Rock in Hydraulic Engineering.*" Balkema, Rotterdam. ISBN: 90 5410 605 0

[4] **LU,** J.Y.; **SU**, C.C; **HONG,** J.H and **CHEN**, E.J. (2012): "*Prediction of Maximum General Scour Depth during a Flood for Intermittent Rivers.*" ICSE6 Paris - August 27-31, 2012, pg. 79-86

[5] **Wikipedia**, "*Stream load" [Stream load figure]*, February 4, 2008. Available from: < http://en.wikipedia.org/wiki/File:Stream_Load.gif >, [01/06/2014]

[6] **Pagliara,** S.; **Hager,** W.H. and **Minor,** H.E. (2004): "*Plunge pool scour in prototype and laboratory"*, Intl. Symp. on Hydraulics of Dams and River Structures, Teheran, Iran, pp. 165-172. 2004

[7] **Van Aswegen,** W.J.; **Dunkley,** E. and **Blake**, K.R.K. (2001): "*Plunge pool scour reproduction in physical hydraulic models.*" WRC Report no. 502/1/01

[8] **Monfette**, M. (2004): "Comprehensive review of plunge pool performance at four of the BC hydro dam sites and assessment of scour extent", Master's Thesis, The University of British Columbia

[9] **Pettersson**, H. and **Pettersson,** J. (2010): "*Safety Evaluation of the Plunge Pool and the Downstream River of the Baihetan Hydropower Station Using Model Experiments.*", Master's Thesis, Department of Hydraulic Engineering at Tsinghua University in Beijing, China.

[10] **Borghei**, S.M. and Zarnani, P. (2008): "*Jet impact geometry and plunge pool dimensions effects on dynamic pressures at pool sidewalls.*" Canadian Journal of Civil Engineering, 2008, 35(4): 408-417, 10.1139/L07-141

[11] **Bollaert**, E.F.R. and **Schleiss**, A.J. (2003): "*Scour of rock due to the impact of plunging high velocity jets: Part I: a state-of-the-art review.*" Journal of Hydraulic Research, IAHR, Delft, The Netherlands. 2003

[12] **Bollaert**, E.F.R.; **Munodawafa,** M.C. and **Mazvidza**, D.Z. (2012): "*Kariba Dam Plunge Pool Scour: quasi-3D Numerical Predictions*." ICSE6 Paris - August 27-31, 2012

[13] **Dey,** D. and **Eldho**, T.I. (2009): "*Effect of spacing of two offset jets on scouring phenomena.*" Journal of Hydraulic Research, Journal of Hydraulic Research, 47:1, 2009, pg. 82-89

[14] **Mehraein**, M.; **Ghodsian,** M. and Schleiss, A.J. (2012): *Scour formation due to simultaneous circular impinging jet and wall jet*, Journal of Hydraulic Research, 50:4, pg. 395-399, DOI: 10.1080/00221686.2012.694174

[15] **Lewis,** T.M.; **Abt,** S.R.; **Wittler**, F.R.J. and **Annandale**, G.W. (1999); *Predicting Impact Velocities of Developed Jets*, Water International, 24:3, 255-265, DOI: 10.1080/02508069908692169

[16] **Ghodsian**, M.; **Mehraein**, M. and **Ranjbar,** H.R. (2012): "*Local scour due to free fall jets in non-uniform sediment.*" Scientia Iranica, Volume 19, Issue 6, December 2012, Pages 1437–1444

[17] **Heng**, S.; **Tingsanchali**, T. and **Suetsugi**, T. (2012): "Analysis of plunge pool scour hole formation below a chute spillway with flip bucket using a physical laboratory model." ASEAN Engineering journal Part C 1 (1), pg. 88 – 101

[18] **Hawkswood**, M.; **Evans**, G. and **Hawkswood**, G. (2013): "*Berth Scour Protection for Fast Ferry Jets."* ICE Marine Structures & Breakwaters 2013

[19] **Manso,** P.F.A.; **Bollaert**, E.F.R. and **Schleiss**, A.J. (2008): "*Evaluation of high-velocity plunging jet-issuing characteristics as a basis for plunge pool analysis."* Journal of Hydraulic Research, 46:2, 147-157, DOI:10.1080/00221686.2008.9521852

[20] **Wu,** l; **Peirson**, B.; **Pells**, S; **Douglas**, K. and **Miller**, B. (2012): "*On the Significance of Aeration in the Assessment of Erosion of Unlined Spillways."* Houille Blanche; no. 3; pp. 30 - 35; 0018-6368 (ISSN)

[21] **Ervine**, D.A. and **Falvey**, H.T. (1987). "*Behaviour of Turbulent Water Jets in the Atmosphere and in Plunge Pools.*" Ice Proceedings 01/1987; 83(1):295-314. DOI: 10.1680/iicep.1987.353

[22] **Hausler**, E. (1983): "*Spillways and outlets with high energy concentration."*, Trans. Int. Symp. Layout of dams in Narrow Gorges, Vol. 2 pp. 177-194Rio de Janeiro;1983

[23] **Tokyay** N.D. "*Chapter 4: Design of Outlet Structures.*" Presentation, Available from: <http://www2.ce.metu.edu.tr/~ce458/CE458-Chapter-4nt.pdf> , Middle East Technical University, [28/08/2015]

[24] **Ervine**, D.A.; **Falvey**, H.T. and **Withers**, W. (1997): "*Pressure fluctuations on plunge pool floors."* Journal of Hydraulic Research, 35:2, 257-279, DOI:10.1080/00221689709498430

[25] **Stratford**, C.E.; **Bollaert**, E.F.R. and **Lesleighter**, E.J. (2013): "*Plunge Pool Rock Scour Analysis Techniques: Wivenhoe Dam Spillway*, Australia, HYDRO2013, Innsbruck, October.

[26] **Schleiss**, A.J. (2002): "*Scour evaluation in space and time – the challenge of dam designers. In rock scour due to falling high-velocity jets."* Proceedings of the international workshop on rock scour in Lausanne, Switzerland. September 25-28

[27] **Ervine**, D.A.; **Mckeogh**, E. and **Elsawy** E.M. (1980): "*Effect of turbulence intensity on the rate of air entrainment by plunging water jets.*" Proceedings of Inst Civ. Eng., Part 2, pp. 425-445.

[28] **Nejad**, J.K.; **Moghadam,** M.F.; **Lashkarara** B. and **Haghighipour**, S. (2011): *Dynamic pressures of flip bucket jets*, World applied sciences journal 12 (8); 1165-1171,2011

[29] **Asadollahi** P. (2009): "Stability Analysis of a Single Three Dimensional Rock Block: Effect of Dilatancy and High-velocity Water Jet Impact." Thesis, The University of Texas at Austin

[30] **Horeni**, P. (1956): "*Disintegration of a free jet of water in air.*" Sesit 93, Praha, Pokbaba

[31] **Castillo,** L.G.E. (2007): "*Pressures Characterization of Undeveloped and Developed Jets in Shallow and Deep Pool."* 32nd Congress of IAHR, the International Association of Hydraulic Engineering & Research Venice, Italy, 1 – 6 July 2007

[32] **Baron**, T. (1949): "*Technical report"*, University of Illinois, no. 4

[33] **Engineeringtoolbox**, "Water surface tension." (surface tension values) Available from: <http://www.engineeringtoolbox.com/water-surface-tension-d_597.html>, [28/08/2015]

[34] **Hoffmans** G.J.C.M. (1998): "*Jet scour in equilibrium phase.*" Journal of hydraulic engineering, April 1998

[35] **Breusers**, H.N.C. and **Raudkivi**, A.J. (1991), "*Scouring."* Balkema, pp. 99 – 122, Rotterdam, ISBN: 90 6191 983 5

[36] **Bollaert**, E.F.R. (2002): "*Transient water pressures in joints and formation of rock scour due to high-velocity jet impact."* Communication No.13 of the Laboratory of Hydraulic Constructions, EPFL, Lausanne, Switzerland.

[37] **Castillo,** L.G. E. (2015): Personal communication, 28 February

[38] **Bollaert**, E.F.R. (2004): "*A comprehensive model to evaluate scour formation in plunge pools.*" Hydropower and dams, Issue one, 2004.

[39] **Annandale**, G.W.; **Witler**, R.J.; **Mefford**, B.W.; **Abt**, S.R. and **Ruff**, J.F. (1995): "*Spillway and dam foundation erosion: Predicting progressive erosion extent.*", Presented At The First International Conference On Water Resources Engineering In San Antonio, Texas, August 14-18, Texas

[40] **Balachandar** R and **Reddy**, H.P. (2013): "*Scour caused by wall jets." Chapter 8, INTECH Open Access Publisher, 2013* , ISBN 953511039X, 9789535110392

[41] **Bollaert**, E.F.R. "*Scour prediction at Srisailam dam (India).*", AquaVision Engineering, Switzerland

[42] **Tokyay** N.D. "Chapter 5: Design of Dissipation Structures." Presentation, Available from: < http://www2.ce.metu.edu.tr/~ce473/458/CE458-Chapter%205.pdf> , Middle East Technical University, [28/08/2015]

[43] **Annandale** G.W. and **George**, M.F. (2011): "*Closure problem to jet scour.*", Journal of Hydraulic Research, 49:2, 276-277, DOI: 10.1080/00221686.2011.568205

[44] **Younkins,** B.D. (2008): "Prediction if scour formation due to turbulent wall jet along a non-cohesive sediment bed.", PHD thesis, The Pennsylvania State University The Graduate School Department of Civil Engineering

[45] **Mazurek,** K.A. and **Rajaratnam,** N. (2005): "*Erosion of sand beds by obliquely impinging plane turbulent air jets.*" Journal of Hydraulic Research, 43:5, 567-573, DOI: 10.1080/00221680509500155

[46] **Mehta**, A.J. (1991): "*Review notes on cohesive sediment erosion".* In Coastal Sediments '91: Proceedings of a Specialty Conference on Quantitative Approaches to Coastal Sediment Processes, Seattle, Wash., 25–27 June 1991. Edited by N.C. Kraus, K.J. Gingerich, and D.L. Kriebel. American Society of Civil Engineers, New York, N.Y. Vol. 1, pp. 40–53.

[47] **Mazurek,** K. A. and **Hossain,** T. (2007), "*Scour by jets in cohesionless and cohesive soil."* NRC Canada

[48] **Paaswell**, R.E. (1973): "Causes and mechanisms of cohesive soil erosion: state of the art." In Soil Erosion: Causes and Mechanisms, Prevention and Control: Proceedings of a Conference–Workshop, Washington, D.C., 26 January 1973. Special Report 135, Highway Research Board, National Research Council, Washington, D.C. pp. 52–74.

[49] **Hickin,** E.J. (2004): "*River hydraulics and channel form"*, Chapter 5: Nature of turbulence and velocity distributions in rivers, Available from: < http://www.sfu.ca/~hickin/FLUIDS/Chapt5-Turbulence.pdf>, [28/08/2015]

[50] **ZHU**, Z.W. and **LIU,** Z.Q. (2012): "*CFD prediction of local scour hole around bridge piers*." J. Cent. South Univ. (2012) 19: 273−281

[51] **Aderibigbe**, O.O. and **Rajaratnam**, N. (1996): "*Erosion of loose beds by submerged circular impinging vertical turbulent jets*." Journal of Hydraulic Research, 34:1, 19-33, DOI: 10.1080/00221689609498762

[52] **Termini**, D. (2010): "Bed scouring downstream of hydraulic structures under steady flow conditions: Experimental analysis of space and time scales and implications for mathematical modelling." Catena 84 (2011) 125–135

[53] **Peiqing,** L. and **Aihua,** L. (2007): "*Fluctuating uplift acting on rock blocks at the bottom of river bed and estimation of the limiting scour depth."* Journal of Hydraulic Research, 45:4, 478-485, DOI: 10.1080/00221686.2007.9521782

[54] **Bollaert**, E.F.R. (2010): "Rock scour at hydraulic structures: a practical engineering approach". Geo-Strata July-August 2010.

[55] **Bollaert**, E.F.R. (2010): "The Comprehensive Scour Model: Theory and Feedback from Practice." 5th International Conference on Scour and Erosion, San Francisco, November 2010.

[56] **George** M.F. and **Sitar**, N. (2012): "Block theory application to scour assessment of unlined rock spillways." Report no. UCB GT 12-02

[57] **Aswegen,** V.W.J.; **Dunkley,** E.; and **Blake,** K.R.K. (2001): "*Plunge Pool Scour Reproduction in Physical Hydraulic Models*." Report of the Water Research Commission, 2001.

[58] **Kieffer** D.S. and **Goodman,** R.E. (2012): "Assessing scour potential of unlined spillways with the block scour spectrum." Geomechanics and Tunnelling Volume 5, Issue 5, pages 527–536, October 2012

[59] **Liu,** P.Q.; **Dong,** J.R. and **Yu,** C. (1998): "Experimental investigation of fluctuation uplift on rock blocks at the bottom of the scour pool downstream of Three-Gorges spillway." Journal of Hydraulic Research, 36:1, 55-68

[60] **Bollaert**, E.F.R. (2010): "*A Prototype scaled rock scour prediction model.*" USSD Annual Meeting, April 12-15 2010, Sacramento, United States.

[61] **Hickin**, E.J. (2004): "*River hydraulics and channel form"*, Chapter 6: sediment transport, Available from: <http://www.sfu.ca/~hickin/FLUIDS/Chapt6-Sediment%20transport.pdf>, [28/08/2015]

[62] **Pagliara**, S.; **Hager**, W.H. and **Minor**, H.E. (2006): "*Hydraulics of plane plunge pool scour.*" Journal of Hydraulic Engineering 132 (5), 450 e 461

[63] **Bollaert,** E.F.R.; **Manso**, P.A. and **Schleiss**, A.J. (2004): "*Dynamic pressure fluctuations at real life plunge pool bottoms.*" Hydraulics of dams and river structures, Teheran, Iran, pp. 117-124. 2004.

[64] **Annandale**, G.W. "Rock scour: past, present and future.", Presentation, Available from: <http://www.seprem.es/st_pe_f/JTAliviaderos2/ROCK_SCOUR.pdf >, [28/08/2015]

[65] **Noret,** C.; **Girard**, J.C.; **Munodawafa**, M.C. and **Mazvidza**, D.Z. (2012): "*Kariba Dam on Zambezi River: Stabilizing the Natural Plunge Pool.*" ICSE6 Paris - August 27-31, 2012

[66] **Bollaert**, E.F.R.; **Duarte**, R.; **Pfister,** M.; **Schleiss**, A. and **Mazvidza,** D. (2012): "*Physical And Numerical Model Study Investigating Plunge Pool Scour At Kariba Dam."* Commission Internationale Des Grands Barrages Vingt-Quatrième Congrès Des Grands Barrages Kyoto, June 2012

[67] **Nevin,** T. (2015) "To the rescue of Kariba Dam." February 17, 2015, Available from: <http://www.bdlive.co.za/business/innovation/2015/02/17/to-the-rescue-of-kariba-dam>, [28/08/2015]

[68] **USBR** (2012): "*Erosion of rock and soil.",* Nov 15, 2012, Available from : <http://www.usbr.gov/ssle/damsafety/Risk/BestPractices/15ErosionOfRockAndSoil20121126.pdf >, [28/08/2015]

[69] **ASCE**, (1995), "*Hydraulic design of spillways*." New York, NY: American Society of Civil Engineers, 978-0-7844-0078-4 / 0-7844-0078-4 (print), 1995, v, 120 pp., Technical Engineering and Design Guides as adapted from the U.S. Army Corps of Engineers, No. 12

[70] **Martinerie**, R.; **Boillat**, J.L.; **Schleiss**, A; **Rizi**, A.P. and **Wohnlich,** A. (2007): "*Experimental Study of the Gated Spillway of the Shahryar Dam in Iran*." Proceedings of the 32nd Congress of IAHR, vol. Theme C (C2.b-157-O)

[71] **Berchtold**, T.H. and **Pfister**, M. (2011): "*Measures to reduce dynamic plunge pool pressures generated by a free jet*." Dams and Reservoirs under Changing Challenges – Schleiss & Boes (Eds) © 2011 Taylor and Francis Group, London, ISBN 978-0-415-68267-1

[72] **Heller**, V. (2012): "*Model Prototype similarity*." Imperial college London, Available from: <http://www.drvalentinheller.com/Dr%20Valentin%20Heller_files/Heller_ModelPrototype%20Similarity.pdf> ,4th CoastLab Teaching School, Wave and Tidal Energy, Porto, 17-20th January 2012, [2015/02/04]

[73] **Cheng**, X.; **Chen** Y. and **Luom** L. (2006): "*Numerical simulation of air-water two-phase flow over stepped spillways." Science in China*, Series E: Technological Sciences 2006 Vol.49 No.6 674—6847

[74] **Boushaba,** F.; **Manso,** P.; **Schleiss**, A.J.; **Yachouti,** A. and **Daoudi**, S. (2013): "*Numerical and Experimental High-Reynolds Jet Diffusion and Impact Pressures in Flat and Laterally Confined Aerated Pools."* International Journal of Hydraulic Engineering 2013, 2(6): 133-141 DOI: 10.5923/j.ijhe.20130206.02

[75] **Neyshabouri,** A.A.S.; **Da Suva**, A.M.F. and **Barron**, R. (2003): "*Numerical simulation of scour by a free falling jet*." Journal of Hydraulic Research, 41:5, 533-539, DOI: 10.1080/00221680309499998

[76] **Jia,** Y.; **Kitamura**, T and **Wang**, S.S.Y. (2001): "*Simulation of scour process in plunging pool of loose bed-material.*" Journal of Hydraulic Engineering, Vol. 127, No. 3, March, 2001. q ASCE, ISSN 0733-9429/01/0003-0219–0229. Paper No. 21545.

[77] **Mason**, P.J. and **Arumugam,** K. (1985): "*Free jet scour below dams and flip buckets.*" Journal of Hydraulic Engineering 1985; 111(2): 220–35.

[78] **Guven** A., (2010): "A multi-output descriptive neural network for estimation of scour geometry downstream from hydraulic structures." Advances in Engineering Software Volume 42, Issue 3, March 2011, Pages 85–93

[79] **Liu**, P. (2005): "*A new method for calculating depth of scour pit caused by overflow water jets.*" Journal of Hydraulic Research, 43:6, 696-702, DOI: 10.1080/00221680509500389

[80] **Kotoulas**, D. (1967): "Das Kolkproblem unter besonderer Beriicksichtiguncj der Faktoren "Zeit" und nGeschiebemischung" im Rahmen der Wild- bachverbauung." Schweizerische Anstalt fiir das Forstliche Versuchswesen, Vol 43, Heft 1.

[81] **Mikhalev**, M.A. (1960): "*Determination of the Depth of Scour of a Non-Rock Base by a Falling Nappe.*" Gidrotekhnicheskoe Stroitel'stvo 9. – as cited in Whittaker and Schleiss [82]

[82] **Whittaker** J.G. and **Schleiss,** A. (1984): "*Scour related to energy dissipators for high-head structures.*" Mitt Nr 73 VAW/ETH, Zurich; 1984.

[83] **Spurr,** K.J.W. (1985): "*Energy approach to estimating scour downstream of a large dam.*" Int. water power and dam construction, July 7

[84] **Bormann**, N.E. and **Julien,** P.Y. (1991): "*Scour downstream of grade-control structures.*" Journal of Hydraulic Engineering 1991;117(5):579–94.

[85] **Sarkar,** A. and **Dey,** S. (2004): "*Review on local scour due to jets.*" Int J Sediment Res 2004;19(3):210–39.

[86] **Veronese,** A. (1937): "*Erosioni di fondo a valle di uno scarico.*" Annal Lavori Pubbl 1937;75(9):717–26 (in Italian)

[87] **Chee,** S.P. and **Yuen,** E.M. (1985): "*Erosion of unconsolidated gravel beds.*" Can J Civ Eng 1985;12:559–66.

[88] **Martins**, R. (1975): "*Scouring of rocky riverbeds and free-jet spillways.*" Int Water Power Dam Contstr 1975;27(5):152–3.

[89] **Bormann**, N.E. (1988): "*Equilibrium local scour downstream of grade-control structures."* Ph.D. thesis, Colorado State University, Fort Collins, Colo; 1988.

[90] **Azar**, F.A. (2000): "*Effect of sediment size distribution on scour downstream of free over fall spillway."* M.S. Thesis, Tarbiat Modares University, Tehran, Iran (2000).

[91] **Ghodsian**, M.; **Melville**, B. and **Tajkarimi**, D.(2006): "*Scour due to free overfall jet.*" Proc. Instn Civ. Engrs., 159(4), pp. 253–260 (2006).

[92] **Rashidian**, S. and **Asadollahi**, P. (2012): *"Assessment of Rock Scour depth in plunge pools."* 2012, ICSE6-053 Paris, 1121 – 1126

[93] **Asadollahi,** P.; **Tonon**, F; **Federspiel,** M.P.E.A. and **Schleiss**, A.J. (2011): "*Prediction of rock block stability and scour depth in plunge pools."* Journal of Hydraulic Research, 49:6, 750-756, DOI: 10.1080/00221686.2011.618055

[94] **Asadollahi** P. and **Tonon**, F. (2010): "Stability of rock blocks subjected to high velocity water jets." ARMA 10-203

[95] **Annandale**, G.W. (1995): "*Erodibility.*" J. Hydraulic Res. 33(4), 471–494.

[96] **Annandale** G.W. (2006): "*Scour technology: mechanics and engineering practice."* New York : McGraw-Hill c2006, ISBN0071440577;ISBN9780071440578

[97] **Annandale**, G.W. and **Schleiss,** A.J. (2007): "*Predicticting rock scour - part II.*" 17 September 2007, Cranes Today

[98] **Kirsten**, H.A.D. (1982): *"Classification System for Excavation in Natural Materials."* The Civil Engineering in South Africa, pages 293–308.

[99] **Mirtskhoulava**, T.E. (1997): "*Erodibility.*" Journal of Hydraulic Research, 35:2, 280-284, DOI: 10.1080/00221689709498431

[100] **Annandale**, G.W.; **Smith**, S.P.; **Nairns**, R. and **Jones**, J.S. (1996): "*Scour power.*" Civil Engineering; Jul 1996; 66, 7; ProQuest pg. 58

[101] **Mok,** C.M.W.; **AW,** E; **Wright**, R. and **Cooley**, J (2014) "*Probalistic dam erosion risk evaluation."* Vulnerability, Uncertainty, and Risk: pp. 2459-2467

[102] **Bollaert**, E.F.R. and **Lesleighter**, E.J. (2014): "*Spillway Rock Scour Experience and Analysis - the Australian Scene over the past Four Decades."* 5th International Symposium on Hydraulic Structures Hydraulic Structures and Society: Engineering Challenges and Extremes ISBN 9781742721156 - DOI: 10.14264/uql.2014.35 Brisbane, Australia, 25-27 June 2014

[103] **Bollaert**, E.F.R. and **Schleiss**, A.J. (2005): "*Physically based model for evaluation of rock scour due to high-velocity jet impact."* ASCE J. of Hydraulic Engineering, March: 153-165.

[104] **Bollaert**, E.F.R. (2011): "*Penstock Scour Formation At Bluestone Dam."* 21st Century Dam Design — Advances and Adaptations, 31st Annual USSD Conference San Diego, California, April 11-15, 2011

[105] **Bollaert**, E.F.R.; **Blancher**, B.; **Chulliat**, O. and **Laugier**, F. (2012): "*Numerical Scour Prediction at Choranche Dam."* ICSE6 Paris - August 27-31, 201

[106] **Puertas**, J. and **Dolz**, J. (2005): "*Plunge Pool Pressures Due to a Falling Rectangular Jet."* Journal Of Hydraulic Engineering © ASCE / May 2005, pg. 404 -407

[107] **Wahl,** T.L.; **Frizell,** K. H. and **Cohen,** E. A. (2008): "*Computing the Trajectory of Free Jets."* Journal Of Hydraulic Engineering © ASCE / February 2008

[108] **Frizell,** K. H. (2009): "*Yellowtail Dam Issue Evaluation - Analysis of the Erosion Potential of Flow Overtopping.*" Hydraulic Laboratory Technical Memorandum No. YEL-8460-IE-2009-1

[109] **Davies**, J.T. (1972): "Turbulence Phenomena." Academic Press, New York and London.

[110] **Castillo**, L.G.; **Carrillo**, J.M. and **Blázquez**, A. (2014): *Plunge pool dynamic pressures: a temporal analysis in the nappe flow case*, Journal of Hydraulic Research, DOI: 10.1080/00221686.2014.968226

[111] **Castillo**, L.G. (1998) "Revisión de las formulaciones de presión en los disipadores de energía en presas bóveda y corrección del coeficiente de presión dinámica". Unpublished. Cited in: **Annandale**, G.W. (2006). "Scour technology: mechanics and engineering practice."

[112] **Bollaert**, E.F.R.; **Manso**, P. and **Schleiss**, A. (2004): "*Experimental investigations on high-velocity jet characteristics and its influence on plunge pool rock scour."* Intl. Symp. on Hydraulics of Dams and River Structures, Teheran, Iran, pp. 173-180. 2004

[113] **Bollaert**, E.F.R. (2004): "*A new procedure to evaluate dynamic uplift of concrete linings or rock blocks in plunge pools*." Intl. Symp. on Hydraulics of Dams and River Structures, Teheran, Iran, pp. 125-132. 2004

[114] **Ervine**. D.A. (1998): "*Air entrainment in hydraulic structures: A review*." Proceedings of the institute of Civil Engineers, Wat., Marit. & Energy Vol130, pp. 142-153

[115] **Castillo**, L.G.E. (2006): "*Aerated Jets and Pressure Fluctuation in Plunge Pools."* The 7th Int. Conf. on Hydroscience and Engineering (ICHE-2006),Sep 10 –Sep 13,Philadelphia,USA

[116] **Bollaert**, E.F.R. (2005): "*The influence of geomechanic and hydrologic uncertainties on scour at large dams: case study of Kariba dam."* (zambia-zimbabwe) 73 rd Annual Meeting of ICOLD Tehran, IRAN May 1- 6, 2005 Paper No.: 0197-S1

[117] **Bollaert**, E.F.R. and **Schleiss**, A. (2001): "*A new approach for better assessment of rock scouring due to high velocity jets at dam spillways*." ICOLD European Symposium, Geiranger, Norway, 25-27 June 2001

[118] **Wylie**, E.B. and **Streeter**, V.L. (1978): "*Fluid Transients."* USA: McGraw-Hill Inc.

[119] **Toso**, J.W. and **Bowers**, C.E. (1988): "*Extreme Pressures in Hydraulic Jump Stilling Basins."* ASCE. Journal of Hydraulic Engineering, Vol. 114, N 8: 829-843.

[120] **Ewalds**, H.L. and **Wanhill**, R.J.H. (1986): "*Fracture Mechanics.*" Netherlands: Delftse Uitgevers Maatschappij.

[121] **Yazdandoost**, F.; **Attari**, J and **de Gruyte**, W. (2004): "*Hydraulics of Dams and River Structures.*" Proceedings of the International Conference on Hydraulics of Dams and River Structures, 26-28 April 2004, Tehran, Iran

[122] **Manso** P.F.D.A. (2006): "The influence of pool geometry and induced flow patterns on rock scour by high-velocity plunging jets." PHD thesis, Laboratory of Hydraulic Constructions, Lausanne, EPFL 2006

[123] **Federspiel** M. (2011): "*Response of an embedded block impacted by high-velocity jets.*" PHD thesis, Communication 47, Laboratory of Hydraulic Constructions, Lausanne, EPFL 2011

[124] **Duarte**, R.X.M (2014): "*Influence of Air Entrainment on Rock Scour Development and Block Stability in Plunge Pools.*" PHD thesis, Laboratory of Hydraulic Constructions, Lausanne, EPFL 2014

[125] **Bollaert**, E.F.R. (2012): "*Wall jet rock scour in plunge pools: a quasi-3D prediction model.*" Intl. Journal of Hydropower & Dams, 2012.

[126] **Bollaert**, E.F.R. (2015): *Personal communication,* 12 March

[127] **Hartung**, F. and **Hausler**, E. (1973): "*Scours, stilling basins and downstream protection under free overfall jets at dams.*" Proceedings of the 11th Congress on Large Dams, Madrid, pp.39-56.

[128] **Beltaos**, S. and **Rajaratnam**, N.(1973): "*Plane turbulent impinging jets*", Journal of Hydraulic research, IAHR, Vol.11, N° 1, pp. 29-59.

[129] **Bohrer**, J.G.; **Abt**, S.R. and **Wittler**, R.J. (1998): "*Predicting plunge pool velocity decay of free falling rectangular jets.*" Journal of hydraulic engineering, October 1998, Pg. 1043-1048

[130] **Reich**, F. (1927): "*Umlenkung eines Freien Flüssigkeitsstrahles an einer ebenen Platte.*" Zeitschrift Verein deutscher Ingenieure 71 (8): p. 261-264.

[131] **Reinius**, E. (1986) "*Rock erosion.*" Int. Water Power Dam Constr. 38 (6), 43–48.

[132] **Pan**, Y.W.; **Li,** K.W. and **Liao**, J.J. (2014): "Mechanics and response of a surface rock block subjected to pressure fluctuations: A plucking model and its application." Engineering Geology 171 (2014) 1–10

[133] **Julien**, P.Y. (1998): "*Erosion and sedimentation."* Cambridge university press, ISBN: 0-521-63639-6

[134] **Sawadogo**, O. (2010): "*Scour of unlined spillways.*" Master's thesis, University of Stellenbosch

[135] **Miedema**, S.A. (2012): "Constructing the shields curve: Part A: Fundamentals of the sliding, rolling and lifting mechanisms for the entrainment of particles." Journal Of Dredging Engineering, Vol. 12, No. 1

[136] **Simons**, D. (1957): "*Theory and design of stable channels in alluvial material.*" PhD thesis: Colorado State University

[137] **Shields**, A. (1936): "Anwendung der Aehnlichkeitsmechanik und der Turbulenzforschung auf die Geschiebebewegung." Mitteilung der Preussischen Versuchsanstalt fur Wasserbau und Schiffbau, Heft 26, Berlin. Belin.

[138] **Tsiatas**, G. (2005): "Stream Stability and Scour Potential for Rhode Island Bridges.", USGS

[139] **Rangel**, H.F.A. (2008): "*Scour of captured sediment from a stormwater hydrodynamic device."* PHD thesis, University of Alabama, 2008

[140] **van Rijn**, L. (1984): "*Sediment transport: Part I: Bed load transport.*" Journal of Hydraulic Engineering, Vol. 110(10), 1431-1456.

[141] **Damgaard,** J.S.; **Whitehouse**, R.J.S. and **Soulsby**, R.L. (1997): "*Bed-load sediment transport on steep longitudinal slopes."* Journal of hydraulic engineering, December 1997

[142] **Soulsby**, R.L. (1996): *"Dynamics of marine sands."* Rep. No. SR 466, HR Wallingford, Wallingford, U.K.

[143] **Guo**, J. (2002): "*Hunter Rouse and Shields Diagram.*" Advances in Hydraulics and Water Engineering, Vol. 2,2002,1068 – 1098

[144] **Hogg**, A. J.; **Huppert**, H. E. and **Dade**, W. B. (1997): "*Erosion by planar turbulent wall jets.*" Journal of Fluid Mechanics, 338:317 – 340, 1997.

[145] **Stein**, O.R.; **Julien**, P.Y. and **Alonso**, C.V. (1993): "*Mechanics of jet scour downstream of a headcut.*" Journal of Hydraulic Research, 31:6, 723-738, DOI: 10.1080/00221689309498814

[146] **Yang**, C.T. (1972): "*Unit Stream Power and Sediment Transport.*" Journal of the Hydraulic Division, ASCE, vol. 18, no. HY 10, pp. 1805 - 1826.

[147] **Stein**, O.R. and **Julien,** P.Y. (1993): "*Criterion delineating the mode of headcut migration.*" J. Hydr. Engrg., ASCE, 119(1), 37–50.

[148] **Huai**, W.; **Wang**, Z.; **Qian**, Z. and **Han**, Y. (2011): "*Numerical simulation of sandy bed erosion 2D vertical jet.*" Science China Technological Sciences Volume 54, Issue 12 , pp 3265-3274

[149] **Fur77tney**, J.; **Zhang**, F. and **Han**, Y. (2013): "Review of methods and applications for incorporating fluid flow in the Discrete Element Method , Continuum and Distinct Element Numerical Modeling in Geomechanics." 2013 Zhu, Detournay, Hart & Nelson (eds.) Paper: 10-01 ©2013 Itasca International Inc., Minneapolis, ISBN 978-0-9767577-3-3

[150] **Brozek,** M. and **Surowiak**, A. (2005): "*The distribution of settling velocity of non-spherical mineral particles.*" Ročník 10 (2005), mimoriadne číslo 1, 27-32

[151] **Mizumura,** K.; **Yamamoto**, M.; **Endo,** T. and **Shiraishi**, N. (1988): "*Reliability analysis of rubble-mound breakwaters.*" Chapter 152, Coastal engineering

[152] **SANRAL**. (2013): *"Drainage manual."* 6th edition. Pretoria: SANRAL

[153] **Saliu,** M.A. and **Lawal**, A.I. (2014), "*Investigations of Weathering Effects on Engineering Properties of Supare Granite Gneiss.*" Journal of Mining World Express Volume 3, 2014 doi: 10.14355/mwe.2014.03.008

[154] **Endress**, "*Proline Promag 10P Electromagnetic flowmeter"* [product specifications], Available from: <http://www.ca.endress.com/en/Tailor-made-field-instrumentation/Flow-measurement-product-overview/Product-Electromagnetic-flowmeter-Proline-Promag-10P> [28/08/2015]

[155] **Nortek**, "*Vectrino 3D water velocity sensor Lab Probe"*, [Vectrino probe product specifications], Available from: <http://www.nortek-as.com/lib/data-sheets/datasheet-vectrino-lab >, [28/08/2015]

[156] **Nortek**, "*Vectrino"*, [Vectrino probe product specifications], Available from: <http://www.nortek-as.com/en/products/velocimeters/vectrino >, [28/08/2015]

[157] **University of Delaware**, "*Hydraulic jump and weir flow*" [lecture notes], Available from: <http://udel.edu/~inamdar/EGTE215/Jump_weirs.pdf >, [28/08/2015]

[158] **Thandaveswara**, B.S., "*Hydraulics*" [Lecture notes], Available from: <http://nptel.ac.in/courses/105106114/pdfs/Unit15/15_2.pdf >, Indian Institute of Technology Madras

[159] **Engineeringtoolbox**, "Drag coefficient." (drag coefficient values) Available from: <http://www.engineeringtoolbox.com/drag-coefficient-d_627.html>, [28/08/2015]

[160] **Elert**, G., (2001), "Diameter of a Raindrop", Available from: <http://hypertextbook.com/facts/2001/IgorVolynets.shtml>

[161] **Das,** K.; **Green**, S. and **Manepally**, C. (2007*): "Flow-3d Version 1.0 Users Manual."* U.S. Nuclear Regulatory Commission Contract NRC–02–02–012

[162] **Savage**, B. and **Johnson**, M. (2006): "Physical and Numerical Comparison of Flow over Ogee Spillway in the Presence of Tailwater."

[163] **Prinos**, P.; **Tsakiri,** M. and **Souliotis,** D. (2012): "A numerical simulation of the WOS and the wave propagation along a coastal dike." Coastal engineering

[164] **FLOW-3D**, FLOW-3D software information, Available from <http://www.flow3d.com/home/products>, [7/6/2014]

[165] **Burnham**, J. "Modeling Dams with Computational Fluid Dynamics: Past Success and New Directions", FLOW 3D

[166] **Itasca**, "*Software*", [Distinct element software], Available from: <http://www.itascacg.com/software>, [7/6/2014]

[167] **Hongyuan**, L. (2002): *Numerical modelling of the rock fracture process under mechanical loading*, Thesis, Department of Civil and Mining Engineering, Lulea University of Technology

[168] **Lasich**, T.J. and **MacLaughlin**, M.M. "*UDEC modelling of an underground opening in rock masses of varying quality.*" Department of Geological Engineering, Montana Tech of The University of Montana, Butte, MT

[169] **Barla**, G. and **Barla**, M. (2000): "*Continuum and discontinuum modelling in tunnel engineering."* Rud,-geol,-naft. Zh, Vol 12, Zagreb, 2000

[170] **Cundall**, P.A. and **Hart**, R.D. (1993): "*Numerical modelling of discontinua.* Comprehensive Rock Engineering, Volume 2. Analysis and design Methods (Hudson J.A., editor) pp. 231-261. Pergamon Press, Oxford

[171] **Karim,** O.A. and **Ali**, K.H.M. (2000): "*Prediction of flow patterns in local scour holes caused by turbulent water jets."* Journal of Hydraulic Research, 38:4, 279-287, DOI: 10.1080/00221680009498327

[172] **Savage**, B. and **Johnson**, M. (2001): *"Flow over ogee spillway: Physical and numerical model case study."* Journal of Hydraulic Eng., 127 8 , 640–649

[173] **Adduce,** C. and **Sciortino**, G. (2006): "*Scour due to a horizontal turbulent jet: Numerical and experimental investigation."* Journal of Hydraulic Research, 44:5, 663-673, DOI: 10.1080/00221686.2006.9521715

[174] **Dasgupta**, B.; **Basu**, D.; **Das**, K. and **Green**, R. (2011): "Development Of Computational Methodology To Assess Erosion Damage In Dam Spillways." U.S. Society on Dams

[175] **Kamanbedast**, A.A. and **Aghamajidi**, R. (2013): "*Cup Ski Jump Length of the Spillway Using FLOW3D Mathematical Model (Case Study: Gotvand Dam).*" Technical Journal of Engineering and Applied Sciences, ©2013 TJEAS Journal-2013-3-23/3399-3404

[176] **Epely-Chauvin**, G.; **De Cesare** G. and **Schwindt**, S. (2014): *Numerical Modelling of Plunge Pool Scour Evolution In Non-Cohesive Sediments*, Engineering Applications of Computational Fluid Mechanics, 8:4, 477-487, DOI: 10.1080/19942060.2014.11083301

[177] **Weidner**, K.L. (2012): "Evaluation of the Jet Test Method for determining the erosional properties of Cohesive Soils; A Numerical Approach." Master's thesis, Virginia Polytechnic Institute and State University, Blacksburg, VA

[178] **Ray**, B.; **Bhaskaran**, R. and **Collins**, L.R. (2012): "*Introduction to CFD Basics*"

[179] **Ho**, D.K.H.; **Boyes**, K.M. and **Donohoo**, S.M. (2001): "*Investigation of Spillway Behaviour under Increased Maximum Flood by Computational Fluid Dynamics Technique.*" 14th Australasian Fluid Mechanics Conference Adelaide University, Adelaide, Australia 10-14 December 2001

[180] **Ho**, D.K.H.; **Boyes**, K.M.; **Donohoo**, S.M. and **Cooper**, B., (2003): "*Numerical Flow Analysis For Spillways.*" 43rd ANCOLD Conference Hobart, Tasmania, 24-29 October 2003

[181] **Holmquist-Johnson** C. "Modelling three-dimensional hydraulics of rock weirs." Reclamation: managing water in the west, US department of the interior Bureau of Reclamation.

[182] **Olsen**, N.R.B. (1999): "*Computational fluid dynamics in hydraulic and sedimentation engineering", class notes*, Norwegian University of Science and Technology, Department of Hydraulic and Environmental Engineering, Available from: < http://folk.ntnu.no/nilsol/cfd/class2.pdf >, [28/08/2015]

[183] **Bakker**, A. (2012), "Computational fluid dynamics lecture notes", March 4, 2012, Available from: <http://www.bakker.org>, [28/08/2015]

[184] **Versteeg**, H. K. and **Malalasekera**, W. (2007): "An Introduction to Computational Fluid Dynamics – The Finite Volume Method." Pearson, Prentice Hall

[185] **Daneshvari**, M. and **De Cesare**, G. (2010): Pamphlet - "Koman dam Albania –Numerical simulation of spillways and plunge pool", EPFL, Available from:< https://documents.epfl.ch/groups/l/lc/lch-unit/www/pdf/mandats/2011/Numerical%20simulation%20for%20Koman,%20spillways%20%26%20plunge%20pool.pdf > , [28/08/2015]

[186] **Daneshvari**, M. and **De Cesare**, G. (2010): Presentation – "*Physical and numerical modelling of the spillways and plunge pools of Koman dam in Albania."* Available from*:* <http://www.polytechnice.fr/jahia/webdav/site/simhydro/shared/actes/day2/session4/Physical%20and%20numerical%20modeling%20of%20the%20spillways%20and%20plunge%20pools%20of%20Koman%20Dam%20in%20Albania.pdf> *, [28/08/2015]*

[187] **ANSYS Inc.** (2015): "*ANSYS FLUENT Theory Guide"*, Release 16.0

[188] **Nguyen**, C. (2005): "*Turbulence modelling"*, November 05, 2005

[189] **Yuan,** B.; **Kang**, Y.; **Yang**, X.F.; **Fang**, Z.L. and **Li**, D. (2012): "*Numerical investigation on high-pressure convergent nozzle by comparative and statistical analysis method.*" 26th IAHR Symposium on Hydraulic Machinery and Systems, IOP Conf. Series: Earth and Environmental Science 15 (2012) 072033

[190] **Boroomand,** M.R., **Neyshabouri**, S.A.A.S. and **Aghajanloo**, K**.** (2007), *"Numerical simulation of sediment transport and scouring by an offset jet.*" Can. J. Civ. Eng. 34: 1267–1275 (2007)

[191] **Hirt,** C.W. and **Nichols**, B.D. (1981): "*Volume of Fluid (VOF) method for the dynamics of free boundaries.*" Journal of computational physics 39, pp. 201-225

[192] **Melling,** G.; **Dix**, J. and **Turnock**, S. (2011): "*CFD-Based Methods For Numerical Modelling Of Scour."* University of Southampton

[193] **Chanel,** P.G. and **Doering**, J.C. (2007): "*An Evaluation of Computational Fluid Dynamics for Spillway Modelling*." 16th Australasian Fluid Mechanics Conference, December 2007

[194] **Tulimilli**, B.R.; **Majumdar**, P. and **Kostic**, M. "*Development of CFD Simulation for 3-D Flooding Flow and Scouring Around a Bridge Structure*." Latest Trends on Urban Planning and Transportation, ISBN: 978-960-474-204-2

[195] **Avila** H. and **Pitt**, R. (2008): "*The Calibration and use of CFD Models to Examine Scour from Stormwater Treatment Devices – Hydrodynamic Analysis*." 11th International Conference on Urban Drainage, Edinburgh, Scotland, UK, 2008

[196] **Qian**, Z.; **Hu,** X.; **Huai,** W. and **Xue,** W. (2010): "*Numerical simulation of sediment erosion by submerged jets using an Eulerian model*." December 2010 Vol.53 No.12: 3324–3330 doi: 10.1007/s11431-010-4165-3

[197] **Guha**, A.; **Barron**, R.M. and **Balachandar**, R. (2010): "*An experimental and numerical study of water jet cleaning process."* Civil Engineering Department, The University of British Columbia, Vancouver, BC Canada

[198] **ANSYS Inc**. (2015): "*ANSYS FLUENT Tutorial Guide*." Release 16.0

[199] **Qfinsoft** (2015): Personal communication with CFD modellers/engineers

[200] **Chen**, Q.; **Dai**, G. and **Liu**, H. (2002): "*Volume of fluid model for turbulent numerical simulation of stepped spillway overflow*." Journal of hydraulic engineering, Vol. 128, No. 7

[201] **Xiangju,** C.; **Yongcan**, C. and **Lin**, L. (2006): "*Numerical simulation of air-water two-phase flow over stepped spillways*." Science in China, Series E: Technological Sciences 2006 Vol. 49 674-684

[202] **Sumer**, B.M. (2007): "*Mathematical modelling of scour: A review.*" Journal of Hydraulic Research,45:6, 723-735, DOI: 10.1080/00221686.2007.9521811

[203] **Wilcox**, D.C. (1993): "*Turbulence modelling for CFD.*" DCW Industries, Inc. La Canada, California, ISBN: 0-9636051-0-0

[204] **Morgans**, R.C.; **Dally**, B.B.; **Nathan**, G.J.; **Lanspearym**, P.V. and **Fletcher**, D.F. (1999): "*Application of revised Wilcox (1998) k-ω turbulence model to a jet in co-flow."* Second international conference on CFD in the minerals and process industries, CSIRO, Melbourne, Australia, 6-8 December 1999

[205] **Menter**, F. R.; **Kuntz**, M. and **Langtry**, R. (2003): "*Ten Years of Industrial Experience with the SST Turbulence Model.*" Turbulence, Heat and Mass Transfer 4, Begell House, Inc.

[206] **Roulund**, A.; **Sumer**, B.M.; **FredsØe**, J. and **Michelsen,** J. (2005): *"Numerical and Experimental Investigation of Flow and Scour around a Circular Pile".* J. Fluid Mechanics, 534, 351–401.

[207] **Engineeringtoolbox**, "Flow section channel." (Hydraulic diameter values) Available from: <http://www.engineeringtoolbox.com/flow-section-channels-d_965.html > [28/08/2015]

[208] **ANSYS Inc**. (2015): "*ANSYS FLUENT User Guide"*, Release 16.0

[209] **Danielle** (2012, 7 March) "*How to determine time step and Max. Iterations per time step."* [Online forum comment] Message posted to: <http://www.cfd-online.com/Forums/fluent/98249-how-determine-time-step-size-max-iterations-per-time-step.html > [06/09/2015]

[210] **Qfinsoft** (2015): Personal communication with experienced CFD modellers at Qfinsoft

[211] **Lai,** A. C. K. and **Chen**, F. Z. (2007): "*Comparison of a new Eulerian model with a modified Lagrangian approach for particle distribution and deposition indoors.*" Atmospheric Environment, vol. 41, pp. 5249-5256, 2007.

[212] **Sebesta,** C.J. (2012): "Modeling the Effect of Particle Diameter and Density on Dispersion in an Axisymmetric Turbulent Jet." Masters' thesis, Virginia Polytechnic Institute and State University, Blacksburg, Va

[213] **Cook**, C.B. and **Richmond**, M.C. (2001): "*Simulation of Tailrace Hydrodynamics Using Computational Fluid Dynamics Models."* U.S. Army Corps Of Engineers, Portland District

[214] **Kotze**, D. (2015) "*The prediction of scour hle geometry for plunging jets.*" Undergraduate study, University of Stellenbosch, South Africa

Appendix A

Table A-1 -Turbulence intensity and kinetic energy correction factor for different spillway types

Case	Schematic	Type of jet	Type of intake	Boundary development layer	Outlet structure	Hydrodynamics	Aeration	Angle of lower nappe	Angle of upper nappe	Turbulence intensity *Tu* (%)	Kinetic energy correction factor (–)
1			WES weir (gated or non-gated)	Fully or partially developed	Ski jump (plane bucket)	$P(n)$ concave $V(n)$ deformed logaritmic tending to uniform	Partially or fully aerated core	Tang(lip)	Approx. tange(lip), eventual correction	4–8%, take 4% for high velocities	Tending toward 1.0 for high velocities
2		Trajectory	Orifice, low head	Non-developed	Curved lip	$P(n)$ hydrostatic, $V(n)$ turbulent ev. swirling tending to uniform for high V	Depending on submergence	Tang(lip)	Approx. tange(lip), eventual correction	3–8%	Tending toward 1.0 for high velocities
3			Orifice, high head	Non-developed	Curved lip	$P(n)$ hydrostatic, $V(n)$ quasi-uniform	None	Tang(lip)	Approx. tang(lip), eventual correction	2–4%	Approx. 1.0
4			WES weir, short chute	Partially developed	Straight lip	$P(n)$ approximately parabolic, $V(n)$ almost uniform	None	Tang(lip)	Approx. tang(lip)	Low, < 3%	Approx. 1.0
5		Overfall	WES weir, long chute	Partially or fully developed	Straight or Curved lip	$P(n)$ hydrostatic, $V(n)$ turbulent uniform	Partially aerated	Tang(lip)	Approx. tang(lip)	4–5%	Approx. 1.1
6			Broad-crested weir	Non-developed	Straight lip	$P(n)$ approx. parabolic, $V(n)$freefall quadratic	None	Horizontal	Approx. 4–5°	Low, < 3% but may depend on crest details	Approx.1.0
7		Complex	WES weir	Partially or fully developed	Blocks or deflectors	Mixed	Partially or fully aerated	Tang(lip)	Approx. tang(lip)	8% overall or more	—

$P(n)$ and $V(n)$ stand for pressure and velocity profile at issuance, respectively. Initial jet turbulence intensity and kinetic energy correction factor α are according to the type of outlet based on experimental results with high-velocity jet flows.

Appendix B

Annandale EIM geological parameter tables [98]:

Table B-1 - Mass strength number rock (M_s) [96,98,99]

Strength	Description of Condition	Unconfined Compressive Strength (MPa)	Mass Strength Number (M_s)
Very Weak Rock	Material crumbles under firm (moderate) blows with sharp end of a geological pick and can be peeled with a knife; too hard to cut triaxial sample by hand	< 1.7 1.7-3.3	0.87 1.86
Weak Rock	Can be just scraped and peeled with a knife; indentations 1 mm to 3 mm show in the specimen with firm (moderate) blows with the pick point	3.3-6.6 6.6-13.2	3.95 8.39
Strong Rock	Cannot be scraped or peeled with a knife; hand-held specimen can be broken with hammer end of geological pick with a single firm (moderate) blow	13.2-26.4	17.70
Very Strong Rock	Handheld specimen breaks with hammer end of pick under more than one blow	26.4-53.0 53.0-106.0	35.0 70.0
	[UCS 106-212 MPa missing from table]	106-212	none listed
Extremely Strong Rock	Specimen requires many blows with a geological pick to break through intact material	> 212.0	280.0

Table B-2 - Joint set number rock (J_n) [96,98,99]

Description of joint sets	J_n
Intact, no or few joints/fissures	1.00
One joint/fissure set	1.22
One joint/fissure set plus random	1.50
Two joint/fissure sets	1.83
Two joint/fissure sets plus random	2.24
Three joint/fissure sets	2.73
Three joint/fissure sets plus random	3.34
Four joint/fissure sets	4.09
Multiple joint/fissure sets	5.00

Table B-3- Joint roughness number (J_r) [96,98,99]

Joint separation	Joint surface condition	Joint roughness number (Jr)
Joints are tight or become closed during hydraulic flow	Discontinuous joints; stepped	4.0
	Rough/irregular; undulating (e.g., tension joints, rough sheeting joints, rough bedding)	3.0
	Smooth undulating	2.0
	Slickensided; undulating	1.5
	Rough/irregular; planar	1.5
	Smooth; planar (e.g., planar sheeting joints, planar foliation and bedding)	1.0
	Slickensided; planar	0.5
Joints are open and remain open during hydraulic flow	Joints, fractures, or bedding either open or contains relatively soft gouge of sufficient thickness to prevent wall contact during turbulent stream flow	1.0
	Shattered or micro-shattered	1.0

Table B-4 - Joint alteration number (J_a) [96,98,99]

Joint surface condition	< 1mm	1 – 5mm	≥5mm
Joint tightly healed with hard, nonsoftening, impermeable mineral filling, e.g., quartz, calcite, or epidote	0.75	1.0	1.5
Clean, open joint with fresh or discoloured (unweathered) walls only; no infilling.	1.0	1.5	2.0
Discoloured to disintegrated joint walls; infilling is sand or gravel with < 15% cohesionless fines in matrix; with or without disintegrated or crushed rock fragments.	2.0	4.0	6.0
Discoloured to disintegrated joint walls; cohesion less, non-swelling, low to non-plastic fines in matrix; with or without disintegrated or crushed rock fragments.	3.0	6.0	10.0
Disintegrated to decomposed joint walls; nonswelling, lean clay or clay matrix, or low friction clays, such as chlorite, talc, mica, serpentine, gypsum, graphite, kaolinite, or other sheet silicates; with or without disintegrated or crushed rock fragments.	4.0	8.0	13.0
Disintegrated to decomposed joint walls; fat clay, swelling clay, such as montmorillonite, or clay matrix, with or without disintegrated or crushed rock fragments.	5.0	10.0	18.0

Some general ratios for different rock types are shown in the table below [103]:

Table B-5 - Relative ground structure number (J_s) [96,98,99]

Dip Direction of Closer Spaced Joint Set (degrees)	Dip Angle of Closer Spaced Joint Set (degrees)	Ratio of Joint Spacing (1:r)r=y/x where x is short and y is long dimension [use J_s for 1:8 if r > 1:8]			
		1:1	1:2	1:4	1:8
180/0	Vertical 90	1.14	1.20	1.24	1.26
Dip Direction Downstream (Against Direction of Water Flow)	89	0.78	0.71	0.65	0.61
	85	0.73	0.68	0.61	0.57
	80	0.67	0.60	0.55	0.52
	70	0.56	0.50	0.46	0.43
	60	0.50	0.46	0.42	0.40
	50	0.49	0.46	0.43	0.41
	40	0.53	0.49	0.46	0.45
	30	0.63	0.59	0.55	0.53
	20	0.84	0.77	0.71	0.67
	10	1.25	1.10	0.98	0.90
	5	1.39	1.23	1.09	1.01
	1	1.50	1.33	1.19	1.10
0/180	Horizontal 0	1.14	1.09	1.05	1.02
Dip Direction Upstream (Against Direction of Water Flow)	-1	0.78	0.85	0.90	0.94
	-5	0.73	0.79	0.84	0.88
	-10	0.67	0.72	0.78	0.81
	-20	0.56	0.62	0.66	0.69
	-30	0.50	0.55	0.58	0.60
	-40	0.49	0.52	0.55	0.57
	-50	0.53	0.56	0.59	0.61
	-60	0.63	0.68	0.71	0.73
	-70	0.84	0.91	0.97	1.01
	-80	1.26	1.41	1.53	1.61
	-85	1.39	1.55	1.69	1.77
	-89	1.50	1.68	1.82	1.91
180/0	Vertical -90	1.14	1.20	1.24	1.26
		Use 1.0 for intact, unjointed rock mass			